THE INFLUENCE OF A MAGNETIC FIELD ON THE SORPTION OF RADIONUCLIDES BY CLINOPTILOLITE AND COMPOSITE SORBENTS BASED ON ZEOLITES

Oleksii Yu. Lonin*, Volodymyr V. Levenets, Oleksandr M. Bovda

National Science Center "Kharkov Institute of Physics & Technology",
1, Akademichna St., Kharkiv, 61108, Ukraine
*Corresponding Author e-mail: a_lonin@kipt.kharkov.ua, a_lonin@ukr.net

Two methods of using permanent NdFeB magnets and their impact on the sorption of radionuclides (Cs, Sr, Co) by clinoptilolite and composite sorbents based on zeolites are discussed. Sorption processes were considered under dynamic conditions with liquid circulation. No changes in sorption processes were observed when magnetic treatment was applied to solutions containing radionuclide ions. The natural zeolite clinoptilolite and synthetic zeolites NaX and NaA were considered at this stage. In the work, clinoptilolite from the Sokirnitske deposit in the Zakarpattia region of Ukraine was used. Ukraine possesses significant deposits of clinoptilolite. When magnets were applied to the sorbent during the sorption process, an increase in cobalt sorption of 10% was observed for clinoptilolite, and strontium sorption increased by 17%. The influence of a magnet on clinoptilolite is due to the presence of iron ions in the composition of clinoptilolite. The iron content ranges from 0.9% to 2.5%. The composition of the composite sorbent included clinoptilolite and synthetic zeolite NaX. No increase in radionuclide sorption was observed for composite sorbents, likely due to the presence of clinoptilolite in the sorbent composition and the corresponding iron content. The analytical part of the study was carried out using the PIXE (Particle Induced X-ray Emission) method on the analytical nuclear-physics complex "Sokil." The energy range of the accelerator was 200-2000 keV. The complex made it possible to carry out all the main methods of analysis using ion beams. The targets were placed in the exit, at the Chamber for PIXE. To excite the atoms of cesium, strontium, and cobalt a proton beam with an energy of $E_p \approx 1400$ keV was used.

Keywords: *Clinoptilolite; Synthetic zeolite; Dynamic sorption; Cesium; Strontium; Permanent magnet*
PACS: 68.48.Mn;82.75.-z;82.80Ej;85.70.-w

The challenging conditions of modern times indicate a growing threat of technogenic accidents related to nuclear energy. The causes of accidents can stem not only from technical failures associated with the operation of nuclear facilities but also from armed conflicts near nuclear energy facilities and threats associated with the activities of terrorist groups. Given these factors, there is an increasing demand for sorbents that can be used in nuclear energy. The main criteria for the use of sorbents are the ratio of sorbent effectiveness to its cost. In such circumstances, the use of natural sorbents comes to the forefront. One such sorbent is zeolites. However, the use of zeolites is associated with several limitations. The first limitation is significant variations in composition depending on the location of the deposit and its depth. The second limitation is the limited range of radionuclides that zeolites can absorb. A notable example of a natural zeolite is clinoptilolite. Clinoptilolite exhibits high selectivity for cesium but lags in the sorption of other radionuclides. Therefore, one effective approach to using clinoptilolite is the creation of composite sorbents by adding synthetic zeolites that do not have the mentioned limitations. The application of synthetic zeolites is effective for the sorption of strontium and cobalt.

There are alternative methods to enhance the sorption properties of clinoptilolite besides creating composite sorbents. Special attention is required for the use of zeolite activation methods, which can increase sorption properties without a significant increase in the cost of sorbent production. Such methods include thermal activation and the activation of sorbents using a magnetic field. The possibilities and results of thermal activation were discussed by us earlier.

The potential application of magnets to increase sorption has been explored by various authors [4].

When considering the possibility of magnetic activation of sorption processes, we chose permanent magnets as our preferred option. This decision was influenced by factors such as the mobility of the sorption setup and the elimination of the need to seek additional power sources for alternating current magnets.

The experiment was divided into two directions:

1. The influence of a permanent magnet on a solution containing radionuclides that was moving through a system of pipelines.

2. The influence of a permanent magnet on the sorbent located in the sorption column.

The impact of the permanent magnet on the solution involved placing the magnet on the pipeline of the sorption setup. As a result, cesium ions present in the solution and moving through the pipeline system of the sorption setup were subjected to the influence of magnetic fields. This was expected to enhance the interaction of polarized ions with the exchange centers of the sorbent.

Another approach involved the continuous influence of magnets on the sorbent. The idea of the magnetic influence on the sorbent is related to the composition of natural zeolite (clinoptilolite). According to existing literature and based on the data we obtained; iron is part of the composition of clinoptilolite. The continuous influence of a magnetic field should

polarize the iron ions that are part of clinoptilolite's composition. Some authors conduct additional synthesis of zeolite to increase the magnetic influence on clinoptilolite. This synthesis involves additional treatment of zeolite intending to increase the iron content. In our work, we did not perform additional treatment and used zeolite with its natural iron content. The Fe_2O_3 content is 0.9%. Some aluminum atoms in the clinoptilolite structure are replaced with iron atoms (Figure 1).
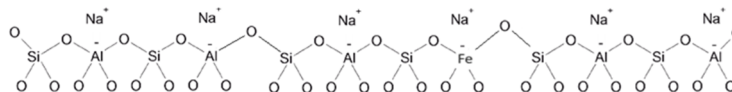
Figure 1. Structure of clinoptilolite with the substitution of aluminum ions by iron ions

It should be noted that synthetic zeolites do not contain iron in their composition unless specified by the synthesis conditions. The synthetic zeolites considered in the study do not contain iron in their composition.

The study examined two mechanisms of the influence of permanent magnets on the sorption of radionuclides by clinoptilolite and composite sorbents.

The first mechanism investigated the effect of permanent magnets on a solution containing radionuclides. The influence of magnets was expected to enhance the polarization of radionuclide ions and increase their sorption when interacting with the exchange centers of zeolites.

The second mechanism studied the influence of permanent magnets on clinoptilolite due to the presence of iron ions in its composition.

All experiments were conducted without protection from the Earth's magnetic field, which generally ranges from $2.5 \cdot 10^{-5}$ T (at the magnetic equator) to $6.5 \cdot 10^{-5}$ T (at the geomagnetic poles). With knowledge of the distribution, it is possible to determine the intensity of the magnetic field at the research location for sorption. However, the magnetic field created by the NdFeB magnet is 1.26 T, which is significantly higher than the Earth's magnetic field, and therefore, the latter was not considered.

MATERIALS AND METHODS
Research Objects

Experiment Objects and Materials As sorbents, natural zeolite (clinoptilolite), synthetic zeolite NaX, and zeolite NaA were used. In the work, clinoptilolite from the Sokirnitske deposit in the Zakarpattia region of Ukraine was used. Ukraine possesses significant deposits of clinoptilolite. Additionally, the following sorption compositions based on zeolites were utilized:
1. Clinoptilolite - 100% + Zeolite NaX - 0% (ClSZ_1).
2. Clinoptilolite - 50% + Zeolite NaX - 50% (ClSZ_2).
3. Clinoptilolite - 25% + Zeolite NaX - 75% (ClSZ_3).

NdFeB magnets manufactured by NSC KIPT [10,11] were used as permanent magnets.

Cesium, strontium, and cobalt nitrates were used as contaminating substances.

EXPERIMENT ON DYNAMIC SORPTION WITH THE PLACEMENT OF MAGNETS ON THE PIPELINE

The design of the setup for dynamic sorption, which had been used previously, was modified to accommodate the use of magnets [12].
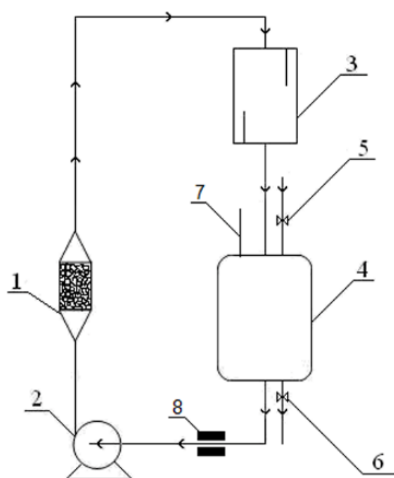
Figure 2. Sorption setup scheme: 1 - sorption column, 2 -- pump, 3 - measuring cylinder, 4 - collection reservoir, 5,6 - supply and drain valves, 7 - air supply tube, 8 - magnets

Before the solution passed through the sorption column on the pipeline, two magnets were installed (Figure 2). The pipeline had a diameter of 16 mm, and two square magnets, each measuring 30×30 mm with a magnet thickness of 6 mm, were installed on the pipeline. The magnetic force of these magnets was approximately 13 kg, with a residual magnetic induction of 1.22 - 1.26 T. The magnet's grade was N38. Using this setup design, 40 cycles of sorption were conducted with clinoptilolite and synthetic zeolites NaX and NaA.

EXPERIMENT ON DYNAMIC SORPTION WITH MAGNETS PLACED ON THE SORPTION COLUMN

In the second scheme, a magnet was used to activate the iron that is part of clinoptilolite, resulting in a change in the material used for the sorption column (plastic). Taking into account that the magnet may affect the pump, the positioning of the sorption column relative to the pump was changed (Figure 3). For magnetic treatment, two magnetic discs were used, which were positioned around the sorption column filled with sorbent. For a greater impact of the magnets, the sorption column was made of polymer materials. The external diameter of the sorption column was 16

mm. The magnetic discs had an inner diameter of 16 mm, an outer diameter of 40 mm, and a magnet thickness of 10 mm. The magnetic force of the magnet was approximately 13 kg, with a residual magnetic induction of 1.22 - 1.25 T, the coercive force from magnetization ≥955 kA/m, and a grade of N38.
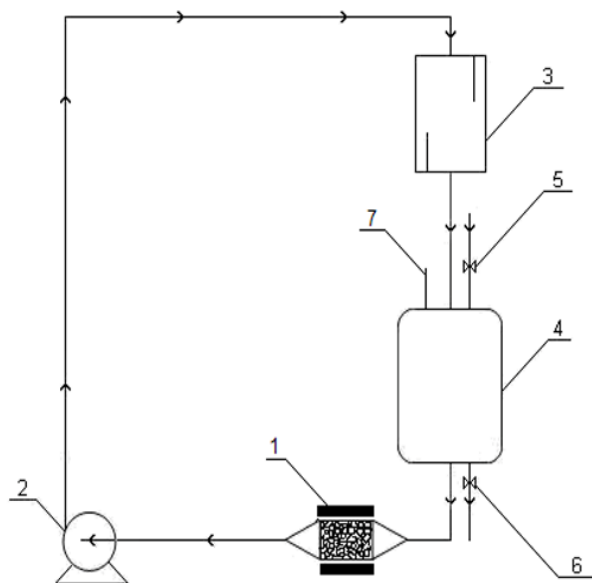
Figure 3. Sorption setup scheme: 1 - sorption column with magnet, 2 - pump, 3 - measuring cylinder, 4 - collection reservoir, 5,6 - supply and drain valves, 7 - air supply tube

PREPARATION OF TARGETS

To prepare the targets, a carbon substrate made from carbon rods was used. The carbon substrate had the shape of a rectangle with dimensions of 10 mm in length, 5 mm in width, and 2 mm in thickness. A solution containing a mixture of cesium, strontium, and cobalt isotopes was applied to the carbon substrate in an amount of 0.05 ml and dried by heating to 35°C. The solution was applied using an adjustable volume automatic pipette.

ANALYTICAL PART OF THE EXPERIMENT

The analytical investigations of Co, Sr, and Cs content were performed using the PIXE method (Particle Induced X-ray Emission). The analytical part of the work was carried out at the analytical nuclear-physical complex "Sokil" [13]. The energy range of the accelerator was 200-2000 keV. Targets were placed in a cassette located in the irradiation chamber. Before conducting measurements, a vacuum was created in the chamber with a pressure of 10^{-4} Pa. To excite characteristic X-ray radiation (XRR) of Cs, Sr, and Co atoms, a proton beam with a current of 200 nA and an energy of 1400 keV was used [12, 14, 15]. At this energy, the characteristic X-ray radiation of the L-series of cesium atoms and the K-series of strontium and cobalt is effectively excited. Measurement of characteristic X-ray radiation was carried out using the XR-100CR Si-pin X-ray detector. The detector was located outside the irradiation chamber at a distance of 7 cm from the target, at an angle of 135° to the direction of the proton beam. XRR exited the chamber through a 25 μm thick beryllium foil window. In previous studies to determine the content of cesium, strontium, and cobalt ions, for the optimization of spectrometric conditions for XRR spectra formation, a collimator with hole diameters of Ø 1.5 mm and polyethylene absorbing films 150 μm thick were used [12, 14, 15]. X-ray spectra were processed using the WinQXAS code.

RESULTS AND DISCUSSION

To determine the sorption properties, a sorption coefficient was used to quantitatively assess the interaction of clinoptilolite and composite sorbent with radionuclides. The sorption coefficient (Sorption, %) was calculated using the following formula (1):

$$Sorption, \% = \frac{(C_0 - C_{eq}) \cdot 100\%}{C_0}.$$

(1)

where C_o and C_{eq} are the initial and equilibrium concentrations of the solution, mg/ml.

INFLUENCE OF A PERMANENT MAGNETIC FIELD ON THE SOLUTION

The research aimed to investigate the effect of magnets on a cesium solution during sorption by zeolites in dynamic conditions. The solution was circulated through the setup while being exposed to the magnetic field of the magnets. Analysis of the sorption properties of natural and synthetic zeolites was conducted for their potential use in nuclear energy for the immobilization of high-level radioactive waste. The obtained data indicates that the introduction of magnets into the sorption scheme leads to a 1% change in sorption, which falls within the experimental error of -5%. The sorption process for clinoptilolite in dynamic conditions consists of two stages: rapid and slow. The rapid stage occurs from the 1st to the 30th sorption cycle and is characterized by a quick increase in the sorption coefficient. This is associated with the establishment of partial sorption equilibrium in the solution-adsorbent system. The slow stage of sorption takes place from the 30th to the 40th sorption cycles and is characterized by a gradual increase in the sorption coefficient. It was found that sorption equilibrium for clinoptilolite is achieved after 30 sorption cycles (Figure 4). The maximum value of the sorption coefficient after 30 sorption cycles is 82.46% when using clinoptilolite and 81.50% when using clinoptilolite with magnetic treatment of the solution.

Next, the data for cesium sorption by synthetic zeolites was examined. For zeolite NaX, saturation is achieved after 20 sorption cycles (Figure 5). The fast sorption stage occurs from the 1st to the 20th cycle. The sorption coefficient for zeolite NaX is 82.45% when using only zeolite NaX and 83.40% when using zeolite NaX with magnetic treatment of the solution.

For zeolite NaA, saturation occurs after 10 sorption cycles (Figure 6). The fast sorption stage occurs from the 1st to the 10th cycle. The sorption coefficient after completing the fast stage is 68.15% when using only zeolite NaA and 69.30% when using zeolite NaA with magnetic treatment of the solution.

Figure 4. Kinetic Sorption Curves of Cesium by Clinoptilolite in Dynamic Conditions. B - pure sorbent; C- sorbent with magnetic treatment of the solution
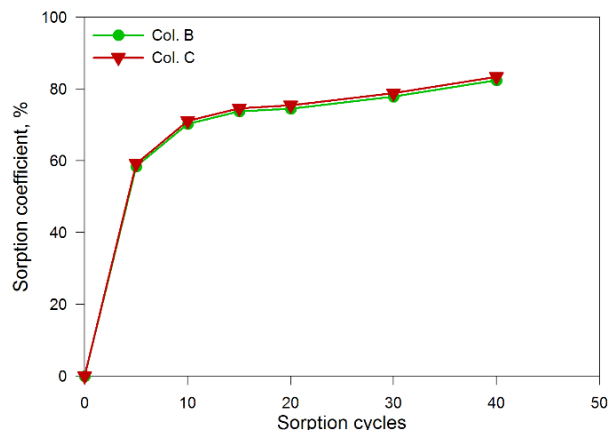
Figure 5. Kinetic Sorption Curves of Cesium by Zeolite NaX in Dynamic Conditions. B - pure sorbent; C - sorbent with magnetic treatment of the solution
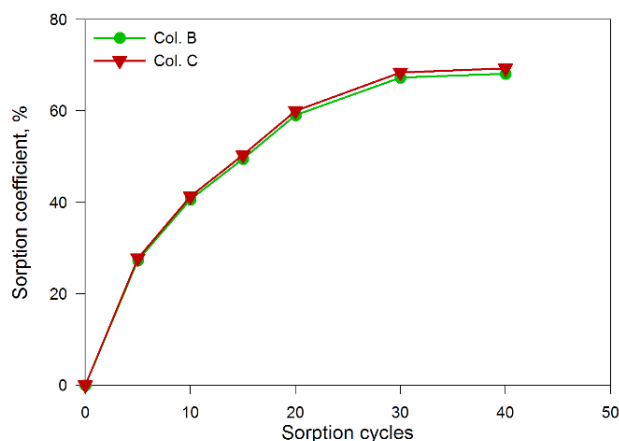
Figure 6. Kinetic Sorption Curves of Cesium by Zeolite NaA in Dynamic Conditions. B - pure sorbent; C - sorbent with magnetic treatment of the solution

The use of magnets on the pipeline during dynamic sorption of cesium by zeolites does not lead to significant changes in sorption and falls within the experimental error. Zeolite NaA did not exhibit significant sorption values. Further research considered the influence of clinoptilolite and composite sorbents based on clinoptilolite and synthetic zeolite NaX in different ratios. Synthetic zeolite NaX showed good sorption properties.

EFFECT OF A PERMANENT MAGNETIC FIELD ON THE SORBENT

According to available data, in clinoptilolite, a portion of aluminum ions is replaced by iron ions. The iron content ranges from 0.9% to 2.5%. Therefore, magnetic fields can have a significant impact on the sorption properties of clinoptilolite. With this in mind, significant changes were made to the sorption setup (Figure 3). The sorbent was placed in a plastic sorption column, and an external magnet, affecting the zeolites inside the column, was located on the outer diameter of the sorption column. The results for a mixture of isotopes and different sorbents are presented in Figures 7-9, and a comparison of sorption with and without the magnet is provided in Table 1. The results in Figures 6-8 indicate that the influence of a permanent magnetic field on the sorbent exhibits unexpected characteristics, resulting in non-typical jumps in the sorption of the examined isotopes for composite sorbents. One of the reasons is the presence of isotopes (ions) in the solution with different atomic radii, which significantly affects the mobility of ions and their distribution in sorption structures. For clinoptilolite, when subjected to the influence of a permanent magnetic field during dynamic sorption, there is an increase in Ks (cobalt) by 10% and Ks (strontium) by 17%, with a 9% decrease in Ks (cesium). For composite sorbents, considering the reduced portion of clinoptilolite (down to 50% and 25%), as well as the changes introduced in the sorption setup (Figure 3), a decrease in sorption indicators is observed. This is related to the contribution of clinoptilolite to the composite sorbents. An increase in the proportion of clinoptilolite leads to enhanced sorption properties of the sorbent for cobalt and strontium. This is because clinoptilolite contains iron oxides, which, unlike aluminum, are significantly affected by the permanent magnetic field.
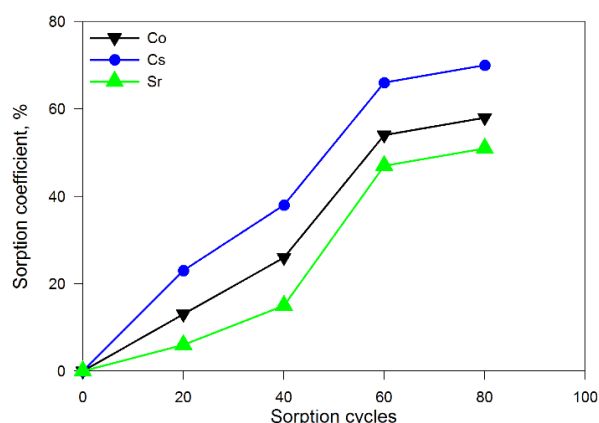
Figure 7. Kinetic curves of the sorption of a mixture of isotopes (Co, Cs, Sr) by clinoptilolite under the influence of a permanent magnetic field
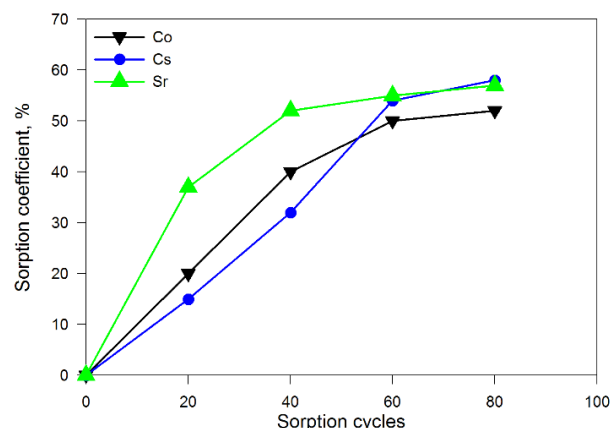
Figure 8. Kinetic curves of the sorption of a mixture of isotopes (Co, Cs, Sr) by a composite sorbent (clinoptilolite - 50 + zeolite NaX - 50) under the influence of a permanent magnetic field
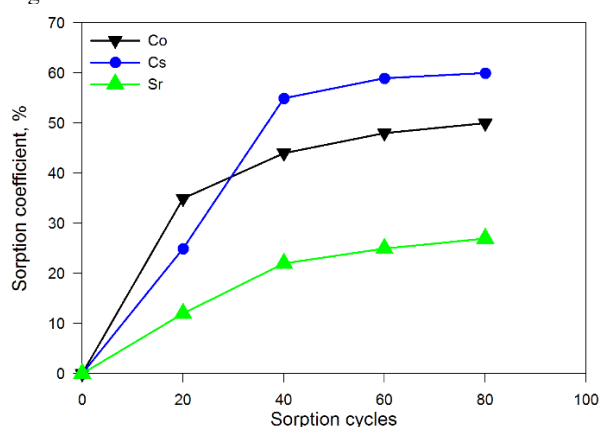
Figure 9. Kinetic curves of the sorption of a mixture of isotopes (Co, Cs, Sr) by a composite sorbent (clinoptilolite - 25 + zeolite NaX - 75) under the influence of a permanent magnetic field

Table 1. Influence of a permanent magnetic field on the sorption properties of clinoptilolite and composite sorbent

Sorbent	Sorption Cycles	Sorption coefficient (Sorption, %)		
		Cobalt	Cesium	Strontium
Clinoptilolite (ClSZ_1)	80	48±1.4%	81±2.4%	34±1.0%
Clinoptilolite (ClSZ_1)+ magnet	80	58±1.7%	70±2.1%	51±1.5%
Clinoptilolite -50+zeolite NaX -50 (ClSZ_2)	80	79±2.4%	80±2.4%	70±2.1%
Clinoptilolite -50+zeolite NaX -50 (ClSZ_2) +magnet	80	52±1.5%	58±1.7%	57±1.7%
Clinoptilolite -25+zeolite NaX -75 (ClSZ_3)	80	71±2.1%	65±1.9%	66±2.0%
Clinoptilolite -25+zeolite NaX -75 (ClSZ_3) + magnet	80	50±1.5%	60±1.8%	27±0.8%

CONCLUSIONS

Experiments were conducted to determine the dynamic sorption under the influence of a permanent magnetic field of the NdFeB magnet, which acted on both the solution and the sorbent.

It was established that the influence of a permanent magnetic field of the NdFeB magnet on the cesium solution moving in the pipeline during dynamic sorption did not increase the sorption coefficients of zeolites. This is because the parameters of the experiment considered in the work (the magnet and the flow rate of the solution) require further research and clarification.

The second part of the work aimed to determine the influence of the magnetic field of NdFeB magnets on the sorbent located in the sorption column. It was found that clinoptilolite, under the influence of a permanent magnetic field, changes its sorption properties due to the presence of iron ions in its composition. An increase in the sorption coefficient for cobalt by 10% and strontium by 17% was observed.

For composite sorbents, there were no changes in sorption under the influence of the permanent magnetic field of the NdFeB magnet. This is because the portion of clinoptilolite in the composition of the composite sorbent with a certain iron content is significantly lower than in pure clinoptilolite. In the composite sorbents considered, the percentage of clinoptilolite was 50% for the ClSZ_2 sorbent and 25% for the ClSZ_3 sorbent.

ORCID
Oleksii Yu. Lonin, https://orcid.org/0000-0002-5386-3825; **Volodymyr V. Levenets,** https://orcid.org/0000-0002-6439-0576
Oleksandr M. Bovda, https://orcid.org/0000-0002-1684-1475

REFERENCES

[1] Mineralogical Society of America, 3635, Concorde Pkwy Ste 500, Chantilly, VA 20151-1110 United States, http://rruff.geo.arizona.edu/AMS/result.php

[2] L. Velarde, M.S. Nabavi, E. Escalera, M.-L. Antti, and F. Akhta, Chemosphere, **328**, 138508 (2023), https://doi.org/10.1016/j.chemosphere.2023.138508

[3] D. Breck, *Zeolite molecular sieves*, (Wiley, New York, 1974).

[4] B.A. Baran, Adsorption Science & Technology, **19**(1), 85 (2001). https://doi.org/10.1260/0263617011493999

[5] M. Václavíková, K. Stefusova, L. Ivaničová, S. Jakabsky, and G.P. Gallios, "Magnetic Zeolite as Arsenic Sorbent," in: *Water Treatment Technologies for the Removal of High-Toxicity Pollutants. NATO Science for Peace and Security Series C: Environmental Security*, edited by M. Václavíková, K. Vitale, G.P. Gallios, L. Ivaničová, (Springer, Dordrecht, 2009). pp. 51-59 https://doi.org/10.1007/978-90-481-3497-7_5

[6] J.-L. Cao, X.-W. Liu, R. Fu, and Z.-Y. Tan, Separation and Purification Technology, **63**(1), 92 (2008). https://doi.org/10.1016/j.seppur.2008.04.015

[7] E. Pérez-Botella, S. Valencia, and F. Rey, Chemical Reviews, **122**24), 17647 (2022). https://doi.org/10.1021/acs.chemrev.2c00140

[8] A.R. Loiola, R.A. Bessa, C.P. Oliveira, A.D.L. Freitas, S.A. Soares, F. Bohn, and S.B.C. Pergher, Journal of Magnetism and Magnetic Materials, **560**, 169651 (2022). https://doi.org/10.1016/j.jmmm.2022.169651

[9] M. Maharana, and S. Sen, Materials Today: Proceedings, **47**(7), 1490 (2021). https://doi.org/10.1016/j.matpr.2021.04.370

[10] A.M. Bovda, D.V. Kutniy, L.V. Onishchenko, V.A. Finkel, O.M. Utva, and V.A. Bovda, PAST, (5), 74 (2000). https://vant.kipt.kharkov.ua/ARTICLE/VANT_2000_5/article_2000_5_74.pdf (in Russian)

[11] O.M. Bovda, V.O. Bovda, G.S. Koshkarev, L.V. Onishchenko, and O.S. Tortika, PAST, (6), 248 (2009). https://vant.kipt.kharkov.ua/ARTICLE/VANT_2009_6/article_2009_6_248.pdf (in Ukrainian)

[12] A.Yu. Lonin, V.V. Levenets, I.M. Neklyudov, and A.O. Shchur, JRNC, **303**, 831 (2015). https://doi.org/10.1007/s10967-014-3597-9

[13] S.G. Karpus, V.V. Kuzmenko, V.V. Levenets, O.Yu. Lonin, A.P. Omelnik, A.O. Shchur, V.I. Sukhostavets, PAST, 2(144), 134 (2023). https://doi.org/10.46813/2023-144-134

[14] V.V. Levenets, A.Yu. Lonin, O.P. Omelnik, and A.O. Shchur, JECE, **4**(4), 3961 (2016). https://doi.org/10.1016/j.jece.2016.09.011

[15] A.Yu. Lonin, V.V. Levenets, O.P. Omelnik, and A.O. Shchur, JRNC, **315**, 163 (2021). https://doi.org/10.1007/s10967-017-5676-1

ВПЛИВ МАГНІТНОГО ПОЛЯ НА СОРБЦІЮ РАДІОНУКЛІДІВ КЛІНОПТИЛОЛІТОМ ТА КОМПОЗИЦІЙНИМ СОРБЕНТОМ НА ОСНОВІ ЦЕОЛІТІВ

Олексій Ю. Лонін, Володимир В. Левенець, Олександр М. Бовда

Національний науковий центр «Харківський фізико-технічний інститут»,
1, вул. Академічна, 61108, Харків, Україна

В роботі розглядається два метода використання постійних магнітів NdFeB та їх вплив на сорбцію радіонуклідів (Cs,Sr,Co) клиноптилолітом та композиційними сорбентами на основі цеолітів. Сорбційні процеси розглядалися в динамічних умовах з циркуляцією рідини. При магнітній обробці розчинів, що містять іони радіонуклідів, змін у сорбційних процесах не спостерігалося. На цьому етапі розглядалися природний цеоліт клиноптилоліт і синтетичні цеоліти NaX і NaA. У роботі використано клиноптилоліт Сокирницького родовища Закарпатської області України. В Україні є значні поклади клиноптилоліту. При застосуванні магнітів до сорбенту в процесі сорбції спостерігалося збільшення сорбції кобальту для клиноптилоліту на 10%, а сорбції стронцію – на 17%. Вплив магніту на клиноптилоліт обумовлений наявністю в складі клиноптилоліту іонів заліза. Вміст заліза коливається від 0,9% до 2,5%. До складу композиційного сорбенту входили клиноптилоліт та синтетичний цеоліт NaX. Збільшення сорбції радіонуклідів для композитних сорбентів не спостерігалося, ймовірно, через наявність у складі сорбенту клиноптилоліту та відповідного вмісту заліза. Аналітичну частину дослідження виконано методом PIXE (Particle Induced X-ray Emission) на аналітичному ядерно-фізичному комплексі «Сокіл». Енергетичний діапазон прискорювача становив 200-2000 кеВ. Комплекс дозволяв проводити всі основні методи аналізу за допомогою іонних променів. Цілі були розміщені на виході, у камері для PIXE. Для збудження атомів цезію, стронцію та кобальту використовувався пучок протонів з енергією Ер≈1400 кеВ.

Ключові слова: *клиноптилоліт; синтетичний цеоліт; динамічна сорбція; цезій; стронцій; постійний магніт*

INVESTIGATION OF TEMPERATURE AND CHANNEL DIMENSION EFFECTS ON CMOS CIRCUIT PERFORMANCE

Zitouni Messai[a,b], Abdelhalim Brahimi[a,b], Okba Saidani[a], Nacerdine Bourouba[b], Abderrahim Yousfi[a]*

*[a] ETA Laboratory, Department of electronics, Faculty of technology, University Mohamed El Bachir
El Ibrahimi of Bordj Bou Arréridj-34030, Algeria*
[b] LIS Laboratory, Department of electronics, Faculty of technology, University Ferhat Abbas Sétif 1, Sétif-19000, Algeria
*Corresponding Author e-mail: Abderrahim.yousfi@univ-bba.dz

This paper presents the impact of temperature variations and alterations in transistor channel dimensions on CMOS (Complementary Metal-Oxide-Semiconductor) circuit technology. To facilitate this investigation, we first identified critical parameters characterizing the device's performance, which could exhibit susceptibility to these influences. The analysis encompassed critical metrics such as the transfer characteristic, drain current, logic levels, inflection points, and truncation points. These parameters enabled us to validate the results obtained from the PSPICE simulator, which demonstrated unequivocal effectiveness. Notably, our simulation results unveiled significant effects resulting from a wide temperature range spanning from -100°C to 270°C, offering valuable in-sights into thermal-induced failures. Additionally, the influence of channel dimension changes on factors like drain current and transfer characteristics, as well as temporal parameters including signal propagation delay and rise and fall times, were meticulously examined and appreciated.
Key words: *CMOS; Channels dimensions; Temperature; PSPICE*
PACS: 85.30.Tv, 82.20.Xr

1. INTRODUCTION

CMOS (Complementary Metal-Oxide-Semiconductor) technology stands as a cornerstone of modern electronics and integrated circuits, transforming the landscape of semiconductor electronics [1-2]. It has ushered in a new era of innovation, impacting the design and operation of electronic devices, from microprocessors in computers to sensors in smartphones and beyond [3]. At its core, CMOS leverages the unique properties of complementary transistor pairs, combining p-type and n-type transistors to create highly efficient and low-power digital logic circuits [4-5]. This complementary behavior results in minimal power consumption during idle states, rendering CMOS ideal for battery-powered and energy-efficient devices [6]. Beyond its energy efficiency, CMOS's scalability to ever-shrinking transistor sizes has been instrumental in advancing computational power in accordance with Moore's Law [7]. Furthermore, CMOS's reliability, noise immunity [8], and compatibility with various semiconductor materials have solidified its position as the backbone of the semiconductor industry [9-10]. The performance and behavior of CMOS devices and circuits are significantly affected by two pivotal factors: temperature and channel dimensions [11-12]. Precisely managing these variables is essential for optimizing integrated circuit operation, as they wield substantial influence over device characteristics, power consumption, and overall circuit performance [13]. Temperature exerts a profound impact on CMOS devices; as temperature rises, the electrical resistance of materials tends to decrease, affecting transistor performance [14-15]. Elevated temperatures can result in increased leakage currents in transistors, reducing efficiency and potentially compromising reliability [16]. Conversely, low temperatures can decelerate transistor response times [17]. To mitigate these effects, CMOS engineers must diligently implement thermal management techniques to ensure devices function within designated temperature ranges [18-19]. The dimensions of the transistor's channel region play a fundamental role in CMOS technology. Altering these dimensions can significantly impact transistor behavior. Scaling down channel dimensions, a common practice in advanced CMOS nodes, allows for greater transistor density on a single chip, enhancing computational power while reducing power consumption [20]. However, smaller dimensions introduce challenges, including increased leakage currents, short-channel effects, and variability in transistor performance [21]. Engineers must strike a delicate balance when resizing channel dimensions to ensure that the benefits of miniaturization outweigh the drawbacks [22-23]. Understanding the implications of temperature and channel dimensions on CMOS technology is imperative for optimizing the performance, power efficiency, and reliability of semiconductor devices. Engineers and researchers continually strive to discover innovative solutions to manage temperature effects and harness the advantages of altering channel dimensions as CMOS technology progresses [24].

This paper aims to investigate the impact of temperature and geometric alterations on CMOS inverter behavior. To facilitate this study, it is imperative to delineate the parameters that characterize device performance and exhibit susceptibility to these influences. The analysis will encompass key parameters, such as the transfer characteristic, drain current, logic levels, propagation delay, and rise and fall times.

---

2.   STATIC STUDY OF CMOS
2.1. DC results

PSPICE empowers users to craft and virtually replicate electronic circuits within a computer-based environment, functioning as a robust framework for creating and assessing circuit diagrams [25]. It embraces a broad spectrum of circuit configurations, spanning analog and digital domains, thereby facilitating comprehensive scrutiny prior to any physical assembly. Users wield the flexibility to input component specifications, forge circuit connections, and apply voltage sources, thus enabling a profound analysis of circuit responses under diverse operational conditions [26]. PSPICE's capabilities extend to the simulation of transient reactions, the execution of steady-state AC assessments, and the exploration of diverse circuit attributes, thereby providing invaluable assistance in enhancing the comprehension of circuit behavior and performance [27].

Figure 1. CMOS inverter circuit in static mode.

To exemplify the utilization of the SPICE program, we have designed a CMOS inverter. In Figure 1, you can discern the incorporation of a DC input voltage spanning the range from 0V to 5V.

2.2. The transfer characteristic

As we sweep the input voltage, Vin, across a range from 0V to 5V, while keeping the inverter at its default operating conditions and an ambient temperature of 27°C, we observe a corresponding output voltage response that transitions from 5V to 0V. Notably, this voltage shift displays an inflection point precisely at the midpoint, where both input and output voltage levels equate to 2.5V, as visualized in Figure 2. Concurrently, the current flowing through the inverter, denoted as Id, exhibits a value of 60μA, illustrated in Figure 3.
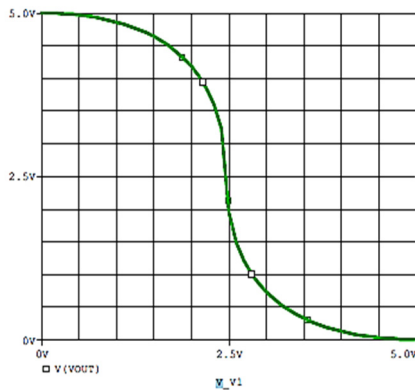
Figure 2. The transfer function Vout =f (Vin).   **Figure 3.** The drain current (Id) of CMOS.
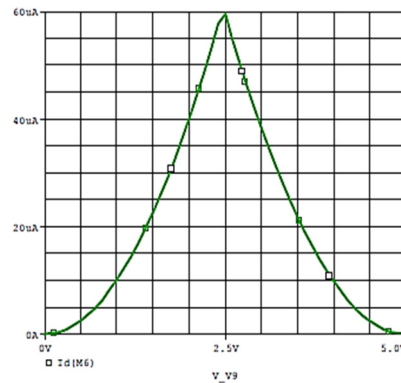
2.3 The temperature effect on CMOS
2.3.1 The effect on the transfer function

When we adjust the temperature of the circuit, both below and above the ambient temperature of 27°C (Figure 4), as detailed in Table 1, we observe a subtle alteration in the transfer functions, where Vout is a function of Vin. This deviation is especially noticeable in the region where the NMOS transistor's behavior is prominent, differing notably from the reference curve indicated in green [28].
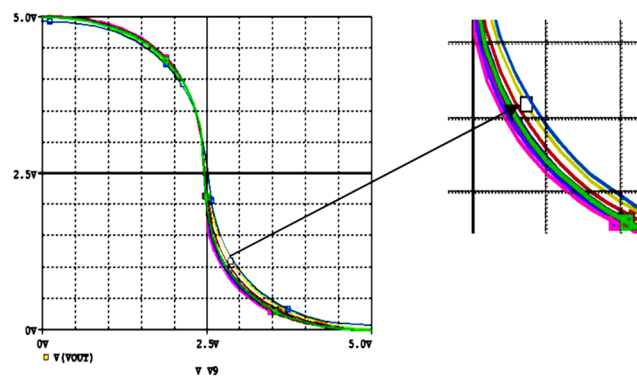
Figure 4. The temperature effect on the transfer function

Table 1. The difference in Idpeak variation as a function of temperature

Temperature (°C)	-100	-50	-20	0	27	50	100	200	270
Idpeak (μA)	118.51	84.353	72.496	66.357	59.558	54.804	46.814	36.42	44.316
ΔIdpeak(μA)	58.952	24.792	12.938	6.799	0	4.754	12.744	23.138	15.242

We note that the maximum drain current (Idpeak) varies with the variation in temperature with a significant difference.

2.3.2. The effect on the drain current:

As depicted in Figure 5, an interesting trend becomes apparent: the peak current, Idpeak, exhibits an inverse relationship with temperature. When the temperature decreases, Idpeak increases, and vice versa. Remarkably, the shape of this relationship remains consistent, with the peak current consistently centered around a voltage Vgs of 2.5V [29]. It's worth noting an exception to this pattern, occurring at the extreme temperature of T = +270°C, where the curve originates with an initial current, Id0, measuring 13.755μA. This initial current serves as the starting point for calculating the incremental changes, as documented in Table 1.
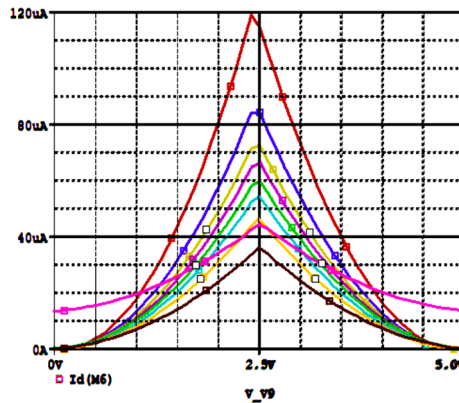
Figure 5. The temperature effect on the drain current.

2.4. The effect of geometric alteration on CMOS
2.4.1. The effect on the drain current

By altering the dimensions of the NMOS transistor channel, specifically the length (referred to as "L") and the width (referred to as "W"), we can observe corresponding variations in two critical parameters: the peak current, Idpeak, and the inflection point. These changes are visually represented in Figures 6 and 7, and their precise values are documented in Table 2 for reference [30].
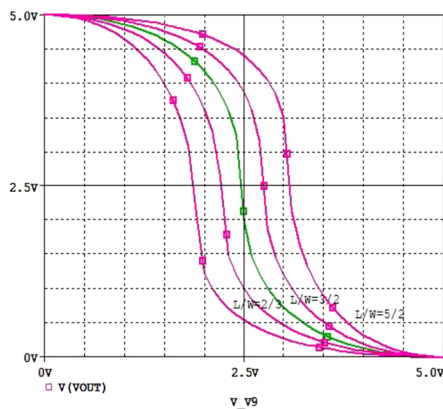
Figure 6. The transfer function Vout =f (Vin)
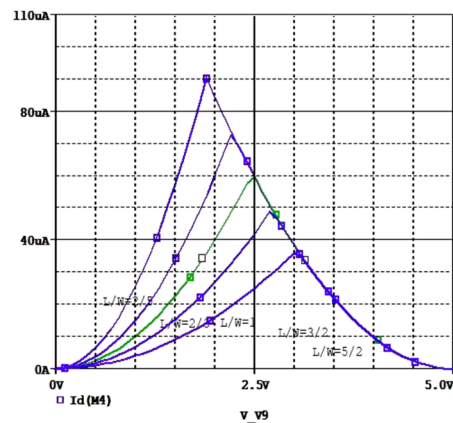
Figure 7. The drain current (Id) of CMOS.

The alteration of the dimensions, namely the width and length, of the NMOS transistor channel has a notable impact on the transfer function of the CMOS circuit. It's evident that this influence causes a lateral shift in the output signal curve (Vout = f(Vin)) when compared to the reference signal (depicted as the green curve) [31]. Specifically, an increase in the width-to-length ratio of WN/LN prompts the curve to shift to the left of the reference, while a decrease in this ratio results in a shift to the right [32]. This shift of the curve corresponds to changes in the inflection point, leading to slight differences in the values of the truncation points, which are detailed in Table .2. Additionally, we observe a noteworthy pattern in the behavior of the maximum drain current, Idpeak. As the WN/LN ratio increases, Idpeak also experiences an increase, and its curve shifts to the left of the reference [33]. Conversely, a decrease in the WN/LN ratio causes Idpeak to decrease, and

its curve shifts to the right relative to the reference curve. This further highlights the significance of the WN/LN ratio in shaping the performance characteristics of the CMOS circuit [34].

Table 2. The maximum drain current Idpeak and the inflection point variation as a function of geometric alteration.

WN/LN	2/5	2/3	1	3/2	5/2
Idpeak (µA)	36.00	48.60	59.559	72.60	90.25
Inflection point (V)	(3.1;2.5)	(2.7;2.5)	(2.5;2.5)	(2.2;2.5)	(1.9;2.5)

2.4.2. Change in PMOS

By adjusting the dimensions of the channel in the PMOS transistor, specifically its length ("L") and width ("W"), we can observe corresponding alterations in two key parameters: the peak current (Idpeak) and the inflection point. These variations are visually represented in Figures 8 and 9, and their precise values are documented in Table 3 for reference. To explain further, changing the dimensions of the PMOS transistor channel influences the behavior of the circuit. This leads to shifts in the curve representing the circuit's output signal (Vout = f(Vin)) concerning the reference signal [35]. The direction of this shift depends on whether the width-to-length ratio (WP/LP) increases or decreases [36]. These shifts correspond to changes in the inflection point and may result in minor differences in the values of the truncation points. This data is detailed in Table 3.
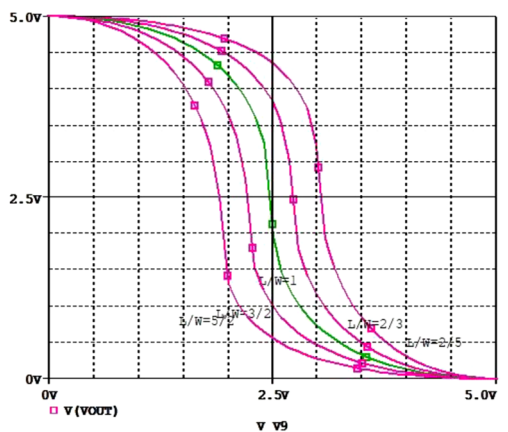
Figure 8. The transfer function Vout =f (Vin)
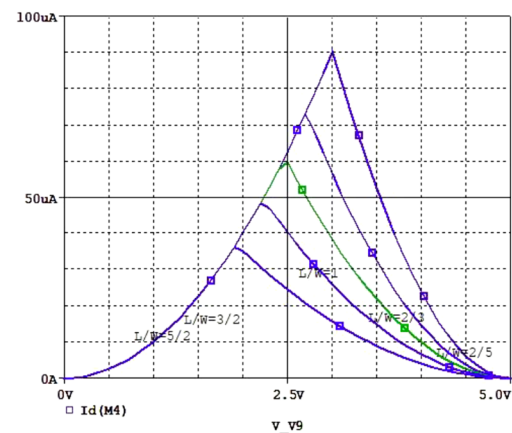
Figure 9. The drain current (Id) of CMOS

As we modify the dimensions of the PMOS transistor channel, specifically the length (LP) and width (WP), a significant influence becomes evident. When we decrease the width-to-length ratio (WP/LP) by a factor of 1, there is a discernible shift in the output signal curve (Vout = f(Vin)) to the left compared to the reference curve [37]. This shift in position includes variations in the location of the inflection point, which can change under different conditions, or it may shift back towards the right. Additionally, this adjustment also impacts the positions of the high and low truncation points. What's particularly interesting is the behavior of the maximum drain current (Idpeak). When the WP/LP ratio increases, Idpeak experiences an increase, but this time, its curve shifts to the right relative to the reference. Conversely, a decrease in the WP/LP ratio by 1 results in a decrease in Idpeak, and the curve shifts left, in contrast to the behavior of the NMOS transistor. This observation underscores the inverse relationship between the WP/LP ratio and the behavior of PMOS and NMOS transistors [38].

Table 3. The maximum drain current Idpeak and the inflection point variation as a function of geometric alteration.

WN/LN	2/5	2/3	1	3/2	5/2
Idpeak (µA)	36.10	48.40	59.558	72.90	90.00
Inflection point (V)	(1.9;2.5)	(2.2;2.5)	(2.5;2.5)	(2.7;2.5)	(3.1;2.5)

2.4.3. Change in NMOS and PMOS

When we concurrently vary the dimensions of both the NMOS and PMOS transistors' channels, including their lengths (LN and LP) and widths (WN and WP), a distinct phenomenon emerges in contrast to the previous scenarios. Notably, the maximum drain current, Idpeak, for the CMOS inverter consistently decreases as these dimensions are altered. However, this decrease is accompanied by a shift in the Idpeak curve to the right of the reference curve if the ratio βN/βP decreases by 1, and to the left if it increases. Furthermore, the curve representing the output voltage (Vout = f(Vin)) also undergoes shifts when βN/βP is modified [39]. If βN/βP increases, the curve shifts to the left of the reference, and conversely, it moves back to the right. These shifts affect the inflection point, as well as the high and low truncation points, all while preserving the characteristic shape of the curve, with no deformations. This phenomenon indicates that each transfer function has a distinct threshold in comparison to the others due to the varying size ratio of the PMOS and NMOS transistors, βN/βP, in different transfer functions [40]. As this ratio increases, the threshold of the CMOS inverter decreases, influencing its performance characteristics (Figures 10 and 11).
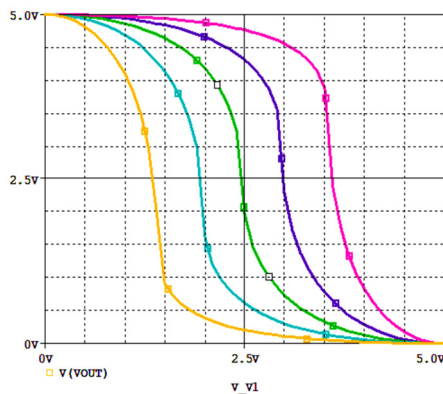
Figure 10. The transfer function Vout =f (Vin)
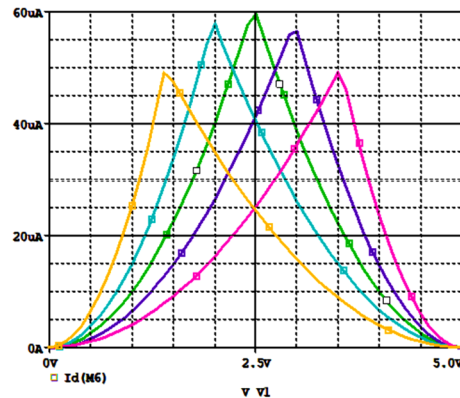
Figure 11. The drain current (Id) of CMOS

Table 4. The maximum drain current Idpeak, the inflection points and truncation points variation as a function of geometric alteration

βN = WN/LN	2/5	2/3	2/5	1	3/2	3/2	5/2
BP = WP/LP	5/2	3/2	2/5	1	3/2	2/3	2/5
βN/βP	0.16	0.44	1	1	1	2.25	6.25
Idpeak (μA)	49.00	56.64	59.56	59.56	59.56	57.714	49.00
Inflection point (V)	3.60	2.99	2.5	2.5	2.5	1.94	1.35
Maximum truncation point (V)	(3.21;4.40)	(2.5;4.31)	(1.7;4.5)	(1.7;4.5)	(1.7;4.5)	(1.16;4.56)	(0.58;4.75)
Minimum truncation point (V)	(4.24;0.42)	(3.72;0.52)	(3.10;0.63)	(3.10;0.63)	(3.10;0.63)	(2.62;0.61;)	(1.71;0.60)

3. DYNAMIC STUDY OF CMOS
3.1. Simulation circuit

To further investigate this study, we utilized the PSPACE design program to conduct experiments with a CMOS inverter. These experiments involved applying an AC input voltage spanning from 0V to 5V, as visually represented in the Figure 12.

3.2. The default output signal

Throughout these simulations, a constant temperature of 27 °C was maintained, and the CMOS configuration remained at its default state, with a width-to-length ratio (W/L) of 1. It's important to note that we employed an inverted CMOS circuit, which means that the output response exhibits an inversion compared to the input signal. The input signal is represented by the red curve, while the green curve corresponds to the output signal (Figures 13).

3.2.1. Rise times and propagation delays:

During signal transitions in a circuit, both the NMOS and PMOS transistors conduct simultaneously, resulting in increased power dissipation. The dissipation is most pronounced when both transistors reach the saturated state, which is undesirable due to the elevated power consumption. To mitigate this issue, it is essential to enhance the rise and fall times of the signals, which are the durations taken for the transitions from low to high and high to low states, respectively. Reducing these times helps minimize power dissipation during transitions [41]. Additionally, the propagation delay, which represents the time it takes for an input change to affect the output, is a critical parameter that needs careful consideration as it significantly impacts the circuit's overall performance and efficiency (Figure 14).

3.3 The temperature effect

In our exploration of temperature's influence on CMOS, we systematically manipulated temperature settings across a wide range, encompassing temperatures from -100°C to the maximum temperature at which CMOS exhibits a reaction, 270°C, as depicted in Figure 15. The impact of temperature on CMOS performance is indeed significant. To illustrate, in terms of propagation delay, a clear trend emerges: higher temperatures correspond to reduced propagation delays, while lower temperatures lead to their increase. Similarly, when considering the rise and fall times of signals, elevated temperatures prompt shorter times, implying faster transitions between logic levels. This phenomenon is likely attributed to an enhancement in carrier mobility, facilitating the swifter movement of charges within the transistors [42]. Conversely, lower temperatures extend the rise and fall times, resulting in slower transitions. This can be attributed to a reduction in carrier mobility under colder conditions.

3.4. The effect of geometric factors (W and L)
3.4.1. Change in NMOS

In Figure 16, we observe the impact of altering the geometric characteristics (specifically, the width, W, and length, L) of the NMOS transistor on the behavior of the CMOS inverter. Notably, an increase in the size of the NMOS

transistor, indicated by a higher W/L ratio, has a beneficial effect on the circuit. It reduces the propagation delay, enhancing the inverter's speed. Additionally, with respect to rise and fall times, an increase in the W/L ratio of the NMOS transistor leads to shorter rise and fall times for signals [43]. This implies that transitions between logic levels occur more swiftly, contributing to improved overall performance.
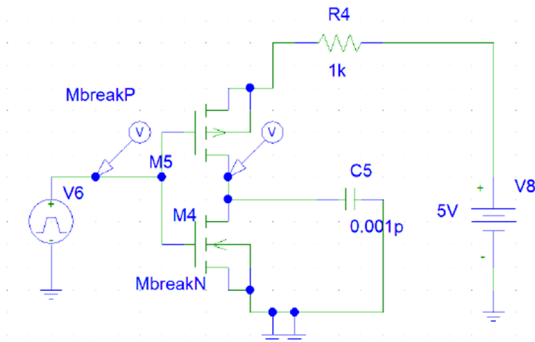
Figure 12. CMOS inverter circuit in dynamic mode

Figure 13. Default input and output signals of CMOS inverter
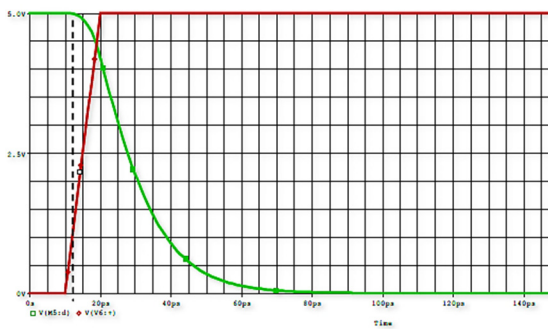
Figure 14. Rise times and propagation delays of CMOS inverter
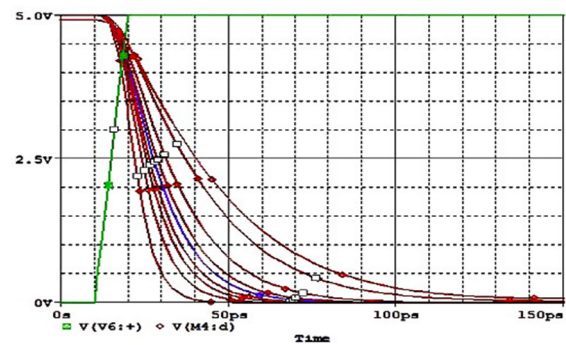
Figure 15. The temperature effect on CMOS

3.4.2. Change in PMOS

As demonstrated in Figure 17, we investigate the influence of altering the geometric parameters (specifically, the width, W, and length, L) of the PMOS transistor on the CMOS inverter. Upon careful examination of the graphical results, it becomes evident that the PMOS geometric factors (W and L) exhibit no discernible impact on the CMOS inverter concerning key performance aspects such as propagation delay and rise/fall times. In other words, variations in the PMOS transistor's geometric characteristics do not yield significant changes in these parameters.
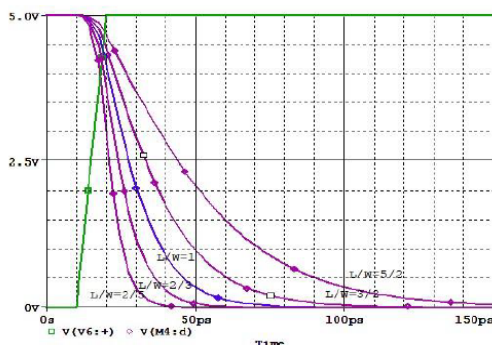
Figure 16. The change in NMOS geometric factors effect on CMOS
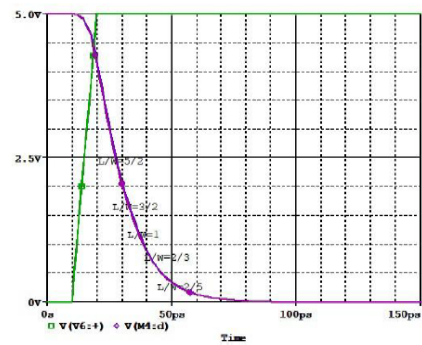
Figure 17. The change in PMOS geometric factors effect on CMOS.

3.4.3. Change in NMOS and PMOS

Figure 18 provides a comprehensive visual representation of the impact of altering both NMOS and PMOS transistor geometric parameters, specifically width (W) and length (L), on the CMOS inverter. A notable observation emerges: the geometric characteristics of the NMOS transistor play a pivotal role in influencing the temporal parameters of the CMOS circuit, while the geometric factors of the PMOS transistor do not appear to have a discernible effect on CMOS [44].

Consequently, the curves depicted in Figure 18 closely resemble those in Figure 16, reinforcing the notion that the NMOS transistor's geometric attributes are the primary drivers of temporal changes in the CMOS inverter.

Figure 18. The change in NMOS and PMOS geometric factors effect on CMOS

4. CONCLUSION

In summary, this study investigates the impact of temperature variations and alterations in transistor channel dimensions on CMOS (Complementary Metal-Oxide-Semiconductor) circuit technology. To facilitate this investigation, we first identified critical parameters characterizing the device's performance, which could exhibit susceptibility to these influences. The analysis encompassed critical metrics such as the transfer characteristic, drain current, logic levels, inflection points, and truncation points. These parameters enabled us to validate the results obtained from the PSPICE simulator, which demonstrated unequivocal effectiveness. Notably, our simulation results unveiled significant effects resulting from a wide temperature range spanning from -100°C to 270°C, offering valuable in-sights into thermal-induced failures. Additionally, the influence of channel dimension changes on factors like drain current and transfer characteristics, as well as temporal parameters including signal propagation delay and rise and fall times, were meticulously examined and appreciated

ORCID

Abderrahim Yousfi, https://orcid.org/0000-0003-2071-728X; **Okba Saidani,** https://orcid.org/0000-0003-0507-5581
Zitouni Messai, https://orcid.org/0000-0002-2508-3696

REFERENCES

[1] N.A. Kumari, and P. Prithvi, "A comprehensive analysis and performance comparison of CombFET and NSFET for CMOS circuit applications," AEU-International Journal of Electronics and Communications, **158**, 154447 (2023). https://doi.org/10.1016/j.aeue.2022.154447

[2] N.A. Kumari, V.B. Sreenivasulu, and P. Prithvi, "Impact of scaling on nanosheet FET and CMOS circuit applications," ECS Journal of Solid State Science and Technology, **12**(3), 033001 (2023). https://doi.org/10.1149/2162-8777/acbcf2

[3] N.A. Kumari, and P.A. Prithvi, "A Comprehensive analysis of nanosheet FET and its CMOS circuit applications at elevated temperatures," Silicon, **15**, 6135-6146 (2023). https://doi.org/10.1007/s12633-023-02496-2

[4] S.N. Hosseini, P.S. Das, V.K. Lazarjan, G. Gagnon-Turcotte, K. Bouzid, and B. Gosselin, "Recent advances in CMOS electrochemical biosensor design for microbial monitoring," IEEE Transactions on Biomedical Circuits and Systems, **17**(2), 202-228 (2023). https://doi.org/10.1109/TBCAS.2023.3252402

[5] L. Constantinou, I.F. Triantis, R. Bayford, and A. Demosthenous, "High-power CMOS current driver with accurate transconductance for electrical impedance tomography," IEEE Transactions on Biomedical Circuits and Systems, **8**(4), 575-583 (2014). https://doi.org/10.1109/TBCAS.2013.2285481

[6] M.B. da Silva, G.I. Wirth, H.P. Tuinhout, A. Zegers-van Duijnhoven, and A.J. Scholten, "Random Telegraph Noise in Analog CMOS Circuits," IEEE Transactions on Circuits and Systems I: Regular Papers, **70**(6), 2229-2242 (2023). https://doi.org/10.1109/TCSI.2023.3261564

[7] B.P. Wong, A. Mittal, G.W. Starr, F. Zach, V. Moroz and A. Kahng, *Nano-CMOS Design for Manufacturability Robust Circuit and Physical Design for Sub-65nm Technology Nodes*, 1st ed. (Wiley, 2008).

[8] K. Zhu, S. Pazos, F. Aguirre, Y. Shen, Y. Yuan, W. Zheng, O. Alharbi, et al., "Hybrid 2D–CMOS microchips for memristive applications," Nature, **618**(7963), 57-62 (2023). https://doi.org/10.1038/s41586-023-05973-1

[9] F. Piro, G.A. Rinella, A. Andronic, M. Antonelli, M. Aresti, R. Baccomi, ... and Villani, A. "A compact front-end circuit for a monolithic sensor in a 65 nm CMOS imaging technology," IEEE Transactions on Nuclear Science, **70**(9), 2191–2200 (2023). https://doi.org/10.1109/TNS.2023.3299333

[10] J. Robertson, and R.M. Wallace, "High-K materials and metal gates for CMOS applications," Materials Science and Engineering R, **88**, 1-41 (2015). https://doi.org/10.1016/j.mser.2014.11.001

[11] T.D. Ngo, Z. Yang, M. Lee, F. Ali, I. Moon, D.G. Kim, T. Taniguchi, et al., "Fermi-Level Pinning Free High-Performance 2D CMOS Inverter Fabricated with Van Der Waals Bottom Contacts," Advanced Electronic Materials, **7**, 2001212 (2021). https://doi.org/10.1002/aelm.202001212

[12] J. Chen, J. Zhu, Q. Wang, J. Wan, and R. Liu, "Homogeneous 2D MoTe$_2$ CMOS Inverters and p–n Junctions Formed by Laser-Irradiation-Induced p-Type Doping," Nano. Micro. Small, **16**, 2001428 (2020). https://doi.org/10.1002/smll.202001428

[13] J.R. Pradhan, M. Singh, and S. Dasgupta, "Inkjet-Printed, Deep Subthreshold Operated Pseudo-CMOS Inverters with High Voltage Gain and Low Power Consumption," Advanced Electronic Materials, **8**, 2200528 (2022). https://doi.org/10.1002/aelm.202200528

[14] V.K. Verma, and J.N. Tripathi, "Device Parameters Based Analytical Modeling of Ground-Bounce Induced Jitter in CMOS Inverters," IEEE Transactions on Electron Devices, **69**, 5462–5469 (2022). https://doi.org/10.1109/TED.2022.3203652

[15] A. Javaid, R. Achar, and J.N. Tripathi, "Development of Knowledge-Based Artificial Neural Networks for Analysis of PSIJ in CMOS Inverter Circuits," IEEE Transactions on Microwave Theory and Techniques, **71**, 1428–1438 (2022). https://doi.org/10.1109/TMTT.2022.3222181

[16] P. Arora, J.N. Tripathi, and H. Shrimali, "Device Parameter-Based Analytical Modeling of Power Supply Induced Jitter in CMOS Inverters," IEEE Transactions on Electron Devices, **68**, 3268–3275 (2021). https://doi.org/10.1109/TED.2021.3082106

[17] A. Gopal, M. Esposito, and N. Freitas, "Large deviations theory for noisy nonlinear electronics: CMOS inverter as a case study," Physical Review B, **106**, 155303 (2022). https://doi.org/10.1103/PhysRevB.106.155303

[18] S. Heo, J. Lee, S. Lee, S. Lee, C. Lee, R.H. Baek, and H. Hwang, "High-Speed Ternary CMOS Inverter by Monolithic Integration of NbO2 Threshold Switch with MOSFET," in: *2021 IEEE International Electron Devices Meeting (IEDM)*, (San Francisco, USA, 2022). https://doi.org/10.1109/IEDM19574.2021.9720520

[19] F. Pezzimenti, H. Bencherif, A. Yousfi, and L. Dehimi, "Current-voltage analytical model and multiobjective optimization of design of a short channel gate-all-around-junctionless MOSFET," Solid-State Electronics, **161**, 107642 (2019). https://doi.org/10.1016/j.sse.2019.107642

[20] S. Venkateswarlu, and K. Nayak, "Ambient Temperature-Induced Device Self-Heating Effects on Multi-Fin Si CMOS Logic Circuit Performance in N-14 to N-7 Scaled Technologies," IEEE Transactions on Electron Devices, **67**, 1530–1536 (2020). https://doi.org/10.1109/TED.2020.2975416

[21] Y. Hernandez, B. Stampfer, T. Grasser, and M. Waltl, "Impact of Bias Temperature Instabilities on the Performance of Logic Inverter Circuits Using Different SiC Transistor Technologies," Crystals, **11**, 1150 (2021). https://doi.org/10.3390/cryst11091150

[22] N.A. Badiger, S. Iyer, and S. Gejji, "Power and Delay Analysis of a CMOS Inverter," in: *2023 International Conference on Data Science and Network Security (ICDSNS)*, 23748343 (2023). (pp. 1-6). https://doi.org/10.1109/ICDSNS58469.2023.10244825

[23] M. Merabet, and N. Bourouba, "DC Hard Faults Detection and Localization in Analog Circuits Using Fuzzy Logic Techniques," Electronics, **23**, 18-25 (2019). https://pdfs.semanticscholar.org/05b2/6e740526d166519db0bb84c76f48b400818f.pdf

[24] N.A. Arabi, N. Bourouba, A. Belaout, and M. Ayad, "Catastrophic faults detection of analog circuits," in: *2015 7th International Conference on Modelling,*" *Identification and Control (ICMIC)*, 2015, pp. 1–6.

[25] A. Yousfi, Z. Dibi, S. Aissi, H. Bencherif, and L. Saidi, "RF/Analog Performances Enhancement of Short Channel GAAJ MOSFET using Source/Drain Extensions and Metaheuristic Optimization-based Approach," Journal of Telecommunication, Electronic and Computer Engineering (JTEC), **10**(2), 81-90 (2018). https://jtec.utem.edu.my/jtec/article/view/3352

[26] F.F. Kemwoue, J.M. Dongo, R.N. Mballa, C.L. Gninzanlong, M.W. Kemayou, B. Mokhtari, F. Biya-Motto, and J. Atangana, "Bifurcation, multistability in the dynamics of tumor growth and electronic simulations by the use of Pspice," Chaos, Solitons and Fractals, **134**, 109689 (2020). https://doi.org/10.1016/j.chaos.2020.109689

[27] Y. Yang, Z. Wang, Y. Ge, G. Xin, and X. Shi, "An Automated Field-Circuit Coupling Simulation Method Based on PSpice-MATLAB-COMSOL for SiC Power Module Design," IEEE Transactions on Power Electronics, **38**, 12634-12647 (2023). https://doi.org/10.1109/TPEL.2023.3293162

[28] Y. Yang, Y. Ge, Z. Wang, and Y. Kang, "An Automated Electro-Thermal-Mechanical Co-Simulation Methodology Based on PSpice-MATLAB-COMSOL for SiC Power Module Design," in*: 2021 IEEE Workshop on Wide Bandgap Power Devices and Applications in Asia*, (WiPDA Asia), (2022).

[29] C. Liu, X. Wang, S. Huang, X. Ma, Y. Wang, S. Zhang, R. Zhao, et al., "A large-signal Pspice modeling of GaN-based MIS-HEMTs," Superlattices and Microstructures, **130**, 499-511 (2019). https://doi.org/10.1016/j.spmi.2019.05.023

[30] Y. Duan, F. Xiao, Y. Jia, Y. Luo, and B. Liu, "A Physics-Based Lumped-Charge Model for SiC MPS Diode Implemented in PSPICE," IEEE Journal of Emerging and Selected Topics in Power Electronics, **7**, 1547-1555 (2019). https://doi.org/10.1109/JESTPE.2019.2923823

[31] G.H. Kim, S.H. Kang, J.M. Lee, M. Son, J. Lee, H. Lee, I. Chung, et al., "Room Temperature-Grown Highly Oriented p-Type Nanocrystalline Tellurium Thin-Films Transistors for Large-Scale CMOS Circuits," Applied Surface Science, 157801 (2023). https://doi.org/10.1016/j.apsusc.2023.157801

[32] P.K. Ghosh, S.Z. Riam, M.S. Ahmed, and P. Sundaravadivel, "CMOS-Based Memristor Emulator Circuits for Low-Power Edge-Computing Applications," Electronics, **12**(7), 1654 (2023). https://doi.org/10.3390/electronics12071654

[33] P. Barla, V.K. Joshi, and S. Bhat, "Spintronic devices: a promising alternative to CMOS devices," Journal of Computational Electronics, **20**(2), 805-837 (2021). https://doi.org/10.1007/s10825-020-01648-6

[34] M.P. Frank, R.W. Brocato, B.D. Tierney, N.A. Missert, and A.H. Hsia, "Reversible computing with fast, fully static, fully adiabatic CMOS," in: *2020 International Conference on Rebooting Computing (ICRC)*, (IEEE, 2020) pp. 1-8.

[35] H.J. Yun, J. Lim, J. Roh, D.C.J. Neo, M. Law, and V.I. Klimov, "Solution-processable integrated CMOS circuits based on colloidal CuInSe2 quantum dots," Nature communications, **11**(1), 5280 (2020). https://doi.org/10.1038/s41467-020-18932-5

[36] P.J. Sung, S.W. Chang, K.H. Kao, C.T. Wu, C.J. Su, T.C. Cho, F.-K. Hsueh, et al., "Fabrication of vertically stacked nanosheet junctionless field-effect transistors and applications for the CMOS and CFET inverters," IEEE Transactions on Electron Devices, **67**(9), 3504-3509 (2020). https://doi.org/10.1109/TED.2020.3007134

[37] S. Du, Y. Jia, C. Zhao, G.A. Amaratunga, and A.A. Seshia, "A nail-size piezoelectric energy harvesting system integrating a MEMS transducer and a CMOS SSHI circuit," IEEE Sensors Journal, **20**(1), 277-285 (2019). https://doi.org/10.1109/JSEN.2019.2941180

[38] M. Sharma, D. Pandey, P. Palta, and B.K. Pandey, "Design and power dissipation consideration of PFAL CMOS V/S conventional CMOS based 2: 1 multiplexer and full adder," Silicon, **14**(8), 4401-4410 (2022). https://doi.org/10.1007/s12633-021-01221-1

[39] F. Cai, J.M. Correll, S.H. Lee, Y. Lim, V. Bothra, Z. Zhang, M.P. Flynn, et al., "A fully integrated reprogrammable memristor–CMOS system for efficient multiply–accumulate operations," Nature electronics, **2**(7), 290-299 (2019). https://doi.org/10.1038/s41928-019-0270-x

[40] S. Schaal, A. Rossi, V.N. Ciriano-Tejel, T.Y. Yang, S. Barraud, J.J. Morton, and M.F. Gonzalez-Zalba, "A CMOS dynamic random-access architecture for radio-frequency readout of quantum devices," Nature Electronics, **2**(6), 236-242 (2019). https://doi.org/10.1038/s41928-019-0259-5

[41] S.J. Bader, H. Lee, R. Chaudhuri, S. Huang, A. Hickman, A. Molnar, H. Grace, et al., "Prospects for wide bandgap and ultrawide bandgap CMOS devices," IEEE Transactions on Electron Devices, **67**(10), 4010-4020 (2020). https://doi.org/10.1109/TED.2020.3010471

[42] I. Park, W. Jo, C. Park, B. Park, J. Cheon, and Y.A Chae, "640×640 Fully Dynamic CMOS Image Sensor for Always-On Operation," IEEE Journal of Solid-State Circuits, **55**(4), 898-907 (2019). https://doi.org/10.1109/JSSC.2019.2959486

[43] Y. Jin, and S.A. Hong, "24-GHz CMOS power amplifier with dynamic feedback and adaptive bias controls," IEEE Microwave and Wireless Components Letters, **31**(2), 153-156 (2020). https://doi.org/10.1109/LMWC.2020.3038041

[44] H. Horiuchi, M. Agetsuma, J. Ishida, Y. Nakamura, D.L. Cheung, S. Nanasaki, D.L. Cheung, et al., "CMOS-based bio-image sensor spatially resolves neural activity-dependent proton dynamics in the living brain," Nature Communications, **11**(1), 712 (2020). https://doi.org/10.1038/s41467-020-14571-y

**ДОСЛІДЖЕННЯ ВПЛИВУ ТЕМПЕРАТУРИ ТА РОЗМІРІВ КАНАЛУ
НА ПРОДУКТИВНІСТЬ СХЕМИ CMOS**

Зітуні Мессай[a], Абдельхалім Брахімі[a,b], Окба Сайдані[a], Насердін Буруба[b], Абдеррахім Юсфі[a]

[a]*Лабораторія ETA, кафедра електроніки, технологічний факультет, Університет Мохамеда Ель Бачіра Ель Ібрагімі, Бордж-Бу-Аррерідж, Алжир*

[b]*Лабораторія LIS, кафедра електроніки, технологічний факультет, Університет Ферхат Аббас Сетіф, Сетіф, Алжир*

У цьому дослідженні представлено вплив коливань температури та змін розмірів каналу транзистора на технологію CMOS (комплементарний метал-оксид-напівпровідник). Щоб полегшити це дослідження, ми спершу визначили критичні параметри, що характеризують продуктивність пристрою, які можуть бути чутливими до цих впливів. Аналіз охоплював критичні показники, такі як характеристика передачі, струм витоку, логічні рівні, точки перегину та точки зрізання. Ці параметри дозволили нам підтвердити результати, отримані від симулятора PSPICE, який продемонстрував однозначну ефективність. Примітно, що результати нашого моделювання виявили значні ефекти, що є наслідком широкого діапазону температур від -100°C до 270°C, пропонуючи цінну інформацію про несправності, спричинені нагріванням. Крім того, було ретельно вивчено та оцінено вплив змін розміру каналу на такі фактори, як струм стоку та характеристики передачі, а також часові параметри, включаючи затримку поширення сигналу та час наростання та спаду.

Ключові слова: *КМОП; розміри каналів; температура; PSPICE*

DEVELOPMENT OF NANOPOROUS AAO BASED CAPACITIVE-TYPE SENSORS FOR HEAVY METAL ION (ARSENIC) SENSING APPLICATION

Trishna Moni Das[a], Devabrata Sarmah[b], Sankar Moni Borah[a], Sunandan Baruah[b]*

[a]Department of Applied Sciences, Gauhati University, Guwahati-781014, Assam, India
[b]Centre of Excellence in Nanotechnology, Assam down town University, Guwahati -781026, Assam, India
*Corresponding Author e-mail: *sunandan.baruah@adtu.in*
[†]E-mail: trishnamani.das@gmail.com, devabratasarmah@gmail.com, sankarmoni@gmail.com

In this work the evolution of a capacitive type sensor based on nanoporous anodic aluminum oxide (AAO) fabricated by a two-step anodization process using a low-cost customized setup designed in-house is reported. The parallel plate capacitors were fabricated using aluminum (Al) as base electrode and gold as top electrode, where the porous AAO was used as the dielectric material. This demonstrated the clear dependence of the capacitance values of the as prepared different sensors on the dielectric material's thickness. The as developed sensors were tested for the detection of arsenic (As) ions. An increase in the capacitance was observed while increasing the concentration of the As ion in aqueous solutions. The presence of As ion was confirmed through EDS (Energy dispersive X-ray spectroscopy) mapping carried out in a FESEM. This change in capacitance can be attributed to the change in dielectric constant of the active material with the incorporation of metal ions.

Keywords*: Capacitive-type sensor; Nanoporous Anodic Aluminum Oxide (AAO); Anodization; Energy dispersive X-ray spectroscopy (EDS)*

PACS:78.67.Rb,07.07. Df, 68.37. Hk, 84.37.+q

1. INTRODUCTION

Self-organized, highly ordered nanopores in Anodic Aluminum Oxide (AAO) with high periodicity and density distribution have found widespread use in a variety of nanoscale applications [1,2]. In addition to its promise as a template for the growth of other nanostructured materials, AAO's increased surface area due to the uniform arrangement of ordered nanopores is showing promising results in the development of sensors. Due to its increased uniform nanoporous surface area that enhances the water adsorption capacity [3,4,5], AAO has been reported as a useful material for the fabrication of capacitive humidity sensors, pressure sensors, and bacteria sensors by a number of researchers [4-9]. Capacitive type sensors are rising in popularity among the many existing sensor types (capacitive, resistive, mass-sensitive, electromagnetic, etc.) due to their improved sensitivity and simpler fabrication procedure [10]. Numerous nanoporous AAO-based capacitive humidity sensors have been reported to date [5- 9]. The widespread contamination of ground water supplies with arsenic has been labeled a modern environmental catastrophe [11-14]. Direct detection of As (III) in ground water using spectroscopic methods is challenging because of its low concentration. Taking advantage of their large surface area, AAO nanopores can be modified to detect a variety of metal ions. For the selective extraction of trace arsenite ions, AAO is used as it is a highly sensitive material [15]. Capacitive type sensors based on AAO have demonstrated excellent sensing of As ions in ground water [15]. AAO can be made using a number of different fabrication methods, including sputtering, sol gel process and Chemical Vapor Deposition (CVD). However, these techniques call for high-end equipment, which drives up costs. However, the electrochemical anodization technique has been proved as a simple and cost-effective process, where the different parameters involved in the fabrication process such as thickness, porosity etc. can be controlled easily [16].

This work describes the development of a AAO based capacitive type sensor using a conventional two-step anodization method starting with a low cost commercially available aluminum alloy. Since the thickness of the dielectric material has an inverse relationship with the capacitance of a parallel plate capacitor, we have emphasized here to develop a thicker AAO layer within a short interval of time. For this purpose, the hard anodization method is involved as it has been proved as a fast fabrication method. The sensing of arsenic ion using the as developed AAO based capacitive type sensor is reported here.

2. MATERIALS AND METHODS

Commercially available aluminum sheet was used for the experiments. The 0.5 mm thick aluminum sheet was cut into required sizes for anodization. Prior to anodization, the aluminum sheets were ultrasonically cleaned in a mixture of acetone and deionized water for 10 minutes and annealed at 250˚C for 4 hours. To dissolve the naturally occurring oxide coating the aluminum sheets were electropolished in a solution mixture of H_3PO_4, H_2SO_4 and deionized water with 2:2:1 weight ratio respectively. The aluminum sheets were then washed several times with deionized water, dried and used as anodes in the developed AAO fabrication set-up. The nanoporous AAO structures were fabricated by a simple two step

hard anodization method where a lead sheet was used as cathode. The anodization process was carried out at 140 V applied voltage at ~ 5°C. 0.3M $H_2C_2O_4$ was used as the electrolyte.

It has been established that the morphology of nanoporous AAO is affected by various parameters like the anodization time, anodization voltage, nature and concentration of the electrolyte, and the temperature of the electrolytic bath. In this work, two different samples namely S1 and S2 were synthesized by varying the anodization time [Table 1]. The morphology of the as prepared AAO structures was observed with a ZEISS Sigma 300 field emission scanning electron microscope (FESEM).

Table 1. The different anodization parameters for the fabrication of nanoporous AAO.

Sample code	Electrolyte concentration	Electrolyte temperature (°C)	Applied Voltage (V)	Anodization time (min)
S1	0.3M	< 5	140	2
S2	0.3M	< 5	140	4

The sensing ability of the as-fabricated nanoporous AAO structures was investigated by fabricating a parallel-plate capacitor by sputtering a thin gold layer (~50 nm) over the AAO structures, with the non-anodized aluminum component at the base functioning as the other electrode. A gold layer with nanotextured topography was formed as a result of direct deposition of gold over the nanoporous AAO. The dielectric layer (nanoporous AAO) relies heavily on this top electrode for the adsorption of heavy metal ions [5]. Five different concentrations of arsenic ions (0.01, 0.05, 0.1, 0.15, and 0.2 ppm) were used for calibrating the sensors. Capacitive response variations due to changes in As ion concentration were recorded by connecting the as-prepared AAO sensors to a LCR meter. Figure 1 shows a schematic of the experimental sequence. The SEM micrographs of the samples S1 and S2 are shown in Figure 2 and 3.
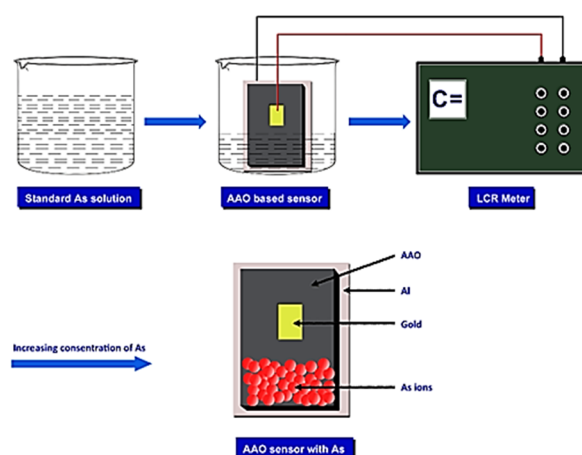
Figure 1. Diagrammatic depiction of the setup for As ion sensing using the as prepared AAO based capacitive type sensor

3. RESULTS AND DISCUSSION
3.1. AAO fabrication and topographical features analysis

Figure 2 (a) and (b) are the SEM micrographs of the top view of the samples S1 and S2, while Figure 3 (a) and (b) are cross sectional SEM micrographs for the samples S1 and S2 respectively. From the SEM micrographs (Top view) of the samples S1 and S2 (Fig 2(a-b)), the extended-range ordering, uniformity, shape and the size of the pores can be observed. From these micrographs, various information regarding the structural morphology like pore diameter, inter-pore distance, porosity etc. is possible to find out. The diameter of the pores is dependent on the nature of the electrolyte, anodization time and anodization voltage. Here, same electrolyte and anodization voltage has been applied to fabricate the two samples by varying the anodization time. As there is slight difference in the anodization times, therefore variations in the pore diameters for the two samples remain insignificant. A noticeable change in the thickness of the two samples can be observed, which will affect the capacitance of the AAO based capacitor.

The porosity P of the hexagonal cell nanoporous AAO with a pore inside each hexagon can be expressed as follows (where each pore is assumed as a perfect circle) [5]

$$P = \frac{pore\ area}{hexagon\ area} = \frac{\pi}{2\sqrt{3}}(\frac{D_p}{D_i})^2, \tag{1}$$

where, D_p and D_i are the diameter of the pores and the interpore distance of the nanoporous AAO respectively, as shown in Figure 2 (a), (b). The pores density, 'n' of the porous AAO with a hexagonal distribution of pores can be described as the overall quantity of pores present in the 1 cm^2 surface area of the porous AAO, and expressed as follows [19]

$$n = \frac{10^{14}}{A_{hex}} = \frac{2x10^{14}}{\sqrt{3}D_i^2}, \tag{2}$$

where A_{hex} is the surface area of a single hexagonal cell (in nm^2). These structural parameters for the as prepared samples S2 and S4 are analyzed through ImageJ software from the SEM micrographs and calculated using equations (1) and (2), which are shown in Table 2.
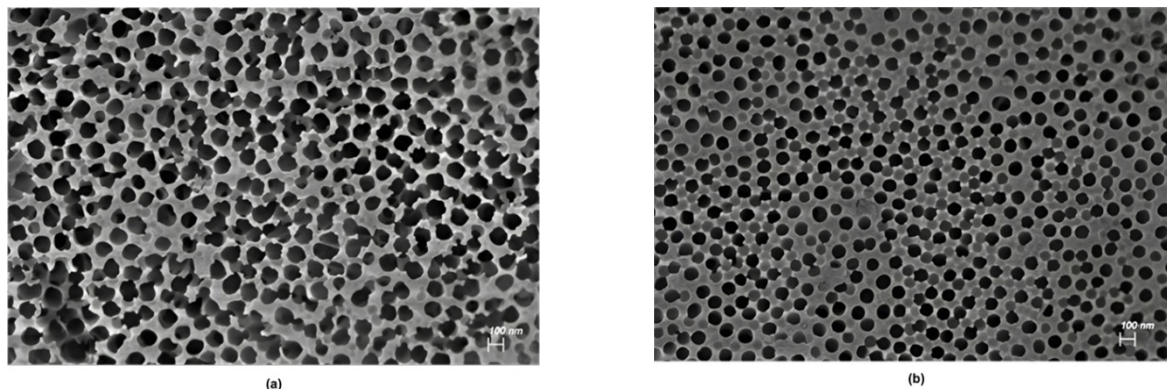
Figure 2. (a-b) SEM micrographs (Top view) of the samples S1 and S2 respectively
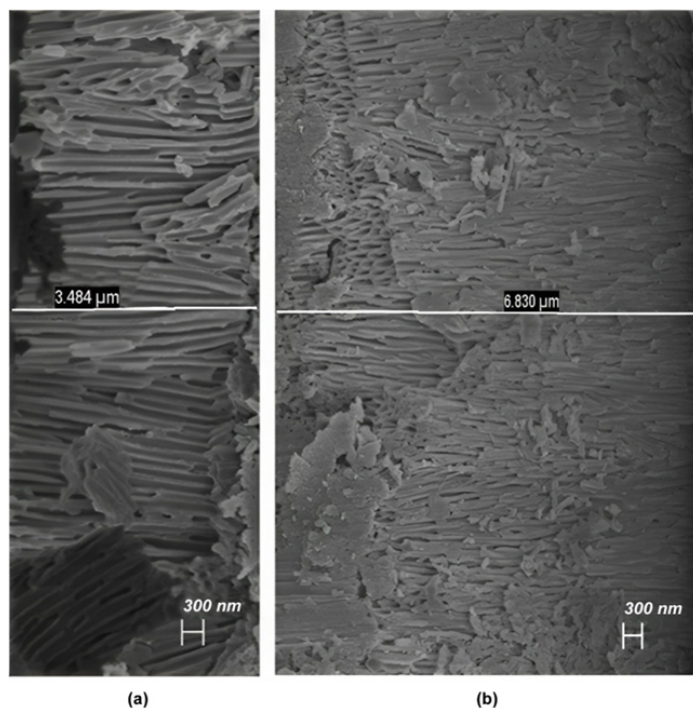
Figure 3. (a-b) Cross-sectional SEM images of the samples S1 and S2 respectively

Table 2. Different structural parameters for the as prepared samples S1 and S2

Sample code	Pore Diameter, D_p(nm)	Interpore Distance, D_i (nm)	Porosity, P (%)	Pore Density, n (Pore/ cm^2)
S1	116	50	4.89	4.6×10^{10}
S2	93	55	2.59	3.82×10^{10}

3.2 Heavy metal ion sensing performance of AAO based sensors

The capacitive response of the as prepared sensors, where the porous AAO layer behaves as a dielectric layer, has been studied with different concentrations of As ions. An increase of the capacitance value was observed with the increase of As concentration for the sensors (Figure 4, 5). This rise in the capacitors' capacitance value can be linked to a modification in their dielectric constant. The permittivity (ε) of a dielectric material is directly proportional to its dielectric constant (k). The relationship can be expressed as $\varepsilon = k \, \varepsilon_o$. Substituting this relationship into the capacitance equation, the equation becomes

$$C = \frac{k\varepsilon_o A}{d} \tag{3}$$

The incorporation of metal ions with dielectric material can modify its dielectric constant. Metal ions may introduce additional charge carriers, which can increase the dielectric constant of the material. Further, metal ions are generally

associated with increased conductivity, therefore, incorporating a dielectric material with metal ions can enhance its electrical conductivity, which can lead to increased leakage current across the capacitor, reducing its overall effectiveness and potentially affecting the charge retention capabilities. The capacitance of the as fabricated sensor S1 is more than that of the sensor S2 which is shown in Figure 4 and Figure 5.
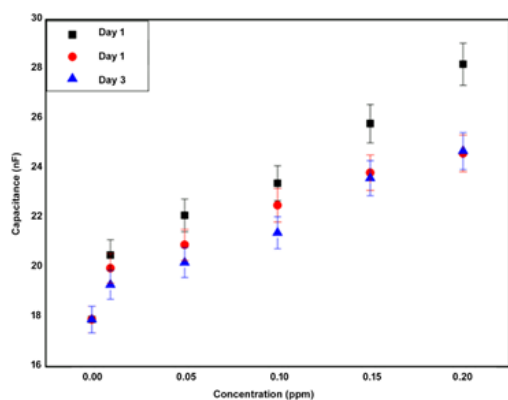
Figure 4. Evolution of capacitance for the sensor S1 as a function of concentration of As ion with 3% error bar
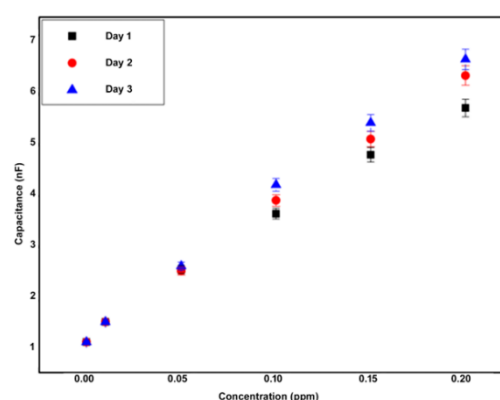
Figure 5. Evolution of capacitance for the sensor S2 as a function of concentration of As ion with 3% error bar

This higher value of the capacitance for the sensor S1 can be attributed to the thickness of the dielectric layer which is thinner than that of sensor S2. But as, the capacitance of a capacitor is inversely proportional to the thickness of the dielectric layer (equation 3), so, the capacitance of S1 is higher than that of S2.

$y = A1*exp(x/t1)+y0$
$y0 = 30.87956$
$A1 = -12.35818$
$t1 = -0.23144$

(a)

$y = A1*exp(x/t1)+y0$
$y0 = 16.92725$
$A1 = -15.7992$
$t1 = -0.51576$

(b)
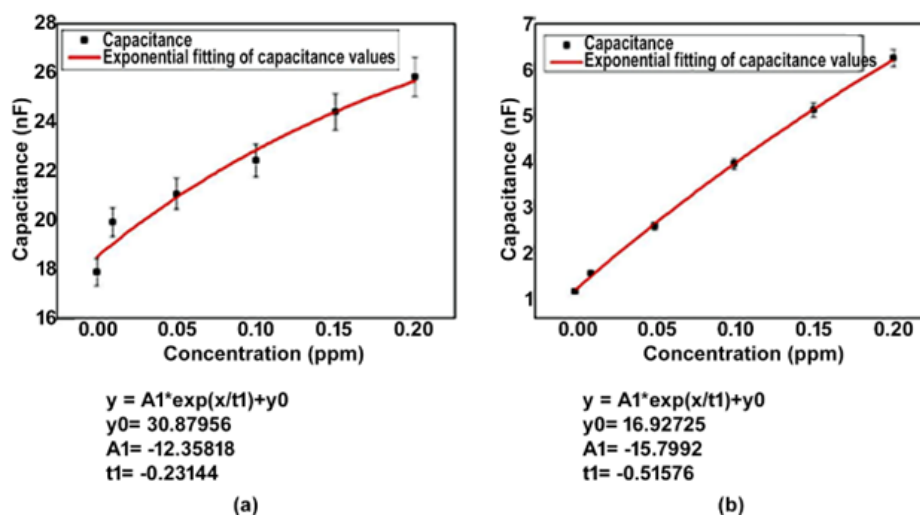
Figure 6. (a-b) Exponential fitting of concentration Vs capacitance curve for the samples S1 and S2 respectively with 3% error bar

The exponential fitting of concentration versus capacitance curve is obtained through Origin pro 8 software for the as prepared samples S1 and S2 respectively (Figure 6). The working of the as prepared capacitive type sensors is schematically shown in the Figure 7.
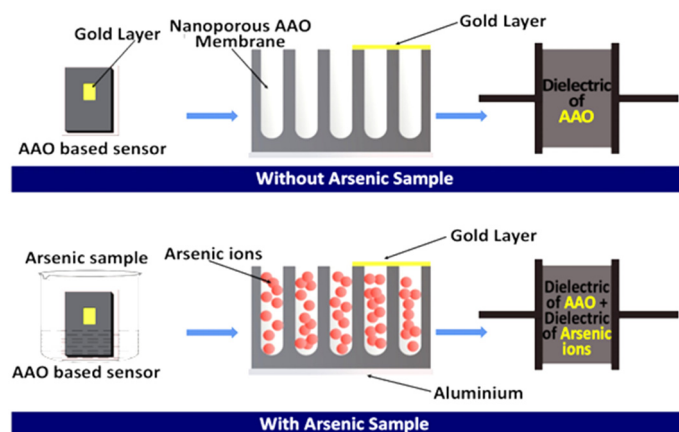
Figure 7. Diagrammatic depiction of the working of the capacitive type sensor with the change in the concentration of the As ions

In order to observe the elemental composition of the as prepared S1 sensor after dipping in the As ion solution, EDS (Energy dispersive X-ray spectroscopy) mapping was carried out in a SEM (Figure 8). The presence of very less amount of As ion (1.35 weight%) has been confirmed through the mapping, as the concentration of As ion solution used in the experiment is very low (0.01 – 0.2 ppm). We have chosen this range of concentrations of As ion as the permissible limit of As in drinking water is up to 0.2 ppm.
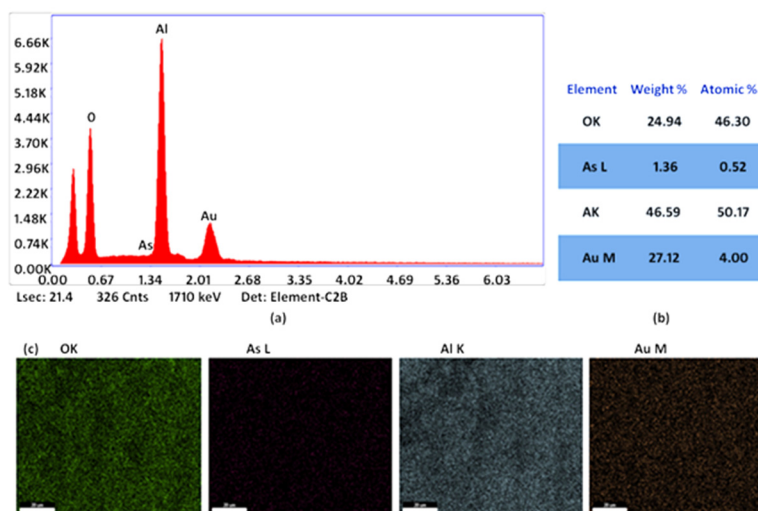
Figure 8. (a-b) EDX pattern of the as developed capacitive sensor S1 after incorporation of As ions (c) EDX mapping of the S1 sensor showing the distribution of O, As, Al and Au atoms

4. CONCLUSIONS

This work reports the successful development of a nanoporous AAO based capacitive type sensor fabricated by a two-step anodization process. Two samples of AAO were prepared by varying the anodization time. Since the anodization time difference maintained here is not high, therefore, a slight change in various parameters like pore diameter, porosity and pore density is observed here. Also, a change in the thickness of the two samples was noticed here. Using these two samples as the dielectric material, two parallel plate capacitive type sensors named S1(2 mins anodization) and S2(4 mins anodization) were prepared, where Aluminum was used as base electrode and Gold as top electrode. To study the sensing behavior of these sensors, an experiment was performed to detect the Arsenic (heavy metal ion) ion. A rise in the capacitance value was observed while the concentrations (in ppm) of the As ion solutions was increased. The mechanism responsible for this performance is directly related to the change in the dielectric constant of the dielectric material (i.e., porous AAO). Incorporation of metal ions into a dielectric material can change the dielectric constant of that material, which directly influences the capacitance of a capacitor. The EDS mapping carried out in a FESEM of the S2 sensor dipped in As ion solutions confirms the presence of As ions.

ORCID
Trishna Moni Das, https://orcid.org/0000-0001-5754-5608; **Sunandan Baruah**, https://orcid.org/0000-0003-2963-6128

REFERENCES
[1] M.A. Kashi, and A. Ramazani, "The effect of Temperature and Concentration on the Self-Organized Pore Formation in Anodic Alumina," J. Phys. D: Appl. Phys. **38**, 2396 (2005). https://doi.org/10.1088/0022-3727/38/14/015
[2] H. Masuda, F. Matsumoto, and, K. Nishio, "Fabrication of Functional Devices Based on Highly Ordered Anodic Porous Alumina," Electrochemistry, **72**, 389 (2004). https://doi.org/10.5796/electrochemistry.72.389
[3] M. Iwai, T. Kikuchi, and R.O. Suzuki, "Self-Ordered Nanospike Porous Alumina Fabricated under a New Regime by an Anodizing Process in Alkaline Media," Sci. Rep. **11**, 7240 (2021). https://doi.org/10.1038/s41598-021-86696-z
[4] T. Islam, A.T. Nimal, U. Mittal, and M.U. Sharma, "A Micro Interdigitated Thin Film Metal Oxide Capacitive Sensor for Measuring Moisture in the Range of 175-625 Ppm," Sens. Actuators B Chem. **221**, 357 (2015). https://doi.org/10.1016/j.snb.2015.06.101

[5] J.O. Carneiro, A. Ribeiro, F. Miranda, I.R. Segundo, S. Landi, V. Teixeira, and M.F.M. Costa, "Development of Capacitive-Type Sensors by Electrochemical Anodization: Humidity and Touch Sensing Applications," Sensors, **21**, 7317 (2021). https://doi.org/10.3390/s21217317

[6] M.A. Kashi, A. Ramazani, H. Abbasian, and A. Khayyatian, "Capacitive Humidity Sensors Based on Large Diameter Porous Alumina Prepared by High Current Anodization," Sens. Actuators A, Phys. **174**, 69 (2012). https://doi.org/10.1016/j.sna.2011.11.033

[7] C.K. Chung, C.A. Ku, and Z.E. Wu, "A High-and- Rapid- Response Capacitive Humidity Sensor of Nanoporous Anodic Alumina by One- step Anodizing Commercial 1050 Aluminum Alloy and Its Enhancement Mechanism," Sens. Actuators B, Chem. **343**, 130156 (2021). https://doi.org/10.1016/j.snb.2021.130156

[8] M.A. Mir, M.A. Shah, and P.A. Ganai, "Nanoporous Anodic Alumina (NAA) Prepared in Different Electrolytes with Different Pore Sizes for Humidity Sensing," J. Solid State Electrochem. **24**, 1679 (2020). https://doi.org/10.1007/s10008-020-04683-2

[9] S.W. Chen, O.K. Khor, M.W. Liao, and C.K. Chung, "Sensitivity Evolution and Enhancement Mechanism of Porous Anodic Aluminum Oxide Humidity Sensor Using Magnetic Field," Sens. Actuators B, Chem. **199**, 384 (2014). https://doi.org/10.1016/j.snb.2014.03.057

[10] C.K. Chung, O.K. Khor, C.J. Syu, and S.W. Chen, "Effect of Oxalic acid Concentration on the Magnetically Enhanced Capacitance and Resistance of AAO Humidity Sensor," Sens. Actuators B, Chem. **210**, 69 (2015). https://doi.org/10.1016/j.snb.2014.12.096

[11] J. Wu, M. Cao, D. Tong, Z. Finkelstein, and E.M.V. Hoek, "Acritical review of point-of-use drinking water treatment in the United States," Npj Clean Water, **4**, 40 (2021). https://doi.org/10.1038/s41545-021-00128-z

[12] L. Weerasundara, Y.-S. Ok, and J. Bundschuh, "Selective removal of arsenic in water: A critical review," Environ. Pollut. **268**, 115668 (2021). https://doi.org/10.1016/j.envpol.2020.115668

[13] Md. G. Uddin, S. Nash, and A.I. Olbert, "A review of water quality index models and their use for assessing surface water quality," Ecol. Indicat. **122**, 107218 (2021). https://doi.org/10.1016/j.ecolind.2020.107218

[14] L. Zheng, Z. Zhou, M. Rao, and Z. Sun, "Assessment of heavy metals and arsenic pollution in surface sediments from rivers around a uranium mining area in East China," Environ Geochem Health, **42**, 1401 (2020). https://doi.org/10.1007/s10653-019-00428-x

[15] H. Ahmad, A.R.A. Abdulwahab, B.H. Koo, and R.A. Khan, "Selective Extraction of Trace Arsenite Ions Using a Highly Porous Aluminum Oxide Membrane with Ordered Nanopores," ACS Omega, **7**, 3044 (2022). https://doi.org/10.1021/acsomega.1c06133

[16] A.P. Li, F. Müller, A. Birner, K. Nielsch, and U. Gösele, "Hexagonal Pore Arrays with a 50-420 nm Interpore Distance Formed by Self-Organization in Anodic Alumina," J. Appl. Phys. **84**, 6023 (1998). https://doi.org/10.1063/1.368911

РОЗРОБКА НАНОПОРИСТИХ СЕНСОРІВ ЄМНІСНОГО ТИПУ НА ОСНОВІ ААО ДЛЯ АНАЛІЗУ НАЯВНОСТІ ІОНІВ ВАЖКИХ МЕТАЛІВ (МИШ'ЯКУ)

Трішна Моні Дас[a], Девабрата Сармах[b], Санкар Моні Борах[a], Сунандан Баруах[b]

[a]Департамент прикладних наук, Університет Гаухаті, Гувахаті-781014, Ассам, Індія
[b]Центр передового досвіду в галузі нанотехнологій, Університет міста Ассам, Гувахаті -781026, Ассам, India

У цій роботі повідомляється про еволюцію датчика ємнісного типу на основі нанопористого анодного оксиду алюмінію (ААО), виготовленого за допомогою двоетапного процесу анодування з використанням недорогої індивідуальної установки, розробленої власними силами. Конденсатори з паралельними пластинами були виготовлені з використанням алюмінію (Al) як базового електрода та золота як верхнього електрода, де пористий ААО використовувався як діелектричний матеріал. Це продемонструвало чітку залежність значень ємності підготовлених різних сенсорів від товщини діелектричного матеріалу. Розроблені датчики були протестовані на виявлення іонів миш'яку (As). При збільшенні концентрації іона As у водних розчинах спостерігалося збільшення ємності. Наявність іонів As було підтверджено за допомогою картографування EDS (енергодисперсійна рентгенівська спектроскопія), виконаного в FESEM. Цю зміну ємності можна пояснити зміною діелектричної проникності активного матеріалу з включенням іонів металу.

Ключові слова: *датчик ємнісного типу; нанопористий анодний оксид алюмінію (ААО); анодування; енергодисперсійна рентгенівська спектроскопія (EDS)*

VIBRATIONAL HAMILTONIAN OF CARBONYL SULPHIDE AND HYDROGEN CYANIDE

K. Lavanya[a,c], A. Ganapathi Rao[b], ⓘJ. Vijayasekhar[c]*

[a]Department of Mathematics, St. Francis College for Women, Begumpet, Hyderabad, India
[b]Department of Basic Sciences and Humanities, GMR Institute of Technology, Rajam, India
[c]Department of Mathematics, GITAM (Deemed to be University), Hyderabad, India
*Corresponding Author e-mail: vijayjaliparthi@gmail.com

This study thoroughly investigates the vibrational frequencies of carbonyl sulphide (12C16O32S) and hydrogen cyanide (HCN) up to the fifth harmonic level. It offers comprehensive insights into vibrational modes by using the Hamiltonian operator formalism and concentrating on invariant operators and algebraic parameters with a one-dimensional Lie algebraic method. The findings are significant for atmospheric chemistry, spectroscopy, and quantum chemistry, contributing to a deeper understanding of molecular dynamics. This research sets the groundwork for future studies in comparable compounds and applications.
Keywords: *Hamiltonian operator; Lie algebraic method; Carbonyl sulphide; Hydrogen cyanide; Morse Oscillator*
PACS: 33.20.-t, 33.20.Ea, 82.80.Gk, 63.50.-x, 45.20. Jj, 47.10.Df, 02.20.Sv

1. INTRODUCTION

The vibrational frequencies of molecules have immense significance in various scientific and practical disciplines. They are essential for understanding atoms interconnectedness and spatial arrangement within a molecule. This knowledge proves essential for precisely identifying molecular structures, especially when addressing complex organic compounds. The motivation behind studying the vibrational frequencies of carbonyl sulphide and hydrogen cyanide is to represent the molecular vibrations precisely, encompassing crucial quantum mechanical complexities. Precision is essential for understanding the molecular dynamics within complex structures. These molecules play a significant role in atmospheric chemistry, and analysing their vibrational frequencies under realistic conditions helps to understand their behaviour, providing valuable insights for atmospheric studies. By studying vibrational frequencies up to the fifth harmonic level, the accuracy of predictions for spectroscopic experiments is improved, facilitating the understanding and analysis of data. This study provides a strong basis for future research and creates opportunities for investigating similar molecules, thereby expanding the knowledge of molecular dynamics.

Essentially, the acquired vibrational frequencies provide an essential understanding of the molecule's behaviour in the atmosphere, offering valuable data for atmospheric monitoring. Moreover, precise data on vibrational frequency play a crucial role in developing and analysing spectroscopic experiments, particularly in environmental monitoring and industrial processes. The results further the development and creation of materials by enhancing our comprehension of their vibrational characteristics concerning desired properties. Moreover, knowing the vibrational frequencies helps evaluate the environmental impact, offering crucial data for assessing potential hazards and implementing measures to minimize negative consequences.

The U(2) Lie algebraic method has been recognized as an effective and widely utilized tool for understanding the complexities of the Heisenberg formulation of quantum mechanics, as evidenced by an essential and expanding body of research. Iachello and Arima are renowned for their systematic application of this method to various physical systems, particularly in their pioneering studies on the spectra of atomic nuclei. Iachello's pioneering work in 1981 expanded the utilization of the Lie algebraic approach to examine vibrational spectra in molecules [1]. The present method focuses on discretizing the Schrödinger wave equation by utilizing a three-dimensional Morse potential function to describe the rovibrational spectra of diatomic molecules precisely. The Lie algebraic method systematically expresses the Hamiltonian using a series expansion that involves a set of operators. This approach illustrates the local and normal modes of the system, offering a systematic framework for analysing experimental rovibrational spectra in polyatomic molecules. By utilizing the concept of dynamical symmetry, it improves our understanding of molecular structure [2, 3, 4].

Furthermore, the Lie algebraic method helps systematically analyse experimental data and allows for generating a Hamiltonian operator. This operator completely encapsulates the rovibrational degrees of freedom within the physical system, improving our ability to comprehend and forecast molecular structure. The Hamiltonian operator, a fundamental component of quantum mechanics, represents the combined effects of the particles' kinetic energy and the potential energy resulting from their interactions [2,3]. When used in vibrational analysis, the Hamiltonian operator provides the most accurate mathematical framework for calculating the quantized energy levels of a molecule. It operates on the system's wave function, producing the corresponding energy eigenvalues. The basic principle governing our ability to analyse and predict the vibrational frequencies of molecules is of the utmost significance in various disciplines, including spectroscopy and chemical kinetics [5,6,7].

This survey highlights a gap in exploring vibrational frequencies for selected molecules, particularly in higher overtones and combination bands. Given the current relevance of this research and the absence of attempts in this direction, the study aims to fill this gap by computing the vibrational frequencies of carbonyl sulphide and hydrogen cyanide up to the fifth harmonic level. To achieve this, a symmetry-adapted one-dimensional Lie algebraic framework will be employed. The anticipated outcome is the generation of accurate vibrational results for the specified molecules, accompanied by high-quality vibrational assignments. Importantly, these calculations are expected to offer a cost-effective alternative to other theoretical methods, such as ab initio approaches, ensuring computational efficiency.

2. LIE ALGEBRAIC METHOD FOR XYZ LINEAR TRIATOMIC MOLECULE OF $C_{\infty v}$ POINT GROUP

The Lie algebraic method is a robust mathematical framework used in quantum mechanics, particularly in studying symmetries and their consequences for physical systems. It involves the application of concepts from the theory of Lie algebras to quantum mechanics. A Lie algebra is a mathematical structure that describes the algebraic properties of certain types of symmetries. In the context of quantum mechanics, symmetries are transformations that leave the physical properties of a system unchanged. The Lie algebraic method is advantageous in studying quantum systems with continuous symmetries. It allows a systematic way to analyse and understand systems' behavior under symmetry operations. The Hamiltonian operator is a central concept in quantum mechanics. It corresponds to the total energy operator of a quantum system. The eigenstates (wavefunctions) of the Hamiltonian operator correspond to the allowed energy states of the system, and the corresponding eigenvalues represent the energies associated with those states. In the Lie algebraic method, one often seeks to find operators that commute with the Hamiltonian. These operators, known as conserved quantities or constants of motion, correspond to the observables associated with the symmetries of the system. The fact that they commute with the Hamiltonian implies that these quantities do not change over time, which is a consequence of Noether's theorem.

By employing the Lie algebraic approach, one can often find a set of operators that form a representation of the Lie algebra associated with the symmetries of the system. These operators can then be used to construct a complete set of commuting observables, which provides a set of compatible measurements that can be simultaneously determined with arbitrary precision.

The Hamiltonian operator (H) associated with the Lie algebraic method for XYZ linear triatomic molecule (involving two stretching bonds, X-Y and Y-Z) is expressed as follows [8, 9, 10, 11, 12]:

$$H = E_0 + \sum_{i=1}^{2} A_i C_i + \sum_{i<j}^{2} A_{ij} C_{ij} + \sum_{i<j}^{2} \lambda_{ij} M_{ij}. \tag{1}$$

A_i, A_{ij}, and λ_{ij} are algebraic parameters (in cm^{-1}) determined based on spectroscopic data. The operator C_i represents an invariant operator of the uncoupled bond, with eigenvalues given by $-4(N_i v_i - v_i^2), i = 1 (\text{for } X - Y), 2 (\text{for } Y - Z)$. For coupled bonds, the operator C_{ij} is diagonal, with matrix elements defined as:

$$\langle N_i, v_i; N_j, v_j | C_{ij} | N_i, v_i; N_j, v_j \rangle = 4\left[(v_i + v_j)^2 - (v_i + v_j)(N_i + N_j) \right], \tag{2}$$

The Majorana operator M_{ij} exhibits both diagonal and non-diagonal matrix elements:

$$\langle N_i, v_i; N_j, v_j | M_{ij} | N_i, v_i; N_j, v_j \rangle = (N_i v_j + N_j v_i - 2v_i v_j)$$

$$\langle N_i, v_i + 1; N_j, v_j - 1 | M_{ij} | N_i, v_i; N_j, v_j \rangle = -[v_j(v_i + 1)(N_i - v_i)(N_j - v_j + 1)]^{\frac{1}{2}}$$

$$\langle N_i, v_i - 1; N_j, v_j + 1 | M_{ij} | N_i, v_i; N_j, v_j \rangle = -[v_i(v_j + 1)(N_j - v_j)(N_i - v_i + 1)]^{\frac{1}{2}}. \tag{3}$$

Where, v_i, v_j represent the vibrational quantum numbers. The vibron numbers N_{X-Y} and N_{Y-Z} for the stretching bonds (X-Y and Y-Z) of the molecule can be calculated using the relation:

$$N_{X-Y} = \frac{(\omega_e)^{X-Y}}{(\omega_e x_e)^{X-Y}} - 1, \quad N_{Y-Z} = \frac{(\omega_e)^{Y-Z}}{(\omega_e x_e)^{Y-Z}} - 1. \tag{4}$$

Here, $\omega_e, \omega_e x_e$ are the spectroscopic constants of diatomic molecules [13, 14]. The initial guess values for the parameters A_{X-Y}, A_{Y-Z} can be obtained using the energy equation for the single-oscillator fundamental mode, given by:

$$E(v = 1) = -4A_i(N_i - 1), i = 1 (\text{for } X - Y), 2 (\text{for } Y - Z). \tag{5}$$

The initial guess for A_{ij} may be taken as zero. The parameter λ_{ij} can be obtained from the relation:

$$\lambda_{ij}^{X-Y} = \frac{|E_i - E_j|}{3N_{X-Y}}, \lambda_{ij}^{Y-Z} = \frac{|E_i - E_j|}{3N_{Y-Z}} \tag{6}$$

Where, E_i, E_j are vibrational energies of X-Y and Y-Z stretching bonding. A numerical fitting procedure is required to obtain the parameters, starting from the values provided by equations (5) and (6), for more accurate results.

3. RESULTS

Tables (1) and (2) provide a comprehensive analysis of the fundamental experimental vibrational frequencies of carbonyl sulphide (X: O-C, Y: C-S) and hydrogen cyanide (X: C-H, Y: C-N), offering a detailed comparison with their calculated counterparts. These tables go beyond experimental observations, including the predicted vibrational frequencies up to the fifth harmonic level. Additionally, the stretching combinational bands are intricately detailed, enhancing our understanding of the molecular dynamics of both carbonyl sulphide and hydrogen cyanide. Table 3 compiles optimized values for algebraic parameters and dimensionless vibron numbers utilized in our model. All parameters are expressed in cm^{-1}, except unitless vibron numbers.

Table 1. Carbonyl Sulphide Vibrational Frequencies

Vibrational mode	Vibrational frequencies (cm^{-1})	
	Experimental [15,16]	Calculated
v_1 (CO stretching)	2062.22	2062.22
v_2 (Bending)	520,41	520.41
v_3 (CS stretching)	858.95	858.95
$2v_1$	-	3807
$2v_2$	-	963
$2v_3$	-	1614
$3v_1$	-	5781
$3v_2$	-	1417
$3v_3$	-	2320
$4v_1$	-	7702
$4v_2$	-	1889
$4v_3$	-	3196
$5v_1$	-	9336
$5v_2$	-	2371
$5v_3$	-	3884
v_1+2v_1	-	5869.22
v_1+3v_1	-	7843.22
v_1+4v_1	-	9764.22
v_1+5v_1	-	11398.22
v_3+2v_3	-	2472.95
v_3+3v_3	-	3178.95
v_3+4v_3	-	4054.95
v_3+5v_3	-	4742.95

Table 2. Hydrogen Cyanide Vibrational Frequencies

Vibrational mode	Vibrational frequencies (cm^{-1})	
	Experimental [15,16]	Calculated
v_1 (CH Str)	3311.47	3311.47
v_2 (Bend)	711.98	711.98
v_3 (CN str)	2096.85	2096.85
$2v_1$	-	6320
$2v_2$	-	1324
$2v_3$	-	3867
$3v_1$	-	9290
$3v_2$	-	1983
$3v_3$	-	5832
$4v_1$	-	12422
$4v_2$	-	2729
$4v_3$	-	7650
$5v_1$	-	14924
$5v_2$	-	3224
$5v_3$	-	9344
v_1+2v_1	-	9631.47
v_1+3v_1	-	12601.47
v_1+4v_1	-	15733.47
v_1+5v_1	-	18235.47
v_3+2v_3	-	5963.85
v_3+3v_3	-	7928.85
v_3+4v_3	-	9746.85
v_3+5v_3	-	11440.85

Table 3. Fitted Algebraic Parameters in the Vibrational Hamiltonian Operator

Parameters	carbonyl sulphide	hydrogen cyanide
N_{X-Y}	44	162
N_{Y-Z}	156	178
A_1	-11.98	-5.14
A_2	-1.38	-2.96
A_{12}	-0.23	-1.21
λ_{12}	2.91	1.84

4. CONCLUSION

This study uses the symmetry-adapted one-dimensional U(2) Lie algebras framework for precisely calculating the vibrational frequencies of carbonyl sulphide and hydrogen cyanide up to the fifth harmonic level. This comprises the stretching and combinational bands. Our results are compared with experimental data at the first harmonic level, demonstrating a close approximation to the exact values and strongly agreeing with the results of experiments. The constructed vibrational Hamiltonian, which preserves the $C_{\infty v}$ point group, includes the spectra of interacting bound states of Morse oscillators. Furthermore, to the fundamental mode vibrations, the U(2) Lie algebraic Hamiltonian can be applied to higher overtones and combination bands up to the fifth harmonic level. This approach may offer a more cost-effective computational solution than other theoretical methods. The reliability and accuracy of the U(2) Lie algebraic method in predicting vibrational frequencies is emphasized by this observation. The significant durability of this shows its appropriateness for future research and practical uses, emphasizing its ability to contribute to progress in vibrational spectroscopy and related areas.

ORCID
Jaliparthi Vijayasekhar, https://orcid.org/0000-0002-2745-7401

REFERENCES
[1] F. Iachello, "Algebraic methods for molecular rotation-vibration spectra," Chem. Phys. Lett. **78**(3), 581-585 (1981). https://doi.org/10.1016/0009-2614(81)85262-1
[2] F. Iachello, and R.D. Levine, *Algebraic theory of molecules*, (Oxford University Press, Oxford, 1995).
[3] S. Oss, "Algebraic models in molecular spectroscopy," in: *Advances in Chemical Physics: New Methods in Computational Quantum Mechanics*, edited by I. Prigogine, and S.A. Rice, vol. 93, (John Wiley & Sons, Inc., 1996). pp. 455-649. https://doi.org/10.1002/9780470141526.ch8
[4] F. Iachello, and A. Arima, *The interacting Boson model*, (Cambridge University Press, Cambridge, 1987).
[5] M.R. Balla, and V. Jaliparthi, "Vibrational Hamiltonian of Methylene Chloride Using U(2) Lie Algebra," Mol. Phys. **115**, e1828634 (2021). https://doi.org/10.1080/00268976.2020.1828634
[6] M.R. Balla, S. Venigalla, V. Jaliparthi, "Calculation of Vibrational Frequencies of Sulfur Dioxide by Lie Algebraic Framework," Acta Phys. Pol. A, **140**(2), 138-140 (2021). https://doi.org/10.12693/APhysPolA.140.138
[7] V. Jaliparthi, "Vibrational Energies of Silylene, Difluorosilylene and Dichlorosilylene, Using U(2) Lie Algebraic Model," Ukr. J. Phys. Opt. **23**(3), 126-132 (2022). https://doi.org/10.3116/16091833/23/3/126/2022
[8] N.K. Sarkar, J. Choudhury, S.R. Karumuri, and R. Bhattacharjee, "A comparative study of the vibrational spectra of OCS and HCP using the Lie algebraic method," Eur. Phys. J. D, **53**, 163–171 (2009). https://doi.org/10.1140/epjd/e2009-00094-8
[9] N.K. Sarkar, J. Choudhury, and R. Bhattacharjee, "An algebraic approach to the study of the vibrational spectra of HCN," Molecular Physics, **104**(19), 3051-3055 (2006). https://doi.org/10.1080/00268970600954235
[10] A. Mengoni, and T. Shirai, "Vibron Model Description of Vibrational Spectra of the HCO and DCO Molecules," J. Mol. Spectrosc. **162**(1), 246-256 (1993). https://doi.org/10.1006/jmsp.1993.1281
[11] M.R. Balla, and V. Jaliparthi, "Vibrational Hamiltonian of Naphthalene ($C_{10}H_8$) Using Dynamical U(2) Lie Algebras," Polycycl. Aromat. Compd. **42**(7), 4684-4699 (2022). https://doi.org/10.1080/10406638.2021.1901126
[12] V. Jaliparthi, and M.R. Balla, "Vibrational Hamiltonian of Tetrachloro-, Tetrafluoro-, and Mono- Silanes Using U(2) Lie Algebras," Spectrochim. Acta A, **264**, 120289 (2022). https://doi.org/10.1016/j.saa.2021.120289
[13] K. Nakamoto, *Infrared and Raman Spectra of Inorganic and Coordination Compounds: Part A: Theory and Applications in Inorganic Chemistry*, (Wiley, New York, 2009).
[14] K.P. Huber, and G. Herzberg, *Molecular Spectra and Molecular Structure. IV: Constants of Diatomic Molecules*, (Van Nostrand Reinhold, New York, 1979).
[15] K.K. Irikura, "Experimental Vibrational Zero-Point Energies: Diatomic Molecules," J. Phys. Chem. Ref. Data, **36**(2), 389-397 (2007). https://doi.org/10.1063/1.3167794
[16] T. Shimanouchi, *Tables of Molecular Vibrational Frequencies Consolidated*, vol. I, National Bureau of Standards, **39**, 1-160 (U.S. Government Printing Office, 1972). https://nvlpubs.nist.gov/nistpubs/Legacy/NSRDS/nbsnsrds39.pdf

КОЛИВАЛЬНИЙ ГАМІЛЬТОНІАН КАРБОНІЛСУЛЬФІДУ ТА ЦІАНІДУ ВОДНЮ
К. Лаванья[a,c], А. Ганапаті Рао[b], Дж. Віджаясекхар[c]
[a]Відділ математики, жіночий коледж Св. Франциска, Бегумпет, Гайдарабад, Індія
[b]Відділ фундаментальних і гуманітарних наук, Технологічний інститут GMR, Раджам, Індія
[c]Департамент математики, GITAM, Хайдарабад, Індія
В роботі досліджено частоти коливань карбонілсульфіду (12C16O32S) і ціаніду водню (HCN) до рівня п'ятої гармоніки. Пропонується всебічне розуміння режимів коливань за допомогою формалізму оператора Гамільтона та концентрації на інваріантних операторах і алгебраїчних параметрах за допомогою одновимірного алгебраїчного методу Лі. Ці результати мають важливе значення для хімії атмосфери, спектроскопії та квантової хімії, сприяючи глибшому розумінню молекулярної динаміки. Дослідження закладає основу для майбутніх досліджень порівнянних сполук і застосувань.
Ключові слова: *оператор Гамільтона; алгебраїчний метод Лі; карбонілсульфід; ціаністий водень; осцилятор Морзе*

ISOTHERMAL DECAY ANALYSIS OF THERMOLUMINESCENCE PEAKS OF QUARTZ FOR KINETIC PARAMETER DETERMINATION

Sahib Mammadov*, Muslim Gurbanov, Aqshin Abishov, Ahmad Ahadov

Institute of Radiation Problems, Ministry of Science and Education, Azerbaijan,
9, B. Vahabzade str. Baku, Azerbaijan, 1143
Corresponding Author e-mail: s.mammadov@irp.science.az

This study delves into the intricacies of isothermal decay analysis applied to thermoluminescence (TL) peaks, focusing on determining kinetic parameters. The study challenges the conformity of the trap responsible for the ITL signals to first, second, or general-order kinetics, supported by the non-conforming decay pattern and the inference of two overlapping first-order TL peaks. This work enhances the understanding of TL peaks and establishes a reliable methodology for characterizing luminescence mechanisms in materials, contributing to advancements in luminescence dosimetry research. These observations lead to the conclusion that the TL data originates from more than one trap, and based on existing literature, it is inferred that there are two overlapping first-order TL peaks. The investigation involves the consideration of isothermal decay data at distinct temperatures (T = 250, 260, 270, 280, and 290°C) and explores challenges associated with achieving precise linear fits for different kinetic order values (b). The nature of decay is interpreted based on the monomolecular theory, suggesting adherence to a first-order process. ITL curves were deconvoluted into two exponential decay curves. The slopes of the regression lines provide activation energy (E) values for curve1 and curve2, respectively: $E_1 = 0.99\pm0.16$ eV and $E_2 = 1.32\pm0.18$ eV. The frequency factor (s) is determined from the intercept of the regression line: $s_1 = 1.32\times10^8$ s^{-1} and $s_2 = 1.77\times10^{12}$ s^{-1}.
Keywords: *Isothermal decay; Quartz; Activation energy; Frequency factor*
PACS: 78.60 Kn

INTRODUCTION

Natural minerals are increasingly vital in contemporary science and technology, with many displaying thermoluminescence (TL) characteristics that contribute to our understanding of damage and safety processes in radiation incidents. Among these minerals, quartz is a crucial, cost-effective, and abundant material with numerous advantages for research in radiation, environmental, and clinical radiological applications [1]. When irradiated grains of quartz undergo heating from room temperature to elevated levels, they exhibit various glow curves. These curves depend on chemical composition, impurity types and concentrations, defects, geological origin, irradiation, sensitization, and other experimental conditions [2], [3].

Numerous TL glow peaks within the temperature range of 333–753 K have been reported by various authors for diverse quartz samples [4]–[6]. According to these studies, high-temperature TL peaks demonstrate greater stability post-irradiation than low-temperature peaks, which decay more rapidly due to shorter lifetimes. Despite the diverse capabilities demonstrated by natural quartz, a comprehensive understanding of its detailed irradiation response, defect production and distribution, and thermoluminescence mechanism remains elusive. The challenge arises from the difficulty in comparing TL measurements across different studies, as quartz samples from various origins, conditions, and impurities may exhibit inconsistencies. Therefore, this study explores the TL characteristics and defect production of naturally occurring quartz subjected to high gamma doses (8 kGy).

Luminescence-based measurements in retrospective dosimetry entail assessing the charge stored in localized defect states through external stimuli like heat or light. In thermoluminescence (TL), the exclusive mechanism for stimulation is heat energy. Isothermal signals, termed phosphorescence or isothermal TL (ITL), are employed to estimate the equivalent dose (De) and determine trap parameters such as thermal and optical trap depths (in units of eV), frequency factor (in units of s^{-1}), as well as thermal assistance and thermal-quenching energies. Therefore, a comprehensive understanding of the characteristics and origins of isothermal signals, ITL, is crucial. Signals originating from a constant flux of stimulation energy are anticipated to exhibit a consistent, often exponential, decay pattern.

Current interest in the thermoluminescence of quartz obtained from building materials such as mortar and concrete, especially for dose reconstruction purposes, requires accurate determination of this mineral's thermoluminescence parameters associated with intermediate luminescence peaks [7], [8]. The isothermal TL signal from deep traps holds the potential for retrospective dosimetry [7]. Recently, there have been indications that the high-temperature TL signal (325 °C) demonstrates significantly higher dose saturation compared to OSL. Consequently, efforts have been made to utilize isothermal TL at 310 and 320 °C to develop single-aliquot dose measurement methods.

This study aims to present the findings of an isothermal TL investigation, evaluating various parameters essential for describing the TL process in quartz. The objective is to contribute to understanding natural quartz's luminescence mechanisms. These parameters include the activation energy (E) for TL traps, also known as trap depth, the frequency factor (s), and the order of kinetics (b) of the TL process.

MATERIALS AND METHODS

The quartz samples employed in this experiment were obtained from beach sand through traditional chemical separation methods. The sand underwent sieving to isolate grain size fractions ranging from 80 to 120 μm. Subsequently, this grain size fraction underwent hydrochloric acid (HCl) treatment, separation through heavy liquids, and etching in a 40% hydrofluoric acid (HF) solution. The precipitated fluorides were dissolved using HCl. Before subsequent irradiation, the samples were heated to 600ºC for one hour to eliminate residual thermoluminescence (TL) centers. The irradiation occurred at an ambient temperature using a ^{60}Co source, with dose levels reaching 8 MGy.

In a standard isothermal decay experiment, the established procedure entails rapidly heating the irradiated sample to a specified temperature and maintaining it for a predetermined duration. The quartz grains were affixed to an aluminum disc of 0.1 mm thickness using silicone spray for measurement purposes. Isothermal TL (ITL) measurements were conducted using a Harshaw 3500 manual reader, holding the aliquots for 50 s at a constant temperature. The preheating was executed at a rate of 2ºC s^{-1} in a nitrogen (N$_2$) atmosphere, and the ITL curves were recorded immediately upon reaching the measurement temperature. Under these conditions, we observed monotonically decreasing ITL signals that exhibited no detectable disturbance due to thermal lag. Any significant thermal lag would have manifested as an initial rise to a maximum before subsequent decay [9]. The emitted light, termed phosphorescence decay, is observed over a period, enabling the evaluation of the decay rate of trapped electrons. Graphs depicting the correlation between thermoluminescence (TL) intensity and time at a constant temperature are known as isothermal decay curves.

Garlick and Gibson showcased the methodology of analyzing isothermal decay within the framework of first-order kinetics [10]. When scrutinizing isothermal decay curves at a specific temperature (T_i) for TL peaks following first-order kinetics, the resultant graphs exhibit an exponential relationship with time, as depicted by the Equation:

$$It = I_0 exp\left(-s exp^{\left(-\frac{E}{kT_i}\right)}t\right), \tag{1}$$

where
I_0 = initial TL intensity, I_t = the TL intensity at time t, s = effective frequency factor, E = activation energy, T = temperature of isothermal decay.

This Equation signifies that a plot of ln(I) against time will exhibit a linear relationship for peaks governed by first-order kinetics. Furthermore, the slope of this linear graph will be determined by:

$$slope = m_i = -s exp^{\left(-\frac{E}{kT_i}\right)}, \tag{2}$$

Taking the natural logarithm of the equation yields:

$$(|slope|) = lns - \frac{E}{kT_i}. \tag{3}$$

The graph depicting ln(slope) versus 1/kT is expected to be a straight line with a slope equal to -E and a Y-intercept corresponding to ln(s).

Equations describing the thermoluminescence processes have been provided by Randall–Wilkins for first order, Garlick–Gibson for second order, and May–Partridge for general order kinetics [11]:

$$I(t) = -\frac{dn}{dt} = ns exp^{\frac{-E}{kT}}, \tag{4a}$$

$$I(t) = -\frac{dn}{dt} = \frac{n^2}{N} s exp^{\frac{-E}{kT}}, \tag{4b}$$

$$I(t) = -\frac{dn}{dt} = n^b s' exp^{\frac{-E}{kT}}, \tag{4c}$$

Where n is the trapped charged population.

These equations provide a method for calculating E. In this context, applying isothermal analysis allows determining the kinetics order, denoted as b. By keeping the temperature constant and integrating the general-order equation (4c) with respect to time (t), the following expression is derived:

$$I_t = I_0 \left[1 + s'n_0^{b-1}(b-1)t exp^{\left(-\frac{E}{kT}\right)}\right]^{\frac{b}{1-b}}, \tag{5}$$

Where I_0 and n_0 represent the initial TL intensity and the initial concentration of trapped charges, respectively, I_t is the TL intensity at time t. By rearranging Equation (5), we obtain:

$$I_0 = s'n_0^b exp^{\left(-\frac{E}{kT}\right)}, \tag{6}$$

where
$s' = s/N$ = effective frequency factor, N is the number of traps.
n_0 = initial trapped charged population.

This Equation suggests that a plot of the quantity against time should exhibit a linear trend when an appropriate value of b is determined. Various isothermal decay temperatures produce a series of straight lines with different slopes.

RESULTS AND DISCUSSIONS

Figure 1 illustrates the given data corresponding to five distinct temperatures: T = 250, 260, 270, 280, and 290°C. As previously detailed, the isothermal decay curves for thermoluminescence (TL) peaks conforming to first-order kinetics follow exponential time functions. According to [12], a plot of ln(I) against time (t) will exhibit a linear correlation for first-order kinetics peaks, with the slope of the line determined by equation (3). A plot of ln(|slope|) versus 1/kT is anticipated to display a linear pattern, with a slope equal to -E and a y-intercept equal to ln s if the provided isothermal TL data aligns with first-order kinetics. Initially, we calculate ln (TL) for each isothermal curve and plot ln (TL) against time.

Subsequently, regression lines are computed for the plot with T=250°C in Figure 2. Figure 2 depicts the plot of ln(TL) against time (t), with T=250°C representing the temperature while recording isothermal decay curves. First-order kinetics can be ruled out by inspecting the ln (TL) graph against time, as shown in Figure 2. The resultant plots reveal a nonlinearity, indicating that the data does not conform to first-order kinetics. If we reformulate Equation (5), the isothermal decay curves of TL peaks corresponding to general order kinetics with the kinetic order parameter denoted as "b" will be characterized as follows:
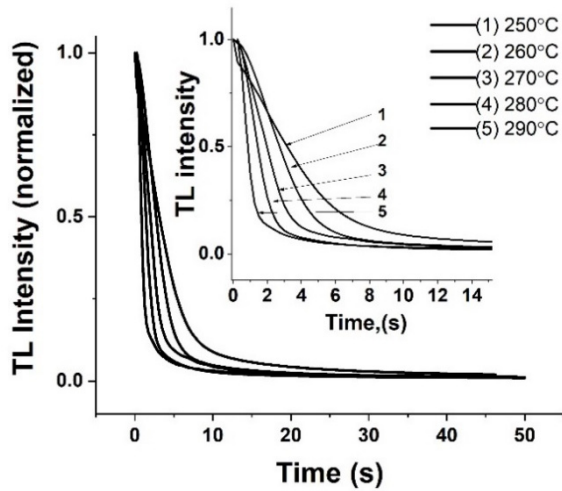
Figure 1. Isothermal TL decay curves of quartz at different temperatures. Quartz irradiated at 8MGy.
Inserting is a magnified part of the spectrum from 0 to 14 s
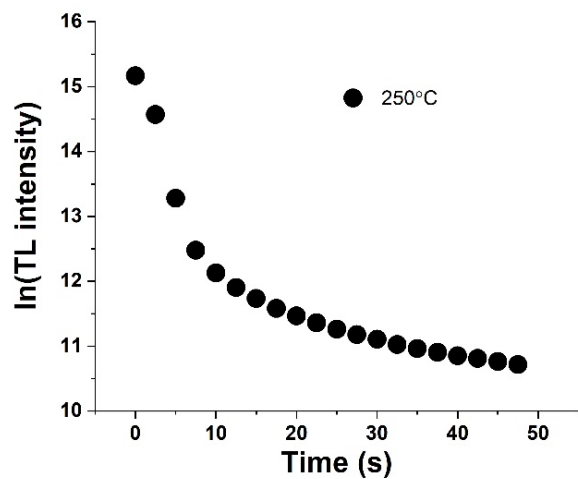
Figure 2 The isothermal decay curves on the semi-log scale for the isothermal decay curve of quartz at 250°C

$$\left(\frac{I_t}{I_0}\right)^{\frac{1-b}{b}} = 1 + s'n_0^{b-1}(b-1)t\exp^{\left(-\frac{E}{kT}\right)}. \tag{7}$$

This Equation suggests that a graph of the quantity $(I_t / I_0)^{(1-b)/b}$ against time t should form a straight line when an appropriate value of b is identified. After determining the value of b, we will plot $(I_t / I_0)^{(1-b)/b}$ against time t for the five different decay temperatures, resulting in a set of straight lines with a slope (m) given by the formula:

$$m = s'n_0^{b-1}(b-1)\exp^{\left(-\frac{E}{kT}\right)}. \tag{8}$$

The activation energy E and the effective frequency factor $s'' = s'n_0^{b-1}$ will be determined from the slope and intercept of the plot of ln(m) versus 1/ kT.

Figure 3 depicts the quantities $(I_t / I_0)^{(1-b)/b}$ for the isothermal decay data at T = 260°C, considering four different values of the kinetic-order parameter (b = 1.9, 2.0, 2.1, and 2.2) as a function of time t. It is evident that none of the four graphs yield satisfactory linear fits.

This situation emphasizes a potential challenge when dealing with isothermal decay data: attaining a precise estimation of the optimal linear fit might prove challenging due to subtle graph variations for different values of b. The computed values of R suggest that the graphs corresponding to different values of b do not provide an accurate linear fit, affirming the consistency of the provided TL data with second-order kinetics. A parallel analysis has been applied to all other four isothermal decay datasets, yielding the same results.

The observed decay in the current investigation is elucidated through the monomolecular (first-order) superposition theory. This type of decay results from the overlay of exponentials associated with different traps and is mathematically represented by the Equation [13]:

$$I_t = I_{01}\exp(-P_1 t) + I_{02}\exp(-P_2 t) + \cdots$$

where I_{on} is the phosphorescence intensity due to electrons in the traps of energy E_n, $P_n = s\exp(-E_n/kT)$ is the probability of an electron escaping from a trap, k is the Boltzmann constant, and *s* is the escape frequency factor. Consequently, each decay curve can be dissected into a series of exponentials using the "unraveling" procedure, enabling the calculation of E values corresponding to each exponential.
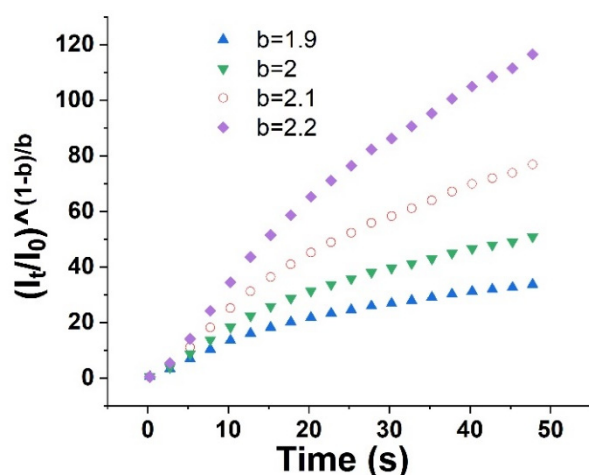
Figure 3. Isothermal decay data at a temperature of 260°C calculated for several values of kinetic order b as a function of time
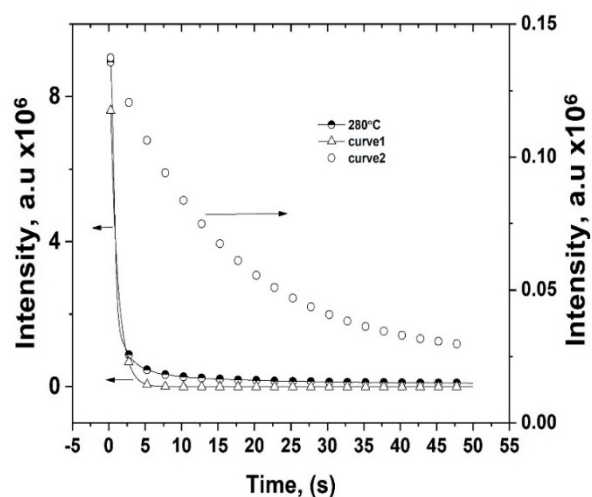
Figure 4. Isothermal decay data for the 280°C deconvoluted into two exponential decay curves

It is observed that each decay curve can be decomposed into two exponentials, as illustrated in the isothermal decay curve at 20°C presented in Fig. 4. For the first curve, I_1= 4.84634E6 and P_1= 0.96471, while for the second curve, I_2 = 114707 and P_2= 0.06435. The nature of decay can thus be interpreted based on the monomolecular theory, suggesting that the luminescence kinetics adhere to a first-order process. The consideration of first-order kinetics is supported by inspecting the linearity in the ln (TL curve1) and ln (TL curve2) plots against time, as depicted in Figure 5. The resulting plots for curve1 and curve2 demonstrate linearity, indicating that the data conforms to first-order kinetics.
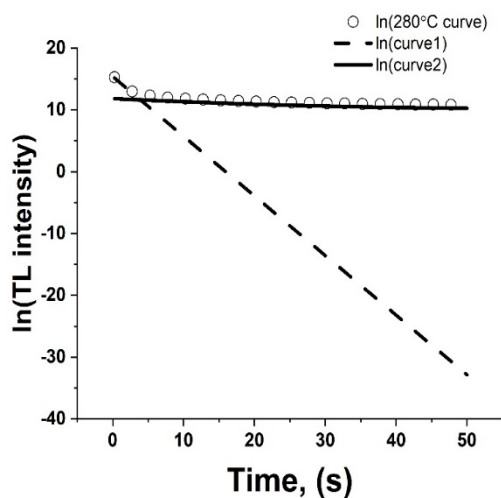
Figure 5. The isothermal decay curves on the semilog scale for the isothermal decay curve of quartz at 280°C and the two deconvoluted cures 1 and 2

Figure 6. The ln(slope) versus 1/kT graph to determine E for TL data of convoluted curves 1 and 2

In the subsequent step, we compile the slopes of these linear graphs in Table 1 and compute the natural logarithm of the slopes, denoted as ln(slope), for all five ITL curves corresponding to the temperatures T = 250, 260, 270, 280, and 290°C. A graph in Figure 6 depicts the ln(slope) of curve 1 and curve 2 against 1/kT, where T represents the temperature (in Kelvin) while recording isothermal decay curves.

Table 1. The slopes of linear isothermal graphs and their natural logarithms ln(slope)

Temperature °C	1/kT (eV^{-1})	Curve1		Curve2	
		slope (s^{-1})	ln(slope)	slope (s^{-1})	ln(slope)
250	22.19	0.2888	-1.24202	0.0388	-3.24934
260	21.77	0.76471	-0.26826	0.06455	-2.74032
270	21.37	1.28707	0.25237	0.12493	-2.08
280	20.99	1.48454	0.3951	0.11639	-2.15081
290	20.61	2.75118	1.01203	0.20012	-1.60884

The slope of the regression line provides the activation energy E, and interceptions for curve1 and curve2 subsequently are:

E1=0.99±0.16 eV; intersept1 = 18.7±3.4 and

E1=1.32±0.18 eV; intersept1 = 28.2±4.2

The frequency factor s can be found from the intercept of the regression line:

$intersept1 = ln(s1) = 18.7$; $s1 = \exp(18.7) = 1.32 \times 10^8$ s^{-1} and

$intersept2 = ln(s2) = 28.2$; $s2 = \exp(28.2) = 1.77 \times 10^{12}$ s^{-1}

As reported in the literature, most natural sedimentary quartz grains exhibit two thermo-luminescence (TL) peaks, at 325 and 375 °C, when the grains are heated between 300 and 400 °C at a rate of 20 °C/s [14] and their luminescence is observed with blue and near UV color glass filters in front of the photomultiplier tube. Previous studies have shown that at a heating rate of 5 °C/s, the peaks occur at 305 and 350 °C, respectively [6]. Our observations also lead to the conclusion that the ITL data described in Figure 1 originates from more than one trap, and based on existing literature, it is inferred that there are two overlapping first-order TL peaks.

CONCLUSIONS

Investigating isothermal decay analysis of thermoluminescence (TL) peaks has provided valuable insights into the kinetic parameters governing this luminescent phenomenon. The challenges associated with achieving precise linear fits for different kinetic order values (b) underscore the intricacies of the analysis. In summary, it can be inferred that the trap responsible for the ITL signals at 250, 260, 270, 280, and 290°C does not conform to first, second, or general order kinetics. This deduction is supported by: (a) The decay pattern of the ITL signal recorded at 250, 260, 270, 280, and 290°C deviates from the behavior described by Eq. (5) for b values ranging from 1 to 2 (refer to Fig. 2 and 3). (b) These observations lead to the conclusion that the TL data depicted in Fig. 4 originates from more than one trap, and based on existing literature, it is inferred that there are two overlapping first-order TL peaks.

This thorough analysis contributes to the understanding of TL peaks and establishes a robust methodology for characterizing luminescence mechanisms in materials. The consistent application of these analytical techniques to isothermal decay data across various temperatures enhances the reliability and applicability of our findings. In summary, our study advances the understanding of kinetic parameters in TL peaks and provides a foundation for future research in luminescence dosimetry.

ORCID
Sahib Mammadov, https://orcid.org/0000-0002-4547-4491; **Muslim Gurbanov,** https://orcid.org/0000-0003-3321-1026
Aqshin Abishov, https://orcid.org/0000-0003-2467-4344; **Ahmad Ahadov,** https://orcid.org/0000-0002-6039-8714

REFERENCES

[1] M. Singh, N. Kaur, and L. Singh, "Thermoluminescence characteristics of high gamma dose irradiated natural quartz," Nucl. Instruments Methods Phys. Res. Sect. B Beam Interact. with Mater. Atoms, **276**, 19–24 (2012). https://doi.org/10.1016/j.nimb.2012.01.007

[2] F. Preusser, M.L. Chithambo, T. Götte, M. Martini, K. Ramseyer, E.J. Sendezera, G.J. Susino, *et al.*, "Quartz as a natural luminescence dosimeter," Earth-Science Rev. **97**(1–4), 184–214 (2009). https://doi.org/10.1016/j.earscirev.2009.09.006

[3] D.A.G. Vandenberghe, M. Jain, and A.S. Murray, "Equivalent dose determination using a quartz isothermal TL signal," Radiat. Meas. **44**(5-6), 439–444 (2009). https://doi.org/10.1016/j.radmeas.2009.03.006

[4] C. Schmidt, and C. Woda, "Quartz thermoluminescence spectra in the high-dose range," Phys. Chem. Miner. **46**, 861–875 (2019). https://doi.org/10.1007/s00269-019-01046-w

[5] M. Jain, G.A.T. Duller, and A.G. Wintle, "Dose response, thermal stability and optical bleaching of the 310 °C isothermal TL signal in quartz," Radiat. Meas. **42**(8), 1285–1293 (2007). https://doi.org/10.1016/j.radmeas.2007.08.008

[6] A.D. Franklin, "On the interaction between the rapidly and slowly bleaching peaks in the TL glow curves of quartz," J. Lumin. **75**(1), 71–76 (1997). https://doi.org/10.1016/S0022-2313(97)00099-9

[7] I. Veronese, A. Giussani, H.Y. Goksu, and M. Martini, "Isothermal decay studies of intermediate energy levels in quartz," Radiat. Environ. Biophys. **43**(1), 51–57 (2004). https://doi.org/10.1007/s00411-004-0228-9

[8] I. Veronese, *The thermoluminescence peaks of quartz at intermediate temperatures and their use in dating and dose reconstruction*, 2005. http://www3.fisica.unimi.it/highlights2005/abstracts/Milazzo/abs-veronese.pdf

[9] M. Jain, L. Bøtter-Jensen, A.S. Murray, and R. Essery, "A peak structure in isothermal luminescence signals in quartz: Origin and implications," J. Lumin. **127**(2), 678–688 (2007). https://doi.org/10.1016/j.jlumin.2007.04.003

[10] V. Pagonis, G. Kitis, and C. Furetta, *Numerical and practical exercises in thermoluminescence,* (Springer, 2006). https://doi.org/10.1007/0-387-30090-2

[11] C. Furetta, and G. Kitis, "Models in thermoluminescence," J. Mater. Sci. **39**, 2277–2294 (2004). https://doi.org/10.1023/B

[12] C. Furetta, *Handbook of Thermoluminescence*, (2nd Edition), (World Scientific Publishing Co. Pte. Ltd., 2006).

[13] M.G. Patil, S.H. Pawar, and R.D. Lawangar, "Relative location of traps and luminescence centres in CaS:Pd phosphors as revealed by photo-, thermo- and electroluminescence studies," Solid State Commun. **34**(2), 105–108 (1980). https://doi.org/10.1016/0038-1098(80)91243-0

[14] M.J. Aitken, *Thermoluminescence Dating*, (Academic Press Inc. 1985).

АНАЛІЗ ІЗОТЕРМІЧНОГО РОЗПАДУ ПІКІВ ТЕРМОЛЮМІНЕСЦЕНЦІЇ КВАРЦУ ДЛЯ ВИЗНАЧЕННЯ КІНЕТИЧНИХ ПАРАМЕТРІВ

Сахіб Мамедов, Муслім Гурбанов, Акшин Абішов, Ахмад Ахадов
Інститут радіаційних проблем Міністерства науки і освіти Азербайджану,
вул. Б. Вахабзаде, 9 Баку, Азербайджан

Це дослідження заглиблюється в тонкощі аналізу ізотермічного розпаду, застосованого до піків термолюмінесценції (TL), зосереджуючись на визначенні кінетичних параметрів. Дослідження ставить під сумнів відповідність пастки, відповідальної за сигнали ITL, кінетиці першого, другого чи загального порядку, що підтверджується невідповідною схемою розпаду та висновком про два перекриваються піки TL першого порядку. Ця робота покращує розуміння піків TL і встановлює надійну методологію для характеристики механізмів люмінесценції в матеріалах, сприяючи прогресу в дослідженнях люмінесцентної дозиметрії. Ці спостереження приводять до висновку, що дані TL походять від більш ніж однієї пастки, і на основі існуючої літератури робиться висновок про наявність двох перекриваючих піків TL першого порядку. Дослідження передбачає розгляд ізотермічних даних розпаду при різних температурах (T = 250, 260, 270, 280 і 290°C) і досліджує проблеми, пов'язані з досягненням точних лінійних відповідностей для різних значень кінетичного порядку (b). Природа розпаду інтерпретується на основі мономолекулярної теорії, яка передбачає дотримання процесу першого порядку. Криві ITL були розведені на дві експоненціальні криві розпаду. Нахили ліній регресії забезпечують значення енергії активації (E) для кривої 1 і кривої 2 відповідно: $E_1 = 0.99 \pm 0.16$ eB і $E_2 = 1.32 \pm 0.18$ eB. Коефіцієнт частоти (s) визначається з точки перетину лінії регресії: $s_1 = 1.32 \times 10^8$ c^{-1} та $s_2 = 1.77 \times 10^{12}$ c^{-1}.

Ключові слова: *ізотермічний розпад; кварц; енергія активації; частотний фактор*

COMPARATIVE EPR ANALYSIS OF MODERN AND FOSSIL TOOTH ENAMEL: UNVEILING AGING-INDUCED COMPONENTS

Sahib Mammadov

Institute of Radiation Problems, Ministry of Science and Education of Azerbaijan Republic; 9, B. Vahabzade str., Baku, Azerbaijan
Corresponding Author e-mail: mammadov.irp@science.gov.az
Received December 7, 2023; revised January, 9, 2024; accepted January 22, 2024

This study involves comparing EPR signals from three-year-old modern cow tooth enamel with the spectra of fossil tooth enamel exposed to natural background radiation over an extended period. The EPR spectrum of the significantly aged fossil tooth enamel displays additional components absent in the EPR spectra of the modern tooth enamel. Specifically, the septet signal associated with isopropyl (or alanine) radicals is not observed in the EPR signals of modern tooth enamel when irradiated up to 1.3 kGy. It is hypothesized that the isopropyl radicals present in fossil tooth enamel are not a result of radiation but rather stem from the natural breakdown of organic components due to the aging process. This characteristic is proposed as a dependable tool for authenticating tooth samples.
Keywords: *Modern tooth enamel; Fossil teeth; EPR dosimetry; Isopropyl radical*
PACS: 78.60 Kn

INTRODUCTION

EPR dosimetry and dating rely on identifying and quantifying an Electron Paramagnetic Resonance (EPR) signal induced by ionizing radiation, provided the signal intensity was once reset to zero. Implicit in this approach is the assumption that a correlation exists between the intensity of the radiation-induced signal and the absorbed radiation dose. This fundamental principle underlies the use of tooth enamel as a natural dosimeter in EPR dosimetry and dating [1]–[5]. Irradiated tooth enamel exhibits a stable EPR signal, the intensity of which corresponds to the absorbed dose [6].

It is well established that the EPR signal in fossilized tooth enamel is of a composite nature, necessitating the isolation of the radiation-induced EPR signal from other paramagnetic signals [4], [7]–[9]. In tooth enamel or bone suitable for dating, a stable CO^{2-} radical generated by radiation is a key signal. Other radicals induced by irradiation, such as CO_3^{3-} and CO^{3-}, are irrelevant for retrospective dosimetry or dating due to their instability [10].

Additionally, the EPR spectrum of tooth enamel contains a native signal present in non-irradiated modern tooth enamel. However, even the youngest tooth is not exempt from weak, radiation-induced EPR signals due to natural background irradiation. Modern enamels from human and other mammals' teeth, when irradiated in the laboratory, have been widely studied using the EPR method. A general observation is that the complete EPR line shape of laboratory-irradiated tooth enamel differs from that of naturally irradiated enamel, although the central part of the spectrum is easily reproducible.

The focus of the current study is a comparison of EPR signals obtained from three-year-old modern cow tooth enamel with the spectra of fossil tooth enamel that has been exposed to natural background radiation for an extended period.

EXPERIMENTAL

The objects under investigation included a remarkably well-preserved fossil tooth from an elephant (Palaeoloxodon antiquus) discovered in the Mingachevir district of Azerbaijan in 2010, as well as a three-year-old modern cow tooth. The extinct straight-tusked elephant (Palaeoloxodon antiquus) once inhabited Europe during the Middle and Late Pleistocene, approximately 781,000 to 50,000 years before the present. Initially believed to be closely related to the living Asian elephant, a shift occurred in 2016 when DNA sequence analysis revealed that its closest living relative is the African forest elephant, Loxodonta cyclotis. Surprisingly, it is more closely related to L. cyclotis than L. cyclotis is to the African bush elephant, L. africana. This finding challenges the current classification of the genus Loxodonta, as outlined in E. Callaway's article "Elephant history rewritten by ancient genomes" in Nature, published in September 2016 (https://doi.org/10.1038/nature.2016.20622). The procedures for sample preparation and Electron Spin Resonance (ESR) measurements were as follows: Initially, the enamel was carefully extracted from the teeth using a dental drill with water cooling. The 1.5-mm average thickness enamel was then immersed in a 30% NaOH solution for a day to disinfect and separate any remaining dentine.

For the fossil tooth enamel samples, a dental drill was employed to remove approximately 50±5 µm from both the inside and outside of the enamel surface, ensuring that natural alpha radiation did not impact the results. In total, 2 g of enamel was collected from both the fossil and modern tooth and air-dried at room temperature for three days. Half of the samples were powdered using an agate mortar, and powder with a size range of 100–50 µm was isolated for subsequent

measurements. The remaining portion was retained as a single fragment of enamel measuring 4mm×1mm×1.5mm. Both enamel powder (0.1 g) and single fragment (bulk) samples were individually placed inside Suprasil glass tubes for the EPR signal measurements.

The ESR signal of the samples was assessed using a Bruker EMXplus (X-band) spectrometer. The spectrometer was configured with the following parameters: a central field of 3,520 G, a scan range of 100 G, an amplitude modulation of 3 G, a modulation frequency of 100 kHz, a time constant of 20.48 ms, and a power of 2.14 mW unless otherwise specified in the text. Subsequently, the samples underwent irradiation at room temperature utilizing a ^{60}Co source, with additional doses applied, and ESR signals were measured under identical conditions.

The dose rate of the ^{60}Co source was determined using the Magnettech Miniscope MS400 EPR Spectrometer, employing individually wrapped barcode-labeled BioMax Alanine Dosimeter Films (developed by Eastman Kodak Company).

RESULTS AND DISCUSIONS

The EPR signal in fossil tooth enamel manifests as an asymmetric signal characterized by three peaks at $g \sim 2.0043$ (T1), $g \sim 2.0013$ (B1), and $g \sim 1.9985$ (B2) (refer to Fig. 1A (1)). The primary contributor to this signal is identified as the CO_2^- radical [11], although other radicals, predominantly carbonate-derived radicals and certain oxygen radicals [11], are suggested to play minor roles. Additionally, a signal at position "a" is observed, attributed to the isopropyl radical with a hyperfine splitting of 2.17 mT [1][4][12]. This septet signal has been previously noted in middle Pleistocene tooth samples by other researchers [13]. However, Duval [14] associated this signal with "free diethyl" radicals. While the experimental separation of the central signal is challenging, the system is commonly simplified by considering three main types of CO_2 [11]: one isotropic at $g \sim 2.0006$ and two anisotropic CO2 radicals—an axial ($g_\perp \sim 2.003$; $g_\parallel \sim 1.997$) and an orthorhombic ($g_x \sim 2.003$; $g_y \sim 1.997$; $g_z \sim 2.001$). Owing to differences in thermal stability and microwave saturation characteristics, the relative proportions of these signals in the ESR signal may vary between natural and irradiated spectra, leading to the observation of distinct yet closely situated g values at positions T_1, B_1, and B_2.
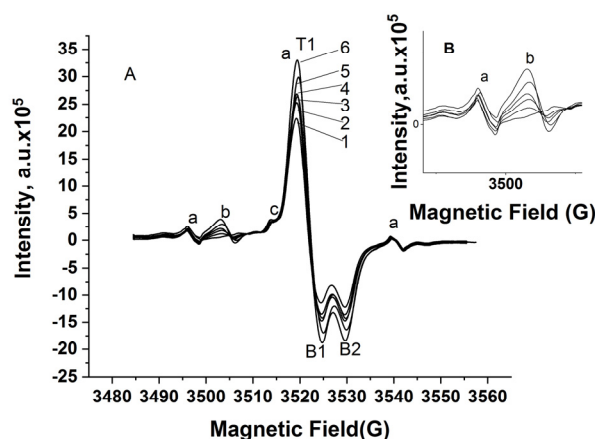
Figure 1. Dose-response spectrum of fossil tooth enamel powder

In panel A, the spectra are presented for various conditions: natural, without additional laboratory dose (1); irradiated at 44.7 Gy (2); 89.4 Gy (3); 114.1 Gy (4); 178.8 Gy (5); and 223.5 Gy (6). The dose rate was 0.149 Gy/s. In panel B, a segment of the spectra around 3,500 G is highlighted. Punctuation and identification of EPR signals have been adopted from [14]: (i) The signal labeled "a" represents a septet centered on the primary CO_2^- signal at $g = 2.0043$, formed by a free dimethyl radical, with only three lines visible in that magnetic field range; (ii) the isotropic line (marked "b") at $g = 2.0114$ could be ascribed to CO_3^-; and the isotropic line at $g = 2.0075$ (marked "c") is typically attributed to a free radical, likely SO_2^- Positions T1, B1, and B2 are indicative of the primary EPR signal

Upon laboratory irradiation, there is an augmentation in the EPR signal, as illustrated in Fig. 1, depicting signal intensity at different doses. Noticeable peak increases occur in the central part of the spectra and at position "b," while peaks associated with isopropyl radicals (position a) remain unchanged (refer to Fig. 2b).

The identical samples were also assessed six months later, as depicted in Figure 2 A minor reduction in the intensity of the central signal was noted, while the signal at position "b" returned to its initial level (refer to Fig. 3B). The intensity of the signal at position "a" remained constant.

The EPR signal in the non-irradiated modern tooth sample is exceedingly faint, requiring special efforts to discern it from the noise signal. Upon subjecting the sample to additional laboratory irradiation, the typical central signal of tooth enamel becomes observable.

The EPR spectra illustrating the dose response of the modern tooth sample are presented in Fig. 3. The tooth samples underwent irradiation with ^{60}Co, ranging from a dose of 174 Gy to 1,305 Gy. The EPR signal of the modern cow tooth enamel is characterized by an asymmetric signal with three peaks at $g \sim 2.0044$ (T1), $g \sim 2.0020$ (B1), and $g \sim 1.9987$ (B2). Notably, the positions of these peaks exhibit minimal changes when compared to the EPR signal of fossil tooth enamel.

A distinctive aspect of the EPR spectra of the modern tooth is the absence of both the peak at position "a" and the peak at position "b." Moreover, these peaks do not appear in the spectrum even up to the irradiation dose of 1.305 Gy. EPR studies on modern tooth samples have been conducted by several researchers [15]–[20], and a general consensus emerges that direct irradiation does not lead to the generation of an EPR signal at position "a".
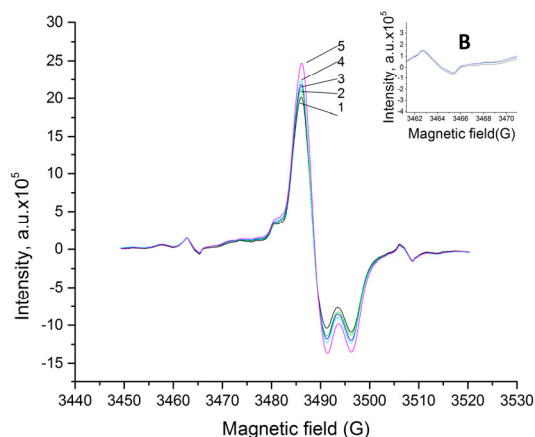
Figure 2. Dose response spectra of fossil tooth enamel powder six months later: irradiated at 44.7 Gy (1); 89.4 Gy (2); 114.1 (3); 178.8 Gy (4); 223.5 Gy (5). B: insert is a magnified part of the spectrum around 3,470 G
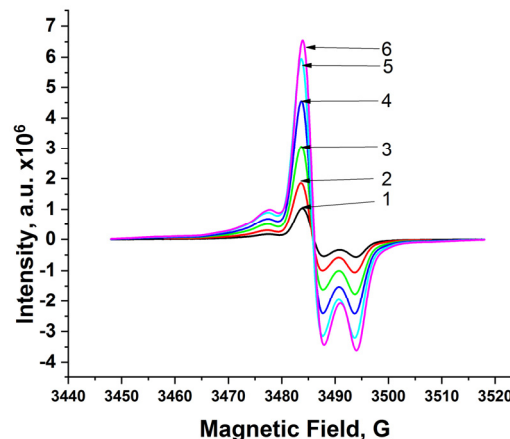
Figure 3. Dose response spectra of modern cow tooth enamel powder: irradiated at 174 Gy (1); 348 Gy (2); 522 Gy (3); 783 Gy (4); 1,044 Gy (5); 1,305 Gy (6)

Ikeya [13] was the first to report the presence of paramagnetic organic radicals at position "a" in γ-irradiated biogenic crystals, such as tooth enamel and fossil shells. The quintet signal with g = 2.0037 and A = 21.9 G was associated with alanine radicals, CH3CH(NH2)COO*, generated from the organic constituent protein in shells (Polinices). He proposed that alanine radicals might be produced by natural irradiation from the alanine amino acids derived from decomposed proteins. According to [20], the intensity of the mentioned signal was not enhanced by further γ-irradiation, and no alanine radicals were detected in fossil shells and bones younger than 10^4 years. In the EPR spectrum of the aragonitic shell (Polinices), which was age-dated using 230Th/234U dating to be 65,000 years old, two additional lines were identified within the quintet signal initially attributed to alanine radicals [13][21]. In this context, the septet signal was associated with isopropyl radicals. The septet signals arising from $(CH3)_2C$--R radicals coincide with a peak of the central line featuring hyperfine splitting of 21.7 G [21]. This septet spectrum has also been observed in fossil horse molars and certain shells, with the radical identified as the isopropyl radical. This radical is known to form in synthetic valine-doped $CaCO_3$ [22].
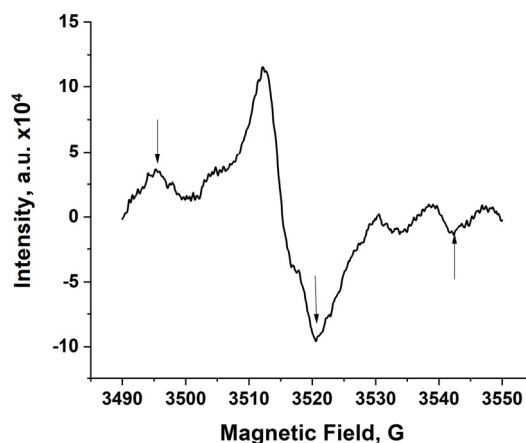
Figure 4. EPR spectrum of the modern cow teeth enamel heated at 160°C for 100 hours. (Central Field 3520 G, Power 2.18 mV, Modulation Frequency 3.2 G, Time constant 20.48 msec, Number of scans 20)

According to annealing experiments conducted with modern tooth enamel from an elephant [23], the alanine (or isopropyl) signal did not manifest solely upon γ-irradiation (400 Gy); it only appeared after subsequent heating, for instance, at 160°C for 48 hours. Furthermore, thermal pretreatment without prior irradiation did not result in the generation of these radicals in recent tooth enamel.

The signal identified at position "a" has been documented in previous studies [22][24], and is acknowledged as indicative of sample annealing due to its presence in the EPR spectra of samples subjected to annealing both before and after irradiation. Notably, the signal at position "a" fails to manifest at 160°C for 48 hours when only the heating stage is applied. However, in our experiments, by prolonging the heating of modern tooth enamel for 100 hours at 160°C, the signal at position

"a" became observable without irradiation, displaying the characteristic quintet signal with g ~ 2.0037 and A ~ 22 G (see Fig. 4).

The peak at position "a" (refer to Fig. 1) is attributed to the presence of isopropyl radicals, indicating that they are not generated during irradiation. Consequently, we assert that the EPR signal observed in fossil tooth enamel at position "a" does not result from radiation but instead stems from the natural decomposition of organic components in tooth enamel due to the aging process.

These characteristic holds potential for various applications and may serve as a quick test to distinguish between ancient and contemporary tooth samples.

CONCLUSIONS

The study involves analyzing EPR spectra of fossil and modern tooth enamel samples, with the fossil sample exhibiting a composite nature requiring careful isolation. In contrast, the modern tooth lacks certain signals, suggesting differences in composition or irradiation effects. The EPR signals were measured using a Bruker EMXplus spectrometer, and subsequent irradiation and dose-response observations were conducted. Six months later, a slight decrease in the central signal's intensity was noted, and the signal at position "b" returned to its original level. Additionally, the absence of peaks at positions "a" and "b" in the modern tooth distinguishes it from the fossil tooth. The presence of isopropyl radicals at position "a" is attributed to sample annealing, unrelated to irradiation, providing potential applications for authentication and differentiating ancient from contemporary tooth samples. The absence of this signal in modern teeth subjected to irradiation may indicate forgery in cases of presenting them as ancient specimens.

ORCID

Ⓞ**Sahib Mammadov,** https://orcid.org/0000-0002-4547-4491

REFERENCES

[1] A. Kinoshita, *et al.*, "ESR dating of teeth from northeastern Brazilian megafauna," Radiat. Meas. **43**(2-6), 809–812 (2008). https://doi.org/10.1016/j.radmeas.2007.11.075

[2] A. Ivannikov, V. G. Skvortsov, V.F. Stepanenko, and K.S. Zhumadilov, "Comparative analysis between radiation doses obtained by EPR dosimetry using tooth enamel and established analytical methods for the population of radioactively contaminated territories," Radiat. Prot. Dosimetry, **159**(104), 125–129 (2014). https://doi.org/10.1093/rpd/ncu132

[3] S. Mammadov, G.R.Z. Dadashov, and A. Ahadov, "Electron Spin Resonance Dating of Tooth Enamel," Int. J. Res. Stud. Sci. Eng. Technol. **4**(7), 1–3 (2017). https://doi.org/10.5281/zenodo.8134294

[4] R. Joannes-Boyau, and R. Grün, "A comprehensive model for CO_2^- radicals in fossil tooth enamel: Implications for ESR dating," Quat. Geochronol. **6**(1), 82–97 (2011). https://doi.org/10.1016/j.quageo.2010.09.001

[5] D. Richter, *et al.*, "The age of the hominin fossils from Jebel Irhoud, Morocco, and the origins of the Middle Stone Age," Nature, **546**(7657), 293–296 (2017). https://doi.org/10.1038/nature22335

[6] M. Duval, and R. Grün, "Are published ESR dose assessments on fossil tooth enamel reliable?," Quat. Geochronol. **31**, 19–27 (2016). https://doi.org/10.1016/j.quageo.2015.09.007

[7] R. Joannes-Boyau, "Detailed protocol for an accurate non-destructive direct dating of tooth enamel fragment using Electron Spin Resonance," Geochronometria, **40**(4), 322–333 (2013). https://doi.org/10.2478/s13386-013-0132-7

[8] R. Grün, M. Aubert, J. Hellstrom, and M. Duval, "The challenge of direct dating old human fossils," Quat. Int. **223–224**, 87-93 (2010). https://doi.org/10.1016/j.quaint.2009.10.005

[9] R. Grün, and C. Stringer, "Direct dating of human fossils and the ever-changing story of human evolution," Quat. Sci. Rev. **322**, 108379 (2023). https://doi.org/10.1016/j.quascirev.2023.108379

[10] E.A. Ainsbury, *et al.*, "Review of retrospective dosimetry techniques for external ionising radiation exposures," Radiat. Prot. Dosimetry, **147**(4), 573–592 (2011). https://doi.org/10.1093/rpd/ncq499

[11] G. Vanhaelewyn, F. Callens, and R. Grün, "EPR spectrum deconvolution and dose assessment of fossil tooth enamel using maximum likelihood common factor analysis," Appl. Radiat. Isot. **52**, 1317–1326 (2000). https://doi.org/10.1016/S0969-8043(00)00090-7

[12] P. Fattibene, D. Aragno, S. Onori, and M. C. Pressello, "Thermal induced EPR signals in tooth enamel," Radiat. Meas. **32**(5), 793–798 (2000). https://doi.org/10.1016/S1350-4487(00)00068-8

[13] M. Ikeya, "Paramagnetic Alanine Molecular Radicals in Fossil Shells and bones," Naturwissenschaften, **68**, 474–475 (1981).

[14] M. Duval, "Electron Spin Resonance (ESR) Dating of Fossil Tooth Enamel," in: *Encyclopedia of Scientific Dating Methods*, edited by W. Jack Rink, and J. Thompson, (Springer Dordrecht, 2015). https://doi.org/10.1007/978-94-007-6326-5

[15] J.E. Aldrich, B. Pass, and C. Mailer, "Changes in the paramagnetic centres in irradiated and heated dental enamel studied using electron paramagnetic resonance," Int. J. Radiat. Biol. **61**(3), 433–437 (1992). https://doi.org/10.1080/09553009214551131

[16] O.I. Scherbina, and A. B. Brik, "Temperature stability of carbonate groups in tooth enamel," Appl. Radiat. Isot. **52**(5), 1071-1075 (2000). https://doi.org/10.1016/S0969-8043(00)00048-8

[17] S. Toyoda, *et al.*, "Gamma-ray dose response of ESR signals in tooth enamel of cows and mice in comparison with human teeth," Radiat. Meas. **37**(4-5), 341–346 (2003). https://doi.org/10.1016/S1350-4487(03)00059-3

[18] A. Roufosse, L.J. Richelle, and O.R. Gilliam, "Electron spin resonance of organic free radicals in dental enamel and other calcified tissues," Arch. Oral Biol. **21**(4), 227–232 (1976). https://doi.org/10.1016/0003-9969(76)90039-X

[19] A.M. Rossi, and G. Poupeau, "Radiation Damage in Bioapatites : The ESR Spectrum of Irradiated Dental Enamel Visited," Nuclear Tracks and Radiation Measurements, **17**(4), 537–545 (1990). https://doi.org/10.1016/1359-0189(90)90014-O

[20] M. Ikeya, *New applications of electron spin resonance: Dating, Dosimetry and Microscopy*, (World Scientific Publishing Co. Pte. Ltd. Singapore, 1993). pp. 500. https://doi.org/10.1016/B978-0-7234-5558-5.00006-3

[21] M. Ikeya, "Chapter 6. Biocarbonates (Fossils)," in: *New Applications of Electron Spin Resonance*, 2008, pp. 87–105. https://doi.org/10.1016/B978-0-7234-5558-5.00006-3

[22] M. Ikeya, "Chapter 2. Introduction to ESR," in: *New Applications of Electron Paramegnetic Resonace*, 2008, p. 44. https://doi.org/10.21832/9781873150887-003

[23] G.J. Hennig, and R. Grün, "ESR dating in quaternary geology," Quat. Sci. Rev. **2**(2-3), 157–238 (1983). https://doi.org/10.1016/0277-3791(83)90006-9

[24] I.P. Vorona, S.S. Ishchenko, and N.P. Baran, "The effect of thermal treatment on radiation-induced EPR signals in tooth enamel," Radiat. Meas. **39**(2), 137-141 (2005). https://doi.org/10.1016/j.radmeas.2004.03.020

ПОРІВНЯЛЬНИЙ АНАЛІЗ ЕПР СУЧАСНОЇ ТА ВИКОПАНОЇ ЗУБНОЇ ЕМАЛІ: ВИЯВЛЕННЯ КОМПОНЕНТІВ, ІНДУКОВАНИХ СТАРІННЯМ

Сахіб Мамедов

Інститут радіаційних проблем Міністерства науки і освіти Азербайджанської Республіки; Баку, Азербайджан
вул. Б. Вахабзаде, 9

Це дослідження передбачає порівняння сигналів ЕПР від зубної емалі сучасної трирічної корови зі спектрами викопної зубної емалі, яка піддавалася впливу природного фонового випромінювання протягом тривалого періоду. Спектр ЕПР викопної зубної емалі значного віку демонструє додаткові компоненти, відсутні в спектрах ЕПР сучасної зубної емалі. Зокрема, септетний сигнал, пов'язаний із ізопропіловими (або аланіновими) радикалами, не спостерігається в сигналах ЕПР сучасної зубної емалі при опроміненні до 1,3 кГр. Гіпотетично ізопропілові радикали, присутні у викопній зубній емалі, не є результатом радіації, а походять від природного розпаду органічних компонентів внаслідок процесу старіння. Ця характеристика пропонується як надійний інструмент для аутентифікації зразків зубів.

Ключові слова: *сучасна зубна емаль; викопні зуби; ЕПР дозиметрія; ізопропіловий радикал*

INTERACTION OF VERY THIN DOUBLE-LAYER FIBRES
WITH ELECTROMAGNETIC RADIATION. 1. NUMERICAL SIMULATION

Mykola G. Kokodii, Denys O. Protektor, Darya V. Gurina*, Mykola M. Dubinin

V.N. Karazin Kharkiv National University, Kharkiv, Ukraine
*Corresponding Author e-mail: dgaryachevskaya@gmail.com

Very thin conductive fibers, whose diameter is much smaller than the wavelength, strongly absorb and scatter electromagnetic radiation. The efficiency factors of absorption, scattering and radiation pressure of metal fibers with a diameter of several micrometers in the centimeter wavelength range reach several thousand. The absorption of electromagnetic radiation in two-layer fibers has been studied. In fibers with a metal core and a lossless dielectric cladding, the absorption is the same as in solid metal fibers. In lossy cladding fibers, strong absorption occurs when the fiber diameter is several nanometers. Fibers with a dielectric core and a metal cladding strongly absorb radiation when the thickness of the cladding is comparable to the thickness of the skin layer.

Keywords: *Double layer fiber; Absorption; Scattering; Attenuation; Electromagnetic radiation*
PACS: 41.20.-q, 04.20.jb

1. INTRODUCTION

The problem of diffraction of electromagnetic radiation on a cylinder is one of the most famous in electrodynamics. The results of its solution are presented in classic monographs [1-3] and numerous articles. Technical applications make it possible to obtain information about the cross-sectional size of the cylinder, its shape, and optical parameters [4-6].

The effect of the wave on the cylinder depends on the relationship between the wavelength and the diameter of the cylinder. It is usually strongest when the diameter of the cylinder is comparable to the wavelength. Then resonances arise, at which the interaction of the wave with the cylinder intensifies [7, 8]. Objects that are small compared to the wavelength are usually "not noticed" by it. But in works [9-12] it was shown that very thin metal wires, semiconductor and graphite fibers, the diameter of which is hundreds of times smaller than the wavelength, strongly absorb and scatter electromagnetic radiation [13].

This effect can be used to solve problems in physics and technology when it is necessary to transfer the energy of laser or microwave radiation to small objects: a spherical target in laser thermonuclear fusion installations, an active element in the form of a thin thread in fiber lasers, etc. In this case, focusing the radiation beam is not necessary. The transverse dimensions of the beam can be thousands of times larger than the size of the target.

Figure 1 shows graphs of the dependence of the absorption efficiency factor of a platinum wire on its diameter for several wavelengths with *E*- polarization of the wave (the electric vector is parallel to the axis of the wire). At certain ratios of the D/λ value, an absorption maximum is observed. For $\lambda = 8$ mm $Q_{abs\ max} = 962$, for $\lambda = 10$ cm - $Q_{abs\ max} = 2615$, for $\lambda = 1$ m - $Q_{abs\ max} = 7928$. The maximum is obtained with very small wire diameters; 4.1 µm at a wavelength of 1 m, 1.5 µm at a wavelength of 10 cm, 0.3 µm at a wavelength of 8 mm.

In the case of the *H*-wave there is no effect.
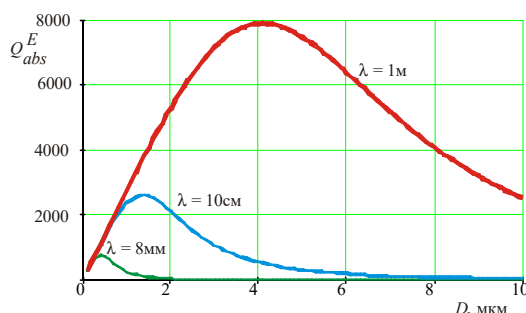
Figure 1. Dependence of the platinum wire absorption efficiency factor on its diameter

The technology also uses two-layer fibers - metal microwires in a glass shell and glass fibers with a metal coating. Therefore, there are works in which the diffraction interaction of an electromagnetic wave with such objects was studied [14-16]. It has been shown that resonances arise in the dielectric coating of a metal fiber, enhancing or weakening the interaction of the wave with it [15]. The work [16] shows the results of calculations on the interaction of microwave radiation with thin double-layer fibers.

Further in this work, the results of studies of the interaction of an electromagnetic wave with two types of two-layer fibers will be presented - a conductor in a dielectric shell and a dielectric fiber with a metal coating.

A cross section of the fiber is shown in Fig. 2. It consists of two layers - an outer shell with a diameter D_1 with refractive index m_1 and core diameter D_2 and refractive index m_2. Both refractive indices can be complex, meaning both the core and the cladding can absorb radiation.

The wave vector of the incident radiation is perpendicular to the fiber axis. The electric vector of the wave is parallel to the fiber axis.

$$\rho = \frac{\pi D_1}{\lambda}$$

$$q = \frac{D_2}{D_1}$$
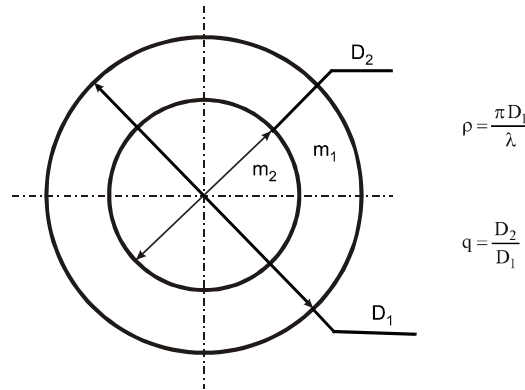
Figure 2. Problem geometry

Attenuation effectiveness factors Q, scattering Q_{sca} and absorption factor Q_{abs} can be calculated using formulas that are superficially similar to the formulas for a solid cylinder [2, 10]:

$$Q = \frac{2}{q\rho} \sum_{l=-\infty}^{\infty} \mathrm{Re}\left(b_l\right), \tag{1}$$

$$Q_{sca} = \frac{2}{q\rho} \sum_{l=-\infty}^{\infty} \left|b_l\right|^2, \tag{2}$$

$$Q_{abs} = Q - Q_{sca}. \tag{3}$$

Here $\rho = \pi D_1 / \lambda$, λ - radiation wavelength, $q = D_2/D_1$ or a metal conductor in a dielectric shell, $q = 1$ for a dielectric fiber in a conductive shell.

The coefficients b_l are described by the following equations:

$$b_l = \frac{\Delta_1}{\Delta}, \tag{4}$$

where

$$\Delta = \begin{vmatrix} H_l^{(2)}(\rho) & H_l^{(2)}(m_1\rho) & J_l(m_1\rho) & 0 \\ H_l^{(2)'}(\rho) & m_1 H_l^{(2)'}(m_1\rho) & m_1 J_l'(m_1\rho) & 0 \\ 0 & H_l^{(2)}(m_1 q\rho) & J_l(m_1 q\rho) & J_l(m_2 q\rho) \\ 0 & m_1 H_l^{(2)'}(m_1 q\rho) & m_1 J_l'(m_1 q\rho) & m_2 J_l'(m_2 q\rho) \end{vmatrix}, \tag{5}$$

$J_l(z)$ – Bessel function, $H_l^{(2)}(z)$ – Hankel function of the 2nd kind, the "prime" sign at the top of the function designation means differentiation over the entire argument.

The determinant of Δ_1 is obtained by replacing in the first column of the determinant of Δ the functions $H_l^{(2)}(\rho)$ and $H_l^{(2)'}(\rho)$ the functions $J_l(\rho)$ и $J_l'(\rho)$ respectively.

We will limit ourselves to the case of the *E*-wave, when the effect of strong absorption of electromagnetic radiation is observed in very thin fibers.

2.   CONDUCTOR IN DIELECTRIC SHELL

Micron-diameter conductors in a glass shell are used in technology. They are used as thermistors, bolometric receivers of electromagnetic radiation, etc.

Figure 3 shows the dependence of absorption in a copper conductor in a glass shell with a refractive index $n = 1.5$. The diameter of the conductor in the sheath is 30 microns. Radiation wavelength 8 mm. Conductor diameter D_2 varies from zero to 1000 nm. The maximum absorption efficiency factor reaches 2000. The position of the maximum is determined by the formula [12]:

$$D \approx 0.1 \lambda_i, \qquad (6)$$

where $\lambda_i = \lambda/n$ – wavelength of radiation in metal, n – real part of the complex refractive index of a metal $m = \sqrt{\dfrac{\sigma\lambda}{4\pi c \varepsilon_0}}(1-i)$, σ – conductivity, c – speed of light, ε_0 – dielectric constant of free space. For copper $n = 3757$ at a wavelength in free space of 8 mm, so $\lambda_t = 2.12\ \mu m$, and the maximum is located at $D_2 \approx 200\,nm$. In the graph, the maximum is located at $D_2 = 154$ nm, which is in satisfactory agreement with the theory [9].
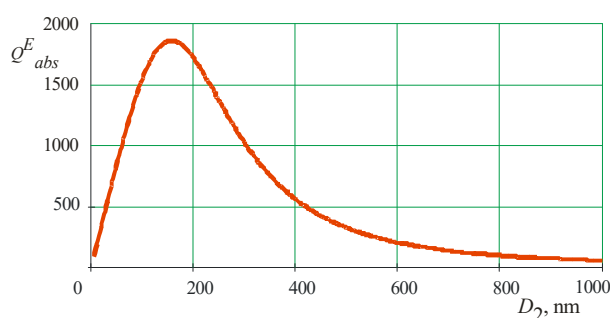
Figure 3. Absorption in glass-clad copper wire ($\lambda = 8$ mm, $n = 1.5$)

The refractive index of the shell does not affect the position of the maximum. It is determined only by the properties of the core metal. But the magnitude of the maximum depends on the shell material. So, for the refractive index of the shell $n = 1.5$ – absorption at maximum is $Q_{abs} = 1865$, for $n = 4$ – $Q_{abs} = 1879$, for $n = 9$ – $Q_{abs} = 1948$. Apparently, the shell focuses the radiation onto the core.

If the shell absorbs radiation, the picture changes. Figure 4a shows the dependence of the absorption efficiency factor of a copper wire in a cladding with a complex refractive index $m = 1.5 - 1i$ (colored absorbing glass) on the core diameter. The general picture is the same as in the previous case, the maximum is in the same place, it is the same in size. But at very small wire diameters, absorption increases. The region of strong absorption is very narrow. Its width, determined by the minimum on the graph, is 9 nm.

Absorption increases with increasing both the real and imaginary parts of the refractive index of the shell. The position of the minimum shifts towards increasing diameter. The minimum value increases. Figure 4b shows a graph for $m = 5 - 5i$ (semiconductor in the microwave range). The minimum is located at 41 nm and is close in value to the absorption maximum. At high refractive indices, the maximum disappears, and the $Q_{abs}(D_2)$ curve decreases monotonically as D_2 increases.

a   b
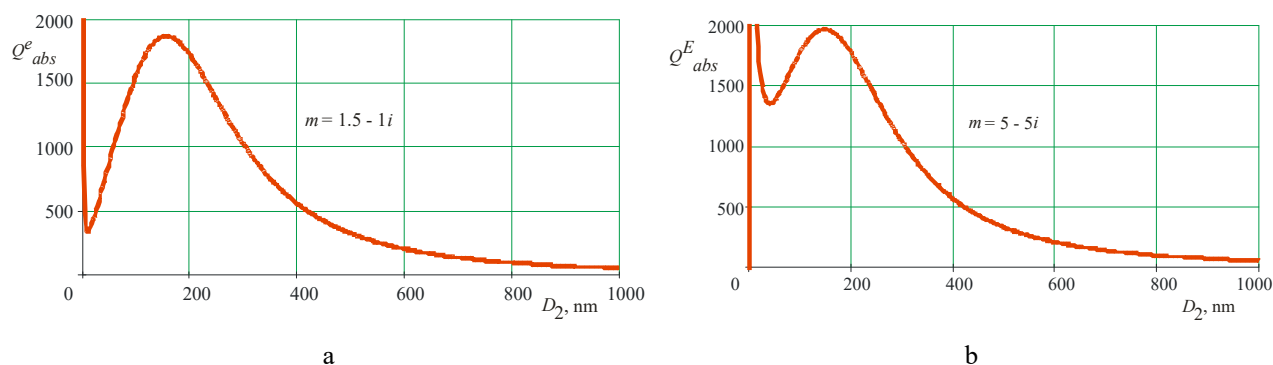
Figure 4. Absorption in copper wire with absorbent sheath a – $m = 1.5 - 1i$, b – $m = 5 - 5i$

It is clear from the graphs that the effect of strong absorption is observed when the diameter of the conductive core is very small - no more than several hundred nanometers.

3.   DIELECTRIC IN A METAL SHELL

Such an object can be a glass fiber coated with a thin layer of metal or other electrically conductive material (graphite, semiconductor).

Figures 5a and 5b show the results of interaction of a 10 cm long electromagnetic wave with a nickel-coated glass fiber. Fiber diameter 30 microns. It is shown how the absorption efficiency factor changes with a change in the diameter of the glass core.
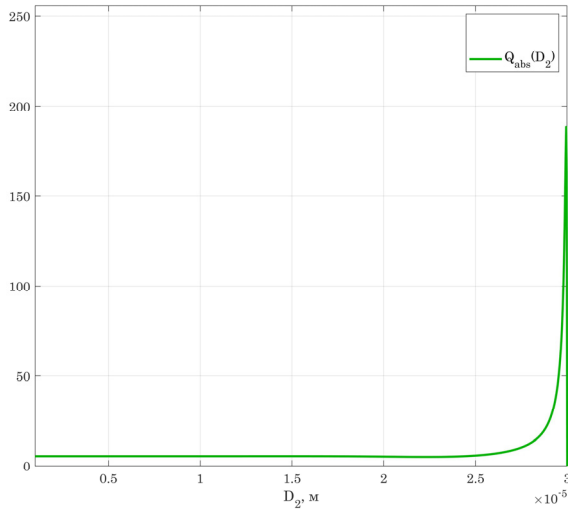
Figure 5a. Absorption in nickel-clad glass fiber
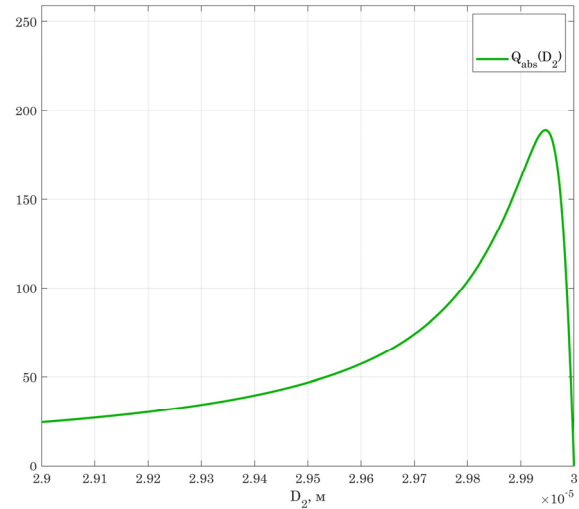
Figure 5b. Absorption in glass fiber with a nickel shell (maximum region)

Figure 5a shows that when the core is thin and the cladding thickness is much greater than the skin thickness, the absorption in the fiber is the same as in a solid metal cylinder with a diameter of 30 μm ($Qabs$ = 5.38). When the thickness of the shell becomes comparable to the thickness of the skin layer (in nickel at a wavelength of 10 cm it is 3.25 μm), absorption increases and reaches a maximum at a shell thickness of 54 nm - $Qabs$ = 187.8 (Fig. 5b). This is 35 times more than for solid nickel fiber with a diameter of 30 microns. For nickel fiber to have an absorption factor of 187.8, its diameter must be 1 micron, that is, it must be very thin.

Therefore, thicker two-layer dielectric fibers with a thin metal shell are much more convenient to use than solid homogeneous metal fibers.

Calculations show that the maximum absorption value does not depend on the conductivity of the shell material. The thickness of the shell at which maximum absorption is observed depends on the conductivity. It is proportional to the resistivity of the material. This is true for a very wide range of resistance values (Fig. 6). There, such a dependence is plotted on a logarithmic scale. The dots indicate resistivity values for several materials.
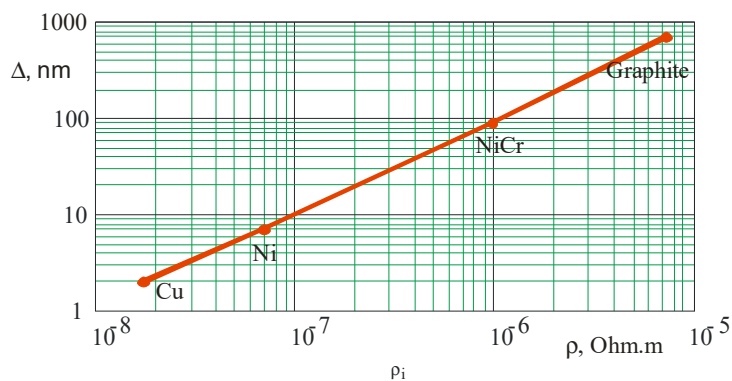
Figure 6. Dependence of the optimal thickness of the metal shell on the resistivity of the material

Figure 7 shows how the optimal cladding thickness depends on the wavelength of the radiation that is incident on the fiber (line 1). The graph is plotted for glass fiber with a diameter of 10 microns with a copper sheath. This is also a linear relationship over a very wide range (in the graph - from 8 mm to 10 m). The same figure shows the dependence of the absorption efficiency factor on the wavelength (line 2). This is also a linear relationship. It differs from the same dependence for a continuous fiber, where absorption is proportional $\sqrt{\lambda}$ [12].

It was indicated above that absorption in the shell becomes strong when its thickness is comparable to the thickness of the skin layer in it. The identical nature of the dependence of the optimal shell thickness on resistivity and wavelength also indicates that it is related to the thickness of the skin layer:

$$\delta = \sqrt{\frac{\lambda\rho}{\pi c \mu\mu_0}} ,$$
(7)

where λ - wavelength, ρ - resistivity, c – speed of light in free space, μ - relative magnetic permeability of the shell material, μ_0 - magnetic permeability of free space.
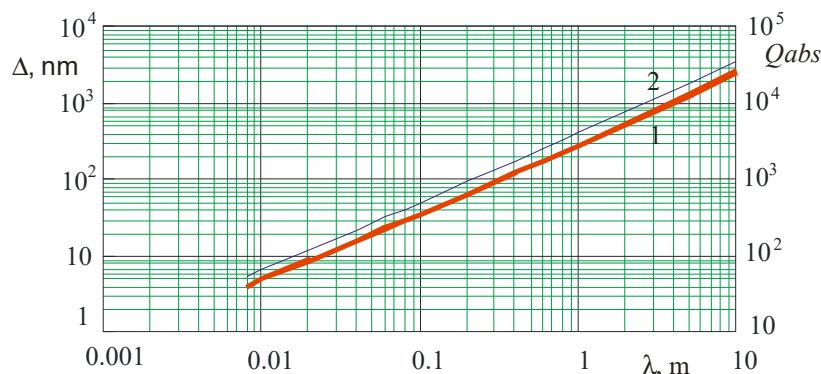
Figure 7. Dependence of the optimal thickness of the metal shell on the radiation wavelength
1 – shell thickness, nm, 2 – absorption efficiency factor

Figure 8 shows that the optimal shell thickness is proportional to the square of the skin layer thickness, which means, as can be seen from expression (4), it should be proportional to the wavelength and resistivity, which is confirmed by the graphs in Figures 6 and 7.

The proportionality coefficient in these relationships depends on the electrical properties of the core and shell and can be found from the analysis of expressions (1) – (3), (7).
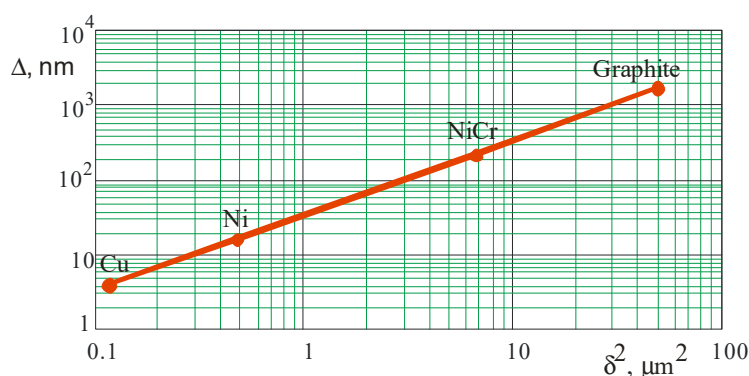
Figure 8. Dependence of the optimal thickness of the metal shell on the thickness of the skin layer

CONCLUSION

1.　Absorption of electromagnetic radiation in a thin fiber ($D \ll \lambda$) with a metal core and a lossless dielectric shell is the same as in a homogeneous metal cylinder with a diameter the same as the core diameter. The absorption maximum in the microwave range is at $D \approx 0.1\lambda_i$, where λ_i – wavelength of radiation in a metal. In the microwave range $D = 100…300$ nm. In a fiber with a high refractive index of the cladding, absorption increases somewhat due to the focusing of radiation by the cladding onto the core.

2.　If there is energy loss in the shell, strong absorption occurs in the metal core of nanometer diameter.

3.　Dielectric fibers with a metal sheath strongly absorb electromagnetic radiation when the diameter of the sheath is comparable to the thickness of the skin layer.

4.　For the same absorption, metal-coated dielectric fibers have a significantly larger diameter than solid metal fibers. This creates significant convenience in their technical applications.

ORCID
Mykola G. Kokodii, https://orcid.org/0000-0003-1325-4563; **Denys O. Protektor,** https://orcid.org/0000-0003-3323-7058
Darya V. Gurina, https://orcid.org/0000-0001-7357-1275; **Mykola M. Dybinin,** https://orcid.org/0000-0002-7723-9592

REFERENCES
[1]　H.C. van de Hulst, *Light scattering by small particles*, (Wiley, New York, 1981).
[2]　M. Kerker, *The scattering of light and other electromagnetic radiation*, (Academic Press, New York, London, 1969).
[3]　C.F. Bohren, and D.R. Huffman, *Absorbing and scattering of light by small particles*, (Wiley, New York, 1983).

[4]   R. Zhang, and E.M. Fedorov, Measurement of thing fiber diameter by the diffraction method, Conference TPU, **2**, 153-158 (2018).

[5]   M. Kokodii, A. Natarova, I. Priz, and O. Biesova, "Express method of measurement of the refractive index of transparent fibers," Ukrainian metrological journal, 3, 43-48 (2022). https://doi.org/10.24027/2306-7039.3.2022.269771

[6]   M. Kokodii, I. Zhovtonizhko, M. Barannik, and A. Natarova, "Computer method of measurement of the optical and color parameters of man hair," Medical informatics and ingenery, 4, 30-38 (2022). (in Ukrainian).

[7]   W.M. Irvine, "Light scattering by spherical particles: radiation pressure, asymmetry factor, and extinction cross section," Journal of the Optical Society of America, **55**(1), 16-21 (1965). https://doi.org/10.1364/JOSA.55.000016

[8]   N.G. Kokodii, "Nature of resonances in a thick refracting cylinder during of an electromagnetic wave," Optics and Spectroscopy, **72**(2), 249-251 (1992).

[9]   V.M. Kuz'michev, N.G. Kokodii, B.V. Safronov, and V.P. Balkashin, "Values of the absorption efficiency factor of a thin metal cylinder in the microwave band," Journal of Communications Technology and Electronics, **48**(11), 1240-1242 (2003).

[10] A. Akhmeteli, N.G. Kokodiy, B.V. Safronov, V.P. Balkashin, I.A. Priz, and A. Tarasevitch, "Efficient non-resonant absorption in thin cylindrical targets: experimental evidence for longitudinal geometry," https://doi.org/10.48550/arXiv.1208.0066

[11] A. Akhmeteli, N. Kokodii, B. Safronov, V. Balkashin, I. Priz, and A. Tarasevich, "Efficient non-resonant absorption of electromagnetic radiation in thin cylindrical targets: experimental evidence," in: *Proc. SPIE 9097, Cyber Sensing 2014*, 90970H. https://doi.org/10.1117/12.2053482

[12] N.G. Kokodii, A.O. Natarova, A.V. Genzarovskiy, and I.A. Priz, "Interaction between thin conductive fibers and microwave radiation," Optical and Quantum Electronics, **55**, 256 (2023). https://doi.org/10.1007/s11082-022-04389-x.

[13] M. Kokodii, S. Berdnik, V. Katrich, M. Nesterenko, I. Priz, A. Natarova, V. Maslov, and K. Muntian, "Measurement of microwave radiation pressure on thin metal fibers," Ukrainian Metrological Journal, 4, 45-50 (2021). (in Ukrainian). https://doi.org/10.24027/2306-7039.3.2020.216802

[14] M. Kerker, and E. Matijevic, "Scattering of electromagnetic wave from concentric infinite cylinder," Journal of the Optical Society of America, **51**(5), 506-508 (1961). https://doi.org/10.1364/JOSA.51.000506

[15] E.A. Velichko, and A.P. Nikolaenko, "Influence of a dielectric coating on the scattering of an electromagnetic wave by a metal cylinder," Radiophysics and Radioastronomy, **18**(1), 65-74 (2013). http://rpra-journal.org.ua/index.php/ra/article/view/1121/759

[16] N.G. Kokodii, "Microwave radiation absorption in an ultrathin double-layer cylinder," Journal of Communications Technology and Electronics, **51**(2), 175–178 (2006). https://doi.org/10.1134/S1064226906020069

ВЗАЄМОДІЯ ДУЖЕ ТОНКИХ ДВОШАРОВИХ ВОЛОКОН
З ЕЛЕКТРОМАГНІТНИМ ВИПРОМІНЮВАННЯМ. 1. ЧИСЕЛЬНЕ МОДЕЛЮВАННЯ

Микола Г. Кокодій, Денис О. Протектор, Дар'я В. Гуріна, Микола М. Дубінін
Харківський національний університет ім. В.Н. Каразина, Харків, м. Свободи, 4, 61022, Україна

Дуже тонкі провідні волокна, діаметр яких набагато менше довжини хвилі, сильно поглинають і розсіюють електромагнітне випромінювання. Фактори ефективності поглинання, розсіювання та тиску випромінювання металевих волокон діаметром кілька мікрометрів у сантиметровому діапазоні довжин хвиль досягають кількох тисяч. Досліджено поглинання електромагнітного випромінювання у двошарових волокнах. У волокнах з металевою серцевиною та діелектричною оболонкою без втрат поглинання таке ж, як у суцільних металевих волокнах. У волокнах з оболонкою з втратами з'являється сильне поглинання, якщо діаметр волокна дорівнює декільком нанометрам. Волокна з діелектричною серцевиною і металевою оболонкою сильно поглинають випромінювання, коли товщина оболонки порівнянна з товщиною скін-шару.

Ключові слова: *двошарове волокно; поглинання; розсіювання; ослаблення; електромагнітне випромінювання*

TEMPERATURE DEPENDENCE OF DIELECTRIC RELAXATION OF ABSORPTION SPECTRA IN THE CHLOROBENZENE – IODOBENZENE SYSTEM

Samir Azizov

Ministry of Science and Education Republic of Azerbaijan, Institute of Physics, Ave. H. Javid, 131, AZ-1143 Baku, Azerbaijan
Corresponding Author e-mail: radiasiya555@rambler.ru

The article presents the results of a study of the temperature dependence of the dielectric constant ε' and the dielectric loss index ε'' of the chlorobenzene-iodobenzene system at wavelengths λ = 6.32; 4.01; 3.21; 2.14; 1.18 and 0.75 V temperature range -40°C÷+30°C. The static dielectric constant was determined at a frequency of 7 MHz. The temperature dependence of the time of dielectric relaxation of molecules in the liquid state was determined. It was established that in the specified temperature-frequency range the dispersion region consists of two parts. Analysis of the temperature dependence of dielectric polarization relaxation in the system chlorobenzene-iodobenzene shows that the relaxation times of the components do not depend on their short-range order. It was also discovered that the rate graph showing the dependence of the logarithm of the relaxation time on the reciprocal of the temperature $\log\tau \sim 1/T$, consists of two parts and the value of the static dielectric permeability ε_∞ is non-additive. To explain these results, it is assumed that clusters are formed in this system, the same as in the pure components.

Keywords: *Dielectric spectroscopy; Dielectric relaxation; Chlorobenzene; İodobenzene; Bromobenzene*
PACS: 61.20.–p; 77.22.–d; 77.22.Gm

INTRODUCTION

In polar liquids, dielectric relaxation is observed in the microwave range, which covers the spectrum of electromagnetic waves with a length from 1 mm to 30 cm [1]. Studying this range makes it possible to study relaxation properties. The interest in the liquids under study is explained by their relatively simple structure, which makes it possible to use existing theories to analyze experimental data. It is known that in chlorobenzene, iodobenzene and bromobenzene there is a small distribution of relaxation times, which decreases with increasing temperature [2]. It is also known that there is a single relaxation time for these same compounds. In this case, the high-frequency limit of the dielectric constant ε_∞ of the Cole – Cole diagram turns out to be greater than the square of the refractive index n2 measured in the infrared range [3,4]. This fact is associated with the probable existence of an additional absorption region of a resonant nature in the sub millimeter range, which manifests itself already at wavelengths from 3 to 7 mm. In pure dipole liquids, increased dielectric relaxation times are usually observed compared to their values in dilute solutions. If in the first case the relaxation process is cooperative, then in dilute solutions the relaxation time, as a rule, characterizes an individual molecule. Therefore, studying the dependence of dielectric relaxation on the concentration of polar molecules is of great interest [5–9].

Using the example of earlier studies of binary systems, it can be argued that the concentration dependence of the ratio of relaxation time τ to viscosity η can be used to estimate the degree of clustering of polar molecules. As a result, it was possible to determine a special relaxation mechanism in the case of concentrated solutions of some cyclohexane derivatives in non-polar solvents [10, 11].

Monohalogen derivatives of benzene are compounds with small rigid molecules, the interactions between which are described predominantly by van der Waals forces. Knowledge of the equilibrium and dynamic dielectric properties of such relatively simple objects is necessary when deciphering the dielectric behavior of systems with different types of relaxers and complicated intermolecular interactions. Analysis of the temperature dependences of the dielectric coefficients of three members of the series chlorobenzene (C_6H_5Cl), bromobenzene (C_6H_5Br), iodobenzene (C_6H_5J), taken in the microwave range for pure liquids and their concentrated solutions in benzene (C_6H_6) and hexane (C_6H_{14}), showed that the kinetic units responsible for the observed absorption are individual molecules [7–11]. It should be noted that dipole – dipole forces do not have a significant effect on the shape of the absorption curve. In addition, indirect indications were obtained of the existence of another absorption region, a resonant type, at higher frequencies.

This work was carried out with the aim of further accumulating experimental data on the nature and mechanism of microwave absorption in the compounds under study. The choice of a polar mixture is explained by the desire to trace the kinetic behavior of each component separately, which is important for studying the influence of short-range order on the process of molecular relaxation.

MATERIALS AND RESEARCH METHODS

Dielectric constants ε' and dielectric losses ε'' of the chlorobenzene – iodobenzene system were measured at wavelengths λ = 6.32; 4.01; 3.21; 2.14; 1.18; 0.75 cm in the temperature range $-40° \div +30°C$, with a volumetric ratio

of components of 1:1. Within the same temperature limits, the equilibrium dielectric constants ε_0 of the system were measured at a frequency of 7 MHz.

Measurements of dielectric constant ε' and dielectric losses ε'' were carried out using the variable thickness method [12 – 14] on six installations that differed only in the cross-sectional sizes of the waveguides. Particular attention was paid to eliminating impedance transformation in the measuring path and ensuring reliable thermal insulation of the measuring cell from the rest of the path and the environment. The measurement errors are: 1% for the dielectric constant ε' and 1 – 3% for the dielectric loss index ε'' at λ = 6.32; 4.01; 3.21; 2.14 cm, 2% for dielectric constant ε' and 3 – 5% for dielectric loss index ε'' at λ = 1.18 and 0.75 cm.

Equilibrium measurements were carried out using the resonance method [15– 7]. The measuring cell consisted of a silver-plated cylindrical capacitor equipped with a heat-insulating shell. The cell temperature was changed by continuous heating at a rate of 0.2 degrees/min. The capacitor was calibrated for hexane, benzene, chlorobenzene and acetone. The error in the equilibrium dielectric constant ε_0 did not exceed 1%. The temperature of the samples was measured with a copper constantan thermocouple with an error of ~0.3°. The components of the mixture and compounds taken for control measurements were carefully dried and distilled on a distillation column. The purity of the compounds was checked by boiling point values and optical refractive indices. All measurements were carried out only on samples of the "high grade" brand.

RESULTS AND DISCUSSION

Table 1 summarizes the measurement data for ε', ε'' and ε_0. The shift of the maximum in the $\varepsilon''(\lambda)$ curves towards shorter wavelengths with increasing temperature indicates the relaxation origin of the studied absorption (Fig. 1).

Table 1. Dielectric coefficients of the chlorobenzene – iodobenzene system

T, °C	ε_0	$\lambda = 6.32$		$\lambda = 4.01$		$\lambda = 3.21$		$\lambda = 2.14$		$\lambda = 1.18$		$\lambda = 0.75$	
		ε'	ε''	ε'	ε''	ε'	ε''	ε'	ε''	ε'	ε''	ε'	ε''
30	5.19	4.69	0.98	4.25	1.21	4.00	1.26	3.55	1.23	3.00	0.96	2.79	0.73
20	5.29	4.65	1.09	4.20	1.26	3.94	1.28	3.48	1.21	2.98	0.91	2.79	0.69
10	5.38	4.57	1.19	4.10	1.31	3.82	1.31	3.39	1.19	2.96	0.86	2.78	0.65
0	5.48	4.49	1.20	4.00	1.36	3.72	1.31	3.32	1.14	2.94	0.81	2.78	0.61
-10	5.59	4.41	1.36	3.90	1.37	3.61	1.29	3.24	1.10	2.92	0.76	2.78	0.59
-20	5.70	4.34	1.41	3.77	1.35	3.20	1.25	3.17	1.03	2.90	0.70	2.78	0.55
-30	5.82	4.23	1.45	3.64	1.32	3.39	1.18	3.10	0.95	2.88	0.64	2.78	0.52
-40	5.95	4.12	1.49	3.50	1.29	3.28	1.12	3.04	0.89	2.86	0.58	2.78	0.49
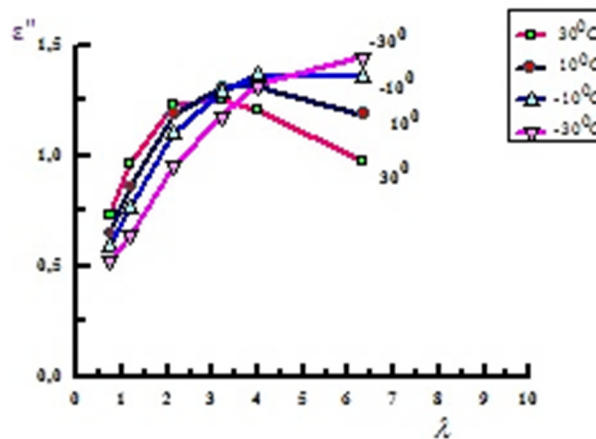
Figure 1. Dependence of the absorption index ε'' on the wavelength (λ cm) at different temperatures.

According to the arc diagrams, the frequency variation of the dielectric constant ε' and the dielectric losses ε'' of the mixture are described by the Cole – Cole equation [18]:

$$\varepsilon' - i\varepsilon'' = \varepsilon_\infty + (\varepsilon_0 - \varepsilon_\infty)\left[1 + (i\omega\tau)^{1-\alpha}\right], \tag{1}$$

or

$$\frac{\varepsilon' - \varepsilon_\infty}{\varepsilon_0 - \varepsilon_\infty} = \frac{1 + (\omega\tau)^{1-\alpha}\sin\frac{\alpha\pi}{2}}{1 + 2(\omega\tau)^{1-\alpha}\sin\frac{\alpha\pi}{2} + (\omega\tau)^{2(1-\alpha)}}, \tag{2}$$

$$\frac{\varepsilon''}{\varepsilon_0 - \varepsilon_\infty} = \frac{(\omega\tau)^{1-\alpha}\cos\frac{\alpha\pi}{2}}{1 + 2(\omega\tau)^{1-\alpha}\sin\frac{\alpha\pi}{2} + (\omega\tau)^{2(1-\alpha)}}, \tag{3}$$

where α is the parameter of the symmetric distribution of dielectric relaxation time values around the most probable value of the relaxation time τ, the equilibrium dielectric constant ε_0 and ε_∞ - low and high frequency dispersion limits.

The discrepancies between the measured values of the equilibrium dielectric constant ε_0 and those extrapolated from the arc diagrams are less than 1%, and for all temperatures the relation is satisfied with the same accuracy

$$\varepsilon_0 = \varepsilon_{01}\, x_1 + \varepsilon_{02}\, x_2, \tag{4}$$

where indices 1 and 2 refer, respectively, to iodine and chlorobenzene, x is the mole fraction.

Additively is violated for the high-frequency (HF) limit and the value of the dielectric constant of the high-frequency limit ε_∞ of the mixture coincides with the value of the dielectric constant of the high-frequency limit ε_∞ of pure chlorobenzene. Thus, at 20°C HF is the limit of the dielectric constant of chlorobenzene $(C_6H_5C_1)$ $\varepsilon_\infty = 2.56$ HF is the limit of the dielectric constant of iodobenzene ε_∞ $(C_6H_5J) = 2.76$, HF is the limit of the dielectric constant of the chlorobenzene - iodobenzene system $\varepsilon_\infty = 2.57 \pm 0.02$. The values of ε_∞ and α found from arc diagrams are given in Table 2.

Table 2. High-frequency dielectric constants ε_∞ and distribution parameters α of the relaxation time of the chlorobenzene - iodobenzene system

T°C	30	20	10	0	-10	-20	-30	-40
ε_∞	2.53	2.57	2.60	2.62	2.64	2.66	2.69	2.71
α	0.030	0.032	0.038	0.039	0.042	0.046	0.049	0.050

Table 3 presents the values of relaxation time τ, determined from points on arc diagrams according to expression (5):

$$(\omega\tau)^{1-\alpha} = [(\varepsilon_0 - \varepsilon')^2 + \varepsilon''^2]^{1/2} \quad [(\varepsilon' - \varepsilon_\infty)^2 + \varepsilon''^2]^{-1/2} \tag{5}$$

Table 3. Relaxation time τ $(10^{-12}$ sec$)$ of the chlorobenzene–iodobenzene system according to equation (1) at different wavelengths

T°C \\ λ (cm)	6.32	4.01	3.21	2.14	1.18	0.75	τ_{cp}
30	15.1	15.3	15.2	14.7	14.4	13.9	15.1
20	17.6	17.0	16.9	16.6	16.0	15.1	17.0
10	20.5	19.5	19.6	18.8	17.9	16.8	19.6
0	23.6	22.1	22.2	21.4	20.2	18.6	22.3
-10	26.7	25.0	25.2	24.4	22.6	20.3	25.3
-20	29.8	29.3	29.5	28.4	26.1	23.0	29.3
-30	34.2	34.4	34.8	33.6	30.6	25.7	34.2
-40	39.2	40.3	41.1	39.6	36.0	28.7	40.1

The average values of relaxation time τ indicated in the last column of Table 3 were obtained by averaging the values of relaxation time τ at $\lambda = 6.32$; 4.01; 3.21; 2.14 cm. All these points fall into the maximum region on the curves of the dependence $\varepsilon''(\lambda)$ and the corresponding values of the relaxation time τ deviate from the average values of the relaxation time τ by only 3 – 6%. For two "short-wave" points much larger values are noted deviations that systematically increase with decreasing temperature, which suggests the presence of additional absorption. To check, it is convenient to use the method of linear diagrams. Transformations of equations (1) - (3) allow us to obtain a number of linear relationships:

$$\varepsilon' = -\{a[\varepsilon'' + (\varepsilon' - \varepsilon_\infty)b]\}\omega^{1-\alpha}\tau^{1-\alpha} + \varepsilon_0 , \tag{6}$$

$$\varepsilon' - \varepsilon''b = \varepsilon'' \,(a\omega^{1-\alpha})^{-1}\,\tau^{-(1-\alpha)} + \varepsilon_\infty, \tag{7}$$

$$[(\varepsilon'')^{-1} - 2b(\varepsilon_0 - \varepsilon_\infty)^{-1}]\,\omega^{1-\alpha} = [a(\varepsilon_0 - \varepsilon_\infty)]^{-1}\omega^{2(1-\alpha)}\,\tau^{1-\alpha} + [a(\varepsilon_0 - \varepsilon_\infty)]^{-1}\,\tau^{-(1-\alpha)}, \tag{8}$$

$$[(\varepsilon'')^{-1} - 2b(\varepsilon_0 - \varepsilon_\infty)^{-1}]\,\omega^{-(1-\alpha)} = [a(\varepsilon_0 - \varepsilon_\infty)]^{-1}\omega^{-2(1-\alpha)}\,\tau^{-(1-\alpha)} + [a(\varepsilon_0 - \varepsilon_\infty)]^{-1}\,\tau^{1-\alpha}, \tag{9}$$

where $a = \cos\frac{\alpha\pi}{2}, b = tg(\frac{\alpha\pi}{2})$

At $\alpha = 0$, equations (6) – (7) transform into the equations previously obtained by Cole [18]:

$$\varepsilon' = -\varepsilon''\omega\tau + \varepsilon_0, \tag{10}$$

$$\varepsilon' = \varepsilon''(\omega\tau)^{-1} + \varepsilon_\infty. \tag{11}$$

If the experimental data follows equation (1), then graphs constructed using equations (6) – (9) should give straight lines with slopes and intercepts equal to the dispersion parameters.

Equations (7) and (9) allow us to trace in more detail the low frequency (LF) absorption edge, and equation (8) allows us to trace the HF edge.

In Fig. 2 – 5 show examples of line diagrams. In all cases, "long-wave" points (λ = 6.32; 4.01; 3.21; 2.14 cm) are placed on one straight line segment, the slope of which gives a relaxation time equal to the average relaxation time τ in Table 3. Intersections this segment with the ordinate axis in Fig. 2, 3 coincide with the values of ε_0 and ε_∞ extrapolated from arc diagrams.

Only two points fall on the other segment (λ = 1.18; 0.75 cm). Poor agreement between the relaxation times τ for them in Table. 3 and lower values of the relaxation time τ at λ = 0.75 cm mean that the true straight line should have a smaller slope.
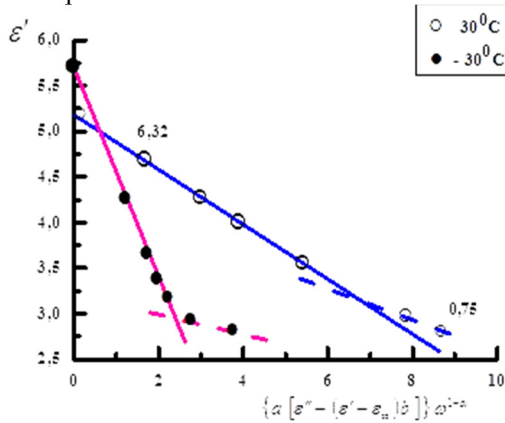
Figure 2. Linear diagram according to equation (6).
Numbers at dots – wavelength (cm)
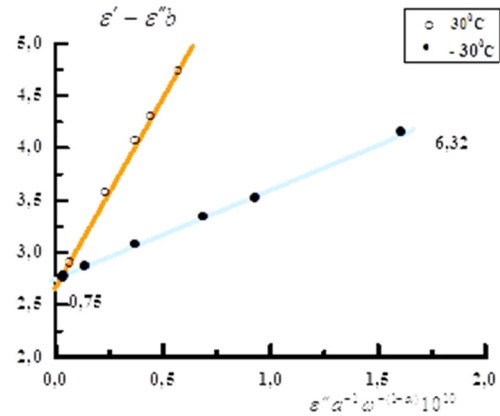
Figure 3. Line diagram according to equation (7)
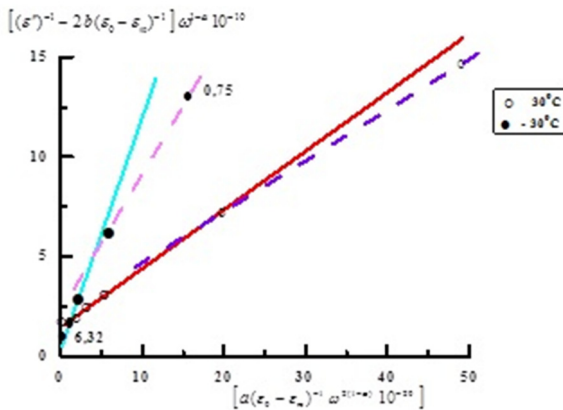
Figure 4. Line diagram according to equation (8)
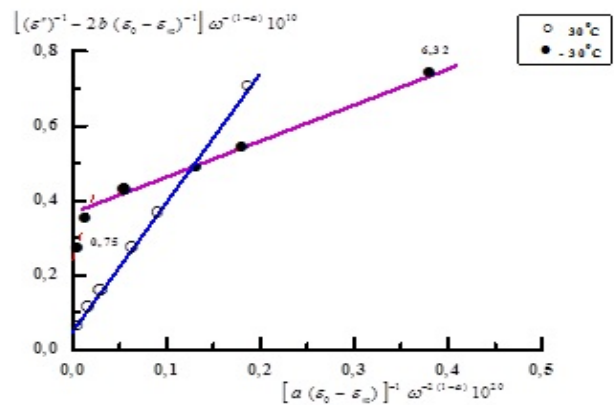
Figure 5. Line diagram according to equation (9)

From the above, we can conclude that the absorption described by the "long-wave" points is created by a single mechanism. Meanwhile, on the velocity graph plotted based on the average values of the relaxation time τ, a clear division into two regions is revealed (Fig. 6).
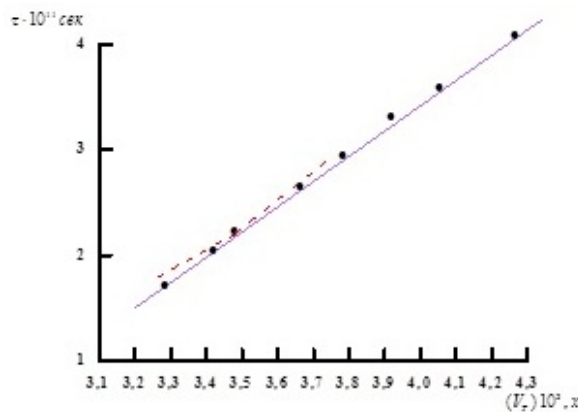
Figure 6. Speed graph built using τ values

In the case of additively of the contributions of both regions to the observed dispersion, we have:

$$\varepsilon' - \varepsilon_{\infty 2} = \Delta_1 (1 + \omega^2 \tau_1^2)^{-1} + \Delta_2 (1 + \omega^2 \tau_2^2)^{-1}, \tag{12}$$

$$\varepsilon'' = \Delta_1 \omega \tau_1 (1 + \omega^2 \tau_1^2)^{-1} + \Delta_2 \omega \tau_2 (1 + \omega^2 \tau_2^2)^{-1}. \tag{13}$$

Here it is assumed that the HF limit $\varepsilon_{\infty 1}$ of the high-temperature region is equal to the HF limit ε_{02} of the low-temperature region, ε_{01} and $\varepsilon_{\infty 2}$ correspond to ε_0 and ε_∞ in equation (1), $\tau_1 > \tau_2$.

Equations (12) and (13) are equivalent to the following:

$$\varepsilon' - \varepsilon_{\infty 2} = (\varepsilon_{01} - \varepsilon_{\infty 2})[C_1 (1 + \omega^2 \tau_1^2)^{-1} + C_2 (1 + \omega^2 \tau_2^2)^{-1}], \tag{14}$$

$$\varepsilon'' = (\varepsilon_{01} - \varepsilon_{\infty 2})[C_1 \omega \tau_1 (1 + \omega^2 \tau_1^2)^{-1} + C_2 \omega \tau_2 (1 + \omega^2 \tau_2^2)^{-1}], \tag{15}$$

where $C_{1,2}$ is the relative weight of the relaxation process,

$$C_1 + C_2 = 1. \tag{16}$$

Taking into account (12) – (13) and (14) – (15), we have:

$$C_1 = \Delta_1 (\varepsilon_{01} - \varepsilon_{\infty 2})^{-1}, C_2 = \Delta_2 (\varepsilon_{01} - \varepsilon_{\infty 2})^{-1}. \tag{17}$$

The results of data processing in terms of equations (12) – (13) and (14) – (15) are summarized in Table 4.

Table 4. Relaxation time ($\tau \cdot 10^{12}$ sec), dispersion amplitudes (Δ_1, Δ_2) and weighting factors according to equations (12)–(13) and (14)–(15)

T, ℃	30	20	10	0	-10	-20	-30	-40
τ_1	24.4	27.8	32.0	37.0	43.6	52.5	63.0	77.0
τ_2	11.1	12.3	14.2	16.2	18.2	21.0	25.2	30.0
Δ_1^*	1.04	1.06	1.09	1.12	1.15	2.18	1.22	1.26
Δ_2^*	1.62	1.67	1.70	1.75	1.81	1.85	1.91	1.97
C_1	0.39	0.39	0.39	0.39	0.39	0.39	0.39	0.39

Taken as initial values, the dispersion parameters of pure components were subject to slight variation [19,20]. The final selection of parameters was determined by the minima of the sum of the root-mean-square deviations of the coefficients calculated using these equations (ε'_{change}, ε''_{change}) from the measured ones (ε', ε''):

$$S = \sum \left\{ [(\varepsilon'_{change} - \varepsilon')(\varepsilon' \xi')^{-1}]^2 + [(\varepsilon''_{change} - \varepsilon'')(\varepsilon'' \xi'')^{-1}]^2 \right\}. \tag{18}$$

where ξ', ξ'' are the errors in measuring the dielectric constant ε' and the dielectric loss index ε'' at a given wavelength λ.

To illustrate the degree of agreement between the measured and calculated dielectric coefficients, Table 5 presents the results of calculations assuming the presence of one dispersion region with a relaxation time distribution. And also two regions, each of which has a single relaxation time τ, with different weight factors. Approximately the same agreement is noted when using equations (2) – (3) or (14) – (15) $C_1 = 0.39$, determined by (17) using the estimated values ($\varepsilon_{01} - \varepsilon_{\infty 1}$) and found from arc diagrams of values ($\varepsilon_{01} - \varepsilon_{\infty 2}$) of dispersion amplitudes. When the value of C changes by ~ 0.1 and the relaxation time τ by 10–15%, the discrepancies with experiment go beyond the calculation errors, which for "long-wavelength" points do not exceed $\sim 5\%$ in the worst case [21,22].

Table 5. Comparison of dielectric constant ε' and dielectric loss index ε'' measured and calculated from (2) - (3) and (14) - (15) at 10°C ($\tau_{av} = 25.3 \cdot 10^{-12}$ sec, $\tau_1 = 43.6 \cdot 10^{-12}$ sec, $\tau_2 = 18.2 \cdot 10^{-12}$ sec)

λ (см)	Measured		Calculated for (2) – (3)		Measured for (14) – (15)					
					$C_1 = 0.39$		$C_1 = 0.48$		$C_1 = 0.39$; $\tau_2 = 16.4 \cdot 10^{-12}$ sec	
	ε'	ε''	ε'	ε''	ε'	ε''	ε'	ε''	ε'	ε''
6.32	4.41	1.36	4.48	1.33	4.46	1.31	4.35	1.33	4.53	1.27
4.01	3.90	1.37	3.89	1.36	3.90	1.34	3.80	1.31	4.00	1.33
3.21	3.61	1.29	3.62	1.30	3.63	1.29	3.54	1.24	3.73	1.29
2.14	3.24	1.10	3.21	1.07	3.22	1.10	3.26	1.03	3.30	1.13
S	----------------		4.87		3.54		24.83		34.72	

The most remarkable result of the analysis performed is the apparent independence of the relaxation time of the mixture components from the short-range order. According to existing theories, the relaxation time τ of a molecule is determined by its structure and short-range order, which is interpreted in terms of viscous inhibition or the degree of order of surrounding molecules, estimated by the entropy term. The relaxation times for chlorine and iodobenzene differ from each other by a factor of 2.2, the viscosity η by a factor of 1.9, while the difference between the molar volumes V is 10%.

Therefore, both within the framework of the Debye model and based on the free volume required to rotate the molecule, the relaxation time of chlorobenzene $\tau_{C_6H_5Cl}$ in the mixture should increase, and the relaxation time of iodobenzene $\tau_{C_6H_5J}$ should decrease, which contradicts experience.

The processes of molecular relaxation are accompanied by structural rearrangements of such large areas of the solution that the individuality of the components becomes insignificant. The exception is solutions composed of associated and non-associated compounds, where the short-range forces are large enough to maintain the stability of regions consisting of molecules of the same type. From this it was concluded that in systems with one relaxation time τ (mixtures of two associated or two unassociated liquids) there is complete solubility at the molecular level. Whereas in the presence of two relaxation times τ, the degree of mixing is determined by the magnitude of the deviation of the relaxation time and from the values for pure components.

It should be noted that the solution we are studying is of the normal type. According to the phase diagram, the components of the mixture have unlimited mutual solubility. Finally, the values of ε_0 and η of the mixture obey the additivity rule. On the other hand, analysis of the equilibrium polarization of the mixture leads to the conclusion that there are deviations of the correlation parameter from unity, which are especially noticeable with decreasing temperature [23]. The presence of two relaxation times τ at room temperature does not necessarily contradict the low-temperature results, because with increasing temperature the lifetime and size of the regions covered by relaxation can become negligibly small. However, we also noted a division into two relaxation times τ at relatively low temperatures. Finally, it is hardly possible to explain on the basis of molecular mixing such facts as the curvature in the velocity graph and the non-additivity of $\varepsilon\infty$. The assumption that the act of orientation is highly localized as a possible reason for the invariance of the relaxation time τ in solution also appears untenable. Since with the transition from chlorine - through bromine - to iodobenzene, the difference between the activation energies for viscous flow and rotational motion tends to zero.

CONCLUSIONS

1. For a consistent interpretation of the entire set of experimental facts, the presence of clusters that preserve the structure of pure components is accepted.
2. In the compounds under study, reorientation of the molecules included in the clusters is possible only after the disintegration of the latter.
3. The duration of existence of clusters should not significantly exceed the time of rotation of molecules, as a result of which the relaxation time is determined by the sum of these quantities.
4. In the series $C_6H_6 - C_6H_5Cl - C_6H_5J$ the values of V are in the ratio 0.9:1.0:1.1, and ~40% decrease in the relaxation time of chlorobenzene $\tau_{C_6H_5Cl}$ in an equimolar benzene solution correlates well with the same decrease upon transition from the relaxation time of iodobenzene $\tau_{C_6H_5J}$ to the average relaxation time τav of the system chlorobenzene – iodobenzene $C_6H_5Cl - C_6H_5J$.

ORCID

Samir Azizov, https://orcid.org/0000-0001-6252-1512

REFERENCES

[1] S.T. Azizov, AJP Phys. **2**, 18 (2020). http://physics.gov.az/physart/251_2020_02_20_en.pdf
[2] S.T. Azizov, Phys. New. **5**, 118 (2020). http://physics.gov.az/Transactions/2020/journal2020(5).pdf. (in Russian)
[3] S.T. Azizov, O.A. Aliyev, and K.E. Zulfugarzade, APJ Phys. **4,** 22 (2017). http://www.physics.gov.az/physart/164_2017_04_22_en.pdf
[4] S.T. Azizov, and O.A. Aliyev, AJP Phys. **3**, 14 (2018). http://physics.gov.az/physart/008_2018_03_14_az.pdf. (in Russian)
[5] D. Kumar, S. Nand, and S. Sahoo, J. Solution Chem. **50**, 690 (2021). https://doi.org/10.1007/s10953-021-01085-4
[6] T. Bachhar, S. Sit, S. Laskar, and S. Sahoo, Bull. Mater. Sci. **44**, 120 (2021). https://doi.org/10.1007/s12034-021-02366-w
[7] F. Kremer, and A. Schonhals, *Broadband Dielectric Spectroscopy*, **12**, 729 (2002). https://link.springer.com/book/10.1007/978-3-642-56120-7
[8] J.P. Poley, Appl. Sci. Res. **4,** 337 (1955). https://doi.org/10.1007/BF02920014
[9] S. Murakami, Y. Akutsu, S. Habaue, O. Haba, and H. Higashimura, Nat. Sci. **2,** 803 (2010). https://doi.org/10.4236/ns.2010.28101
[10] A.J. Van Eick, and J.Ph. Poley, J. Appl. Sci. Res. **6**, 359 (1957). https://doi.org/10.1007/BF02920392
[11] V.A. Durov, and O.G. Tereshin, J. Phys. Chem. B, **110**, 8441 (2006). https://doi.org/10.1021/jp056541y
[12] S.A. Abdel-Latif, and S.E. Mansour, Nat. Sci. **2**, 793 (2010). https://doi.org/10.4236/ns.2010.28100
[13] A. Pillay, M. Elkadi, F. Feghali, S.C. Fok, G. Bassioni, and S. Stephen, Nat. Sci. **2,** 809 (2010). https://doi.org/10.4236/ns.2010.28102
[14] E.Y. Salaev, E.R. Gasimov, S.T. Azizov, and Ch.O. Qajar, Turk. J. of Phys. **5**, 389 (1998). https://journals.tubitak.gov.tr/physics/vol22/iss5/4/
[15] D.M. Fouad, A. Bayoumi, M.A. ElGahami, S.A. Ibrahim, and A.M. Hammam, Nat. Sci. **2**, 817 (2010). https://doi.org/10.4236/ns.2010.28103
[16] A.H. Rageh, S.R. El-Shaboury, G.A. Saleh, and F.A. Mohamed, Nat. Sci. **2**, 828 (2010). https://doi.org/10.4236/ns.2010.28104
[17] S.R. Kasimova, Meas. Tech. **58**, 1372 (2016). https://doi.org/10.1007/s11018-016-0901-9
[18] R.H. Cole, The J. of Chem. Phys. **23**, 493 (1955). https://doi.org/10.1063/1.1742017
[19] R. Aipova, S.A. Aitkeldiyeva, A.A. Kurmanbayev, A.K. Sadanov, and O.B. Topalova, Nat. Sci. **2,** 841 (2010). https://doi.org/10.4236/ns.2010.28105

[20] C.D. Abeyrathne, M.N. Halgamuge, P.M. Farrell, and E. Skafidas, Phys. Chem. Chem. Phys. **16**, 13943 (2014). https://doi.org/10.1039/C4CP00716F

[21] T.M. Mohan, S.S. Sastry, and V.R.K. Murthy, J. of Molec. Struc. **12**, 157 (2010). https://doi.org/10.1016/j.molstruc.2010.03.065

[22] K. Sorimachi, Nat. Sci. **2,** 846 (2010). https://doi.org/10.4236/ns.2010.28106

[23] C.J.F. Böttcher, and P. Bordewijk, *Theory of Electric Polarization*, (Elsevier, Amsterdam, 1978).

ТЕМПЕРАТУРНА ЗАЛЕЖНІСТЬ ДІЕЛЕКТРИЧНОЇ РЕЛАКСАЦІЇ СПЕКТРІВ ПОГЛИНАННЯ У СИСТЕМІ ХЛОРБЕНЗОЛ – ЙОДОБЕНЗОЛ

Самір Азізов

Міністерство науки і освіти Азербайджанської Республіки, Інститут фізики,
пр. Г. Джавіда, 131, AZ-1143 Баку, Азербайджан

У статті наведено результати дослідження температурної залежності діелектричної проникності ε' та показника діелектричних втрат ε" системи хлорбензол-йодбензол в діапазоні довжин хвиль λ = 6,32; 4,01; 3,21; 2,14; 1,18 та 0,75 та у температурному інтервалі -40℃÷+30℃ Визначено статичну діелектричну проникність на частоті 7 МГц. Визначено температурну залежність часу діелектричної релаксації молекул у рідкому стані. Встановлено, що у вказаному діапазоні частот температури дисперсійна область складається з двох частин. Аналіз температурної залежності діелектричної релаксації поляризації в системі хлорбензол-йодбензол показує, що часи релаксації компонентів не залежать від їх ближнього порядку. Також виявлено, що графік швидкості, який показує залежність логарифму часу релаксації від величини, зворотної до температури logτ ~ 1/T, складається з двох частин, а значення статичної діелектричної проникності ε∞ є неаддитивним. Для пояснення цих результатів зроблено припущення, що в цій системі утворюються кластери, як і в чистих компонентах.

Ключові слова: *діелектрична спектроскопія; діелектрична релаксація; хлорбензол; йодобензол; бромбензол*

MECHANISM OF HYDROGEN PRODUCTION IN THE PROCESSES OF RADIATION-HETEROGENEOUS SPLITTING OF WATER WITH THE PRESENCE OF NANO-METAL AND NANO-MeO

Adil Garibov[a], Yadigar Jafarov[a], ⓘGunel Imanova[a,b,c]*, Teymur Agayev[a],
Sevinj Bashirova[d], Anar Aliyev[a]

[a] *Institute of Radiation Problems, Ministry of Science and Education Republic of Azerbaijan, 9 B. Vahabzade str., AZ1143, Baku, Azerbaijan*
[b] *UNEC Research Center for Sustainable development and Creen economy named after Nizami Ganjavi, Azerbaijan State University of Economics (UNEC), 6 Istiglaliyyat Str., Baku 1001, Azerbaijan*
[c] *Khazar University, Department of Physics and Electronics, 41 Mahsati Str., AZ1096, Baku, Azerbaijan*
[d] *MDİ NASA of Space Research of Natural Resources, AZ 1115, Baku, S.S. Akhunzade, 1, Azerbaijan*
*Corresponding Author e-mail: radiasiya555@rambler.ru

In the study, the optimal values of the ratio of the distance between particles to the particle size in the radiation-heterogeneous radiolysis of water in nano-Me and nano-MeO systems were determined. In those systems, the effect of water density and system temperature on the radiation-chemical release of molecular hydrogen obtained from thermal and radiation-thermal decomposition of water was considered. The article also determined the effect of particle sizes and the type of sample taken on the radiation chemical yield of molecular hydrogen. In the presented article, the change of molecular hydrogen according to adsorbed water and catalyst was studied. Thus, in the case of a suspension of nano-zirconium in water, the energy of electrons emitted from the metal is completely transferred to water molecules, which leads to an increase in the yield of hydrogen. When radiolysis of water in the presence of nano-metals, energy transfer can be carried out mainly with the participation of emitted electrons. Therefore, in the case of radiolysis of water in suspension with n-Zr, the yield of hydrogen increases by 5.4 times compared to the processes of radiolysis in an adsorbed state. However, in radiation-heterogeneous processes of obtaining hydrogen from water in contact with metal systems, it is necessary to take into account that as a result of these processes surface oxidation occurs and after a certain time the systems are converted to n-Me-MeO+$H_2O_{liq.}$ systems. For nano sized oxide compounds, the mean free path of secondary electrons formed as a result of primary processes of interaction of quanta with atoms is commensurate with the particle sizes of nano-oxides ($\lambda \approx R_{(H\text{-}oxides)}$). Further, these electrons interact with the electronic subsystem of silicon. For nanocatalysts, the length of free paths of secondary and subsequent generations of electrons is greater than the size of catalyst particles ($R_{cat} \leq 100nm$). Usually, their energy is sufficient to conduct independent radiolytic processes in the contact medium of the catalyst.
Keywords: *Nano-Me and nano-MeO oxides; γ-Radiation; Molecular hydrogen generation; Radiolysis; Second electron cloud*
PACS: 541.15:541.183:620.3

INTRODUCTION

Nanosized metal oxide photocatalyst materials for water splitting have emerged as the promising way for hydrogen generation in a low-cost and sustainable way. Various researchers have reported investigations on co-relation of crystallinity and morphology of nanomaterials to the water-splitting performance. In general, the nanomaterials with high surface-to-volume ratios are expected to promote facile charge separation/transportation of photogenerated charge carriers [1-3].

Overall, more work needs to be done in terms of redox material engineering, reactor technology, heliostat cost reduction and gas separation technologies before commercialization of this technology [4].

The yields of molecular hydrogen, H_2, have been measured in the radiolysis of dodecane and hexane following radiolysis by γ-rays and a variety of heavy ions. Increasing the linear energy transfer (LET) from γ-rays to radiolysis with protons results in a decrease of H_2 yields by about 15% due to the increased importance of second-order H atom combination reactions. A further increase in LET results in a slight increase in H_2 yields [5].

The results suggest that the increase in H_2 production is due to the transfer of energy, possibly by an exciton, from the oxide to the water. O_2 production was at least an order of magnitude less than H_2. The yield of H_2 in the 5 MeV helium ion radiolysis of water on CeO_2 is the same as with γ-rays, but the results with ZrO_2 are substantially lower. The H_2 yields with helium ion radiolysis may be nearly independent of the type of oxide [6-10].

The differences in the relative increases in molecular hydrogen with increasing LET for each of the polymers suggests that self-scavenging reactions may be important for low LET particles [11].

It has been revealed that at increase in mass of the silicon added to water the radiation–chemical yield of the molecular hydrogen received in the process of a water radiolysis grows in direct ratio (m < 0.02 g) and depending on the sizes of particles after a certain mass value (m > 0.02 g) the stationary area is observed. In the Si+H_2O system the maximum radiation-chemical yield of molecular hydrogen is equal to 10.9; 8.07, and 5.24 molecules/100 eV at the sizes of silicon particles d = 50, 100, and 300…500 nm respectively [12].

The kinetics of molecular hydrogen accumulation at a gamma radiolysis of water on n-ZrO_2 surface is investigated. Influence of gamma radiations on n-ZrO_2+water systems is studied at various temperatures T = 300…673 K [13].

At a temperature of T = 673 K, the yield and the rate of formation of molecular hydrogen obtained in the thermal and radiation-thermal transformation of water vapor in the reaction medium increase in direct proportion to the its density at $\rho < 3$ mg/cm^3, and at $\rho \geq 3$ mg/cm^3 a sharp decrease in the angle slope is observed [14].

It has been established that the amount, formation rate and radiationchemical yield of molecular hydrogen defined according to both water and BeO from radiation-heterogeneous transformation of water in these systems, change depending on mass and particle size of BeO added to water [15].

Different strategies could be implemented to improve the water splitting efficiency of semiconductors. Among them, loading of catalyst onto the water splitting material is known to be one of the effective strategies to enhance the H_2 and O_2 production rates. Conclusively, to explore the efficient catalysts for photochemical water splitting require more research contribution towards the understanding of the core reaction mechanism of catalytic process with the use of sustainable and stable materials [16-17].

In the last years, the awareness of climatic change has increased leading to the temptation of exploration of alternative sources of energy. Consequently, the use of nuclear energy is increasing day by day but it is not economically and environmentally favorable [18]. Transforming nuclear energy into a more affordable form of energy remains one of today's needs. Therefore, the request for green energy is the chief objective for the scientists in 21 century. The significant methods include photocatalytic, photo-electrochemical, thermal decomposition and photo-biological radiolysis. Among these, photocatalytic of water is measured as the best one due to green, efficient, inexpensive with the comfort of process and with a good volume of hydrogen formed [19].

For a long time, dissimilar groups of catalysts are being developed and utilized to split water in the light but a good crop of hydrogen could not be attained at a good scale. Nanocatalysts have been produced and utilized in water splitting with good achievements [20].

Zirconium dioxide (ZrO_2) has unique properties of refractoriness, low volatility, high chemical resistance, mechanical strength, wear resistance, low thermal conductivity, wide band gap, oxygen conductivity, and high refractive index. Also, zirconium dioxide has complex polymorphisms, including high-pressure phases. The unique properties have provided a wide and varied application of materials based on ZrO_2 in various fields of science and technology. Currently, the development of new technologies for the production and obtaining nanodioxide zirconium is of particular importance. Nanoscale systems differ in many respects from ordinary single-crystal systems, therefore, the study of their interaction with water under the influence of γ-radiation is of great practical and scientific interest in the field of high-energy chemistry, as well as in solving environmental problems [21].

The results showed that surface morphology is extremely important in the decomposition of liquids at solid interfaces, which may have many consequences ranging from nuclear waste storage to the H_2 economy. The presented work is devoted to the kinetics and mechanism of the formation of hydrogen as a result of the decomposition of water on the surface of nano-ZrO_2 [22].

METHOD

The experiments were performed at the static condition in specific quartz ampoules, with V = 1.0 cm^3 of volume. In order to prevent oil and lubricants from falling on the samples, three nitrogen-cooled holders are connected to the system in a vacuum-absorption device. The products of the radiolysis and thermoradiolysis of water were absent under the selected treatment modes which can be formed in the presence of organic impurities CO and CO_2. The absorption process was the same for both methods (vapor and fluid). The gases generated were inhaled from each adsorbed ampoule to the chromatograph directly [23].

Analysis of molecular hydrogen and hydrogen-containing gases in a vacuum absorption device was carried out under static conditions. Radiation-heterogeneous processes were performed at the gamma ^{60}Co isotope source. The dosimetry of the source was determined by ferrosulfate, cyclohexane and methane dosimeters [24]. The absorbed dose rate of the source was $dD\gamma/dt = 0.40$ Gy/s. The calculation of the absorption dose in these systems was carried out in comparison with the electron density. The absorption dose of gamma quanta was determined under the methods of ferrosulfate, cyclohexane and methane based on chemical dosimeters in the studied systems.

The ampoules were opened in a special box in which the radiolysis products entered the chromatograph column. The analysis of the products of radiation-heterogeneous processes was performed using "Gasochrome-3101", "Color-102", chromatographs.

Analysis of the number of products (H_2, CO_2) gases released in the gas phase during the thermal and radiation-thermal decomposition of water on the nano-Me and nano-MeO+H_2O system was carried out by chromatographic method ("Gasochrome-3101", "Color-102", chromatographs). The molar density of gases in 1 mL was calculated by the following equation:

$$C_i = h_i m K_i$$

where: molar density of C_i-i component, molecule/ml or mol/ml; height of h_i-i-th component, mm; m - sensitivity of the chromatograph; Calibration coefficient of the K_i-i component, molecule/mm or mol/mm.

The following formula was used to calculate the substance content of the components obtained in the gas phase during the experiment:

$$N_i = C_i V$$

where: molar mass, molecular or mole of N_i-i component; Molar density of C_i-i component, molecule/ml or mol/ml; V - a volume of the ampoule tested, ml.

The chromatographic analysis of radiation-catalytic products of water decomposition was carried out.

RESULTS AND DISCUSSION

Obtaining molecular hydrogen during radiation-heterogeneous processes in suspensions of individual nano-elements (n-Zr and n-Si) in water. In order to reveal the contribution of secondary electron fluxes emitted from the solid phase in the radiation-catalytic processes of hydrogen production, the kinetics of hydrogen production processes as a result of heterogeneous decomposition of water in the presence of nano-metal (n-Zr) and individual nano-semiconductor n-Si were studied (Fig. 1).

The effect of n-Zr and n-Si on the release of molecular hydrogen during radiolysis of water is investigated in their suspension in water [25]. The kinetics of hydrogen production are investigated and radiation-kinetic outputs and process speeds are calculated based on them.
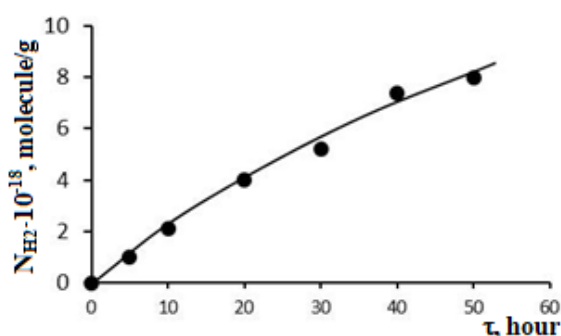
Figure 1. Kinetics of obtaining molecular hydrogen during radiolysis of water in n-Zr+H_2O suspension, at T = 300K, D = 0.15 Gy/s

On the basis of the kinetic curve, the kinetic parameters of hydrogen production are determined

$$W(H_2) = 6.67 \cdot 10^{13} molecules \cdot g^{-1} \cdot s^{-1}; \quad G_{tot}(H_2) = 7.1\ molecules/100eV \tag{1}$$

During radiation-heterogeneous radiolysis of water in a liquid state in the presence of n-Zr, the yield of molecular hydrogen is approximately 5.5 times greater than during the radiolysis of adsorbed states of water on the surface of n-Zr with a monolayer filling of the surface $\theta = 1$.

Thus, in the case of a suspension of nano-zirconium in water, the energy of electrons emitted from the metal is completely transferred to water molecules, which leads to an increase in the yield of hydrogen. However, in radiation-heterogeneous processes of obtaining hydrogen from water in contact with metal systems, it is necessary to take into account that as a result of these processes surface oxidation occurs and after a certain time the systems are converted to n-Me-MeO+$H_2O_{liq.}$ systems.

Under the influence of γ-quanta on n-Si, secondary electrons are generated with an energy

$$E_H \approx E_g + \Delta E_k, \tag{2}$$

where E_g- is the band gap of the semiconductor, ΔE - k are their additional kinetic energies.

Therefore, in the case of radiation-catalytic decomposition of water in the presence of a nano-semiconductor, for efficient energy transfer, it is necessary to have a condition for the interaction of energy carriers with water molecules. The effect of n-Si on the yield of molecular hydrogen during the radiolysis of water in a suspension of n-Si+$H_2O_{liq.}$ was studied at various $H_2O_{liq.}$/n-Si ratios [26]. To do this, we took 5 ml of bidistilled water and poured n-Si with different particle sizes into it in various amounts. Based on the weight of n-Si in the suspension and particle size, the concentrations of n-Si in V = 5 ml of water were calculated.

For this, the n-Si particles were presented as a sphere and the volume of each particle was determined by the average value of the ball radius (R_i) by $V = \frac{4}{3}\pi R^3$. Taking into account the value of the specific gravity of n-Si (ρ=2.33 g), the mass of each particle $m_{particle}$=V·Q was determined.

The ratio of m_{n-Si} to the mass of each particle makes it possible to determine the total number of particles in 5 ml of suspension $N_i = \frac{m_{n-Si}(R_i)}{m_{partic.}(R_i)}$ and based on them the concentration is estimated n-Si with different particle sizes $C_{n-Si} = \frac{N_i(R_i)}{V_{suspen.}}$. The values of the mass and concentration of n-Si for each fraction are shown in Table 1.

Under experimental conditions, the mass of $n - Si$ $m_{n-Si} \leq 0.12\ g$ is much less than the mass of water $\frac{m_{H_2O}}{m_{n-Si(max)}} = 42$. Therefore, the observed yields of molecular hydrogen were calculated both on the energy of absorbed ionizing radiation from the side of water $G_{H2O}(H_2)$ and from the side of n-Si $G_{(n-Si)}(H_2)$. Table 1 shows the values of the radiation-chemical yield of hydrogen during radiation-heterogeneous radiolysis of water in the n-Si + $H_2O_{liq.}$ system at various amounts, concentrations and sizes of the catalyst particle per gamma-radiation energy absorbed from the water side.

With an increase in the concentration of n-Si in water under the influence of gamma rays, the yield of molecular hydrogen increases. Figure 2 (a, b, c) shows the dependences of $G_{H2O}(H_2)$ on the concentration of n-Si with different particle sizes in a suspension of n-Si+$H_2O_{liq.}$.

Table 1. Effect of n-Si Concentration during Heterogeneous Radiolysis of Water in the Presence of n-Si (in Suspension)

$n-Si$ R, Gy	$d = 50nm$			$d = 100nm$			$d = 300-500nm$		
	C_{n-Si}, particle/cm^3	$W(H_2) \cdot 10^{-13}$ molekule$\cdot$ g$^{-1}\cdot$s^{-1}	$G_{H_2O}(H_2)$ molecule/ 100eV	C_{n-Si}, particle/cm^3	$W(H_2) \cdot 10^{-13}$ molecule$\cdot$ g$^{-1}\cdot$s^{-1}	$G_{H_2O}(H_2)$ molecule/100eV	C_{n-Si}, particle/cm^3	$W(H_2) \cdot 10^{-13}$ molecule$\cdot$ g$^{-1}\cdot$s^{-1}	$G_{H_2O}(H_2)$ molecule/100eV
0	0	0,61	0,44	0	0,61	0,44	0	0,61	0,44
0.01	$1.32 \cdot 10^{13}$	5.00	3.64	$1.65 \cdot 10^{12}$	3.40	2.77	$2.56 \cdot 10^{10}$	2.53	1.84
0.02	$2.63 \cdot 10^{13}$	9.67	7.03	$3.3 \cdot 10^{12}$	7.97	5.48	$5.12 \cdot 10^{10}$	5.15	3.75
0.06	$7.89 \cdot 10^{13}$	13.40	9.05	$9.92 \cdot 10^{12}$	9.67	7.03	$15.36 \cdot 10^{10}$	6.30	4.58
0.12	$15.73 \cdot 10^{13}$	15.00	10.90	$12.84 \cdot 10^{12}$	11.10	8.07	$30.72 \cdot 10^{10}$	7.21	5.24
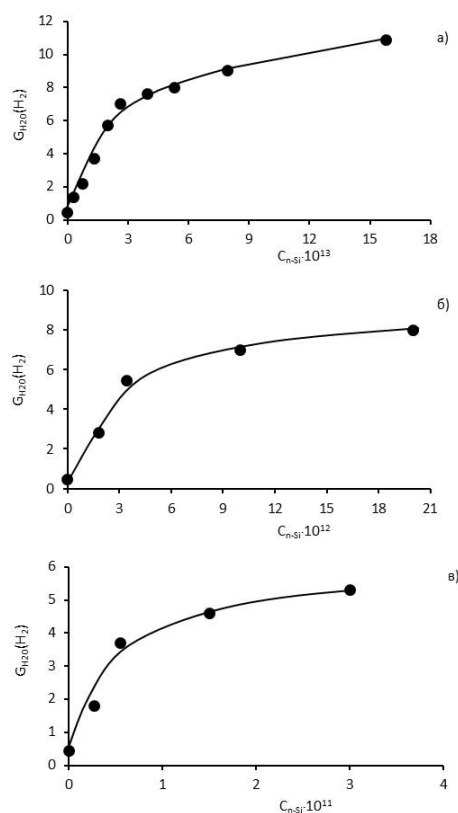
Figure 2. Dependence of $G_{H_2O}(H_2)$ on n-Si concentration in $n - Si + H_2O_{liq.}$ suspension for different particle sizes (a) d = 50nm; (b) d = 100nm; (c) d = 300-500nm, at T = 300K, D = 22 rad/s

As can be seen, the addition of even the smallest amount of n-Si to water causes a sharp increase in the yield of molecular hydrogen during radiation-heterogeneous processes in the n-Si + $H_2O_{liq.}$ system.

Dependence $G_{H_2O}(H_2) = f(C_{n-Si})$ can be conditionally divided into two sections. The first is the initial linear region, where $G_{H_2O}(H_2)$ grows linearly with increasing C_{n-Si}. The second region $G_{H_2O}(H_2) = f(C_{n-Si})$ is characterized by a small slope of the dependence line. If radiation-heterogeneous processes would occur only on the surface of n-Si particles, then the rate and radiation-chemical yields of hydrogen would increase linearly with increasing C_{n-Si}.

The value of C_{n-Si}, at which a transition between these regions is observed, depends on the size of the n-Si particles (Table 2.). For the convenience of calculation for the fraction d=300-500 nm, the average value d̄=400 nm was taken.

Table 2. Influence of n-Si concentration and distance between particles during water radiolysis in the $n - Si + H_2O$ system (in suspension)

$\bar{R}_{n-Si}$, nm	G_{H_2O}, molecule/100eV	C_{n-Si}, particle/cm³	l distance between particles, nm	l , nm	$l_n/d_ч$
25	7.3	$4.0 \cdot 10^{13}$	$l=(60 \div 1.24) \cdot 10^4$	$1.89 \cdot 10^4$	$3.78 \cdot 10^2$
50	6.5	$6.0 \cdot 10^{12}$	$l=(4.6 \div 0.1) \cdot 10^5$	$3.14 \cdot 10^4$	$3.14 \cdot 10^2$
200	4.2	$1.0 \cdot 10^{11}$	$l=(18.4 \div 0.98) \cdot 10^5$	$1.18 \cdot 10^5$	$2.95 \cdot 10^2$

By the value of the number of particles in the suspension and the specific surface of individual spherical particles $S_{particle} = 4\pi R^2$, the surface of the total amount of n-Si is determined in the form

$$S_{tot.} = N_i \cdot S_{particle} \tag{3}$$

where N_i – is the total number of particles in the water.

By the value of ω - the landing area of water on the surface of silica gel ω=0.453 nm², the number of water molecules to fill the surface with a monolayer of water is determined

$$N(\theta = 1) = \frac{S_{tot.}}{\omega_{H_2O}} \tag{4}$$

Then the hypothetical value of the number of monolayers was estimated by the number of water molecules in the suspension $(m = 5g)$ $N_{H_2O} = 1.72 \cdot 10^{23} molecules$ and $N(\theta = 1)$

$$N(monolayers) = \frac{1.72 \cdot 10^{23} molecul}{N(\theta=1)} \tag{5}$$

By the value of the hypothetical value of the monolayers filling the surface of n-Si and the diameter of water molecules d(H₂O) = 0.38 nm, one can approximately determine the distance between the particles in the suspension $n - Si + H_2O_{liq}$.

$$l = d_{H_2O} \cdot N(monolayers) \tag{6}$$

The value of the distance between n-Si particles in the suspension was determined both in the entire region of n-Si concentration and at the transition point between the regions of dependences $G_{H_2O}(H_2) = f(C_{n-Si})$.

To characterize the distance of influence of individual n-Si particles on radiation-heterogeneous processes in a suspension, distances l is given per unit of particle diameter l_n/d_{n-Si}.

As can be seen from Table 2, with an increase in the size of the n-Si particle in the H₂O + n-Si suspension, the radiation-chemical yield of hydrogen, calculated for the energy of γ - radiation absorbed from the water side, decreases. It was found that the value of the distance, given per unit of n-Si diameter within the limits of accuracy, is constant $\bar{l}/d \approx 3.3 \cdot 10^2 nm$.

This distance is consistent with the mean free path of secondary electrons with energy $E \approx 10^2 - 10^3$ in water.

To characterize the efficiency of using the energy absorbed from the n-Si side during the radiolysis of water in the $n - Si + H_2O_{liq.}$ suspension, based on the kinetic curves of hydrogen accumulation, the values of the radiation-chemical yield of hydrogen for the absorbed radiation dose from the n-Si side were calculated. Figure 3. shows the dependence of $G_{n-Si}(H_2)$ on the concentration of n-Si in water.

As can be seen, up to the value of the n-Si concentration corresponding to the transition (Table 2) $G_{n-Si}(H_2)$, remains high. Then, a region of strong decline begins with a transition to a region of decrease with a small slope of the curves.

The n-Si particles play the role of converting the energy of primary quanta into the energy of secondary electron radiation. The energy of secondary electron radiation is in the region of $E \leq 10^3 eV$ eV. Figure 3 shows the dependence of the radiation-chemical yield of molecular hydrogen, calculated on the energy absorbed only from the side of $n - Si$ $G_{n-Si}(H_2)$, on the concentration of n-Si with particle sizes d=50nm in suspension. As can be seen, in the initial region

$C_{n-Si} \leq 2.5 \cdot 10^{13} particle/cm^3$, the hydrogen yield in the limit of determination accuracy is stably high $G_{n-Si}(H_2) \approx 1700\text{-}1780$ molecules/100 eV. At optimal concentrations of n-Si in suspension with water, the observed yields of hydrogen exceed the value of the yield during radiolysis of water under the action of γ-radiation and accelerated electrons [27].
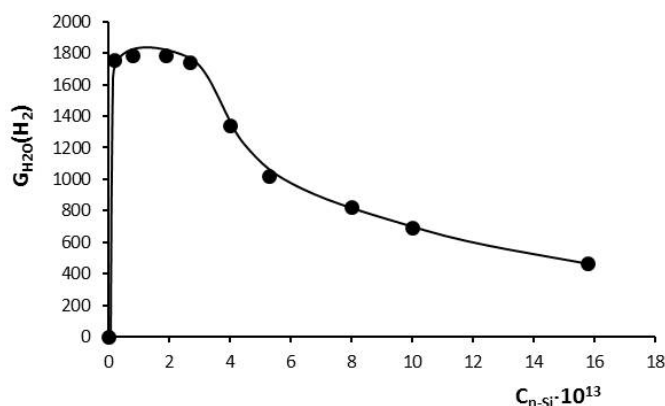
Figure 3. Dependence of $G_{n-Si}(H_2)$ during radiolysis of water in n-Si suspension with d = 50 nm in water on n-Si concentration, T = 300K, $\dot{D} = 22\ Rad/s$.

Apparently, at the initial values of the concentration $C_{n-Si} \leq C_{n-Si}$ (transition), a region with a high electron density is created around the particle, and the decomposition of water molecules occurs according to the mechanism of decomposition of water in a nonequilibrium plasma [28]. An increase in the concentration of $C_{n-Si} \geq 2.5 \cdot 10^{13}$ particles/cm³ causes a decrease in the yield of $G_{n-Si}(H_2)$ from 1780 to 430 molecules/100 eV at $C_{n-Si} = 15.8 \cdot 10^{13}$ particles/cm³. The observed dependences of $G_{n-Si}(H_2)$ and $G_{n-Si}(H_2)$ on C_{n-Si} in suspension show that after certain values of C_{n-Si} radiation processes occur, which cause a decrease in the conversion efficiency energy of ionizing radiation into the energy of hydrogen. Therefore, after C_{n-Si} (transition), the growth rate of $G_{H_2O}(H_2)$ decreases, and $G_{n-Si}(H_2)$ sharply decreases.

Based on the results obtained on the effect of the n-Si concentration in water on the yield of molecular hydrogen during water radiolysis, it can be concluded that the optimal range of n-Si concentration values for efficient conversion of ionizing radiation energy into hydrogen energy. Since at values $l/d \geq 3 \cdot 10^{-2}$ there is an efficient conversion of the energy of ionizing radiation into the energy of hydrogen. In the region $l/d \leq 3 \cdot 10^{-2}$, at which the distance between the particles related to the size unit n-Si decreases, the recombination of charged and intermediate decomposition products of water molecules increases.

The maximum yield of hydrogen during radiolysis of water in an n-Si suspension under the optimal regime corresponds to $G_{H_2O}(H_2) = 10.9$ molecules/100eV. The efficiency of converting the energy of ionizing radiation into relative conditions is

$$\eta = 2.96G(H_2) = 32.3\ \%. \tag{7}$$

And during the radiolysis of water in suspension with $n-ZrO_2$, the yield of molecular hydrogen calculated for the energy absorbed by the total system $-ZrO_2 + H_2O_{ж}$ равно $G_{tot.}(H_2) = 13.5\ molecule/100eV$.

The efficiency of converting the energy of ionizing radiation will be equal to

$$\eta = 2.97G_{tot.}(H_2) \approx 39.96\ \%. \tag{8}$$

Radiation-thermal processes of hydrogen production from water in the presence of nano-oxide compounds. Thermo-radiation processes for producing hydrogen are designed to convert the energy of high-temperature reactor models. As can be seen, an increase in temperature during radiation-thermal-catalytic processes stimulates the diffusion of energy carriers on the surface and secondary processes of transformation of intermediate products to final products. For nano sized oxide compounds, the mean free path of secondary electrons formed as a result of primary processes of interaction of quanta with atoms is commensurate with the particle sizes of nano-oxides ($\lambda \approx R_{H-oxides}$). Therefore, temperature will most of all affect the secondary physicochemical and chemical processes of heterogeneous water radiolysis. Thermal and radiation heterogeneous processes were carried out under the same conditions [29]. Kinetic parameters of thermocatalytic and radiation-thermocatalytic processes are determined on the basis of kinetic curves. The rate of radiation-catalytic processes of hydrogen production is determined by the difference in the values of experimentally determined radiation-thermal catalytic $W_{PT}(H_2)$ and $W_T(H_2)$ thermocatalytic processes.

$$W_R(H_2) = W_{RT}(H_2) - W_T(H_2) \tag{9}$$

Based on the values of $W_R(H_2)$, the values of the radiation-chemical yields of hydrogen ($G(H_2) = W \cdot J^{-1} \cdot 10^2$) were calculated. $n-SiO_2$, $n-Al_2O_3$ and $n-ZrO_2$ were taken as the object of research.

Their physicochemical properties are given in the previous sections. Figure 4 shows typical forms of kinetic curves for hydrogen production in the results of thermocatalytic (1) and radiation-thermocatalytic (2) decomposition of water at T = 673 K in the presence of $n-ZrO_2$.

The effect of temperature on the radiation-catalytic properties of nano-oxides was studied in the temperature range T = 300÷673 K at the water vapor density in the reactor $\rho = 5mG/cm^3$.

Table 3 shows the rates of radiation-thermal, thermal and radiation processes, as well as radiation-chemical yields of hydrogen, calculated for the energy absorbed by the common catalyst system+H_2O.
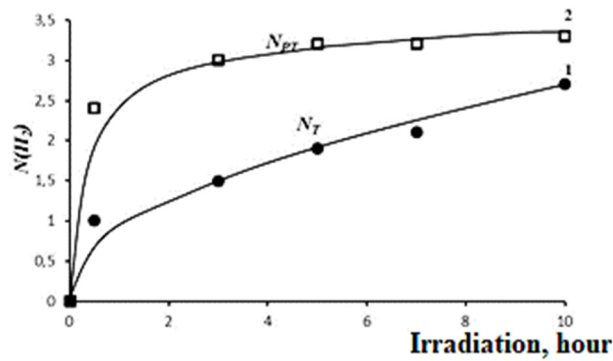
Figure 4. Kinetic curves for the production of molecular hydrogen during thermocatalytic (1) and radiation-thermocatalytic (2) decomposition of water in the presence of n$-ZrO_2$, $d = 20 - 30nm$, $T = 673K$, $\rho_{H_2O} = 5mG/cm^3$, $\dot{D} = 0.26g/s$

Table 3. The value of the rates of processes and radiation-chemical yields of hydrogen during thermal and radiation-thermal catalytic processes of water decomposition in the presence of n-ZrO₂ at different temperatures

№	T, K	$W_i(H_2) \cdot 10^{-14} molecule/g \cdot s$			$G_{tot}(H_2)$, molecule/100eV
		$W_{RT}(H_2)$	$W_T(H_2)$	$W_R(H_2)$	
1	300	-	-	0,44	2,14
2	373	0.91	0.13	0.78	4.80
3	423	1.67	0.44	1.23	6.20
4	473	2.08	0.55	1.52	8.35
5	573	3.33	1.11	2.22	13.60
6	673	6.94	2.78	4.16	25.70

The corresponding methods determined the values of the rates of processes and radiation-chemical yields of hydrogen during radiation-thermal processes of water decomposition in the temperature range T = 300÷673K in the presence of, n$-Al_2O_3$ and $n-SiO_2$.

The results obtained are shown in Tables 4 and 5.

Table 4. Influence of temperature on thermo- and radiation-thermal catalytic processes of obtaining molecular hydrogen in the system n$-Al_2O_3 + H_2O$, $\rho_{H_2O} = 5mG/sm^3$

№	T, K	$\dot{D}$, Gy/s	$W_i(H_2) \cdot 10^{-13} molecule/g \cdot s$			$G_{tot}(H_2)$, molecule/100eV
			$W_{RT}(H_2)$	$W_T(H_2)$	$W_R(H_2)$	
1	300	0.26	-	-	3.10·10¹³	1.75
2	373	0.14	2.78·10¹³	0.69·10¹³	2.09·10¹³	2.75
3	473	0.14	5.83·10¹³	2.22·10¹³	3.61·10¹³	4.15
4	673	0.13	9.44·10¹³	4.17·10¹³	5.27·10¹³	8.60

Table 5. Influence of temperature on thermo- and radiation-thermal catalytic processes of obtaining molecular hydrogen in the system n$-SiO_2 + H_2O$, $\rho_{H_2O} = 5mG/sm^3$

№	T, K	$\dot{D}$, Gy/s	$W_i(H_2) \cdot 10^{-13} molecule/g \cdot s$			$G_{tot}(H_2)$, molecule/100eV
			$W_{RT}(H_2)$	$W_T(H_2)$	$W_R(H_2)$	
1	300	0.20	-	-	0.89·10¹²	0.61
2	373	0.11	0.86·10¹³	0.12·10¹³	0.74·10¹³	1.07
3	473	0.11	2.70·10¹³	0.99·10¹³	1.71·10¹³	1.98
4	673	0.11	5.23·10¹³	2.4·10¹³	2.83·10¹³	4.15

As can be seen n-ZrO$_2$ exhibits a relatively high radiation-thermal catalytic activity. At T = 673K, the observed value of the radiation-chemical yield of molecular hydrogen during radiolysis of water in the presence of $n - ZrO_2$ is equal to $G_{tot}(H_2) = 25.7 molecul/100eV$. The process of thermo-radiolysis of water occurs in the gaseous state, and therefore the efficiency of the energy conversion process in this system is

$$\eta(H_2) = 2.51 G_{tot.}(H_2) = 64.51 \%. \tag{10}$$

Thus, radiation-thermocatalytic processes of hydrogen production from water at T ≥ 673K can compete with electrolysis processes in terms of efficiency.

Radiolytic decomposition of water molecules at T≥673K in the presence of $n - ZrO_2$ can occur both with the participation of energy carriers at the surface levels and with secondary electron radiation from $n - ZrO_2$ in the gas phase. The band gap width of $n - ZrO_2$ can be taken as $E_g = 5.4$ eV and the yield of such energy carriers as an electron and a hole will be equal to

$$G = \frac{100eV}{2E_g} \approx 9 \ vapor/100eV. \tag{11}$$

At T ≥ 673K, the intermediate H atoms are transformed into H_2 according to reaction (11).

$$H + H_2O \rightarrow H_2 + OH \tag{12}$$

Therefore, the output of molecular hydrogen as a result of radiolysis of water with the participation of non-equilibrium charge carriers formed under the action of ionizing radiation will correspond to $G_{tot.}(H_2) = 9 \ molecule/100eV$.

On the other hand, excitons are also generated in $n - ZrO_2$ under the action of γ-quanta, which can participate in the process of energy transfer. The size of the investigated samples of $n - ZrO_2$ varies in the region d = 20-30 nm, which is less than the mean free path of secondary electrons λ ≥ 2R and it can be expected that a certain part of the electrons will be emitted into the contact medium with $n - ZrO_2$. Ultimately, these energy transfer channels from $n - ZrO_2$ in water can provide the observed value of the hydrogen yield.

Influence of temperature on the output of molecular hydrogen during radiolysis of water in the presence of n-Zr and n-Si. When radiolysis of water in the presence of nano-metals, energy transfer can be carried out mainly with the participation of emitted electrons. Therefore, in the case of radiolysis of water in suspension with n-Zr, the yield of hydrogen increases by 5.4 times compared to the processes of radiolysis in an adsorbed state. Based on the results of the radiation-thermocatalytic processes of hydrogen production from water presented in the previous sections, it is possible to conclude that their speed depends on the following parameters of the process regime.

$$W_{RT}(H_2) = f(T, \dot{D}, \rho_{H_2O}, S/V, LET), \tag{13}$$

where is the temperature, $\dot{D}$-radiation, LET-linear radiation energy transfer, ρ_{H_2O} is the density or pressure of water vapor in the reaction medium, S/V dispersion of microsized or particle size of nanosized solids.

In order to reveal the regularities of the effect of temperature on the yield of molecular hydrogen, the kinetics of water radiolysis in the presence of n-Zr was studied in the temperature range T = 300÷673K, at a water vapor density in the reaction medium ρ_{H_2O} = 5mg/cm^3 and power exposure doses $\dot{D}$ = 0.32÷0.26 Gy/s [30]. The values of the rates of the processes and the radiation-chemical yield of molecular hydrogen are given in Table 6.

Table 6. The value of the rates of thermo-, radiation-thermal and radiation-catalytic processes in the n-Zr+H$_2$O contact and the radiation-chemical release of hydrogen in the temperature range, T= 300 ÷ 673K, $\rho_{H_2O} = 5mG/cm^3$, $\dot{D} = 0.32 ÷ 0.26 Gy/s$

№	T, K	$W_{RT}(H_2),$ $molecule/g \cdot s$	$W_T(H_2),$ $molecule/g \cdot s$	$W_R(H_2),$ $molecule/g \cdot s$	$G_{tot}(H_2),$ $molecule/100eV$
1	300	-	-	1,22·10^{13}	1,30
2	373	4.10·10^{13}	2.60·10^{13}	1.50·10^{13}	2.10
3	473	5.56·10^{13}	2.77·10^{13}	2.79·10^{13}	3.70
4	573	8.88·10^{13}	5.00·10^{13}	3.88·10^{13}	5.20
5	673	1.33·10^{14}	0.70·10^{14}	0.63·10^{14}	8.40

The value of the activation energy of the processes of thermo-heterogeneous and radiation-thermal processes on the basis of the dependencies $\ln W_i(H_2) \geq f\left(\frac{1}{T}\right)$ was determined to be 33.8 and 22.3 kJ/mol, respectively [30].

The value of $G_{tot.}(H_2)$ during radiation-thermal decomposition of water at T = 673K, $G_{tot.}(H_2) = $ 8.4 molecules/100eV does not differ much from the values of hydrogen yield during radiolysis of water in n-Zr

suspension $G_{tot.}(H_2)$ =7.1 molecules/100eV. The observed difference in the values of the hydrogen yield can be explained by the course of process (12).

The efficiency of converting the energy of ionizing radiation into the energy of hydrogen in radiation-thermal catalytic processes at T = 673K in the gaseous state in the presence of nano-zirconium is equal to

$$\eta = 2.51 G(H_2) = 21 \%. \tag{14}$$

The authors [31-32] studied the effect of temperature on thermal processes, radiation-thermal processes in the $n - Si + H_2O$ contact at various temperatures T = 300÷673K and water vapor density $\rho_{H_2O} = 5$mg/cm³.

The effect of water vapor density on the value of kinetic parameters of heterogeneous processes of water decomposition was studied at T = 673 K, $\rho_{H_2O} = 0.25÷8$ mg/cm³ in the presence of n-Si with particle size d = 50 nm. The research results are shown in Table 7.

Table 7. The value of the rates of thermo-heterogeneous, radiation-thermal and radiation-chemical processes, the production of hydrogen in the n-Zr+H₂O system at the size of the n-Si particle d = 50nm and at the temperature T = 673K at the density of water vapor in the reaction medium $\rho_{H_2O} = 0.25 \div 8 \, mG/cm^3$

№	$\rho, mG/cm^3$	$W_{RT}(H_2)$, $molecule/g \cdot s$	$W_T(H_2)$, $molecule/g \cdot s$	$W_R(H_2)$, $molecule/g \cdot s$	$G_{tot}(H_2)$, $molecule/100eV$
1	0.25	$1.68 \cdot 10^{14}$	$1.73 \cdot 10^{14}$	$0.05 \cdot 10^{14}$	0.45
2	0.5	$3.34 \cdot 10^{14}$	$3.45 \cdot 10^{14}$	$0.10 \cdot 10^{14}$	0.89
3	1.0	$6.49 \cdot 10^{14}$	$6.70 \cdot 10^{14}$	$0.21 \cdot 10^{14}$	1.85
4	3	$18.74 \cdot 10^{14}$	$19.15 \cdot 10^{14}$	$0.41 \cdot 10^{14}$	3.60
5	8	$20.10 \cdot 10^{14}$	$20.60 \cdot 10^{14}$	$0.50 \cdot 10^{14}$	4.40

At a constant value of water vapor density ρ_{H_2O}, d_к is the catalyst particle size, $\dot{D}$ is the radiation power and LET in (14), the effect of temperature in the region T=300÷673K on the velocities and $G_{tot.}(H_2)$ at thermo-radiolysis of water in the $n - Si + H_2O$ system. The observed research results are shown in Table 8.

Table 8. Effect of temperature on the kinetic parameters of hydrogen production during thermo-radiolysis of water in the presence of n-Si with d = 50nm, ρ_{H_2O}=8 mg/cm³ under the action of gamma radiation with $\dot{D}$ = 0.18 Gy/s

№	$\rho, mG/cm^3$	$W_{RT}(H_2)$, $molecule/g \cdot s$	$W_T(H_2)$, $molecule/g \cdot s$	$W_R(H_2)$, $molecule/g \cdot s$	$G_{tot}(H_2)$, $molecule/100eV$
1	300	-	$0.32 \cdot 10^{14}$	$0.32 \cdot 10^{14}$	2.87
2	373	-	$0.33 \cdot 10^{14}$	$0.33 \cdot 10^{14}$	2.90
3	473	-	$0.36 \cdot 10^{14}$	$0.36 \cdot 10^{14}$	3.20
4	573	$2.40 \cdot 10^{14}$	$2.88 \cdot 10^{14}$	$0.48 \cdot 10^{14}$	4.20
5	623	$7.22 \cdot 10^{14}$	$7.71 \cdot 10^{14}$	$0.49 \cdot 10^{14}$	4.32
6	673	$2.01 \cdot 10^{15}$	$2.06 \cdot 10^{14}$	$0.50 \cdot 10^{14}$	4.40

The activation energies of thermal and radiation-thermal processes of hydrogen production in the $n - Si + H_2O$ system is determined based on the temperature dependences of the process rates in the Arrhenius coordinates $\ln W_i(H_2) = f\left(\frac{1}{T}\right)$. It was found that in the temperature range T=300÷473K, the radiolysis of water in the presence of n-Si occurs only as a result of radiation-heterogeneous decomposition of water with E = 1.07 kJ/mol. As can be seen from Table 8, in the temperature range T = 573÷673K in the $n - Si + H_2O$ system, thermo-heterogeneous and radiation-thermo-heterogeneous processes of water decomposition are observed. The activation energies of these processes are 68.60 and 53.83 kJ/mol, respectively. Comparison of the activation energies of the processes $W_P(H_2)$, $W_{PT}(H_2)$ and $W_T(H_2)$ shows that radiation processes in the $n - Si + H_2O$ system cause a decrease in the activation energy of the water decomposition process [33-35].

After radiation-heterogeneous processes, oxide phases, hydrides (ZrH$_x$, SiH$_x$), hydroxyl groups Zr-OH, Si-OH are formed on the surface. SEM and IR spectrometry methods reveal oxide phases on the surface of the initial n-Zr and n-Si samples. Therefore, radiation-heterogeneous processes of water decomposition actually occur in the contact $n - Si - SiO_2 + H_2O$, $n - Zr - ZrO_2 + H_2O$. As can be seen from tables 7 and 8, n-ZrO₂ have a relatively high radiation-catalytic activity in the process of water decomposition. Therefore, during radiation-thermocatalytic processes of hydrogen production in the $n - Zr - ZrO_2 + H_2O$ system, high yields of molecular hydrogen are observed relative to $n - Si + H_2O$ systems. The values of radiation-chemical yields of hydrogen during thermoradiolysis of water in the systems $n - SiO_2 + H_2O$ and $n - Si + H_2O$ in the temperature range T ≥ 573 K are comparable and vary in the range of 4.15-4.40 molecules/100eV. Therefore, radiolysis and thermo-radiolysis processes in the $n - Zr - ZrO_2 + H_2O$ and $n - Si + H_2O$ systems can be used as model systems for revealing the patterns of energy transfer and surface radiation-chemical processes.

The Mechanism of Radiation-Catalytic Processes for Hydrogen Production from Water

When ionizing radiation interacts with nano-catalysts, primary processes generate free secondary electron radiation, electrons in the conduction band, holes in the valence band, and excitons:

$$nano - cat. \xrightarrow{ion.radiation} e_v + e_{pr} + p + ex \qquad (15)$$
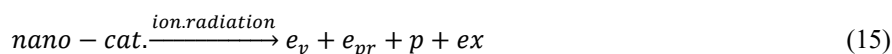
In the scheme (15), e_v -are secondary electrons, e_{pr} - are electrons in the conduction band, p-holes in the valence band, ex-excitons, which are formed as the end product of a cascade of processes of interaction of secondary elements with catalyst atoms. As an example, let's look at the physical stage of processes occurring in the $n - Si + H_2O$ system under the action of gamma - quanta with energy $\bar{E}$ = 1.25 MeV [12-15].

It is revealed that the interaction of gamma-quanta with the atoms of the systems occurs mainly according to the mechanism of Compton scattering. With Compton scattering of gamma-quanta from silicon atoms, depending on the scattering angle, the kinetic energy of Compton electrons varies in the range of 0 ... 1.02 MeV. For nanocatalysts, the length of free paths of secondary and subsequent generations of electrons is greater than the size of catalyst particles ($R\_cat \leq 100nm$). Therefore, in scheme (1), secondary electrons for radiation-heterogeneous processes involving nanoscale catalysts are also indicated as end products.

The physical stage of radiation-heterogeneous processes proceeds for $\tau \leq 1fs$ (femtoseconds) and as a result, ionization (e, p, H_2O^*), excitation ex, H_2O^*) and generation of high-energy electrons [20] occur according to the scheme (15).

Water on the surface of oxide systems creates electron-donor complexes H₂Os, which capture holes formed under the action of ionizing radiation (16). Many radiation catalytic active oxide compounds have broad valence levels, and therefore the holes in them are highly mobile. In the presence of levels of water molecules on the surface, they interact according to the reaction:

$$\oplus + H_2O_s \rightarrow H_2O_s^+ \qquad (16)$$

Electrons formed in radiation-catalytically active oxides under the action of ionizing radiation can have energies in a wide range and enter into multiple interactions with the electronic structures of oxides. As a result, they go through approximately the following energy stages.

1. The electron energy becomes less than the ionization energy of the medium $E_e^1 \leq W(I)$, where W(I) is the threshold energy, of the formation of ion vapors in the medium. The value of E_e^1 is the dependence of the band gap for radiation-catalytically active catalysts and is equal to $E_e^1 \approx 2 \div 3 \ E_g$ [20]. Taking into account the values of the water ionization potential for W(I) ≈ 30 eV, these electrons can be characterized as underionization electrons. Electrons with energy $E_e^1 \leq W(I)$ in a medium can enter into an electron-electron interaction and generate an excited state of excitons. After certain energies, the electrons are localized in the structural centers and eventually thermolyzed. Exciton levels of radiation catalytic active oxides $E_{ex} \approx E_g - \sigma E$.

2. The value of E_g in radiation catalytic active catalysts varies in the range of 5÷10 eV [21]. And therefore, the localized exciton levels of these oxides are smaller than the values of the band gap and vary in the range $E_{ex} \sim 5 - 8$ eV [22]. For example, in SiO₂ the energy of underexcitation electrons is equal to E ~ 7.4 eV.

3. After the generation of excitons in oxide systems, underexcitation electrons appear, which have a lower E_{ex} ($E_{II}^1 \leq 10 \ eV$). These electrons first interact with LO photons and then with acoustic phonons.

In oxide systems, electrons with energies below the ionization threshold W_i can create excitons and enter into an electron-phonon interaction. The electron-phonon interaction is more probable in the electron energy range 4÷20 eV [66]. The electron-phonon interaction occurs first with LO photons and then with acoustic phonons. After numerous collisions, thermalization of electrons occurs. For example, in SiO₂ electrons with an energy of 1÷8 eV, the thermalization time varies in the range $\tau \leq 1fs$ [28]. On average, electrons with energy $E_э \leq W_2(I)$ are thermalized in time τ = 250÷350 fs. The thermalization time of electrons with energy $E_э \leq W_2(I)$ in water is comparable to the thermalization time in SiO₂, which approximately vary in the range τ = 250÷350fs. During thermalization, electrons in both phases in $SiO_2 - H_2O$ systems can move at a distance of several nanometers. For example, for pure SiO₂, electrons with an energy of 3 eV during thermalization can migrate from 8 to 30 nm distances. Table 9 shows the values of relative permittivity (ε_0), onsager radius ($R_0 = q^2/(4\pi\varepsilon_0 k_B T)$), diffusion constant $D = \mu k_B T/q$ and recombination constant of electron with cations (holes) $\gamma = R_0/(4Dt)^{\frac{1}{2}}$: where, q - charge, k_B - Boltzmann constant, T - temperature, μ - particle mobility, t - time [25].

Table 9. The value of the parameters of processes involving nonequilibrium carriers in SiO₂ and H₂O charges

$SiO_2 - H_2O$	ε_0	$R_0(nm)$	$D(nm^2 \cdot s^{-1})$	γ
H_2O	78	0.72	$1.4 \cdot 10^{13}$	0.2
SiO_2	3.9	14.0	$0.5 - 3.0 \cdot 10^{14}$	0.8

As can be seen, the values of the electron-hole recombination constants in SiO₂ are 4 times greater than in water. The on sager radius is about 20 times smaller than in SiO₂. And therefore, in water, secondary electrons can propagate a large distance from the parent ion.

Thus, by analyzing the processes occurring in $E_3 \leq W_2$ radiation-catalytic active oxides, one can imagine the mechanism of radiation-heterogeneous processes of water decomposition with the participation of energy carriers according to scheme (15).

Formed according to the scheme H_2O^* interacts with electrons from the conduction band:

$$e + H_2O_s^+ \rightarrow H_2O_3^* \tag{17}$$

$H_2O_s^*$ singlet-excited water molecules in the $A'B$ state (E=8.4eV) undergo decay [13]:

$$H_2O_3^* \rightarrow H + OH \tag{18}$$

However, during the recombination of H_2O_s ions with quasi-free electrons, the energy corresponding to dissociative recombination with E ≈ 11 eV is released:

$$e + H_2O_s \rightarrow H_2O_3^* \rightarrow H_2 + OH \tag{19}$$

During the radiation-catalytic decomposition of water in the presence of nanocatalysts at T ≥ 673K, the transformation of H atoms into H_2 can occur according to the reaction [15]:

$$H + H_2O \rightarrow H_2 + OH \tag{20}$$

The radiolysis of water on the surface of oxide systems can involve subexcited electrons formed in the oxide phase [16-18]:

$$e_{subexcited} + H_2O_s \rightarrow H^- + HO\cdot \tag{21}$$

$$H^- + H_2O \rightarrow H_2 + OH^- \tag{22}$$

The course of these reactions was confirmed by the authors as a result of a study of the dissociative capture of electrons with energy $E_e \leq 12$ eV [12]. According to reaction (17) - (22), the maximum yield is observed at the electron energy $E_e = 7.4$ eV.

As is known, during the radiation-catalytic decomposition of water into a surface-adsorbed state, the maximum yield of hydrogen is limited by the total yields of nonequilibrium charge carriers and excitons and is equal to G(H_2)~8-9 molecules/100eV. A particularly high yield of molecular hydrogen is observed during the radiolysis of water in suspension with nano-oxides [24-26] and nanosized individual elements Ze, Si [27]. The observed yield of hydrogen in these processes cannot be explained within the framework of the existing theoretical concepts of energy transfer in radiation-heterogeneous processes.

First, it is necessary to analyze the processes of the physical and physical-chemical stages in individual components of H_2O+nanocatalysts. Under the influence of gamma-quanta and electrons on water, the yield of electron-ion pairs is 3.4 vapor/100 eV [32]. Radiation-catalytically active catalysts in terms of electrical properties can be attributed to insulators Eg~4÷9 eV (nZrO_2, nSiO_2, nAl_2O_3) and n-Si semiconductors with Eg ≈ 1.5 eV. The threshold energies of the formation of electron-hole pairs in them are equal to En (dielectric)=2.0 Eg; En (semiconductor) = 3.0 Eg and the yields of electron-hole pairs when exposed to quanta are 12.5-5.5 vapor/100eV for dielectrics, 22vapor/100eV for semiconductors. On the other hand, the density of solids is greater than that of water. For these reasons, when γ-quanta are exposed to the system of nanocatalysts +H_2O, the concentration of secondary electrons in the solid phase will be much higher than in water. For example, in the n-Si+H_2O system, the number of electron-hole pairs inside a silicon particle is about 18 times greater than in pure water [30].

Individual particles of nanocatalysts can be represented as a sphere with radius R. The mean free path of energy carriers inside this sphere is λ. Effective energy transfer to the surface of the contacting medium can occur if $\lambda \gtrsim$R. Therefore, with a decrease in the particle size of nanocatalysts, the yield of molecular hydrogen during the radiation-catalytic decomposition of water increases [31].

As the energy of secondary electrons increases, the mean free path in dielectrics and semiconductors decreases [56]. Therefore, in the field of action of γ radiation on nanocatalysts, the energy of electrons emitted from them is low and usually lies in the range ≤10^2 eV. The maximum free path of electrons with an energy of 100 eV in water corresponds to 20 nm [33]. Therefore, it can be imagined that during radiation-catalytic processes with the participation of nanocatalysts, a spherical shell with a radius of 20 nm with a high concentration of electrons with energy E≪10^2 eV is formed around a spherical particle of catalysts with a radius R.

In the reactor of radiation-catalytic processes, nano-particles are in the form of densely packed spheres. Many physical properties of adsorbed water molecules, such as ionization potential, ion formation energy, excited states, and dissociation energy, differ greatly from those of pure water [35]. Therefore, the yields of target products in the radiation-catalytic decomposition of water, depending on the layer of adsorbed states, differ greatly [21-24]. Secondary electron radiation emitted from nanocatalysts after a multiple cascade of processes of electron-electron interactions cause ionization, excitation in the water phase in the volume between nanoparticles and finally become underexcitation electrons ($E < 7.4\ eV$):

$$H_2O \xrightarrow{e} H_2O^+ + e + e \tag{23}$$

$$H_2O^+ \xrightarrow{e} H_2O^* \tag{24}$$

The resulting H_2O^+ ions can recombine with electrons, forming H_2O^*:

$$H_2O^+ + e \rightarrow H_2O^* \tag{25}$$

Excited water molecules can decompose according to the reaction:

$$H_2O^* \rightarrow H + OH \tag{26}$$

After multiple electron-electron, electron-phonon interactions during the time $\tau = 10^{-15} - 10^{-12}$ s, electrons can be solvated:

$$e^- + H_2O \rightarrow e_{aq}^- \tag{27}$$

With the participation of e_{aq}^-- in an aqueous medium, the formation of hydrogen can occur according to the following reactions [25-30]:

$$e_{aq}^- + e_{aq}^-(+2H_2O) \rightarrow H_2 + 2OH^- \tag{28}$$

$$k_1 = 5,5 \cdot 10^9 m^{-1}c^{-1}$$

$$e_{aq}^- + H(+H_2O) \rightarrow H_2 + OH^- \tag{29}$$

$$k_2 = 2,5 \cdot 10^9 m^{-1}s^{-1}$$

$$H + H \rightarrow H_2 \tag{30}$$

$$k_3 = 7,8 \cdot 10^9 m^{-1}s^{-1}$$

However, as a result of these processes, the yield of molecular hydrogen does not exceed the yield of molecular hydrogen during the radiolysis of water under the action of electrons [60-65]. Radiation-catalytic processes of water decomposition in the presence of nano-semiconductor and nano-metal cannot be explained by the above mechanisms of energy transfer in adsorbed water molecules. During the radiolysis of water in contact with metals, the observed high yields of molecular hydrogen are explained by the decomposition of water with the participation of secondary electron radiation emitted from the metal [66].

In the volume between the grains of nanocatalysts during the radiation-catalytic decomposition of water, electrons enter from all sides, forming a volume with a high concentration of electrons (n_e). Approximately, this volume of water can be represented as a sphere with a radius of 20 nm. In this volume $= \frac{4}{3}\pi R^3 = 3.35 \cdot 10^{-17} cm^3$ under normal conditions there will be $n \sim 10^7$ water molecules. If we take into account that the number of gamma quanta falling per unit time and the number of secondary electrons formed as a result of scattering of primary quanta and secondary electrons, we can be sure that in the volume between nanoparticles without a concentration of secondary electrons there will be a high value of the ratios $n_e/[H_2O]$ will be quite high. Therefore, the mechanism of one-stage nonequilibrium discharges can be applied [67].

Under excited electrons can expend their energy on vibrational excitation of water molecules and enter into a dissociative attachment reaction with a water molecule. Under excitation electrons lose their excess energy in $\sim 10^{-13}$ s and then thermalize or solvate [56].

The maximum of the dissociative attachment cross section occurs at the electron energy $E_e \approx 6$ eV:

$$e + H_2O \rightarrow H^- + OH \tag{31}$$

In the electron energy range Ee ~ 1-30 eV, multiple dissociative attachment of electrons can occur:

$$e + H^- \rightarrow H + e + e \tag{32}$$

Multiple use of the electron is possible due to the high-rate $K_e = 10^{-6} cm^3/s$ of the destruction of the negative ion H^- by electron impact according to reaction (23-32).

It has been established that at low electron energies (Te $\approx$ 1eV), the electron energy is spent on vibrational excitation of water molecules. The characteristic vibrational quantum of water molecules is equal to $h\omega = 0.2$ eV. Sequential vibrational excitation of water molecules occurs in the reaction medium, as a result of which highly excited states are populated into vibrational V-V relaxation, and at the end, a reaction occurs with the participation of H_2O^* [57]:

$$H_2O^* + H_2O \rightarrow H + OH + H_2O \tag{33}$$

The rate of this process is expressed with the formula:

$$v_0 = k_0[H_2O]^2 exp[-D(H_2O)/T_v] \tag{34}$$

where $k_0 = 3 \cdot 10^{-10} cm^3/s$ is the collision constant; $D(H_2O) =5$ eV – water dissociation energy, T_v – vibrational water temperature.

The resulting H and OH radicals carry out chain processes involving vibrationally excited molecules:

$$H + H_2O^* \rightarrow H_2 + OH; \tag{35}$$

$$\Delta H = 15 kcal/mol, E_{a_1} = 21 kcal/mol$$

$$OH + H_2O^* \rightarrow H + H_2O_2; \tag{36}$$

$$\Delta H = 61 kcal/mol, E_{a_2} = 70 kcal/mol$$

Chain termination occurs as a result of three-body recombination:

$$H + OH + H_2O \rightarrow H_2O + H_2O; \tag{37}$$

$$k_3 = 3 \cdot 10^{-31} cm^6/s$$

A parallel chain propagation channel can occur in the reaction medium:

$$OH + H_2O^* \rightarrow H_2 + HO_2; \tag{38}$$

$$\Delta H = 51 kcal/mol, E_a = 75 kcal/mol$$

$$HO_2 + H_2O^* \rightarrow H_2O_2 + OH; \tag{39}$$

$$E_a = 30 kcal/mol$$

However, these reactions are inferior to reactions (33) - (39) due to the high activation barrier. At high temperatures T ≥ 673K, H atoms are transformed into H$_2$ according to the reaction [65]:

$$H + H_2O \rightarrow H_2 + OH \tag{40}$$

As a result of these processes, the yield of molecular hydrogen is doubled.

If we assume that the chain decomposition of water in radiation-catalytic processes with the participation of nanocatalysts begins with the participation of non-equilibrium charge carriers and excitons formed under the action of ionizing radiation on the catalysts ex, the initial outputs are equal

$G_{a.c} = G_{ex} + G_{n.n} = 8 \, particle/100eV$. Using these approximate values, you can estimate the length of the chain of hydrogen production processes by the expression:

$$\gamma = \frac{G(H_2)}{G_{a.c.}} \tag{41}$$

During radiation-catalytic processes of water decomposition at T ≥ 673K in the presence of microsized oxide catalysts:

$$\gamma = \frac{G(H_2)}{G_{a.c.}} \tag{42}$$

In the case of the presence of nanosized catalysts G(H$_2$) ~ 14-26 molecules/100eV and the chain length:

$$\gamma = 1.75 \div 3.75 \tag{43}$$

Thus, in the process of hydrogen production during the radiation-catalytic decomposition of water in the presence of nanocatalysts, an unbranched chain mechanism occurs.

During radiolysis of a suspension of nanocatalyst + H$_2$O and adsorbed water on the surface of nanocatalysts, water is in a liquid state. Therefore, the efficiency of hydrogen production in these processes is determined by the expression:

$$\eta = 2.96 \, G(H_2) \tag{44}$$

If we take into account that the values of molecular hydrogen during the radiation-catalytic decomposition of liquid water in the presence of nano-catalysts reach G(H$_2$)=13.5 molecules/100eV values, the efficiency of the processes will be equal to:

$$\eta = 40 \, \% \tag{45}$$

During thermoradiation-catalytic processes of hydrogen production, the decomposition of water occurs in a vapor state ($\Delta H = 242 \, kC/mol$):

$$\eta = 2.5 \, G(H_2) \tag{46}$$

Efficiency for radiation-thermocatalytic processes T = 673K with output $G(H_2) = 25.7 \, molecul/100eV$:

$$\eta = 64 \, \% \tag{47}$$

Thus, radiation-catalytic and radiation-thermal catalytic processes of hydrogen production in the presence of nano-catalysts ($n - ZrO_2$, $n - Al_2O_3$ и $n - SiO_2$) can be recommended as effective methods for converting the radiation and thermal components of nuclear-technological and energy processes (40) - (47).

Radiation-catalytic processes can be on technological radiation installations (isotope, accelerators and sources of bremsstrahlung).

Radiation-thermal catalytic processes can be implemented by a combination of radiation installations and high-temperature modular nuclear reactors. The schematic diagram of these complexes is shown in Figure 5.

At a temperature of T $\geq$6 73K, a high efficiency occurs during the radiation-thermocatalytic decomposition of water. The hydrogen obtained by the membrane separation from oxygen can be further used for various purposes or for the production of electricity.
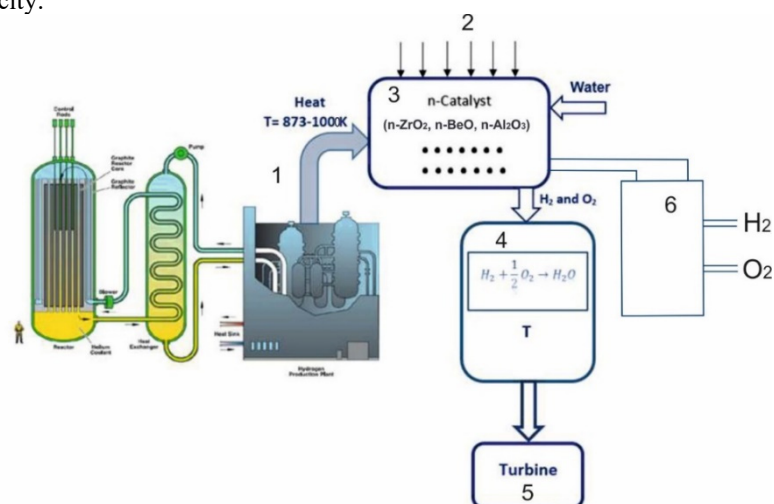
Figure 5. Scheme of the technological complex for obtaining molecular hydrogen by radiation-thermal catalytic decomposition of water with a combination of high-temperature nuclear reactors

1 - high-temperature module reactor (SMR); 2 - sources of ionizing radiation; 3 - reactor for carrying out radiation-thermal processes of hydrogen production in the presence of catalysts $n - ZrO_2$, $n - Al_2O_3$ и $n - BeO$); 4 - system for igniting the mixture and generating steam for the turbogenerator; 5 - turbogenerator for generating electricity; 6 - column for membrane separation of a mixture of $H_2 + O_2$.

CONCLUSION

Based on the results obtained on the effect of the n-Si concentration in water on the yield of molecular hydrogen during water radiolysis, it can be concluded that the optimal range of n-Si concentration values for efficient conversion of ionizing radiation energy into hydrogen energy. Since at values $l/_d \geq 3 \cdot 10^{-2}$ there is an efficient conversion of the energy of ionizing radiation into the energy of hydrogen. In order to reveal the contribution of secondary electron fluxes emitted from the solid phase in the radiation-catalytic processes of hydrogen production, the kinetics of hydrogen production processes as a result of heterogeneous decomposition of water in the presence of nano-metal (n-Zr) and individual nano-semiconductor n-Si were studied. Thus, in the case of a suspension of nano-zirconium in water, the energy of electrons emitted from the metal is completely transferred to water molecules, which leads to an increase in the yield of hydrogen. When radiolysis of water in the presence of nano-metals, energy transfer can be carried out mainly with the participation of emitted electrons. Therefore, in the case of radiolysis of water in suspension with n-Zr, the yield of hydrogen increases by 5.4 times compared to the processes of radiolysis in an adsorbed state. However, in radiation-heterogeneous processes of obtaining hydrogen from water in contact with metal systems, it is necessary to take into account that as a result of these processes surface oxidation occurs and after a certain time the systems are converted to n-Me-MeO+H$_2$O$_{liq.}$ systems. For nano sized oxide compounds, the mean free path of secondary electrons formed as a result of primary processes of interaction of quanta with atoms is commensurate with the particle sizes of nano-oxides ($\lambda \approx$ R_(H-oxides)). Further, these electrons interact with the electronic subsystem of silicon. For nanocatalysts, the length of free paths of secondary and subsequent generations of electrons is greater than the size of catalyst particles (R_cat$\leq$100nm). Usually, their energy is sufficient to conduct independent radiolytic processes in the contact medium of the catalyst.

ORCID

Gunel T. Imanova, https://orcid.org/0000-0003-3275-300X

REFERENCES

[1] M. Alam, F. Miserque, M. Taguchi, and L. Boulanger, "Renanli Tuning hydrogen production during oxide irradiation through surface grofting," J. Mater Chem. **19**, 4261-4267 (2009). https://doi.org/10.1039/B901936G

[2] R. Yamada, Y. Hatano, and Z. Yoshida, "Hydrogen production of aqueous sulfuric acid solutions containing Al_2O_3, SiO_2, TiO_2 or ZrO_2 fine particles," Int. J. Hydrogen Energy, **33**, 929-936 (2008). https://doi.org/10.1016/j.ijhydene.2007.11.028

[3] S. Le Caër, "Water radiolysis: Influence of oxide surfaces on H_2 production under ionizing radiation," Water, **3**(1), 235-353 (2011). https://doi.org/10.3390/w3010235

[4] N.G. Petrik, A.B. Alexandrov, and A.I. Vall, "Interfaced energy transfer during gamma radiolysis of water on the surface of ZrO_2 and some other oxides," J. Phis. Chem. B, **105**, 5935-5944 (2001). https://doi.org/10.1021/jp004440o

[5] J.A. LaVerne, and L. Tandon, "H_2 production in the radiolysis of water on CeO_2 and ZrO_2," The Journal of Physical Chemistry B, **106**, 380-386 (2002). https://doi.org/10.1021/jp013098s

[6] J.A. LaVerne, and S.E. Tonnies, "H_2 production in the radiolysis of aqueous SiO_2. Suspensions and Slurries," The Journal of Physical Chemistry B, **107**, 7277-7280 (2003). https://doi.org/10.1021/jp0278418

[7] K. Skotnicki, and K. Bodrowski, "Molecular hydrogen formation during water radiolysis in the presence of zirconium dioxide," J. Radioanal Nucl. Chem. **304**, 473-480 (2014). https://doi.org/10.1007/s10967-014-3856-9

[8] C. Fourdrin, H. Aarrachi, C. Latrille, S. Esnouf, F. Bergaya, and S.Le. Caer, "Water Radiolysis in Excahnged-Montmorillonites: The H_2 Production Mechanisms," Environ. Sci. Technol. **47**, 9530-9537 (2013). https://doi.org/10.1021/es401490t

[9] T.N. Agayev, A.A. Garibov, G.T. Imanova, and S.Z. Melikova, "Radiation-induced heterogeneous processes of water decomposition in the presence of mixtures of silica and zirconia nanoparticles," J. High Energy Chemistry, **52**(2), 145-151 (2018). https://doi.org/10.1134/S0018143918020029

[10] I.I. Mustafayev, and H.M. Mahmudov, "Radiation-thermal desulphurization of organic fuels", J. of Radiation Researches, **2**(2), 65–70 (2015).

[11] L.Y. Jabbarova, I.I. Mustafayev, R.Y. Akbarov, and A.S. Mirzayeva, "Study of post-radiation processes in model hexane/hexene binary systems," J. of Radiation Research, **9**(1), 58–63 (2022).

[12] E.A. Carrasco-Flores, and J.A. LaVerne, "Surface species produced in the radiolysis of zirconia nanoparticles," J. Chem. Phys. **127**, 234703 (2007). https://doi.org/10.1063/1.2806164

[13] O. Roth, B. Dahlgren, and J.A. La Verne, "Radiolysis of Water on ZrO_2 Nanoparticles," J. Phys. Chem. C, **116**, 17619-17624 (2012). https://doi.org/10.1021/jp304237c

[14] A.R. Puigdollers, F. Illas, and G. Pacchioni, "Reduction of Hydrogenated ZrO_2 Nanoparticles by Water Desorption," ACS Omega, **2**, 3878-3885 (2017). https://doi.org/10.1021/acsomega.7b00799

[15] S. Le Caër, P. Rotureau, F. Brunet, T. Charpentier, G. Blain, J.P. Renault, and J.-C. Mialocq, "Radiolysis of Confined Water: Hydrogen Production at a High Dose Rate," Chem. Phys. Chem. **6**, 2585-2596 (2005). https://doi.org/10.1002/cphc.200500185

[16] J.A. LaVerne, and S.M. Pimblott, "New mechanism for H_2 formation in Water," J. Phys. Chem. B, **104**, 9820-9822 (2000). https://doi.org/10.1021/jp002893n

[17] O.D. Roth, and J.A. LaVerne, "Radiolysis of Water on ZrO_2 Nanoparticles," J. Phys. Chem. C, **116**, 17619-17624 (2012). https://doi.org/10.1021/jp304237c

[18] J. McGrady, S. Yamashita, A. Kimura, S. Kano, H. Yang, Z. Duan, T. Sato, et al., "γ-radiation effects on metal oxide particles and their wetted surfaces," Journal of Nuclear Science and Technology, **57**, 463-471 (2019). https://doi.org/10.1080/00223131.2019.1691075

[19] S. Le Caër, "Water Radiolysis: Influence of Oxide Surfaces on H_2 Production under Ionizing Radiation," Water, **3**, 235-253 (2011). https://doi.org/10.3390/w3010235

[20] H. Ouerdane, B. Gervais, H. Zhou, M. Beuve, and J.-Ph. Renault, "Radiolysis of Water Confined in Porous Silica: A Simulation Study of the Physicochemical Yelds," J. Phys. Chem. C, **114**, 12667-12674 (2010). https://doi.org/10.1021/jp103127j

[21] T. Miyazaki, Y. Kuroda, and K. Marishige, "Interaction of the surface of BeO with water: in connection with the two – Deminsional Condensation of water," J. Colloid and Interface Sci. **106**(1), 154-160 (1985). https://doi.org/10.1016/0021-9797(85)90391-1

[22] A. Hofmann, S.J. Clark, M. Oppel, and I. Hahndorf, "Hydrogen adsorption on the tetragonal ZrO_2(101) surface: a theoretical study of an important catalytic reactant," Phys. Chem. Chem. Phys, **4**, 3500-3508 (2002). https://doi.org/10.1039/B202330J

[23] Y. Kumagai, A. Kimura, M. Taguchi, R. Nagaishi, I. Yamagishi, and T. Kimura, "Hydrogen production in gamma radiolysis of the mixture of mordenite and seawater," Journal of Nuclear Science and Technology, **50**(2), 130-138 (2013). https://doi.org/10.1080/00223131.2013.757453

[24] V F. Crumière, J. Vandenborre, R. Essehli, G. Blain, J. Barbet, and M. Fattahi, "LET effects on the hydrogen production induced by the radiolysis of pure water," Radiation Physics and Chemistry, **82**, 74-79 (2013). https://doi.org/10.1016/j.radphyschem.2012.07.010

[25] P. Rotureau, J.P. Renault, B. Lebeau, J. Patarin, and J.-C. Mialocq, "Radiolysis of Confined Water: Molecular Hydrogen Formation," Chem. Phys. Chem. **6**(7), 1316-1323 (2005). https://doi.org/10.1002/cphc.200500042

[26] M.E. Dzaugis, A.J. Spivack, and S.D. Hondt, "A quantitative model of water radiolysis and chemical production rates near radionuclide-containing solids," Radiation Physics and Chemistry, **115**, 127-134 (2015). https://doi.org/10.1016/j.radphyschem.2015.06.011

[27] J.A. LaVerne, and L. Tandon, "H_2 Production in the Radiolysis of Water on UO_2 and Other Oxides," J. Phys. Chem. B, **107**(49), 13623–13628 (2003). https://doi.org/10.1021/jp035381s

[28] S. Ismail-Beigi, and S.G. Louie, "Self-Trapped Excitons in Silicon Dioxide: Mechanism and Properties," Phys. Rev. Lett, **95**, 156401 (2005). https://doi.org/10.1103/PhysRevLett.95.156401

[29] S.C. Reiff, and J.A. LaVerne, "Radiolysis of water with aluminum oxide surfaces," J. Radiation Physics and Chemistry, **131**, 46-50 (2017). https://doi.org/10.1016/j.radphyschem.2016.10.022

[30] N.M. Dimitrijevic, A. Henglein, and D. Meisel, "Charge separation across the silica nanoparticle," Water Interface, J. Phys. Chem. B, **103**(34), 7073–7076 (1999). https://doi.org/10.1021/jp991378q

[31] T. Schatz, A.R. Cook, and D. Meisel, "Capture of charge carries at the silica nanoparticle-water interface," J. Phys. Chem. B, **103**, 10209-10219 (1999).

[32] D. Meisel, *Radiation effects in nanoparticle suspensions. Nanoscale materials*, 1st edition (Springer, Berlin, 2004).

[33] S. Isamel-Beigi, and S.G. Louie, "Self-trapped excitons in silicon-dioxide: Mechanism and Properties," Phys. Rev. Lett. **95**, 156401 (2005). https://doi.org/10.1103/PhysRevLett.95.156401

[34] V.P. Kovalev, *Secondary electrons*, (Energoatomizdat, Moscow, 1987). (in Russian)

[35] Y.D. Jafarov, S.M. Bashirova, and S.M. Aliyev, "Dependence of the yield of molecular hydrogen obtained from radiation-heterogeneous decomposition of water on particle size of silica and filling rate of particle surface of water in Si+H$_2$O system by the influence of gamma-quanta," Journal of Radiation Researches, **4**(2),16-23 (2017).

МЕХАНІЗМ ПРОДУКЦІЇ ВОДНЮ В ПРОЦЕСАХ РАДІАЦІЙНОГО ГЕТЕРОГЕННОГО РОЗШПИЛЕННЯ ВОДИ ЗА НАЯВНОСТЮ НАНО-МЕТАЛУ ТА НАНО-MeO

Аділь Гарібов[a], Ядігар Джафаров[a], Гюнель Іманова[a,b,c], Теймур Агаєв[a], Севіндж Баширова[d], Анар Алієв[a]

[a] Інститут радіаційних проблем Міністерства науки і освіти Азербайджанської Республіки, вул. Б. Вагабзаде, 9, AZ1143, Баку, Азербайджан

[b] Науково-дослідний центр UNEC для сталого розвитку та Creen-економіки імені Нізамі Гянджеві, Азербайджанський державний економічний університет (UNEC), вул. Істиглаліят, 6, Баку 1001, Азербайджан

[c] Хазарський університет, факультет фізики та електроніки, вул. 41 Махсаті, AZ1096, Баку, Азербайджан

[d] МІ НАСА космічних досліджень природних ресурсів, AZ 1115, Баку, С.С. Ахунзаде, 1, Азербайджан

У дослідженні визначено оптимальні значення відношення відстані між частинками до розміру частинок при радіаційно-гетерогенному радіолізі води в системах нано-Me та нано-MeO. У цих системах розглядався вплив густини води та температури системи на радіаційно-хімічне виділення молекулярного водню, отриманого при термічному та радіаційно-термічному розкладанні води. У статті також визначено вплив розмірів частинок і типу взятої проби на радіаційно-хімічний вихід молекулярного водню. У представленій статті досліджено зміну молекулярного водню залежно від адсорбованої води та каталізатора. Так, у разі суспензії наноцирконію у воді енергія електронів, що вилітають з металу, повністю передається молекулам води, що призводить до збільшення виходу водню. При радіолізі води в присутності нанометалів передача енергії може здійснюватися в основному за участю випущених електронів. Отже, при радіолізі води в суспензії з n-Zr вихід водню збільшується в 5,4 рази порівняно з процесами радіолізу в адсорбованому стані. Однак при радіаційно-гетерогенних процесах отримання водню з води, що контактує з металевими системами, необхідно враховувати, що в результаті цих процесів відбувається поверхневе окислення і через певний час системи перетворюються на n-Me-MeO+H$_2$O$_{liq}$ системи. Для нанорозмірних оксидних сполук довжина вільного пробігу вторинних електронів, що утворюються в результаті первинних процесів взаємодії квантів з атомами, співмірна з розмірами частинок нанооксидів ($\lambda \approx$ R$_{(H-оксиди)}$). Далі ці електрони взаємодіють з електронною підсистемою кремнію. Для нанокаталізаторів довжина вільного пробігу вторинних і наступних поколінь електронів перевищує розмір частинок каталізатора (R$_{cat} \leq$ 100 нм). Зазвичай їх енергії достатньо для проведення самостійних радіолітичних процесів у контактному середовищі каталізатора.

Ключові слова: *нано-Me та нано-MeO оксиди; γ-випромінювання; утворення молекулярного водню; радіоліз; друга електронна хмара*

SPECTRA OF ULTRASOUND DOPPLER RESPONSE USING PLANE-WAVE COMPOUNDING TECHNIQUE

Evgen A. Barannik, Mykhailo O. Hrytsenko*

Department of Medical Physics and Biomedical Nanotechnologies, V.N. Karazin Kharkiv National University
4 Svobody Sq., 61022, Kharkiv, Ukraine
*Corresponding Author e-mail: mykhailo.hrytsenko@student.karazin.ua

Within the framework of a simple model of the sensitivity function, the Doppler spectra are considered for different ways of generating response signals using plane wave compounding. A Doppler spectrum is obtained for coherent compounding of signals received at different steering angles of waves during their period of changing. Compared to traditional diagnostic systems, the Doppler spectrum width is increased only by limiting the duration of the signals. There is no additional increase in the spectrum width if the compound signals are formed by adding with cyclic permutation, in which signals from each new wave angle are compounded. When a Doppler signal is formed directly from Doppler signals at different steering angles, the spectral width increases both in comparison with the traditional method of sensing with stationary focused ultrasound fields and with the case of coherent signal compouding. The obtained increase in the spectral width has an intrinsic physical meaning. The increase in width is connected with a dynamic change in the Doppler angle, which increases the interval of apparent projections of the velocities of motion of inhomogeneities along the direction of transmitting of a plane wave without inclination.

Keywords: *Ultrasound; Doppler spectrum; Plane wave compounding; Synthetic aperture method; Spectral dispersion; Projection of the inhomogeneity velocity*
PACS: 43.28.Py, 43.35.Yb, 43.60.-c, 87.63.D-, 87.63.dk

INTRODUCTION

As it is known in traditional ultrasound medical diagnostic systems, focused waves have a focus on one strictly defined depth in the patient's body [1,2]. This approach has a number of disadvantages connected with resolution limitations outside the defined focal area and the inability to obtain sufficient data to accurately determine the flow of biological fluids and the structure of the body's subcutaneous biological structures, including tendons, muscles, blood vessels and internal organs. The image is acquired sequentially along one line, which imposes a strict limit on the frame rate, which is important in a real-time imaging system. A low frame rate means that fast-moving structures (e.g. heart valves) are difficult to image continuously in time. The general idea behind synthetic aperture in ultrasound diagnostics is that the ultrasound response is recorded by all elements of the ultrasound transducer for a sequence of different emitted wave fields. The response for each point in space is then identified as a complex value for the different fields, which is coherently summed, resulting in a high-resolution image (with focus) at each point in space [3].

The synthetic aperture method requires a lot of calculations, and as a result, such equipment is expensive [4, 5]. There is a demand for methods that can be integrated directly into existing commercial ultrasound devices [6, 7]. Moreover, it is necessary to optimize the parameters that characterize the quality of images obtained using aperture synthesis technology [8-15]. The method has been significantly developed with the advent of ultrasound scanners that use parallel signal processing to generate images. Along with the use of multilinear data processing in ultrasound diagnostics, it became possible to visualize vital blood flows, which, in comparison with conventional Doppler methods, allowed for the development of methods to determine the velocity vector [16-18], simultaneously visualize blood flow and vessel wall motion in arteries, visualize low-velocity blood flow in small vessels, and perform three-dimensional imaging for all Doppler techniques (color Doppler, 3-D ultrafast energy Doppler, pulsed Doppler, etc.) [19-21, 8].The effect of the movement of ultrasonic scatterers on the correlation function of the Doppler signal and the ways to correct the effect of this impact were investigated in [22, 23]. Using the synthetic aperture method, it is possible to implement imaging methods that use plane waves with different propagation directions or wave fronts with different spatial configurations [24-26,9,12]. This made it possible to generate full-field tissue displacement images and Doppler images with high frame rate and high resolution for various medical applications in modern shear-wave elastography, Doppler ultrasound [27,20,11], etc. The development of methods for coherent compounding of ultrasound response signals has improved spectral estimates in spectral Doppler compared to traditional Doppler techniques. This makes it possible to estimate local pulse wave velocities, visualize contrast agents, etc. [28-30]. There are a number of experimental works on new techniques within the plane wave compounding method that allow to improve image quality in terms of lateral resolution and contrast-to-noise ratio for two-dimensional images [31,32] and for Doppler technique [33].

The width of the Doppler spectra plays an important role for the accuracy of all pulse Doppler methods. The reason for the increase in the spectrum width and its distortion can be: high gradients of the velocity of inhomogeneities, in

---

particular, red blood cells, inside the measuring volume, even in laminar blood flows; turbulence of the blood flow, in which the projection of the velocity can change not only the value but also its sign; fluid movement with acceleration, which increases the range of velocities; the influence of speckle noise. Earlier, the model of the effect of inhomogeneity velocity gradients was considered in [39]. Some models of the effect of blood flow turbulence, diffusion of inhomogeneities and dependence of spectral width on the correlation radius of inhomogeneities were proposed in [34], and the effect of accelerated motion of inhomogeneities was considered in [36]. The aim of this paper is to develop and analyze the Doppler spectra and its width using the synthetic aperture technology, namely, plane wave compounding with different methods of forming Doppler response signals.

THEORETICAL MODEL

Within the framework of the continuum model of the biological medium, the low-frequency Doppler signal $e_d(t)$ under the pulsed mode of ultrasound wave emission [34,35] depends on the motion of the density inhomogeneities $\rho(\vec{r}, t)$ and compressibility $\beta(\vec{r}, t)$. It also depends on the complex sensitivity function $G_p'(\vec{r}, t)$ over the emission-receiving field. For the synthetic aperture technology, this value is time-dependent and is determined by the duration of the sensing pulses, the complex amplitude of the transmitted field $G_t'(\vec{r}, t)$, with its deviation from a plane wave without inclination and by the complex receiver sensitivity function $G_r'(\vec{r})$:

$$G_p'(\vec{r}) = G_t(\vec{r}, t)G_r(\vec{r})b\left(T_1 - \frac{x'}{c_0} - \frac{x'\cos\Phi(t)}{c_0}\right), \tag{1}$$

where x' is the distance along the transducer axis from its emitting surface to the origin of the x, y, z coordinate system with the beginning at the sensing depth l_0, as shown in Fig. 1, $b(t)$ is the envelope of the probing pulse, T_1 is the delay in the strobing time relative to each moment of the pulse emission, which determines the probing depth, c_0 is the propagation velocity of the reflected wave beam front along the x' axis, $c_0/\cos\Phi(t)$ is the propagation velocity along the x' axis of the incident plane wave front with the deflection angle $\Phi(t)$ of the wave vector. In the most general case of the synthetic aperture technology, the sensitivity function to scattered waves may also depend on time t.
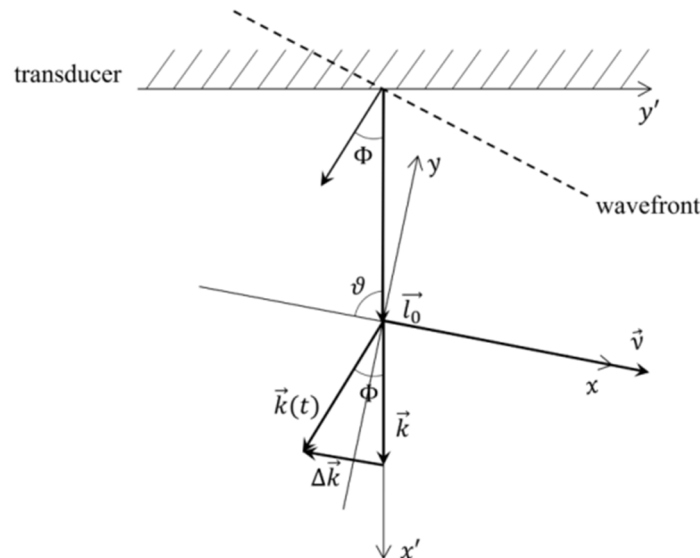
Figure 1. The position of the unshaded coordinate system connected with the measuring volume relative to the ultrasonic transducer and the angle of deflection of the wave vector $\vec{k}(t)$ of the current wave from the wave vector $\vec{k}$ of the wave without inclination

Taking into account the deflection of waves from a plane wave without inclination, the complex amplitude of incident plane waves is given by

$$G_t(\vec{r}, t) = e^{i\{\vec{k}(t) - \vec{k}\}\vec{r}}g(z),$$

where $g(z)$ is the distribution of the ultrasonic transmitted field along the z-axis perpendicular to the (x, y) plane shown in Fig. 1. The time dependence is caused by small deviations of the wave vector from the wave vector of plane waves without inclination. Earlier [35], in this approximation, the Fourier image of the function $G_t(\vec{r}, t)$ was found with a linear dependence on time of the wave vector deflection angle $\Phi(t) = \Omega t$.

Most conventional pulse systems use sequential emission of pulses characterized by the same spatial geometry and configuration of wavefronts. This means that in this case, the functions $G_t'(\vec{r})$ and $G_r'(\vec{r})$ are time-independent, and the Doppler spectrum has the form [34]:

$$S(\omega_p) = \frac{k^4}{(2\pi)^3}\int d\vec{q}\, C(\vec{q}, \omega_p)\left|G(\vec{q} + 2\vec{k})\right|^2 \tag{2}$$

where $C(\vec{q}, \omega_p)$ is the space-time Fourier image of the function of the inhomogeneity fluctuation correlator

$$C(\vec{r}_1 - \vec{r}_0, \tau) = \nu \left\langle (\tilde{\beta} - \tilde{\rho})^2 \right\rangle \delta(\vec{r}_1 - \vec{r}_0 - \tau\vec{V}),$$

ν is a constant determined by the radius of correlation of the inhomogeneities and $\vec{V}$ is the velocity of the dimensionless inhomogeneities $\tilde{\beta}$ and $\tilde{\rho}$.

In the case of the synthetic aperture technology, it is possible to generate an ultrasonic Doppler response signal directly from discrete signal values from different sequential angles of revolution of the wave vector. For a given range of angles Φ, the ultrasonic Doppler response signals are registered for a limited period of time, after which the registration procedure is repeated periodically. Then the power spectrum of the Doppler signal is equal to [36, 37]

$$S(\omega_p) = \frac{k^4}{(2\pi)^3} \sum_{j=-\infty}^{\infty} \int d\vec{q} \, C(\vec{q}, \omega_p - \omega_j) \left| G(\vec{q} + 2\vec{k}, \omega_j) \right|^2. \tag{3}$$

where $\omega_p = 2\pi p/T$ is the Fourier expansion variable, and T is the period of repeating a given set of deflection angles.

There is another way to generate an ultrasonic Doppler signal. Discrete values are obtained by coherent compounding of complex signal values at different angles of rotation for the entire period of angle change T. Then the spectrum can be written as follows [37]:

$$S(\omega_p) = T^2 \frac{k^4}{(2\pi)^3} \int d\vec{q} \, C(\vec{q}, \omega_p) \left| G(\vec{q} + 2\vec{k}, 0) \right|^2 \tag{4}$$

$$G(\vec{q} + 2\vec{k}, 0) = \frac{1}{T} \int_{-\frac{T}{2}}^{\frac{T}{2}} G(\vec{q} + 2\vec{k}, t + t') dt'.$$

Within the framework of the model described in [35-37], it follows from (4) that in this case the sensitivity function is independent of frequency similar to (2).

RESULTS

To reduce the effect of the rectangular window spectrum (which for periodic functions is formed by limiting the integration to $\pm T/2$ limits) on the calculated spectra weight windows are used. In particular, the Gaussian weighting window, which has the following form.

$$W(\tau) = \exp(-\tau^2/T_W^2), \tag{5}$$

where $2T_W \cong T$ is the length of the window along the e^{-1} level. Taking into account the weighting window (5), the integrals over time τ converge well at $\tau \to \pm\infty$. This makes it possible to extend the integration limits to $\pm\infty$ when calculating the spectra. In this approximation, the spectrum of the correlation function of inhomogeneity fluctuations takes the form:

$$C(\vec{q}, \omega_p) = \nu \left\langle (\tilde{\beta} - \tilde{\rho})^2 \right\rangle \sqrt{\pi T_W^2} e^{-\frac{T_W^2(\vec{q}\vec{V} - \omega_p)^2}{4}}. \tag{6}$$

Using (5), it is possible to obtain a sensitivity function with completely suppressed side lobes, unlike in [35]:

$$G_t(\vec{r}, \omega_j) = T^{-1} g(z) \sqrt{\pi T_W^2} e^{-\frac{T_W^2(k\Omega y' + \omega_j)^2}{4}}. \tag{7}$$

The resulting expressions (6) and (7) allow us to write the spectrum (3) in the form:

$$S(\omega_p) = \nu \left\langle (\tilde{\beta} - \tilde{\rho})^2 \right\rangle T^{-1} \sqrt{\pi T_W^2} \frac{k^4}{(2\pi)^3} \sum_{j=-\infty}^{\infty} \int d\vec{q} \, e^{-\frac{T_W^2(q_x V - \omega_p + \omega_j)^2}{4}} \left| G(q_x + 2k\cos\vartheta, q_y - 2k\sin\vartheta, q_z, \omega_j) \right|^2. \tag{8}$$

In expression (8), only the sensitivity function depends on the variables q_y and q_z. Therefore, the inverse Fourier transform can be used to change the function variables to the y, z and simplify the expression. The expression for the contribution of the individual flow lines of the medium to the spectrum can then be written as

$$S(\omega_p, y, z) = \nu \left\langle (\tilde{\beta} - \tilde{\rho})^2 \right\rangle k^4 T^{-1} \sqrt{\pi T_W^2} \sum_{j=-\infty}^{\infty} \int \frac{dq_x}{2\pi} \left| G(q_x + 2k\cos\vartheta, y, z, \omega_j) \right|^2 e^{-\frac{T_W^2(q_x V - \omega_p + \omega_j)^2}{4}}. \tag{9}$$

The flow lines differ in the y and z coordinates and in sum give the full Doppler spectrum. This makes it possible to separate the integration over coordinates from the integration over the wave vector component and summation over frequency.

For further comparison of the spectra, we first obtain an estimate of the spectral distribution for the traditional method of pulsed Doppler sensing. To do this, we will choose the sensitivity function (1) in its simplest form:

$$G(\vec{r}) = exp\left\{-2\frac{y'^2 + z^2 + (x' - l_0)^2}{a^2}\right\} = exp\left\{-2\frac{\vec{r}^2}{a^2}\right\}. \tag{10}$$

In Equation (10), it is assumed that the waves are plane. That is, we neglect the curvature of the wave fronts, which always occurs due to the focusing and diffraction of ultrasonic waves. In addition, the duration of the probing pulses is chosen such that the measured volume acquires a spherical shape. This approximation is often used to estimate the ultrasonic Doppler response spectra [38,34].

Analogously to (9), using (10), we obtain the spectrum of the Doppler response signal of the flow line in the form

$$S(\omega_p, y, z) = \nu\left\langle(\tilde{\beta} - \tilde{\rho})^2\right\rangle T^{-1} k^4 \sqrt{\pi T_W^2}\frac{\pi a^2}{2} exp\left\{-4\frac{y^2 + z^2}{a^2}\right\} \times$$

$$\times \int \frac{dq_x}{2\pi} exp\left\{-\frac{(q_x + 2k cos\vartheta)^2 a^2}{4} - \frac{T_W^2(q_x V - \omega_p)^2}{4}\right\}$$

Then the full spectrum of the Doppler signal is obtained after integration over the coordinates of the flow lines:

$$S(\omega_p) = \nu\left\langle(\tilde{\beta} - \tilde{\rho})^2\right\rangle T^{-1} k^4 \sqrt{\pi T_W^2}\frac{\pi^2 a^4}{8}\int \frac{dq_x}{2\pi} exp\left\{-\frac{(q_x + 2k cos\vartheta)^2 a^2}{4} - \frac{T_W^2(q_x V - \omega_p)^2}{4}\right\}.$$

Finally, after integration over q_x, we obtain the final formula for the Doppler spectrum:

$$S(\omega_p) = \nu\left\langle(\tilde{\beta} - \tilde{\rho})^2\right\rangle T^{-1} k^4 \frac{\pi^3 a^3}{4}\sqrt{\frac{T_W^2 a^2}{a^2 + T_W^2 V^2}} exp\left\{-\frac{T_W^2 a^2}{a^2 + T_W^2 V^2}\frac{(\omega_p - \omega_d)^2}{4}\right\}, \tag{11}$$

$$\sigma^2 = 2\frac{a^2 + T_W^2 V^2}{T_W^2 a^2} = 2\left(\frac{1}{T_W^2} + \frac{V^2}{a^2}\right), \tag{12}$$

where $\omega_d = -2kV cos\vartheta$ is the Doppler shift frequency, σ^2 is the dispersion of the Doppler frequency spectrum.

In the case of coherent accumulation of signals obtained at different sensing angles, it follows from expressions (4) and (7) that the Doppler spectrum is determined by the amplitude of the incident plane waves. So, it can be written in the following form.

$$G_t(\vec{r}, \omega_j = 0) = T^{-1}\sqrt{\pi T_W^2}e^{-\frac{1}{4}T_W^2 k^2 \Omega^2 y'^2 - \frac{z^2}{a^2}}.$$

In physical terms, synthetic aperture technologies are designed to improve resolution. Therefore, it is expediently to choose a value of the maximum angle $T_W\Omega$ of the wave vector deviation at which $\frac{1}{4}T_W^2\Omega^2 k^2 = \frac{1}{4}\Phi_{max}^2 k^2 = a^{-2}$. In this case, the resolution is not worse than resolution of traditional Doppler systems. In addition, it is possible to get transmit focusing at all points of the biological object at all depths. As a result, the full model sensitivity function can be represented in a form similar to (10)

$$G(\vec{r}, \omega_j = 0) = G_t(\vec{r}, \omega_j = 0)G_r(\vec{r})b\left(T_1 - \frac{2x'}{c_0}\right) = T^{-1}\sqrt{\pi T_W^2} exp\left(-2\frac{\vec{r}^2}{a^2}\right),$$

and the expression for the Doppler spectrum is obtained in a similar way to (11) and has the form

$$S(\omega_p) = \nu\left\langle(\tilde{\beta} - \tilde{\rho})^2\right\rangle T^{-1} T_W^2 k^4 \frac{\pi^4 a^3}{4}\sqrt{\frac{T_W^2 a^2}{a^2 + T_W^2 V^2}} exp\left\{-\frac{(\omega_p - \omega_d)^2}{2\sigma^2}\right\}. \tag{13}$$

This spectrum differs only in the higher amplitude of the spectrum due to the increased power of the Doppler response due to the coherent accumulation of signals.

For the ultrasonic Doppler response, when the signal is formed directly from the Doppler signals received at different steering angles, the full sensitivity function can be written as:

$$G(x, y, z, \omega_j) = T^{-1}\sqrt{\pi T_W^2}e^{-\frac{T_W^2(k\Omega y' + \omega_j)^2}{4}}e^{-\frac{x^2 + y^2 + 2z^2 + (x' - l_0)^2}{a^2}}.$$

As with the finding of the spectrum (13), we assume that the equality $\frac{1}{4}\Phi_{max}^2 k^2 = a^{-2}$ holds. As a result, we obtain

$$\left|G\left(q_x + 2k\cos\vartheta, y, z, \omega_j\right)\right| = T^{-1}\sqrt{\pi T_W^2} exp\sqrt{\frac{\pi a^2}{2}}\left(-\frac{1}{4}T_W^2\omega_j^2\right) \times$$

$$\times exp\left\{-\frac{2y^2 + T_W\omega_j a\cos\vartheta y + 2z^2}{a^2}\right\} \times exp\left\{-\frac{(q_x + 2k\cos\vartheta)^2 a^2 - (T_W\omega_j\sin\vartheta)^2}{8}\right\}.$$

Using expression (9), we can now find the full spectrum and write it in the form. Let's take out of the integral over the coordinate all the factors that do not depend on y, z:

$$S(\omega_p) = \nu\left\langle\left(\tilde{\beta} - \tilde{\rho}\right)^2\right\rangle k^4 T^{-3}\pi T_W^2\sqrt{\pi T_W^2}\frac{\pi a^2}{2}\sum_{j=-\infty}^{\infty} exp\left\{\frac{\sin\vartheta^2 T_W^2\omega_j^2}{4}\right\} \times$$

$$\times exp\left\{-\frac{T_W^2\omega_j^2}{2}\right\}\iint dydz\, exp\left\{-2\frac{2y^2 + T_W\omega_j a\cos\vartheta y + 2z^2}{a^2}\right\} \times$$

$$\times \int\frac{dq_x}{2\pi} exp\left\{-\frac{T_W^2(q_x V - \omega_p + \omega_j)^2}{4}\right\} exp\left\{-\frac{(q_x + 2k\cos\vartheta)^2 a^2}{4}\right\}.$$

Finally, after integration over y and z, we obtain the full Doppler spectrum for the case under consideration, which can be presented in a form similar to (11) and (13):

$$S(\omega_p) = \nu\left\langle\left(\tilde{\beta} - \tilde{\rho}\right)^2\right\rangle k^4 T^{-3}T_W^2\frac{\pi^3 a^3}{8}\sqrt{\frac{T_W^2 a^2}{a^2 + T_W^2 V^2}}\sum_{j=-\infty}^{\infty} exp\left\{-\frac{1}{4}T_W^2\omega_j^2\right\}exp\left\{-\frac{T_W^2 a^2}{a^2 + T_W^2 V^2}\frac{\left(\omega_p - \omega_d - \omega_j\right)^2}{4}\right\}$$

It is easy to see that for the component of the sum with $j = 0$ and, accordingly, with $\omega_j = 0$, this expression transforms to the spectrum of (11) and (13) with an accuracy of a numerical factor.

An estimate of the full spectrum of the Doppler response signal can now be obtained by summing over j. If the measurement period T is sufficiently long, then the frequency step $2\pi/T$ in the Fourier transform is small. This means that the sum over j can be replaced by a frequency integral according to the rule

$$\sum_{j=-\infty}^{\infty} \dots \to \frac{T}{2\pi}\int_{-\infty}^{\infty} \dots d\omega,$$

As a result, after some simple but cumbersome calculations, we come to the final expression for the ultrasonic Doppler response spectrum:

$$S(\omega_p) = \left\langle\left(\tilde{\beta} - \tilde{\rho}\right)^2\right\rangle k^4 T^{-2}T_W^2\frac{\pi^2 a^4}{8}\sqrt{\frac{\pi}{2a^2 + T_W^2 V^2}}exp\left\{-\frac{T_W^2 a^2(\omega_p - \omega_d)^2}{4(2a^2 + T_W^2 V^2)}\right\}. \tag{14}$$

The dispersion of this Doppler spectrum

$$\sigma^2 = 2\frac{2a^2 + T_W^2 V^2}{T_W^2 a^2} = 2\left(\frac{2}{T_W^2} + \frac{V^2}{a^2}\right),$$

is greater than the dispersion (12) of the spectra (11) and (13) by $\Delta\sigma^2 = 2/T_W^2$.

DISCUSSION

The considered simple physical model for the sensitivity function demonstrates that, in general, the contribution to the spectral width of the Doppler signal is made not only by the parameters of the incident and reflected ultrasonic fields, which form the sensitivity function, but also by the signal duration. The spectral characteristics of the inhomogeneity fluctuation correlator depend on the signal duration. If the width of the weighting window is large, then in the limiting case $T_W \to \infty$, the spatial spectrum of the fluctuation correlator (6) is described by the δ-function

$$C(\vec{q}, \omega) = 2\pi\nu\left\langle\left(\tilde{\beta} - \tilde{\rho}\right)^2\right\rangle\delta\left(\vec{q}\vec{V} - \omega_p\right),$$

which, when integrated over q_x, equates its value to $q_x = \omega_p/V$. In this case, the largest contribution to the width of the spectra (11), (13), and (14) will be made by the component $2V^2/a^2$, which is related to the value $\sqrt{2}a$, which, according to (10), determines the diameter of the measuring volume at the level of e^{-1}.

On the contrary, as the measuring volume increases ($a \to \infty$), the dispersion of the spectra (11) and (13) tends to $2/T_W^2$, and dispersion of the spectrum (14) to $4/T_W^2$, i.e., it is determined by the duration of the weighting window, which effectively limits the length of the Doppler signal. In this case, the spectrum of the sensitivity function becomes δ-shaped, which equals $q_x = -2k\cos\vartheta$. However, in both cases, the maximum of the Doppler spectra (11), (13) and (14) is always at the classical Doppler shift frequency ω_d. In traditional pulsed ultrasound diagnostic systems, sequential pulses with a constant spatial geometry and configuration of wavefronts are used. In this case, Doppler signals are practically unlimited in time and therefore the spectral width is the smallest possible and does not depend on T_w.

The reason for the increase in the width of the Doppler spectrum when forming a signal from Doppler signal counts obtained at different steering angles is the change in the projection of the motion velocity onto the direction of the current wave vector due to a change in the Doppler angle, as shown in Fig. 2. This situation can be interpreted as a movement with acceleration:

$$V_{x'} = V\cos\vartheta(t) = V\cos(\vartheta \mp \Phi) = V(\cos\vartheta\cos\Phi \pm \sin\vartheta\sin\Phi) \cong V\{\cos\vartheta \pm \sin\vartheta\Omega t\},$$

where the upper sign describes a situation equivalent to a uniformly accelerated motion, and the lower sign corresponds to a uniformly decelerated motion.
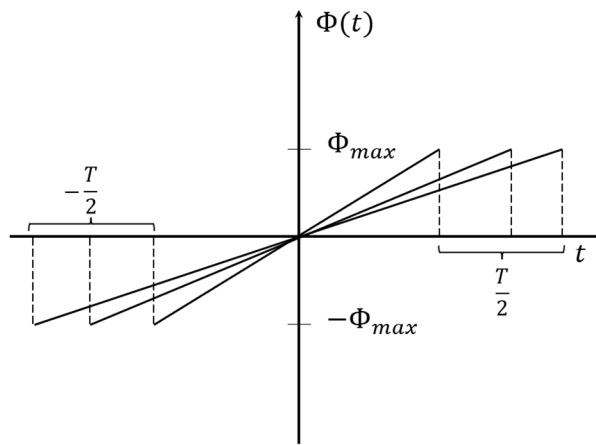
Figure 2. Model dependence of the wave vector deflection angle on time

In practice, the width of the weight window satisfies the ratio $T_w \cong T/2$. And the rate of change of the angle of view can be represented as $\Omega = 2\Phi_{max}/T$. Then the projection of the velocity on the x' axis is equal:

$$V_{x'} = V\cos\vartheta \pm V\sin\vartheta \frac{\Phi_{max}}{T_w} t.$$

Thus, the notional acceleration is inversely proportional to the time T_w. It is clear that both during acceleration and deceleration, the range of velocities during time T for a given range of angles is the same, so the width of the spectrum cannot depend on the sign of the acceleration. Because of this, in (14), compared to (13), there is a quadratic acceleration term in the form of $2/T_W^2$. From Fig. 2, it is easy to see that the larger T and, accordingly, T_w, the smaller the acceleration at a given range of angles Φ_{max}, the smaller the range of velocities and, accordingly, the additional dispersion of the Doppler frequency spectrum. Obviously, such terms can be neglected when the strong inequality $1/T_W^2 \ll V^2/a^2$ is satisfied.

Fig. 3 schematically shows the dependence of the complex ultrasonic Doppler response signal on time when the inclination of $N = 3$ transmitted plane waves is periodically repeated. If the velocity $V_{x'}$ apparently increases due to a decrease in the angle $\vartheta(t)$, then for each subsequent time interval $\Delta T = T/N = t_n - t_{n-1}$ between probings, the phase difference of the complex Doppler signals will also increase: $\Delta\varphi_n = 2k\Delta x'_n = 2kV_{x'}\Delta T$. It is this apparent increase in the range of differential phases $\Delta\varphi_n$ that leads to an increase in the spectral width (14). In accordance with (4) a compound signal can be written as follows:

$$e_c(t_n) = \sum_{m=-(N-1)/2}^{(N-1)/2} e_d(t_{n+m}), \tag{15}$$

and Fig. 3 shows that the phase difference for two consecutive compound signals e_c remains unchanged. This means that, unlike (14), there is no additional increase in the spectral width if the compound signals e_c are formed by cyclic permutation taking into account the signal at every new angle. This important circumstance means that accurate measurements of the velocity are possible not only using the compound signals of the form

$$e_c(\mathbf{n^i}) = e_d(\mathbf{n^i} - (N-1)/2) + e_d(\mathbf{n^i} - (N-3)/2) + \ldots + e_d(\mathbf{n^i}) + \ldots + e_d(\mathbf{n^i} + (N-3)/2) + e_d(\mathbf{n^i} + (N-1)/2),$$

but also, those obtained by cyclic permutation (15). This means that no time is lost in obtaining the entire set of response signals for waves with different inclinations.

Note that the results presented here are based on a linear approximation of the time dependence of the deviation of the wave vector $\Delta \vec{k}(t) = \vec{k}(t) - \vec{k}$. This means that only the projection of the vector $\Delta \vec{k}(t)$ onto the y'-axis was taken into account [35], which is small due to the small values of the angles $\Phi(t)$. At the same time, this vector also has a projection on the x' axis, which depends on the square of time.
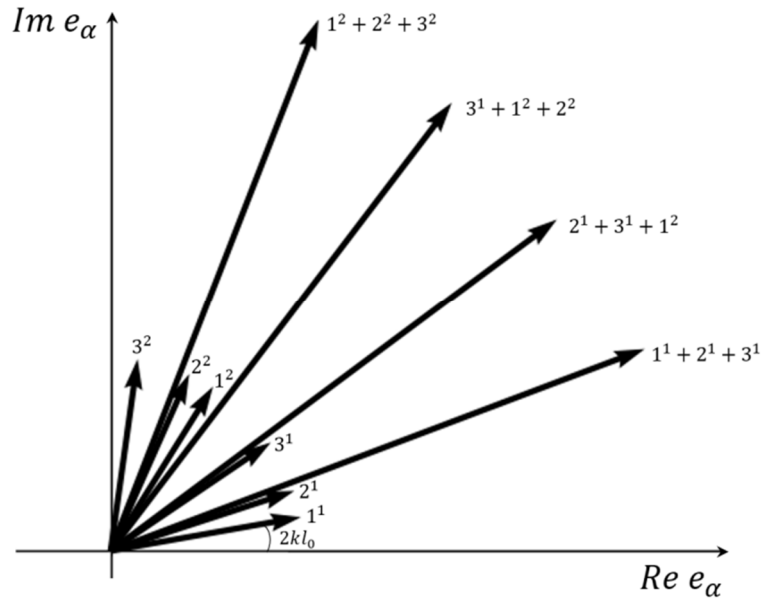
Figure 3. Non-linear time growth of the phase difference $\Delta\varphi_n$ for the complex Doppler signal and the phase difference for the compound signals when the number of different inclination angles is $N = 3$: **n^i** - Doppler response signal e_d at the **n**-th inclination angle at the **i**-th probing period; **1^1+2^1+3^1, 2^1+3^1+1^2, 3^1+1^2+2^2, 1^2+2^2+3^2**... - compound signals e_c obtained by cyclic permutation taking into account the signal from each new angle, as described by expression (15).

The importance of taking into account such quadratic terms is due to the fact that not only the spectrum of the ultrasonic Doppler response signal, but also the resolution of the system formed by the plane wave compounding technology may depend on them.

CONCLUSIONS

The technology of plane wave compounding uses a periodic repetition of the sequence of waves with different inclinations. Therefore, a periodic extension of all time-dependent physical parameters naturally occurs, which leads to a limitation of the duration of ultrasonic Doppler response signals. The influence of limiting the duration of the response signals and its anodization by weight windows on the spectral properties of the correlator of inhomogeneity motion and the spectrum of the sensitivity function of the ultrasonic system is determined. In contrast to the spectrum of the correlation function, the width of the sensitivity function spectrum depends on both the size of the measuring volume and the duration of the signals.

Within the framework of a simple model of the sensitivity function, the Doppler spectra are considered for different ways of forming response signals using plane wave compounding. A Doppler spectrum is obtained by coherent compounding of signals received at different angles of inclination of waves during their repetition period. Compared to traditional diagnostic systems, the Doppler spectrum width is increased only by limiting the duration of the signals. There is no additional increase in the spectrum width if the compound signals are formed by accumulation with cyclic permutation, in which signals from each new wave angle are added.

When forming a Doppler signal directly from Doppler signals at different inclination angles, the spectral width increases both in comparison with the traditional method of sensing with stationary focused ultrasonic fields and with the case of coherent signal accumulation. In terms of the internal physical meaning, the invented increase in the spectral width is connected with a dynamic change in the Doppler angle, which increases the interval of apparent projections of the velocities of motion of inhomogeneities along the direction of transmitting of a plane wave without inclination. The influence of nonlinear terms depending on the time of deviation of the wave vector from the wave vector without inclination requires additional study.

ORCID
Evgen A. Barannik, https://orcid.org/0000-0002-3962-9960; **Mykhailo O. Hrytsenko,** https://orcid.org/0009-0002-5670-5686

REFERENCES

[1] A. Carovac, F. Smajlovic, and D. Junuzovic, Acta Informatica Medica, **19**(3), 168 (2011). https://www.ncbi.nlm.nih.gov/pmc/articles/PMC3564184/

[2] V. Chan, and A. Perlas, "Basics of Ultrasound Imaging," in: *Atlas of Ultrasound-Guided Procedures in Interventional Pain Management*, (Springer: Berlin/Heidelberg, Germany, 2011). pp. 13-19. http://dx.doi.org/10.1007/978-1-4419-1681-5_2

[3] I. Trots, A. Nowicki, M. Lewandowski, and Y. Tasinkevych, *Synthetic Aperture Method in Ultrasound Imaging,* (IntechOpen, London, UK, 2011). http://dx.doi.org/10.5772/15986

[4] S.I. Nikolov, B.G. Tomov, and J.A. Jensen, in: *2006 Fortieth Asilomar Conference on Signals, Systems and Computers*, (Pacific Grove, CA, USA, 2006), pp. 1548-1552. https://doi.org/10.1109/ACSSC.2006.355018

[5] M. Tanter, and M. Fink, IEEE Trans. Ultrason. Ferroelectr. Freq. Control. **61**(1), 102 (2014). https://doi.org/10.1109/TUFFC.2014.6689779

[6] M.A. Lediju, G.E. Trahey, B.C. Byram and J.J. Dahl, IEEE Trans. Ultrason. Ferroelec. Freq. Contr. **58**(7), 1377 (2011). https://doi.org/10.1109/TUFFC.2011.1957

[7] Y.L. Li, and J.J. Dahl, J. Acoust. Soc. Am. **141**(3), 1582 (2017). https://doi.org/10.1121/1.4976960

[8] J. Provost, C. Papadacci, C. Demene, J. Gennisson, M. Tanter, and M. Pernot, IEEE Trans. Ultrason. Ferroelec. Freq. Contr. **62**(8), 1467 (2015). https://doi.org/10.1109/TUFFC.2015.007032

[9] G. Montaldo, M. Tanter, J. Bercoff, N. Benech, and M. Fink, IEEE Trans. Ultrason. Ferroelectr. Freq. Control. **56**(3), 489 (2009). https://doi.org/10.1109/TUFFC.2009.1067

[10] J. Jensen, M.B. Stuart, and J.A. Jensen, IEEE Trans. Ultrason. Ferroelec. Freq. Contr. **63**(11), 1922 (2016). https://doi.org/10.1109/TUFFC.2016.2591980

[11] C. Papadacci, M. Pernot, M. Couade, M. Fink, and M. Tanter, IEEE Trans. Ultrason. Ferroelec. Freq. Contr. **61**(2), 288 (2014). http://doi.org/10.1109/TUFFC.2014.6722614

[12] J. Cheng, and J.Y. Lu, IEEE Trans. Ultrason. Ferroelec. Freq. Contr. **53**(5), 880 (2006). https://doi.org/10.1109/TUFFC.2006.1632680

[13] N. Oddershede, and J.A. Jensen, IEEE Trans. Ultrason. Ferroelec. Freq. Contr. **54**(9), 1811 (2007). https://doi.org/10.1109/TUFFC.2007.465

[14] B. Denarie et al., IEEE Trans. Med. Imaging, **32**(7), 1265 (2013). https://doi.org/10.1109/TMI.2013.2255310

[15] R. Moshavegh, J. Jensen, C.A. Villagómez-Hoyos, M.B. Stuart, M.C. Hemmsen, and J.A. Jensen, in: *Proceedings of SPIE Medical Imaging*, (San Diego, California, United States, 2016) pp. 97900Z-97900Z-9. https://doi.org/10.1117/12.2216506

[16] J.A. Jensen, and N. Oddershede, IEEE Trans. Med. Imag. **25**(12), 1637(2006). https://doi.org/10.1109/TMI.2006.883087

[17] J. Udesen, F. Gran, K.L. Hansen, J.A. Jensen, C. Thomsen, and M.B. Nielsen, IEEE Trans. Ultrason. Ferroelec. Freq. Contr. **55**(8), 1729 (2008). https://doi.org/10.1109/TUFFC.2008.858

[18] S. Ricci, L. Bassi and P. Tortoli, IEEE Trans. Ultrason. Ferroelec. Freq. Contr. **61**(2), 314 (2014).https://doi.org/10.1109/TUFFC.2014.6722616

[19] Y.L. Li, and J.J. Dahl, IEEE Trans. Ultrason. Ferroelec. Freq. Contr. **62**(6), 1022 (2015). https://doi.org/10.1109/TUFFC.2014.006793

[20] J. Bercoff, G. Montaldo, T. Loupas, D. Savery, F. Meziere, M. Fink, and M. Tanter, IEEE Trans. Ultrason. Ferroelec. Freq. Contr. **58**(1), 134 (2011).https://doi.org/10.1109/TUFFC.2011.1780

[21] Y.L. Li, D. Hyun, L. Abou-Elkacem, J. K. Willmann, J.J. Dahl, IEEE Trans. Ultrason. Ferroelec. Freq. Contr. **63**(11), 1878 (2016). https://doi.org/10.1109/TUFFC.2016.2616112

[22] D. Hyun, and J.J. Dahl, J. Acoust. Soc. Am. **147**(3), 1323 (2020). https://doi.org/10.1121/10.0000809

[23] I.K. Ekroll, M.M. Voormolen, O.K.-V. Standal, J.M. Rau, and L. Lovstakken, IEEE Trans. Ultrason. Ferroelec. Freq. Contr. **62**(9), 1634 (2015). https://doi.org/10.1109/TUFFC.2015.007010

[24] J.A. Jensen, S.I. Nikolov, K.L. Gammelmark, and M.H. Pedersen, Ultrasonics, **44**(1), e5 (2006). https://doi.org/10.1016/j.ultras.2006.07.017

[25] M. Tanter, J. Bercoff, L. Sandrin, and M. Fink, IEEE Trans. Ultrason. Ferroelectr.Freq. Contr. **49**(10), 1363 (2002). https://doi.org/10.1109/TUFFC.2002.1041078

[26] J.-l. Gennisson, et al., IEEE Trans. Ultrason. Ferroelec. Freq. Contr. **62**(6), 1059 (2015). https://doi.org/10.1109/TUFFC.2014.006936

[27] J. Bercoff, M. Tanter, and M. Fink, IEEE Trans. Ultrason. Ferroelec. Freq. Contr. **51**(4), 396 (2004). https://doi.org/10.1109/TUFFC.2004.1295425

[28] H. Hasegawa, and H. Kanai, IEEE Trans. Ultrason. Ferroelec. Freq. Contr. **55**(12), 2626 (2008). https://doi.org/10.1109/TUFFC.2008.978

[29] J. Vappou, J. Luo, and E.E. Konofagou, Am. J. Hypertens. **23**(4), 393 (2010). https://doi.org/10.1038/ajh.2009.272

[30] O. Couture, M. Fink, and M. Tanter, IEEE Trans. Ultrason. Ferroelec. Freq. Contr. **59**(12), 2676 (2012). https://doi.org/10.1109/TUFFC.2012.2508

[31] C. Zheng, Q. Zha, L. Zhang, and H. Peng, IEEE Access, **6**, 495 (2018). https://doi.org/10.1109/ACCESS.2017.2768387

[32] Y.M. Benane, et al., in: 2017 *IEEE International Ultrasonics Symposium (IUS)*, (Washington, DC, USA, 2017). pp. 1-4. https://doi.org/10.1109/ULTSYM.2017.8091880

[33] C.-C. Shen, and Y.-C. Chu, Sensors, **21**, 4856 (2021). https://doi.org/10.3390/s21144856

[34] I.V. Skresanova, and E.A. Barannik, Ultrasonics, **52**(5), 676 (2012). https://doi.org/10.1016/j.ultras.2012.01.014

[35] I.V. Sheina, and E.A. Barannik, East Eur. J. Physics, (1), 116 (2022). https://doi.org/10.26565/2312-4334-2022-1-16

[36] E.A. Barannik, and O.S. Matchenko, East Eur. J. Phys. **3**(2) 61 (2016). https://doi.org/10.26565/2312-4334-2016-2-08 (in Russian)

[37] I.V. Sheina, O.B. Kiselov, and E.A. Barannik, East Eur. J. Phys. (4), 5 (2020). https://doi.org/10.26565/2312-4334-2020-4-01

[38] C.A.C. Bastos, P.J. Fish, R. Steel, and F. Vaz, Ultrasonics, **37**(9), 623–632 (2000). https://doi.org/10.1016/S0041-624X(00)00004-4

[39] E.A. Barannik, Acoust. Phys. **43**(4), 387 (1997). http://www.akzh.ru/pdf/1997_4_453-457.pdf. (in Russian)

СПЕКТРИ СИГНАЛІВ УЛЬТРАЗВУКОВОГО ДОППЛЕРІВСЬКОГО ВІДГУКУ ПРИ ВИКОРИСТАННІ ТЕХНОЛОГІЇ КОМПАУНДИНГА ПЛАСКИХ ХВИЛЬ

Євген О. Баранник, Михайло О. Гриценко

Кафедра Медичної Фізики та Біомедичних Нанотехнологій, Харківський Національний університет ім. В.Н. Каразіна, 61022, Україна, м. Харків, м. Свободи, 4

В межах простої моделі функції чутливості розглянуті доплерівські спектри при різних способах формування сигналів відгуку з використанням компаундингу пласких хвиль. Винайдений доплерівський спектр при когерентному компаундингу сигналів, отриманих при різних кутах нахилу хвиль на протязі періоду їх повторення. У порівнянні з традиційними діагностичними системами збільшення ширини доплерівського спектру відбувається тільки за рахунок обмеження тривалості сигналів. Додаткове збільшення ширини спектру відсутнє, якщо компаундні сигнали формуються шляхом накопичення з циклічною перестановкою, при якій додаються сигнали від кожного нового кута нахилу хвиль. При формуванні доплерівського сигналу безпосередньо з доплерівських сигналів при різних кутах нахилу відбувається збільшення ширини спектру як у порівнянні з традиційним методом зондування стаціонарними сфокусованими ультразвуковими полями, так і з випадком когерентного накопичення сигналів. За внутрішнім фізичним змістом винайдене збільшення ширини спектру пов'язане з динамічною зміною доплерівського кута, яке збільшує інтервал позірних проекцій швидкостей руху неоднорідностей вздовж напрямку випромінювання пласкої хвилі без нахилу.

Ключові слова: *ультразвук; доплерівський спектр; метод синтезованої апертури; компаудинг пласких хвиль; дисперсія спектру; швидкість руху неоднорідностей*

MODELING THE TEMPERATURE DEPENDENCE OF SHUBNIKOV-DE HAAS OSCILLATIONS IN LIGHT-INDUCED NANOSTRUCTURED SEMICONDUCTORS

Ulugbek I. Erkaboev*, Rustamjon G. Rakhimov, Jasurbek I. Mirzaev,
Nozimjon A. Sayidov, Ulugbek M. Negmatov
Namangan Institute of Engineering and Technology, 160115, Namangan, Uzbekistan
Corresponding Author e-mail: erkaboev1983@gmail.com

In this work, the influence of light on the temperature dependence of transverse magnetoresistance oscillations is studied. A generalized mathematical expression that calculates the temperature and light dependence of the quasi-Fermi levels of small-scale p-type semiconductor structures in a quantizing magnetic field is derived. New analytical expressions have been found to represent the temperature dependence of transverse differential magnetoresistance oscillations in dark and light situations, taking into account the effect of light on the oscillations of the Fermi energy of small-scale semiconductor structures. A mathematical model has been developed that determines the light dependence of the second-order derivative of the transverse magnetoresistance oscillations of p-type semiconductors with quantum wells by magnetic field induction. A new theory is proposed, which explains the reasons for the significant shift of the differential magnetoresistance oscillations along the vertical axis measured in the experiment for dark and light conditions.
Keywords: *Semiconductor; Heterostructure; Oscillation; Magnetoresistance; Quantum well*
PACS: 73.63.Hs, 73.21.Fg, 73.21.−b

INTRODUCTION

Currently, the fundamental physical parameters of several new small-scale materials, including semiconductors and crystals, are being studied. Among them are thin films, nanotubes and two-dimensional (2D) structures [1-10]. In particular, quantum oscillation effects under the influence of a magnetic field and electromagnetic waves (light) have been observed in several new classes of narrow band quantum well heterostructures, for example, oscillations of transverse and longitudinal magnetoresistance, Shubnikov-de Haas oscillations and quantum Hall effects [11-20]. In works [21-23], the effect of temperature dependence of magnetoresistance oscillations, magnetic susceptibility oscillations, and quantum Hall effects in bulk and nano-scale semiconductor structures on external factors was investigated. In particular, a theory was developed based on the exact mathematical model of experimental results of quantum oscillation effects for bulk semiconductor materials as a function of temperature [24-26]. However, the effect of light on magnetoresistance oscillations for materials with quantum well heterostructures has not been studied in these works. In these works [13, 27, 28-34], the effect of light on the magnetoresistance oscillations of heterostructures with narrow band quantum wells was experimentally applied. That is, it was observed that magnetoresistance oscillations under the influence of light significantly shift compared to darkness. Even the dependence of these quantum oscillation effects on the frequency of light has been studied at different low temperatures. However, in these works, the reason why the experimental results (oscillation amplitudes) are fundamentally different in light and darkness has not been shown, that is, its perfect theory has not been developed.

The main aim of this work is to study the effect of light on the temperature dependence of transverse magnetoresistance oscillations in heterostructured semiconductors with p-type quantum wells.

MODEL
Calculation of the Influence of Light on Fermi Level Oscillations in Low-Dimensional Semiconductors in a Quantizing Magnetic Field

In quantum well heterostructures in a strong magnetic field, the continuous energy spectrum of free charge carriers becomes discrete Landau levels. As a result, the Landau levels in the conductivity field begin to be filled with free electrons, starting from the lower energy, based on the Pauli principle, that is, the distribution of free electrons by energy occurs. Increasing Landau levels filled with free electrons causes changes in the quantized Fermi level. This, of course, has a strong effect on the oscillation process of the transverse magnetoresistance. It follows that the light-induced shift of transverse electrical conductivity (or magnetoresistance) oscillations is explained by the appearance of quantized Fermi quasi-levels. The dependence of Fermi energy levels on temperature, magnetic field and concentration for 2D and 3D semiconductor materials has been thoroughly studied both theoretically and practically in several literatures. However, the dependence of Fermi quasi-levels on light in semiconductors with quantum wells under the influence of a quantizing magnetic field has not been considered at all.

It is known that the quantized Fermi level in a semiconductor with a quantum well in the state of thermodynamic equilibrium under the influence of a quantizing magnetic field, that is, in the absence of illumination, at constant low temperatures, is determined by the concentration of equilibrium charge carriers in the conduction and valence zones. However, it is required to know the number of charge carriers that fill the Landau levels in the allowed zones with the illumination of the quantum well heterostructure. For this, it is necessary to use the Fermi-Dirac distribution function. Let the probability of a free electron being in a state with energy E in the conduction zone of a quantum well in a strong magnetic field be equal to $f_0(E,\mu,T)$.

In that case, the number of charge carriers on a unit surface whose energy is in the range from E to $E+dE$ is equal to the following:

$$dn = f_0(E,\mu,T)N_s^{2d}(E,B)dE \tag{1}$$

Here, $f_0(E,\mu,T) = \dfrac{1}{e^{\frac{E-\mu}{kT}}+1}$ is the Fermi-Dirac distribution function, μ is the Fermi energy, $N_s^{2d}(E,B)$ is the energy density of states of the conduction band of the quantum coil in the quantizing magnetic field. B – magnetic field induction.

Then, if we divide expression (1) by $N_s^{2d}(E,B)dE$:

$$\frac{1}{e^{\frac{E-\mu}{kT}}+1} = \frac{1}{N_s^{2d}(E,B)}\frac{dn}{dE} \tag{2}$$

We separately define the exponential expression given in (2):

$$e^{\frac{E-\mu}{kT}} = \frac{N_s^{2d}(E,B)}{\dfrac{dn}{dE}} - 1 \tag{3}$$

We determine the Fermi energy μ by taking the natural logarithm of both sides of the expression (3):

$$e^{\frac{E-\mu}{kT}} = \frac{N_s^{2d}(E,B)}{\dfrac{dn}{dE}} - 1 \tag{4}$$

$$\mu = E - kT\ln\left[\frac{N_s^{2d}(E,B)}{\dfrac{dn}{dE}} - 1\right] \tag{5}$$

In two-dimensional semiconductors under the influence of a quantifying magnetic field, we convert $\dfrac{dn}{dE}$ to the following expression for the smallest energetic levels, according to the definition of the derivative:

$$\frac{dn}{dE} = \lim_{E\to 0}\frac{\Delta n}{\Delta E} = \frac{n_2 - n_1}{E_2 - E_1} = \frac{\Delta n}{\hbar\omega_c} \tag{6}$$

In that case, using (6) and (5) can be reduced to the following form:

$$\mu = E - kT\ln\left[\frac{N_s^{2d}(E,B)}{\dfrac{\Delta n}{\hbar\omega_c}} - 1\right] \tag{7}$$

As can be seen from expression (7), the Fermi energy of two-dimensional materials depends on temperature, energy, density of two-dimensional energy states, concentration of charge carriers, and magnetic field induction.

However, often in non-equilibrium conditions, for example, when small-scale semiconductors are illuminated with light, the concentration of free electrons or holes in their allowed zones begins to change. If there is darkness (in the absence of light), the Fermi level of small semiconductors depends only on the concentration of equilibrium charge carriers in the conduction or valence band. However, when the small semiconductor is exposed to light, the concentration of charge carriers increases. It depends on the intensity of the light. From this, it is observed that the Fermi level moves up in the non-equilibrium state compared to the equilibrium state. At the same time, the concentration of holes also increases, and in this case, the Fermi level shifts downwards (Fig.1). However, the Fermi level cannot move up and down under the influence of light at the same time Consequently, it is not possible to introduce a single Fermi level under this

condition. Therefore, the state distribution of electrons and holes in non-equilibrium conditions cannot be described by the Fermi-Dirac equilibrium function with one Fermi level, the concept of a quasi-Fermi level is used.

As mentioned above, the concentration of charge carriers strongly depends on the light intensity. Let's consider a *p*-type quantum well heterostructure under the influence of light, as shown in Fig.1. In that case, the concentration of holes will be:

$$p = p_0 + \Delta p \tag{8}$$

Here, p_0 is the concentration of holes in the equilibrium state. Δp is the concentration of holes in the presence of external influence (in the presence of light).
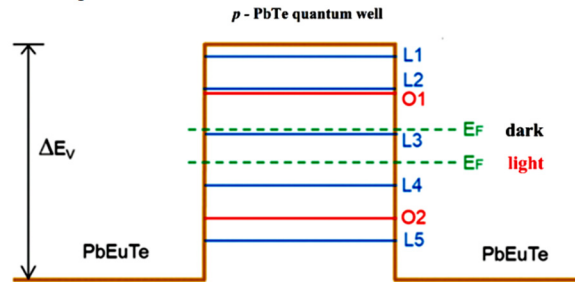
Figure 1. Energy diagrams of light and heavy holes of charge carriers together with the Fermi energy for *B* = 0 in *p*-type quantum well *PbTe* semiconductors in light and dark conditions [28]

The change in the value of Δp strongly depends on the light intensity *I*. When exposed to constant light, the generation process increases, in which case the concentration in lighting is determined by the following expression [35]:

$$\Delta p = \alpha \beta I \tau_p \tag{9}$$

Here, α is the light absorption coefficient, β is the quantum yield that determines the number of electron-hole pairs created by one photon, and *I* is the light intensity. Δp is also called stationary concentration of non-equilibrium holes.

According to the theory of quantum physics, in accordance with the special absorption mechanism of light for small-scale semiconductor structures, the absorption coefficient [35]:

$$\alpha^{2d}\left(h\nu, B\right) = A_1 \frac{\left(h\nu - E_g^{2d}\left(B, d\right)\right)^{\frac{1}{2}}}{h\nu} \tag{10}$$

For prohibited transitions, it is equal to:

$$\alpha^{2d}\left(h\nu, B, d\right) = A_2 \frac{\left(h\nu - E_g^{2d}\left(B, d\right)\right)^{\frac{3}{2}}}{h\nu} \tag{11}$$

Here, A_1, A_2 are constant coefficients independent of frequency.

It follows that, using (8), (9), (10) and (11) to determine the Fermi quantum levels (7) of heterostructures with *p*-type quantum wells, the following new analytical expression is derived:

$$\mu^{2d}\left(E_V, B, T, d, h\nu\right) = E_V - kT \ln\left[\frac{N_s^{2d}\left(E_V, B\right)}{\frac{p_0 + \alpha^{2d}(h\nu, B, d)\beta I \tau_p}{\hbar\omega_c}} - 1\right] \tag{12}$$

The obtained equation (12), that is, $\mu^{2d}\left(B, T, d, h\nu\right)$, means that the quasi-Fermi level of semiconductors with a quantum layer heterostructure depends on the magnetic field, temperature, thickness of the quantum layer, and light energy.

Calculation of the Influence of Light on Fermi Level Oscillations in Low-Dimensional Semiconductors in a Quantizing Magnetic Field

In our previous works [36-43], a new mathematical model was proposed that determines the temperature dependence of the first-order differential transverse magnetoresistance for magnetic field induction for small-scale semiconductor structures. In these works, the temperature dependence of $\frac{\partial\left(\rho_\perp^{2d}(E, B, T, d)\right)}{\partial B}$ was calculated by linear decomposition method of $\left(\frac{\partial f_0(E, \mu, T)}{\partial E}\right)$. In this case, the change of μ Fermi level under the influence of external factors is not taken

into account. However, according to the equation (12), the Fermi level for small-scale *p*-type semiconductor structures is strongly dependent on the thickness of the quantum well, magnetic field induction, temperature, and the frequency of the light particle-photon.

Then, according to (12), the $\left(\dfrac{\partial f_0(E,\mu,T)}{\partial E}\right)$ term there takes the following form:

$$\left(\frac{\partial f_0(E_v,T,B,h\nu,d)}{\partial E_v}\right)=\frac{\partial\left(1+\exp\left(E_v-E_v+kT\ln\left[\dfrac{\dfrac{N_s^{2d}(E_v,B,d)}{p_0+\alpha^{2d}(h\nu,B,d)\beta I\tau_p}-1}{\hbar\omega_c}\right]\right)\right)^{-1}}{\partial E_v}$$ (13)

or, after a series of mathematical reductions:

$$\left(\frac{\partial f_0(E_v,T,B,h\nu,d)}{\partial E_v}\right)=\frac{\partial\left(1+\exp\left(kT\ln\left[\dfrac{\dfrac{N_s^{2d}(E_v,B,d)}{p_0+\alpha^{2d}(h\nu,B,d)\beta I\tau_p}-1}{\hbar\omega_c}\right]\right)\right)^{-1}}{\partial E_v}$$ (14)

According to the proposed new model taking into account the quasi-Fermi level of a small-scale *p*-type semiconductor structure in a quantizing magnetic field strongly dependent on light and temperature and taking into account the expression (14) $\dfrac{\partial\left(\rho_\perp^{2d}(E,B,T,d)\right)}{\partial B}$ oscillations it can also be observed that it changes significantly with respect to light. In particular, expression (14) becomes:

$$\rho_\perp^{2d}(E_v,B,T,h\nu,d)=$$
$$=\frac{1}{\left[\begin{array}{l}\dfrac{e^3B}{2\pi m*c}\sqrt{\dfrac{2}{\pi}}\dfrac{1}{G}\cdot\\[2mm]\int_0^\infty\sum_{n_L}\exp\left[-2\left(\dfrac{E_v-\left[\hbar\omega_c\left(n_L+\dfrac{1}{2}\right)+\dfrac{\pi^2\hbar^2}{2m*d^2}n_Z^2\right]}{G}\right)^2\right]\gamma_\perp(k_0T)^\beta E_v^{\alpha+\frac{3}{2}}\left(\dfrac{\partial f_0(E_v,T,B,h\nu,d)}{\partial E_v}\right)dE\end{array}\right]}$$ (15)

It follows that the vertical axis of the transverse magnetoresistance oscillations of small-scale *p*-type semiconductor structures under the influence of darkness and light, moving the quasi-Fermi levels (see Fig.1) up or down in the non-equilibrium state leads to serious changes throughout. Of course, the shifts of these oscillations are given in the experiments, but their theoretical and physical meaning is justified for the first time using the Equation (15).

According to a series of experiments, the results of the second-order derivative of transverse magnetoresistance oscillations by magnetic field induction in light and dark conditions were compared. Therefore, according to (15):

$$\frac{\partial^2\left[\rho_\perp^{2d}(E_v,B,T,h\nu,d)\right]}{\partial B^2}=$$
$$=\frac{\partial^2\left[\begin{array}{l}\dfrac{e^3B}{2\pi m*c}\sqrt{\dfrac{2}{\pi}}\dfrac{1}{G}\cdot\\[2mm]\int_0^\infty\sum_{n_L}\exp\left[-2\left(\dfrac{E_v-\left[\hbar\omega_c\left(n_L+\dfrac{1}{2}\right)+\dfrac{\pi^2\hbar^2}{2m*d^2}n_Z^2\right]}{G}\right)^2\right]\gamma_\perp(k_0T)^\beta E_v^{\alpha+\frac{3}{2}}\left(\dfrac{\partial f_0(E_v,T,B,h\nu,d)}{\partial E_v}\right)dE\end{array}\right]^{-1}}{\partial B^2}$$ (16)

As can be seen from the Equation (16), $\dfrac{\partial^2\left[\rho_\perp^{2d}(E_v,B,T,h\nu,d)\right]}{\partial B^2}$ can be obtained in graphical form only with the help of a package of practical mathematical programs (Maple, Mathcad, Mathematica). Fig.2 shows $\dfrac{\partial^2\left[\rho_\perp^{2d}(E_v,B,T,h\nu,d)\right]}{\partial B^2}$ graphs calculated based on the Equation (16) for dark and light conditions. These graphs were obtained for a *p-GaAs/AlGaAs* quantum well semiconductor structure, in which the bandgap of the hollow quantum well is 1.51 eV at T = 7 K, and the width of the quantum well is 3 nm [44] and the magnetic field induction was calculated in the range from 0.1 T to 3 T. The photon energy under the influence of light is taken to be equal to 1.4 eV. The graph in red is the $\dfrac{\partial^2\left[\rho_\perp^{2d}(E_v,B,T,h\nu,d)\right]}{\partial B^2}$ under the influence of light, while the oscillations in blue are the graph obtained in the dark. As can be seen from these graphs, it is observed that the amplitudes of $\dfrac{\partial^2\left[\rho_\perp^{2d}(E_v,B,T,h\nu,d)\right]}{\partial B^2}$ oscillations under the influence of light are greater than those in the dark.

Fig.3 shows the experimental results of $\dfrac{\partial^2\left[\rho_\perp^{2d}(E_v,B,T,h\nu,d)\right]}{\partial B^2}$ magnetoresistance oscillations of *p*-type PbTe quantum coil in dark and light [28]. An infrared light-emitting diode with a wavelength of 940 nm and a power density of 12 mW/m^2 was used as light. The temperature is 1.9 K, the magnetic field induction range is from 0 T to 9 T.
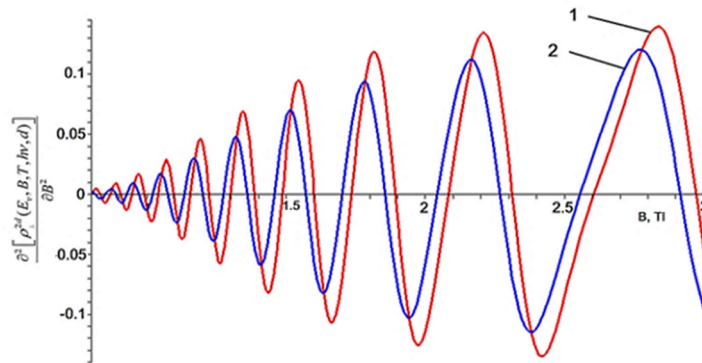
Figure 2. Transverse magnetoresistance oscillations of *p-GaAs/AlGaAs* quantum well semiconductor structure under light and dark conditions. 1 – In light mode; 2 – In the dark
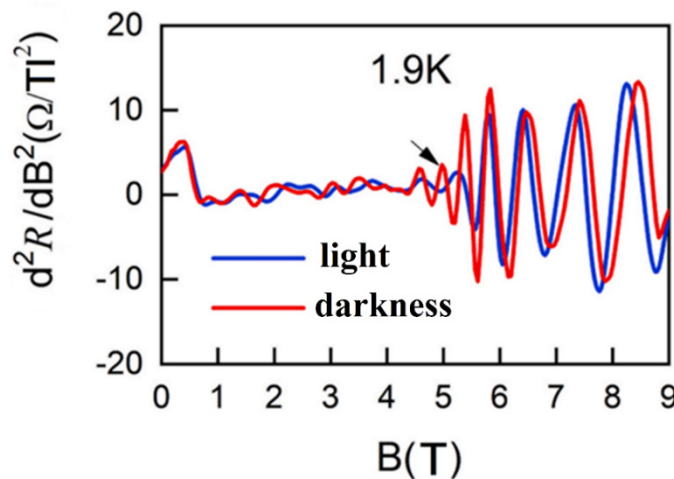
Figure 3. $\partial^2\left[\rho_\perp^{2d}(E_v,B,T,h\nu,d)\right]\big/\partial B^2$ magnetoresistance oscillations of *p*-type *PbTe* quantum well in dark and light conditions [28].

The thickness of the quantum well was equal to 10 nm. In Fig.4, theoretical graphs were obtained using the above-mentioned experimental values of the *p*-type *PbTe* quantum well and based on the Equation (16). $\dfrac{\partial^2\left[\rho_\perp^{2d}(E_v,B,T,h\nu,d)\right]}{\partial B^2}$ oscillations in both light and dark conditions are presented here. As you can see from these images, the experimental and theoretical graphs in light and dark conditions seem to be quite different. In fact, it is not

so, on the contrary, quantum oscillations are practically not visible in the range of magnetic field induction from 0.1 T to 4 T. We know theoretically that discrete Landau levels should be observed under the condition $kT << \hbar\omega_c$. It is at T = 1.9 K that the condition $kT << \hbar\omega_c$ is fulfilled since the magnetic field induction is 1.5 T. So, the equation (16) not only justifies the experimentally obtained shifts in Fig.3, but also allows to prove the existence of quantum oscillation effects, which are not noticed by the experiment. At the same time, based on the proposed model, it is possible to apply the temperature dependence of $\dfrac{\partial^2 \left[\rho_\perp^{2d}(E_v, B, T, h\nu, d) \right]}{\partial B^2}$ oscillations in light and dark conditions.
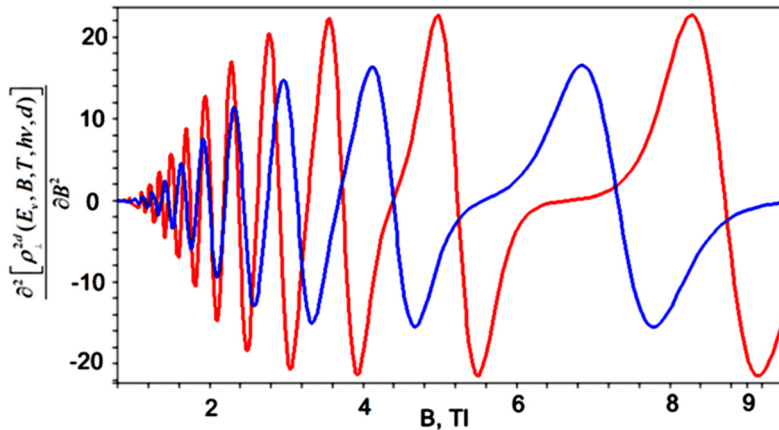
Figure 4. Effect of light on $\partial^2 \left[\rho_\perp^{2d}(E_v, B, T, h\nu, d) \right] / \partial B^2$ magnetoresistance oscillations of *p*-type *PbTe* quantum coil calculated according to the Equation (16).

CONCLUSIONS

The following conclusions can be drawn from the important results of this research:

1. A new Equation (12) expressing the dependence of the quasi-Fermi level of quantum wound heterostructure semiconductors on the magnetic field, temperature and light energy has been derived.
2. Movement of the quasi-Fermi levels in the non-equilibrium state up or down leads to a significant change of transverse magnetoresistance oscillations along the vertical axis of small-scale p-type semiconductor structures under the influence of darkness and light (12) was proved based on the Equation. The displacements of these oscillations are given in experiments, but their theoretical physical meaning was justified using the equation (15).
3. A mathematical model has been developed that determines the dependence of $\dfrac{\partial^2 \left[\rho_\perp^{2d}(E_v, B, T, h\nu, d) \right]}{\partial B^2}$ oscillations of *p*-type semiconductors in the light and dark state on external factors.
4. A new theory was proposed that explains the reasons for the significant shift of the differential magnetoresistance oscillations measured in the experiment along the vertical axis for dark and light conditions.

ORCID
Ulugbek I. Erkaboev, https://orcid.org/0000-0002-6841-8214; **Rustamjon G. Rakhimov,** https://orcid.org/0000-0003-0850-1398
Jasurbek I. Mirzaev, https://orcid.org/0000-0002-3402-1059; **Nozimjon A. Sayidov,** https://orcid.org/0000-0001-9382-8779
Ulugbek M. Negmatov, https://orcid.org/0000-0002-0680-3328

REFERENCES
[1] N.T. Bagraev, E.S. Brilinskaya, E.Yu. Danilovskii, L.E. Klyachkin, A.M. Malyarenko, and V.V. Romanov, Semiconductors, **46**(1), 87 (2012). https://doi.org/10.1134/S1063782612010022
[2] V.V. Romanov, V.A. Kozhevnikov, C.T. Tracey, and N.T. Bagraev, Semiconductors, **53**(12), 1629 (2019). https://doi.org/10.1134/S1063782619160231
[3] N.T. Bagraev, V.Yu. Grigoryev, L.E. Klyachkin, A.M. Malyarenko, V.A. Mashkov, and V.V. Romanov, Semiconductors, **50**(8), 1025 (2016). https://doi.org/10.1134/S1063782616080273
[4] G. Gulyamov, U.I. Erkaboev, and A.G. Gulyamov, J. Nano- Electron. Phys. **11**(1), 01020 (2019). https://doi.org/10.21272/jnep.11(1).01020
[5] U.I. Erkaboev, G. Gulyamov, J.I. Mirzaev, R.G. Rakhimov, and N.A. Sayidov, Nano, **16**(9), 2150102 (2021). https://doi.org/10.1142/S1793292021501022
[6] S.D. Liu, N. Tang, X.Q. Shen, J.X. Duan, F.C. Lu, X.L. Yang, F.J. Xu, X.Q. Wang, T. Ide, M. Shimizu, W.K. Ge, and B. Shen, J. Appl. Phys. **114**(3), 033706 (2013). https://doi.org/10.1063/1.4813512
[7] G. Gulyamov, U.I. Erkaboev, R.G. Rakhimov, J.I. Mirzaev, and N.A. Sayidov, Mod. Phys. Lett. B. **37**(10), 2350015 (2023). https://doi.org/10.1142/S021798492350015X
[8] G. Gulyamov, M.G. Dadamirzaev and S.R. Boidedaev, Semiconductors, **34,** 260 (2000). https://doi.org/10.1134/1.1187967

[9]   M. Ahmetoglu(Afrailov), G. Kaynak, S. Shamirzaev, G. Gulyamov, A. Gulyamov, M.G. Dadamirzaev, S.R. Boydedayev, and N. Aprailov, Int. J. Mod. Phys. B. **23**(15), 3279 (2009). https://doi.org/10.1142/S0217979209053084

[10] G. Gulyamov, M.G. Dadamirzaev, and S.R. Boidedaev, Semiconductors, **34,** 555 (2000). https://doi.org/10.1134/1.1188027

[11] V.A. Kulbachinskii, N.A. Yuzeeva, G.B. Galiev, E.A. Klimov, I.S. Vasil'evskii, R.A. Khabibullin, and D.S. Ponomarev, Semicond. Sci. Technol. **27**(3), 035021 (2012). https://doi.org/10.1088/0268-1242/27/3/035021

[12] K. Požela, A. Šilėnas, J. Požela, V. Jucienė, G.B. Galiev, J.S. Vasil'evskii, and E.A. Klimov, Appl. Phys. A. **109**(1), 233 (2012). https://doi.org/10.1007/s00339-012-7039-7

[13] G. Gulyamov, U.I. Erkaboev, R.G. Rakhimov, and J.I. Mirzaev, J. Nano- Electron. Phys. **12**(3), 03012 (2020). https://doi.org/10.21272/jnep.12(3).03012

[14] U.I. Erkaboev, U.M. Negmatov, R.G. Rakhimov, J.I. Mirzaev, and N.A. Sayidov, Int. J. Appl. Sci. Eng. **19**(2), 2021123 (2022). https://doi.org/10.6703/IJASE.202206_19(2).004

[15] N.Q. Bau, and B.D. Hoi, Int. J. Mod. Phys. B. **28**(03), 1450001 (2014). https://doi.org/10.1142/S0217979214500015

[16] U. Erkaboev, R. Rakhimov, J. Mirzaev, N. Sayidov, U. Negmatov, and M. Abduxalimov, AIP Conf. Proc. **2789**(1), 040055 (2023). https://doi.org/10.1063/5.0145554

[17] N.Q. Bau, N.V. Hieu, and N.V. Nhan, Superlattices Microstruct. **52**(5), 921 (2012). https://doi.org/10.1016/j.spmi.2012.07.023

[18] U. Erkaboev, R. Rakhimov, J. Mirzaev, N. Sayidov, U. Negmatov, and A. Mashrapov, AIP Conf. Proc. **2789**(1), 040056 (2023). https://doi.org/10.1063/5.0145556

[19] N.Q. Bau, and B.D. Hoi, J. Korean Phys. Soc. **60**(1), 59 (2012). https://doi.org/10.3938/jkps.60.59

[20] U. Erkaboev, R. Rakhimov, J. Mirzaev, U. Negmatov, and N. Sayidov, Int. J. Mod. Phys. B. (2023). https://doi.org/10.1142/S0217979224501856

[21] E.E. Vdovin, M. Ashdown, A. Patanè, L. Eaves, R.P. Campion, Yu.N. Khanin, M. Henini, and O. Makarovsky, Phys. Rev. B. **89**(20), 205305 (2014). https://doi.org/10.1103/PhysRevB.89.205305

[22] U.I. Erkaboev, and R.G. Rakhimov, e-J. Surf. Sci. Nanotechnol. (2023). https://doi.org/10.1380/ejssnt.2023-070

[23] M.L. Peres, H.S. Monteiro, V.A. Chitta, S. de Castro, U.A. Mengui, P.H.O. Rappl, N.F. Oliveira, Jr, E. Abramof, and D.K. Maude, J. Appl. Phys. **115**(9) (2014) 093704. https://doi.org/10.1063/1.4867627

[24] U.I. Erkaboev, N.A. Sayidov, R.G. Rakhimov and U.M. Negmatov, Euroasian J. Eng. Sci. Technol. **3**(1) 47 (2021). https://doi.org/10.37681/2181-1652-019-X-2021-1-8

[25] U.I. Erkaboev, G. Gulyamov, J.I. Mirzaev, and R.G. Rakhimov, Int. J. Mod. Phys. B. **34**(7), 2050052 (2020). https://doi.org/10.1142/S0217979220500526

[26] G. Gulyamov, U.I. Erkaboev, N.A. Sayidov and R.G. Rakhimov, J. Appl. Sci. Eng. **23**(3), 453 (2020). https://doi.org/10.6180/jase.202009_23(3).0009

[27] H. Phuphachong, B.A. Assaf, V.V. Volobuev, G. Bauer, G. Springholz, L.A. De Vaulchier, and Y. Guldner, Crystals, **7**(1), (2017). https://doi.org/10.3390/cryst7010029

[28] E.A. Morais, I.F. Costa, E. Abramof, D.A.W. Soares, P.H.O. Rappl, and M.L. Peres, Phys. E: Low-Dimens. Syst. Nanostructures. **127,** 114575 (2021). https://doi.org/10.1016/j.physe.2020.114575

[29] R. Rakhimov, and U. Erkaboev, Scientific and Technical Journal of Namangan Institute of Engineering and Technology, **2**(11), 27 (2020). https://namdu.researchcommons.org/journal/vol2/iss11/5/

[30] U.I. Erkaboev, R.G. Rakhimov, and N.A. Sayidov, Mod. Phys. Lett. B. **35**(17), 2150293 (2021). https://doi.org/10.1142/S0217984921502936

[31] Z. Han, V. Singh, D. Kita, C. Monmeyran, P. Becla, P. Su, J. Li, X. Huang, L.C. Kimerling, J. Hu, K. Richardson, D.T.H. Tan, and A. Agarwal. Appl. Phys. Lett. **109**(7), 071111 (2016). https://doi.org/10.1063/1.4961532

[32] U.I. Erkaboev, R.G. Rakhimov, and N.Y. Azimova, Glob. Sci. Rev. **12,** 33 (2023). https://scienticreview.com/index.php/gsr/article/view/156

[33] U.I. Erkaboev, R.G. Rakhimov, J.I. Mirzaev, and N.A. Sayidov, Int. J. Eng. Innov. Technol. **9**(5), 1557 (2021). http://doi.org/10.35940/ijitee.E2613.039520

[34] F.S. Pena, M.L. Peres, M.J.P. Pirralho, D.A.W. Soares, C.I. Fornari, P.H.O. Rappl, and E. Abramof, Appl. Phys. Lett. **111**(19), 192105 (2017). https://doi.org/10.1063/1.4990402

[35] G. Gulyamov, M.G. Dadamirzaev, and M.O. Kosimova, Rom. J. Phys. **68**, 603 (2023). https://rjp.nipne.ro/2023_68_1-2/RomJPhys.68.603.pdf

[36] U.I. Erkaboev, and R.G. Rakhimov, East Eur. J. Phys. **3,** 133 (2023). https://doi.org/10.26565/2312-4334-2023-3-10

[37] U.I. Erkaboev, and R.G. Rakhimov, e-Prime- Adv. Electr. Electron. Eng. Elect. Energ. **3,** 100236 (2023). https://doi.org/10.1016/j.prime.2023.100236

[38] U.I. Erkaboev, G. Gulyamov and R.G. Rakhimov, Ind. J. Phys. **96**(8), 2359-2368 (2022). https://doi.org/10.1007/s12648-021-02180-4

[39] U.I. Erkaboev, R.G. Rakhimov, N.A. Sayidov, and J.I. Mirzaev, Ind. J. Phys. **97**(4), 1061 (2023). https://doi.org/10.1007/s12648-022-02435-8

[40] U.I. Erkaboev, R.G. Rakhimov, J.I. Mirzaev, U.M. Negmatov, and N.A. Sayidov, Ind. J. Phys. **98**(1), 189 (2024). https://doi.org/10.1007/s12648-023-02803-y

[41] U.I. Erkaboev, N.A. Sayidov, U.M. Negmatov, J.I. Mirzaev, and R.G. Rakhimov, E3S Web Conf. **401,** 01090 (2023). https://doi.org/10.1051/e3sconf/202340101090

[42] U.I. Erkaboev, N.A. Sayidov, U.M. Negmatov, R.G. Rakhimov, and J.I. Mirzaev, E3S Web Conf. **401,** 04042 (2023). https://doi.org/10.1051/e3sconf/202340104042

[43] U.I. Erkaboev, R.G. Rakhimov, U.M. Negmatov, N.A. Sayidov, and J.I. Mirzaev, Rom. J. Phys. **68,** 614 (2023). https://rjp.nipne.ro/2023_68_5-6/RomJPhys.68.614.pdf

[44] M.Ya. Vinnichenko, I.S. Makhov, N.Yu. Kharin, S.V. Graf, V.Yu. Panevin, I.V. Sedova, S.V. Sorokin, and D.A. Firsov, Semiconductors, **55**(9), 710-716 (2021). https://doi.org/10.1134/S1063782621080212

МОДЕЛЮВАННЯ ТЕМПЕРАТУРНОЇ ЗАЛЕЖНОСТІ ОСЦИЛЯЦІЙ ШУБНІКОВА-ДЕ ГААЗА
У СВІТЛОІНДУКОВАНИХ НАНОСТРУКТУРНИХ НАПІВПРОВІДНИКАХ

Улугбек І. Еркабоєв, Рустамжон Г. Рахімов, Джасурбек І. Мірзаєв, Нозімжон А. Саїдов, Улугбек М. Негматов

Наманганський інженерно-технологічний інститут, 160115, Наманган, Узбекистан

У даній роботі досліджено вплив світла на температурну залежність коливань поперечного магнітоопору. Отримано узагальнений математичний вираз, який обчислює температурну та світлову залежність квазірівнів Фермі дрібномасштабних напівпровідникових структур p-типу в квантуючому магнітному полі. Було знайдено нові аналітичні вирази, які представляють температурну залежність коливань поперечного диференціального магнітоопору в темних і освітлених ситуаціях, враховуючи вплив світла на коливання енергії Фермі дрібномасштабних напівпровідникових структур. Розроблено математичну модель, яка визначає світлову залежність похідної другого порядку осциляцій поперечного магнітоопору напівпровідників p-типу з квантовими ямами від індукції магнітного поля. Запропоновано нову теорію, яка пояснює причини значного зсуву коливань диференціального магнітоопору вздовж вертикальної осі, виміряної в експерименті для темних і світлих умов.

Ключові слова: *напівпровідник; гетероструктура; коливання; магнітоопір; квантова яма*

PHASE FORMATION PROCESS IN CdSe THIN FILMS

L.N. Ibrahimova[a], N.M. Abdullayev[b], M.E. Aliyev[c], G.A. Garashova[d], ⬤Y.I. Aliyev[d,e*]

[a]Institute of Natural Resources, Nakhchivan, AZ-7000, Azerbaijan
[b]Institute of Physics, Ministry of Science and Education of Azerbaijan, Baku, AZ-1143, Azerbaijan
[c]Nakhchivan State University, Nakhchivan, AZ-7012, Azerbaijan
[d]Azerbaijan State Pedagogical University, Baku, AZ-1000, Azerbaijan
[e]Western Caspian University, Baku, AZ-1001, Azerbaijan
*Corresponding Author e-mail: yusifafshar@gmail.com
Received January 5, 2023; revised February 15, 2024; accepted February 21, 2024

In this work, thin films of cadmium selenide of difrent thicknesses were obtained by chemical deposition and the processes of phase formation in them were studied. Thin layers with a thickness of $d = 150 - 500$ nm were obtained. Structural studies were carried out using X-ray diffraction. The spectra obtained at room temperature were analyzed. The presence of structural features of the CdSe compound in thin layers has been established. After a thickness $d = 400$ nm, the process of phase formation begins. The observed atomic planes and Miller indices during the phase formation process are determined.
Keywords: *Chemical deposition; CdSe thin film; Crystal structure; X-ray diffraction*
PACS: 68.90.+g; 61.10.Nz; 61.46.−w

INTRODUCTION

Semiconductor crystals are widely studied materials. Their structure and physical properties are studied using modern research methods [1-5]. The main reason for interest in these materials is their use in various devices. It has been established that creating thin layers of materials and using them in devices leads to a reduction in size. At this time, smaller converters can be obtained. Therefore, extensive research has recently been carried out in the direction of obtaining thin layers of materials and studying the processes of phase formation in them [6-10].

Cadmium selenide CdSe, which belongs to the group of diamond-like semiconductors, crystallizes in the form of two polymorphic modifications: B3 with a sphalerite-type lattice (space group F43m) in a cubic crystal structure [11] and a Wurchite hexagonal structure of type B4 (space group P6₃mc) in more thermodynamically stable [12]. CdSe is an n-type semiconductor with a small bandgap ($Eg = 1.74$ eV for sphalerite and $Eg = 1.80$ eV for wurtzite). These values are within the optimal range of absorption of sunlight and its conversion into electrical energy, and together with the high absorption coefficient, CdSe is considered a promising material for the manufacture of solar cells [13,14]. The CdSe compound is used as an active medium in semiconductor lasers [15], liquid crystal displays, gamma radiation detectors, and gas analyzers [16]. In addition, CdSe is a promising compound for photoresistors and LEDs [17,18], high-performance thin-film transistors [19], optical amplifiers, photocatalysts, and materials for photocatalytic systems [20]. The production of thin layers of materials determines the possibility of their use in smaller sizes. Therefore, to determine the application possibilities of each material, it is important to study their thin layers. Therefore, the CdSe compound is also studied in small sizes.

Although the optical and electrical properties of thin layers of the CdSe compound have been studied, the processes of phase formation in these layers have not been sufficiently studied. It is known that the crystal structure of this compound has high symmetry. Therefore, thin layers can also be formed with high symmetry. Therefore, it is important to obtain thin layers of various thicknesses and study their crystal structure. In this work, thin CdSe films of various thicknesses were obtained by chemical deposition, and their crystal structure was studied by X-ray diffraction. The X-ray diffraction method is considered a unique method for studying the structure of crystals, phase transitions and phase formation processes. The structure of nanolayers with a thickness $d = 150$-500 nm was analyzed and the processes of phase formation in thin CdSe layers were studied.

EXPERIMENTAL PART

In the course of research using the chemical deposition method, thin CdSe films of various thicknesses were obtained. The solution used for chemical deposition of the CdSe thin film was prepared by taking equal amounts (13 ml) of each of the prepared solutions of the following composition: 0.5 M cadmium chloride ($CdCl_2 \times 2.5H_2O$), 13.4 M (25%) sodium chloride (NH_3OH), 7.4 M triethanolamine ($C_6H_{15}NO_3$) and 0.2 M sodium selenosulfate (Na_2SSeO_3). The chemical precipitation process was carried out in a 60 ml beaker at room temperature.

Sodium selenosulfate (Na_2SeSO_3) was prepared by reacting 6 grams of selenium powder and 10 grams of sodium sulfite (Na_2SO_3) in 100 ml of distilled water solution for 7 hours at 90 ºC in a counter refrigerator. After the reaction,

the solution was cooled to room temperature and insoluble selenium particles were removed from the solution through a filter. As a result, a clear solution of sodium selenosulfate was obtained. When using sodium selenosulfate as a selenium component in the production of CdSe, the best results can be obtained at a solution pH of 9. A thin layer of CdSe with a crystalline structure can be obtained only at a pH of 9, so that the pH of the solution in the above mixture is equal to 9. To measure the pH of the solution, an Aquilon pH-410 pH meter was used.

Amorphous glass substrates (38×26×1 mm) were kept in a chromium solution for several hours, washed with distilled water and air dried before being introduced into the solution. Glass coasters are placed vertically in a glass with a solution. The chemical deposition process was carried out at room temperature (27 ºC) for 48 hours without rotation. During the process, a white precipitate formed at the bottom of the glass. After three to four hours, this precipitate and the clear solution in the beaker first turned dark yellow and then red, consistent with CdSe. After this procedure, the saucer was removed from the glass, washed with distilled water and dried. As a result, homogeneous thin layers of red CdSe with good adhesion to the substrate were obtained. The thickness of the resulting layers was determined by the gravimetric method and it was found that their thickness d = 150-500 nm.

Structural studies of CdSe thin films were carried out using X-ray diffraction. The experiments were carried out at room temperature and under normal conditions. X-ray diffraction of the samples was carried out on a D8 Advance diffractometer (Bruker) with the following parameters: 40 kV, 40 mA, CuKα radiation (λ = 1.5406 Å). The resulting spectra were analyzed in the Origin program, and the crystallographic parameters of thin CdSe films were determined: diffraction peaks, Miller indices.

RESULTS AND DİSCUSSİONS

In order to study the processes of phase formation in thin films of cadmium selenide obtained by chemical deposition, structural studies were carried out. The crystal structure of CdSe thin films was studied by X-ray diffraction at room temperature. X-ray diffraction spectra obtained in the diffraction angle range $5° \leq 2\theta \leq 80°$ are presented in Fig. 1.
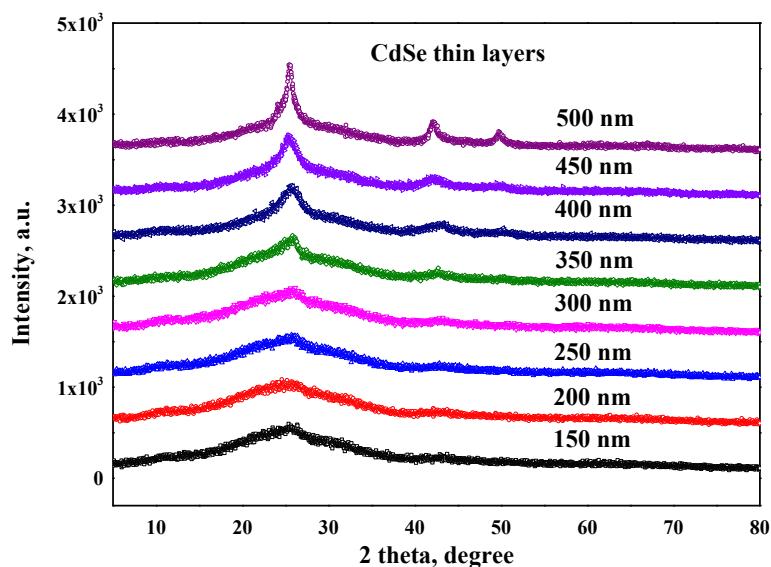
Figure 1. X-ray diffraction spectra of thin CdSe films obtained with different thicknesses.

From the spectra shown in Fig. 1, it is clear that in the resulting thin layers with a thickness of d = 150-500 nm, a phase corresponding to CdSe crystals was formed. The central peak, located at the diffraction angle $2\theta = 25°$, corresponds to the atomic planes belonging to the Miller indices in the crystal structure of the hexagonal symmetry (111) of the CdSe compound. It is clear from the spectra that the intensity of the peaks increases with increasing thickness of the thin layers. However, this phase was also observed in a thin layer d = 150 nm with the smallest thickness. To more accurately observe the peaks in the spectra, the X-ray diffraction spectra of the thinnest and thickest thin layers were analyzed separately. In Fig. 2 shows the spectrum of a thin CdSe film with a thickness of d = 150 nm. It can be seen from the figure that the peak is clearly visible at the diffraction angle $2\theta = 25°$. In addition, a new peak was also observed at the diffraction angle $2\theta = 43°$. From the results obtained when studying the crystal structure of the CdSe compound, it is known that this peak (220) corresponds to atomic planes belonging to the Miller indices [21].

To study the processes of phase formation in thin CdSe films, the X-ray spectra of thin films of greater thickness were also analyzed. Figure 1 shows that after a thickness of d = 400 nm, new peaks begin to appear. This is a sign of the formation of a more perfect phase. It is clear from the spectra that as the thickness of thin layers increases, the intensity of these peaks also begins to increase. Therefore, the spectrum with the greatest thickness was analyzed separately. The X-ray diffraction spectrum of a thin CdSe film with a thickness of d = 500 nm is shown in Fig. 3. From Fig. 3 it can be

seen that 3 peaks are observed in the spectrum. Two of these peaks correspond to atomic planes belonging to the Miller indices (111) and (220), observed in previous spectra at diffraction angles $2\theta = 25°$ and $43°$. It was found that the peak observed at diffraction angles $2\theta = 50°$ corresponds to the atomic plane belonging to the MIller indices (311).
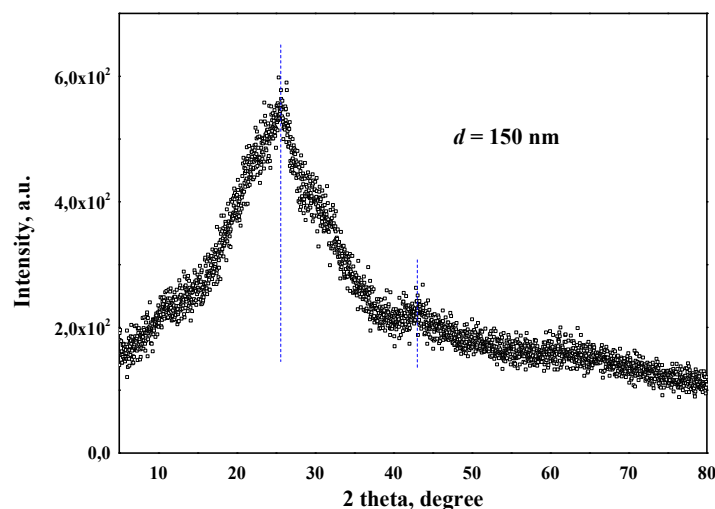
Figure 2. X-ray diffraction spectrum of a thin CdSe film with a thickness of $d = 150$ nm
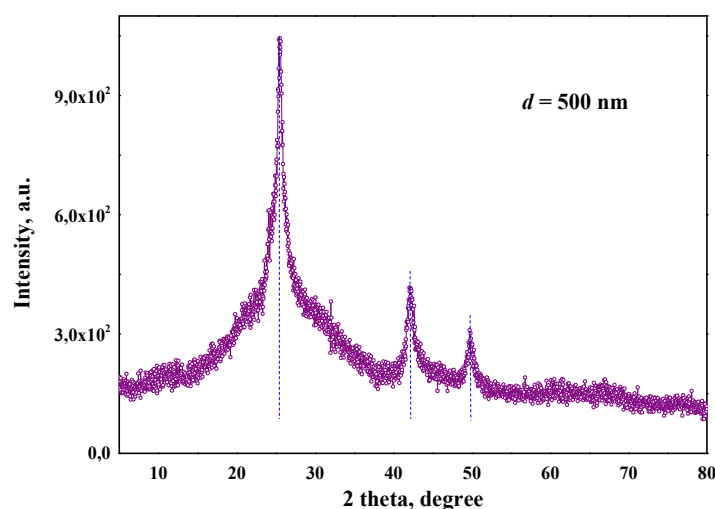
Figure 3. X-ray diffraction spectrum of a thin CdSe film with a thickness of $d = 500$ nm

The lattice parameters of the CdSe compound are $a = b \approx 4$ Å (0.4 nm), $c \approx 7$ Å (0.7 nm) [12]. Since CdSe thin films with dimensions $d \sim 100$ nm consist of several layers, structural features cannot be completely formed. However, as the layer thickness increases, the process of phase formation begins. First, the peak corresponding to the (220) plane along with the (111) plane is fully formed. At thicknesses $d > 400$ nm, the process of phase formation begins and a peak corresponding to the (311) plane is also formed. As can be seen, thin CdSe films starting with a size $d \sim 100$ nm can retain their properties. It is known that the semiconductor CdSe is a material that is widely used in modern electronics. A study of the structure of thin layers obtained by chemical deposition shows that using them it is possible to obtain converters of smaller sizes.

CONCLUSIONS

In this work, thin CdSe films were obtained and their structure was studied. There is extensive information on the technology for producing thin films of the semiconductor CdSe. It has been established that the chemical deposition method can produce thin layers of this material on glass. Layers of varying thicknesses were obtained depending on the synthesis conditions and the stoichiometric amount of chemical elements. The process of phase formation in thin films with a thickness $d = 150\text{-}500$ nm has been studied. The studies were carried out using the X-ray diffraction method. Each of the spectra obtained at room temperature was analyzed separately. It was found that in layers of different thicknesses 3 different diffraction peaks are obtained. Analysis revealed that these peaks correspond to the (111), (220) and (311) atomic planes. Although the structural features of the CdSe compound were observed in each of the thin layers, the phase formation process began at a size of 400 nm.

ORCID

🔵**Y.I. Aliyev,** https://orcid.org/0000-0001-8896-2180

REFERENCES

[1] B.G. Tagiyev, O.B. Tagiyev, A.I. Mammadov, V.X. Quang, T.G. Naghiyev, S.H. Jabarov, M.S. Leonenya, et al., "Structural and luminescence properties of $Ca_xBa_{1-x}Ga_2S_4$: Eu^{2+} chalcogenide semiconductor solid solutions," Physica B: Condensed Matter, **478**, 58-62 (2015). https://doi.org/10.1016/j.physb.2015.08.061

[2] G.M. Agamirzayeva, G.G. Huseynov, Y.I. Aliyev, T.T. Abdullayeva, and R.F. Novruzov, "Crystal structure and magnetic properties of the compound $Cu_3Fe_{0.5}Se_2$," Advanced Physical Research, **5**(1), 19-25 (2023). http://jomardpublishing.com/UploadFiles/Files/journals/APR/V5N1/Agamirzayeva_et_al.pdf

[3] S.H. Jabarov, "First principles study of structural phase transition in Ag_2S under high pressure," Integrated Ferroelectrics, **230**(1), 23-28 (2022). https://doi.org/10.1080/10584587.2022.2102794

[4] A.S. Alekperov, A.O. Dashdemirov, A.E. Shumskaya, and S.H. Jabarov, "High-Temperature Exciton Photoconductivity of $Ge_{1-x}Nd_xS$ Crystals," Crystallography Reports, **66**, 1322-1327 (2021). https://doi.org/10.1134/S1063774521070026

[5] N.A. Aliyeva, Y.I. Aliyev, and A.S. Abiyev, "Study of thermal properties of $Cu_4Se_{1.5}Te_{0.5}$ and $Cu_4Te_{1.5}Se_{0.5}$ compounds by differential thermal analysis," Advanced Physical Research, **4**(2), 94-99 (2022). http://jomardpublishing.com/UploadFiles/Files/journals/APR/V4N2/Aliyeva_et_al.pdf

[6] Kh.N. Ahmadova, and S.H. Jabarov, "Obtaining of Al nanosized thin layers and their structural properties," Arabian Journal for Science and Engineering, **48**, 8083-8088 (2023). https://doi.org/10.1007/s13369-022-07449-2

[7] E.Sh. Alekperov, S.G. Jabarov, T.A. Darzieva, G.B. Ibragimov, A.M. Nazarov, and S.S. Farzaliev, "Effect of an electric field on the crystallization behavior of amorphous $TlIn_{1-x}Sn_xSe_2$ films," Inorganic Materials, **59**(1), 8-11 (2023). https://doi.org/10.1134/S0020168523010028

[8] N.N. Mursakulov, N.N. Abdulzade, S.H. Jabarov, and Ch.E. Sabzalieva, "Investigation of $CuIn_{1-x}Ga_xSe_2$ thin films for solar cells obtained by the magnetron sputtering method from two magnetrons shifted to each other," New Materials, Compounds and Applications, **6**(2), 140-147 (2022). http://jomardpublishing.com/UploadFiles/Files/journals/NMCA/v6n2/Mursakulov_et_al.pdf

[9] R.S. Madatov, A.S. Alekperov, and A.E. Nabiyev, "Influence of Sm impurity atoms on the switching effect in thin films of GeS, "Izvestiya of Saratov University. Physics, **16**(4), 212-217 (2016).

[10] A.O. Dashdemirov, "Thermal emission properties of Re-C thin film systems," Advanced Physical Research, **2**(2), 102-107 (2020). http://jomardpublishing.com/UploadFiles/Files/journals/APR/V2N2/Dashdemirov.pdf

[11] D.M. Freik, L.I. Nykyruy, T.O. Parashchuk, and B.P. Volochanska, "Thermodynamic properties of CDSE crystals using first principles calculations and experiment," International Journal of Engineering and Innovative Technology (IJEIT), **4**(2), 99-104 (2014). https://www.ijeit.com/Vol%204/Issue%202/IJEIT1412201408_19.pdf

[12] Y.N. Xu, and W.Y. Ching, "Electronic, optical, and structural properties of some wurtzite crystals," Physical Review B, **48**, 4335-4351 (1993). https://doi.org/10.1103/PhysRevB.48.4335

[13] C. Li, F. Wang, and Y. Chen, "Characterization of sputtered CdSe thin films as the window layer for CdTe solar cells," Materials Science in Semiconductor Processing, **83**, 89-95 (2018). https://doi.org/10.1016/j.mssp.2018.04.022

[14] C.D. Lokhande, E.-H. Lee, K.-D. Jung, and O.S. Joo, "Ammonia-free chemical bath method for deposition of microcrystalline cadmium selenide films," Materials Chemistry and Physics, **91**, 200-204, 2005. https://doi.org/10.1016/j.matchemphys.2004.11.014

[15] S. Wageh, "Raman and photoluminescence study of CdSe nanoparticles capped with a bifunctional molecule," Physica E: Low Dimensional Systems and Nanostructures, **39**, 8-14 (2007). https://doi.org/10.1016/j.physe.2006.12.003

[16] R.A. Potyrailo, and A.M. Leach, "Selective gas nanosensors with multisize CdSe nanocrystal/polymer composite films and dynamic pattern recognition," Applied Physics Letters, **88**, 134110 (2006). https://doi.org/10.1063/1.2190272

[17] F. Li, W-N. Li, S-Y. Fu, and H-M. Xiao, "Formulating CdSe quantum dots for white light-emitting diodes with high color rendering index," Journal of Alloys and Compounds, **647**, 837-843 (2015). https://doi.org/10.1016/j.jallcom.2015.05.232

[18] X. Dai, Z. Zhang, Y. Jin, Y. Niu, H. Cao, X. Liang, L. Chen, et al., "Solution-processed, highperformance light-emitting diodes based on quantum dots," Nature, **515**, 96-99 (2014). https://doi.org/10.1038/nature13829

[19] F.Y. Gan, and I. Shih, "Preparation of thin-film transistors with chemical bath deposited CdSe and CdS thin films," IEEE Transactions on Electron Devices, **49**(1), 15-18 (2002). https://doi.org/10.1109/16.974742

[20] A. Kubacka, M. Fernández-García, and G. Colón, "Advanced nanoarchitectures for solar photocatalytic applications," Chemical Reviews, **112**, 1555-1614 (2012). https://doi.org/10.1021/cr100454n

[21] A. Singh, A. Kunwar, and M.C. Rath, "L-cysteine capped CdSe quantum dots syntesized by photochemical route," Journal of Nanoscience and Nanotechnology, **18**, 3419-3426 (2017). https://doi.org/10.1166/jnn.2018.14687

ПРОЦЕС ФАЗОУТВОРЕННЯ В ТОНКІХ ПЛІВКАХ CdSe

Л.Н. Ібрагімова[a], Н.М. Абдуллаєв[b], М.Е. Алієв[c], Г.А. Гарашова[d], Ю.І. Алієв[d,e]
[a]Інститут природних ресурсів, Нахічевань, AZ-7000, Азербайджан
[b]Інститут фізики Міністерства науки і освіти Азербайджану, Баку, AZ-1143, Азербайджан
[c]Нахічеванський державний університет, Нахічевань, AZ-7012, Азербайджан
[d]Азербайджанський державний педагогічний університет, Баку, AZ-1000, Азербайджан
[e]Західно-Каспійський університет, Баку, AZ-1001, Азербайджан

У даній роботі методом хімічного осадження отримано тонкі плівки селеніду кадмію різної товщини та досліджено процеси фазоутворення в них. Отримано тонкі шари товщиною d = 150 – 500 нм. Структурні дослідження проводили методом рентгенівської дифракції. Аналізували спектри, отримані при кімнатній температурі. Встановлено наявність структурних особливостей сполуки CdSe в тонких шарах. Після товщини d = 400 нм починається процес фазоутворення. Визначено спостережувані атомні площини та індекси Міллера в процесі фазоутворення.

Ключові слова: *хімічне осадження; тонка плівка CdSe; кристалічна структура; рентгенівська дифракція*

MOLECULAR DYNAMICS STUDY OF THE LYSOZYME-BASED DRUG DELIVERY NANOSYSTEMS LOADED WITH ANTIVIRAL DRUGS AND CYANINE DYES

Olga Zhytniakivska*, Uliana Tarabara, Kateryna Vus, Valeriya Trusova, Galyna Gorbenko

Department of Medical Physics and Biomedical Nanotechnologies, V.N. Karazin Kharkiv National University
4 Svobody Sq., Kharkiv, 61022, Ukraine
Corresponding Author: olga.zhytniakivska@karazin.ua

Protein-based drug nanocarriers are increasingly recognized as promising candidates for effective drug delivery, owing to a multitude of beneficial advantages over synthetic materials including low cytotoxicity, biocompatibility, biodegradability, abundance, renewability, and high drug loading capacity mediated by diverse functional groups and interactions. In the present study the molecular dynamics simulation was employed to explore the stability of lysozyme-based drug delivery nanosystems functionalized by the antiviral drugs (favipiravir, molnupiravir, nirmatrelvir and ritonavir) and cyanine dyes (AK7-5, AK5-6, AK3-11). A series of 5 ns or 100 ns MD simulations for the top-scored docked drug-dye-protein complexes, obtained using the PatchDock server was performed at 310 K with GROMACS software using the CHARMM General Force Field. The MD results have been analyzed in terms of the parameters, such as the backbone root mean-square deviation, gyration radius, solvent accessible surface area, the root means square fluctuations. The analysis of calculated parameters for the studied systems enabled us to improve the previously acquired molecular docking data. Taken together, the results obtained indicate that Lz-F-AK3-11, Lz-R-AK75, Lz-R-AK56, Lz-N-AK75, Lz-N-AK3-11, and Lz-M-AK75 systems exhibit the highest stability among the examined dye-drug-protein systems and represent potential candidates for the targeted delivery of the explored antiviral agents.
Keywords: *Protein-drug-dye complexes, antiviral agents, cyanine dyes, molecular dynamics*
PACS: 87.14.C++c, 87.16.Dg

Over the past few decades protein-based drug delivery nanosystems have emerged as a promising avenue in the field of pharmaceutical and biomedical research due to a multitude of their beneficial biochemical and biophysical advantages over synthetic materials such as: i) biocompatibility and biodegradability; ii) remarkable capacity to bind various drugs owing to the presence of numerous binding pockets and functional groups within proteins; iii) safeguarding the drugs from enzymatic breakdown and swift renal excretion; iv) ample availability of proteins sourced from nature v) the ability to attach surface ligands specific to target tissues; vi) efficient and cost-effective synthesis procedures [1-7], etc. A critical aim in the fabrication of efficient protein-based nanotherapeutics is their optimization, which demands both: i) a profound knowledge of the behavior of the designed nanocarrier in various conditions as well as ii) a comprehensive understanding of potential interactions within the system [8,9]. Despite the increasing sophistication of experimental endeavors to design and optimize the structure and dynamics of the protein-based drug delivery nanosystems, such research inevitably encounters intrinsic and practical limitations since the systematic variations in the nanocarrier properties like the type of protein or visualizing agent, protein size, hydrophobicity, surface charge, etc. can be prohibitively time-consuming and expensive. Hence, relying solely on experimental research makes it challenging to elucidate the general biophysical and biochemical principles that connect the effectiveness of a potential protein-based drug delivery system with its composition. Given this, the methods of computer modeling are becoming widespread in the early-stage development and optimization of potential protein-based drug-delivery nanosystems [10-14].

In our previous work, we employed the multiple ligand simultaneous docking technique to evaluate the possibility of functionalization of protein-based nanoparticles by the antiviral drugs and cyanine dyes [15,16]. More specifically, we evaluated the suitability of a series of cyanine dyes (four monomethines, six trimethines, seven pentamethines and two heptamethines) to serve as visualizing agents in the drug-protein-dye systems, encompassing four functionally significant proteins (cytochrome *c*, serum albumin, lysozyme and insulin) and four antiviral drugs (favipiravir (F), molnupiravir (M), nirmatrelvir (N) and ritonavir (R)) [15,16]. We identified the ternary systems with the highest dye-protein surface shape complementarity for each group of the examined cyanine dyes and assessed the impact of cyanine dye structure on the stability of the drug-protein-dye complexes [15,16]. In continuation of our previous work, in the present study the molecular dynamics simulation was performed to elucidate the stability of the most prospective drug delivery systems obtained by multiple ligand simultaneous docking approach [15,16]. To this end, the present study aimed to characterize the effects of three cyanine dyes (AK7-5, AK5-6, AK3-11) and 4 antiviral drugs (favipiravir, molnupiravir, nirmatrelvir and ritonavir) on the structure and dynamics of lysozyme (Lz) in the drug-protein-dye systems.

MOLECULAR DYNAMICS SIMULATIONS

The top-scored docked drug-dye-protein complexes, obtained using the PatchDock server as described in [15,16], were considered as a starting structure for the molecular dynamic's simulations. First, the .pdb-file of docked system

was corrected in PDB Editor [17] to add the missing chain ID for ligands. Next, this .pdb-file was uploaded in the web-based graphical interface CHARMM-GUI [18] to obtain the input files for MD calculations. The .itp files of cyanines (AK7-5, AK5-6, AK3-11) and antiviral drugs (favipiravir, molnupiravir, nirmatrelvir and ritonavir) were constructed from the dye.mol2 files, using the CHARMM General Force Field, followed by replacing the dye/drug partial charges with those assigned by RESP ESP charge Derive Server [19]. The drug-dye-protein complexes were solvated in a rectangular box with a minimum distance of 10 Å from the protein to the box edges and 0.15 M NaCl (neutralizing ions) were added to the systems. The TIP3P water model was used. The molecular dynamics simulations and analysis of the trajectories were performed using the GROMACS software (version 2023.3) with the CHARMM36m force field in the NPT ensemble with the time step for MD simulations 2 fs. The calculations were performed at a temperature of 310 K. The minimization and equilibration of the systems were carried out during 50000 and 125000 steps, respectively. The V-rescale thermostat provided the constant temperature conditions. The time interval for MD calculations was 5 ns for stability complex preview and 100 ns for the most stable systems. The molecular dynamics trajectories were corrected after the MD run, using the gmx trjconv GROMACS command [20,21]. The GROMACS commands gmx rms, gmx gyrate, gmx rmsf were used to calculate the protein backbone root-mean-square deviation (RMSD), protein radius of gyration (R_g), root-mean-square fluctuations of the C-alpha atoms (RMSF). Visualization of the snapshots of the MD runs and analysis of the protein secondary structures, calculating distances between the dye/drug and protein centers of geometry and protein solvent-accessible surface area (SASA) were performed in VMD.

RESULTS AND DISCUSSION

Lysozyme, a globular functional protein containing 129 amino acids in the monomeric state, is currently widely employed in the development of drug-delivery systems, due to lysozyme ability to bind the drugs and facilitate their accumulation at target sites [22,23]. Beyond its drug-delivery role, lysozyme exhibits various intrinsic medicinal properties, including anti-inflammatory, antiviral, immune-modulatory, antihistaminic, and antitumor activities [24, 25]. In our previous studies we evaluated the possibility of creating the lysozyme-based nanosystems carrying antiviral drugs and cyanine dyes as visualizing agents [15,16]. Varying both the structure of the cyanine dyes (mono-, tri-, penta- and heptamethines) and the antiviral agents (favipiravir, molnupiravir, nirmatrelvir and ritonavir), we identified three cyanines (AK7-5, AK5-6, AK3-11) as the most promising candidates for the fabrication of multicomponent drug-delivery nanosystems [15,16]. To verify the stability of the obtained ternary complexes, the next logical step was to perform the molecular dynamics simulation for the obtained systems with the highest docking score. Initially, the 5 ns simulation was performed for all dye-lysozyme-drug complexes. The representative snapshots are shown in Figure 1.

Figure 1. Representative snapshots of the drug-lysozyme-dye complexes. Cyanine dyes are colored green, and antiviral drugs are marked as blue.

At the first stage of our study we investigated the overall stability of the systems during the simulation time through analyzing the time course evolution of the set of structural parameters such as the protein backbone root-mean-square deviation (RMSD), protein radius of gyration (R_g) and root-mean-square fluctuations of the C-alpha atoms

(RMSF) and solvent accessible surface area. Figure 2 shows the changes in the backbone root mean square deviations (RMSD) and the radius of gyration (R_g) with time.

Figure 2. Time course evolution of the root-mean-square deviation and the radius of gyration for drug-lysozyme-dye complexes

As seen in Fig. 2, the calculated RMSD values for the potential drug-delivery nanosystems do not exceed 0.1 nm, except for short-time fluctuations of Lz-F-AK75, Lz-F-AK56, Lz-N-AK56 and Lz-M-AK3-11. More specifically, the

time dependence of RMSD for the Lz-F-AK75 is characterized by the two periods: 1) slight fluctuations ~ 0.07 nm during the first 2.5 ns of simulation and 2) increase of RMSD values to 0.12-0.14 nm during the next 0.5 ns followed by the fluctuations at this level during the remaining time of the simulation. For the Lz-F-AK56 system, a substantial increase of RMSD values to 0.15 nm was detected starting from ~4.6 ns. The Lz-F-AK75, Lz-N-AK56 and Lz-M-AK3-11 produced less stable trajectories in comparison with the other systems. The radius of gyration (R_g) serves as an indicator of the structural compactness of a protein. A lower R_g indicates a more tightly packed polypeptide chain, while a higher value of the radius of gyration suggests a more open protein structure. Figure 3 shows the minor fluctuation of the radius of gyration for all examined systems. Notably, for the Lz-F-AK75 drug-protein-dye system the R_g value was decreased from 1.44 to 1.41 nm at 2.3 ns of simulation. After 2.3 ns, the R_g seems to be stabilized and equilibrated during the entire simulation period of 5 ns. The obtained results indicate the strongest fluctuations in the systems containing ritonavir. To determine the dynamic behavior of amino acid residues, the RMSF values of the C-alpha atoms of lysozyme were calculated (Figure 3). The RMSF values for the majority of the protein residues ranged from 0.05 to 0.15 nm during the simulation. The exception was the residues 105-115 for all systems under study and the residues 45-54 for the ritonavir- and nirmatrelvir-containing systems.
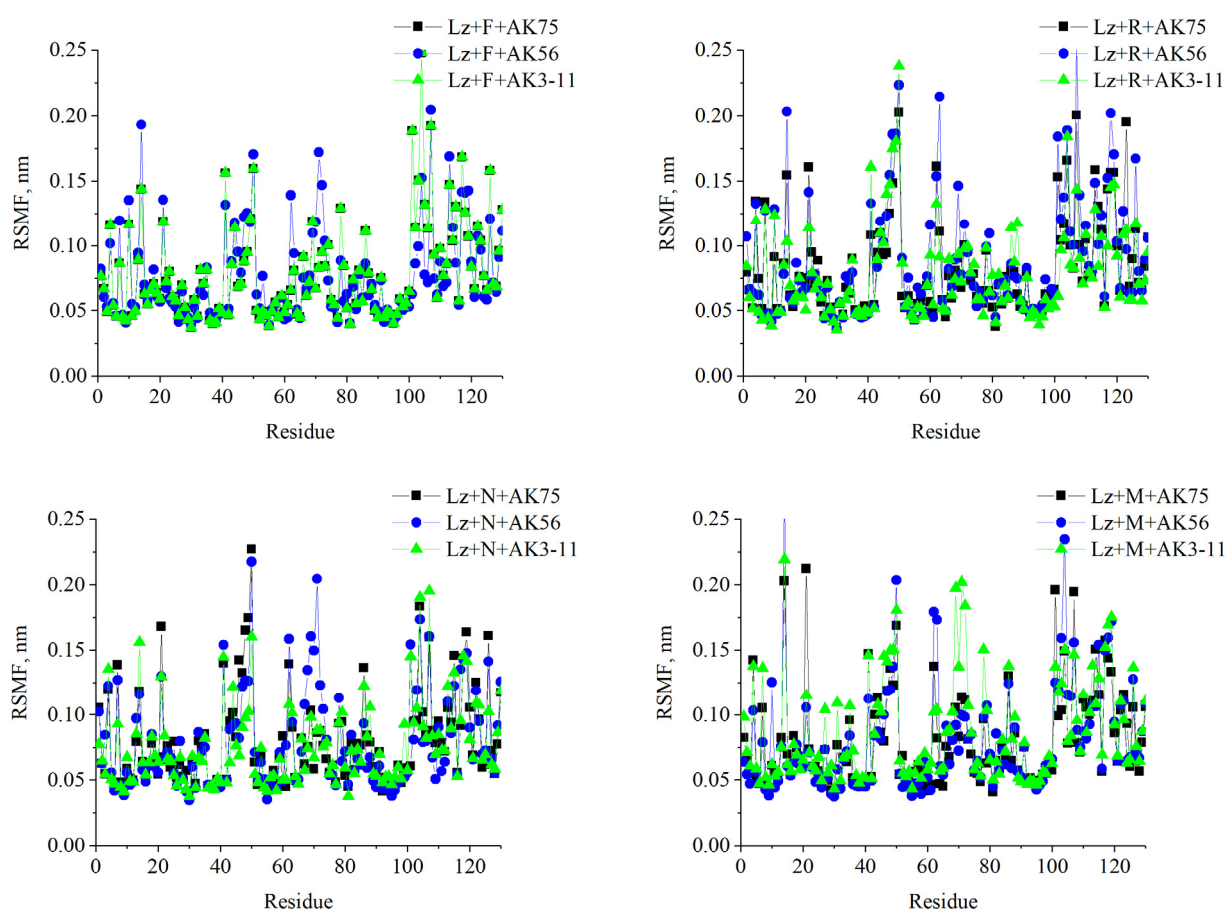
Figure 3. Time course evolution of the root-mean-square deviation for the drug-lysozyme-dye complexes

To assess the alterations in the environment of protein residues during the simulation, we concentrated on the solvent-accessible surface area per residue SASA (Figure. 4). It was observed that the SASA of the majority of complexes under study fluctuated within the range 71-75, while the SASA of Lz-M-AK3-11 and Lz-R-AK3-11 slightly increased during the simulation. The SASA of the Lz-N-AK56 complex increased from 72 to 78 during the initial 3 ns of simulation and maintained equilibrium during the rest of the simulation time.

Taken together, the comparison of the calculated parameters such as the protein backbone root-mean-square deviation (RMSD), protein radius of gyration (R_g) root-mean-square fluctuations of the C-alpha atoms (RMSF) and solvent accessible surface area for the investigated systems allowed us to determine the most stable systems, *viz.* Lz-F-AK3-11, Lz-R-AK75, Lz-R-AK56, Lz-N-AK75, Lz-N-AK3-11 and Lz-M-AK75. The obtained results indicate that during the 5 ns MD simulation, the antiviral drugs and cyanines undergo the changes in their binding interactions in the docked complexes with the protein to adjust to the potential energy function from the MD force field resulting in the destabilization of the drug-dye-protein interactions and unbinding either the drug or the dye from the protein for some systems. Notably, to assess the efficacy of 5 ns MD simulations in determining the stability of the dye-protein-drug complexes, we conducted additional 100 ns MD simulations for the three chosen systems (Figure 5).
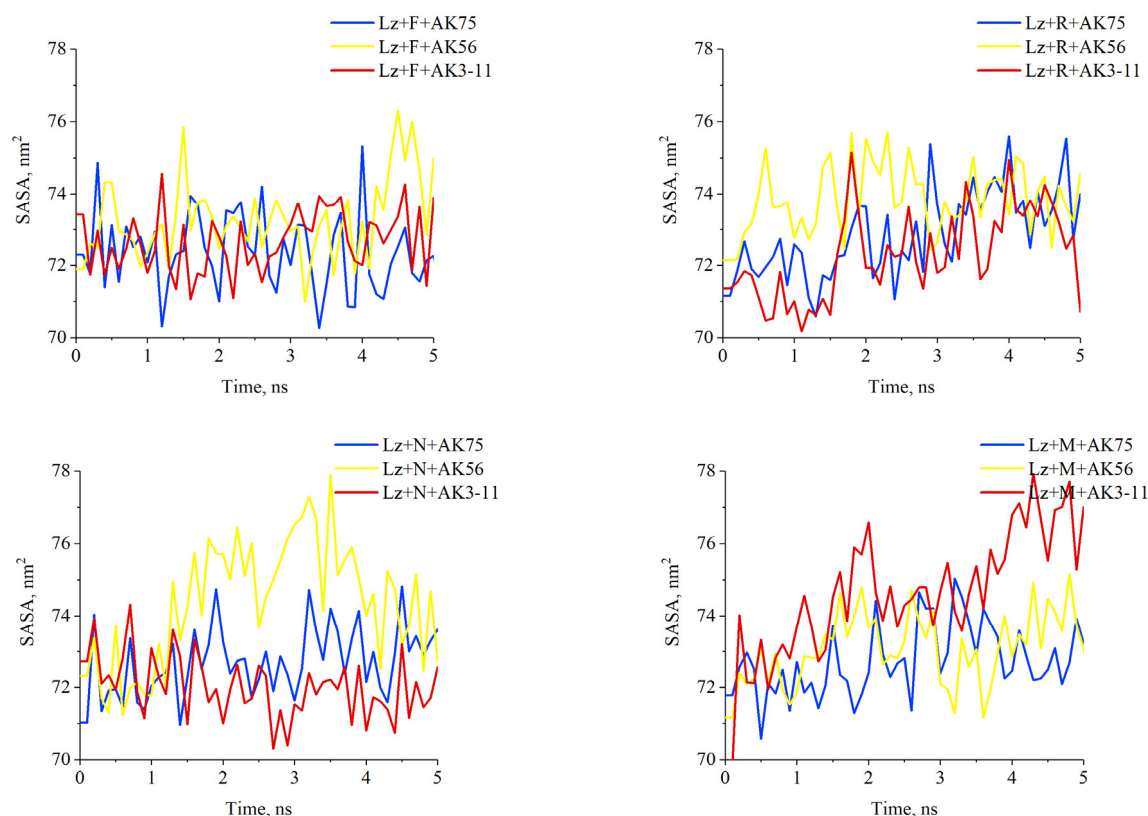
Figure 4. Time course evolution of the solvent-accessible surface area for the drug-lysozyme-dye complexes
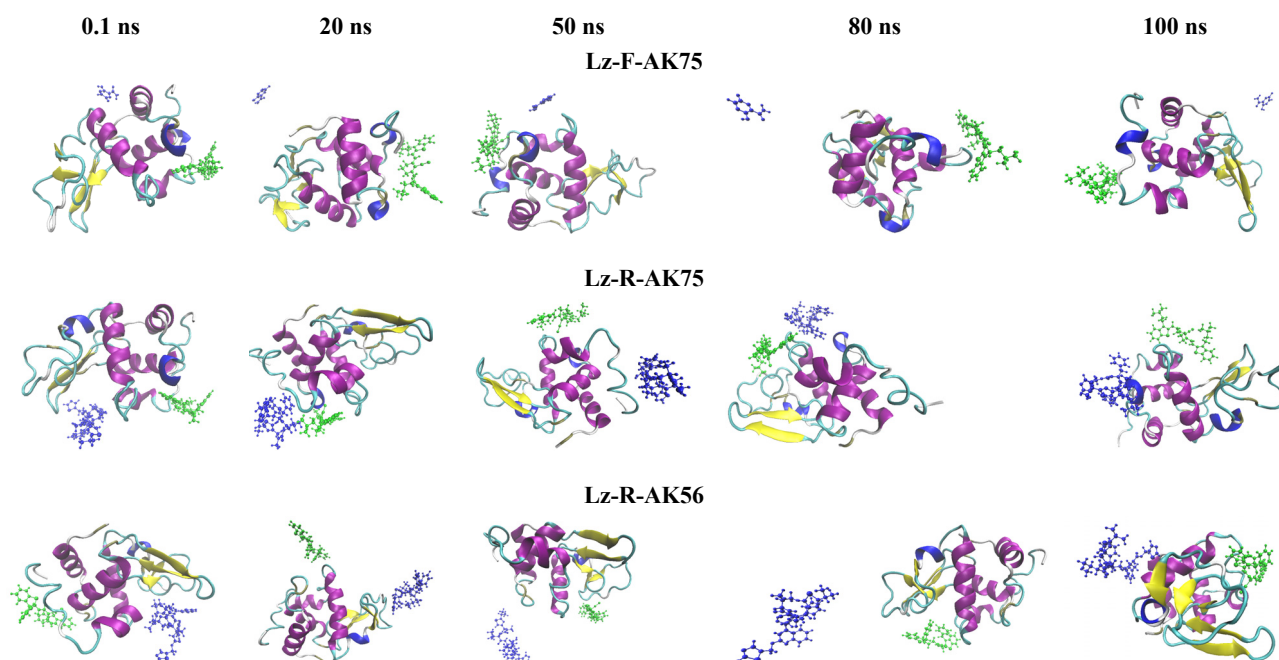
Figure 5. 100 ns snapshots of the drug-lysozyme-dye complexes. Cyanine dyes are colored green, and antiviral drugs are marked as blue.

As shown in Figure 5, the Lz-R-AK75 exhibits the highest stability among the three selected complexes, as both the cyanine dye and the antiviral drug remain bound to the lysozyme during the entire simulation time. On the contrary, in the case of Lz-F-AK75, the antiviral drug detached from the protein at the beginning of the simulation. Additionally, the stability Lz-F-AK56 complex is lower compared to Lz-R-AK75, as we observed the detachment of dye molecule in the middle of the 100 ns simulation, followed by the binding of AK56 to the Lz-ritonavir complex in the end of MD trajectory. The time course evolution of RMSD parameters confirmed the highest stability of the Lz-R-AK75 drug-protein-dye system (Figure 6).
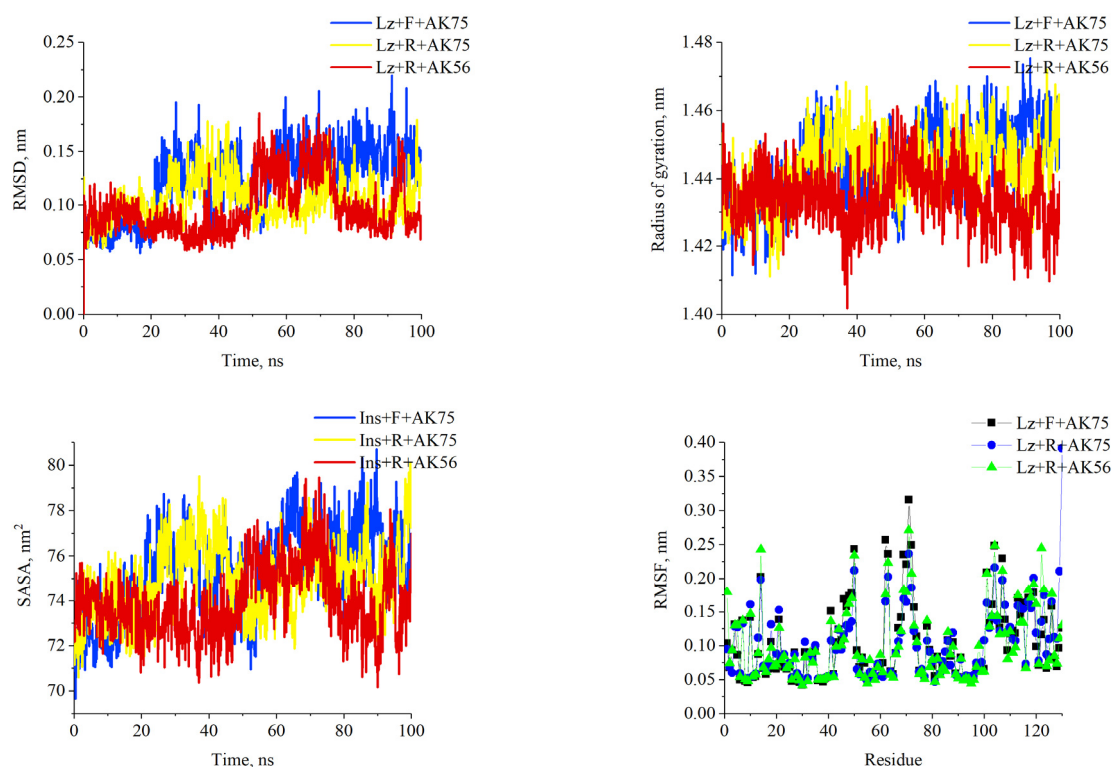
Figure 6. Time course evolution of the MD parameter for the drug-lysozyme-dye complexes obtained during the 100 ns simulation

CONCLUSIONS

In conclusion, in the present study we evaluated the potential stability of the drug-dye-lysozyme complexes functionalized with antiviral drugs (favipiravir, molnupiravir, nirmatrelvir and ritonavir) and the cyanine dyes (AK3-11, AK7-5 and AK5-6). The 5-ns and 100 ns MD simulations were performed to elucidate the stability of the top-scored docked drug-dye-protein complexes obtained using the molecular docking method in our previous work. It was found that the performed molecular dynamics simulations were highly effective in the improvement of the results obtained by the molecular docking studies. The analysis of calculated parameters, including the protein backbone root-mean-square deviation (RMSD), protein radius of gyration (Rg), root-mean-square fluctuations of the C-alpha atoms (RMSF), and solvent accessible surface area, for the studied systems enabled the identification of the most stable systems such as Lz-F-AK3-11, Lz-R-AK75, Lz-R-AK56, Lz-N-AK75, Lz-N-AK3-11, and Lz-M-AK75.

ORCID

Olga Zhytniakivska, https://orcid.org/0000-0002-2068-5823; **Uliana Tarabara,** https://orcid.org/0000-0002-7677-0779
Kateryna Vus, https://orcid.org/0000-0003-4738-4016; **Valeriya Trusova,** https://orcid.org/0000-0002-7087-071X
Galyna Gorbenko, https://orcid.org/0000-0002-0954-5053

REFERENCES

[1] A.L. Martínez-López, C. Pangua, C. Reboredo, R. Campión, J. Morales-Gracia, and J.M. Irache, Int. J. Pharm. **581**, 119289 (2020). https://doi.org/10.1016/j.ijpharm.2020.119289

[2] Y. Wang, H. Igbal, U. U.-Rehman, L. Zhai, Z. Yuan, A. Razzaq, M. Lv, et al., J. Drug Deliv. Sci. Technol. **79**, 104072 (2023). https://doi.org/10.1016/j.jddst.2022.104072.

[3] C. Wen, J. Zhang, H. Zhang, Y. Duan, Foods. 11, 1701 (2022). https://doi.org/10.3390/foods11121701.

[4] L. Xu, S.-B. Wang, C. Xu, D. Han, X.-H. Ren, X.-Z. Zhang, S.-X. Cheng, ACS Appl. Mater. Interfaces. **11**, 38385 (2019). https://doi.org/10.1021/acsami.9b11263.

[5] E. Kianfar, J. Nanobiotechnol. 19, 159 (2021). https://doi.org/10.1186/s12951-021-00896-3

[6] A.O. Elzoghby, W.M. Samy, N.A. Elgindy, Journal of Controlled Release **161**, 38 (2012). https://doi.org/10.1016/j.jconrel.2012.04.036

[7] S. Lee, T.C. Pham, C. Bae, Y. Choi, Y.K. Kim, J. Yoon, Coord. Chem. Rev. **412**, 213258 (2020). https://doi.org/10.1016/j.ccr.2020.213258.

[8] S. Fuchs, C. Coester, J. Drug. Deliv. Sci. Technol. **20**, 331 (2010). https://doi.org/10.1016/S1773-2247(10)50056-X.

[9] S. Ding, N. Zhang, Z. Lye, W. Zhu, Y.C. Chang, et al., MaterialsToday. **43**, 166 (2021). https://doi.org/10.1016/j.mattod.2020.11.015

[10] S. Mollazadeh, A. Sahebkar, M. Shahlaei, S. Moradi. J. Mol. Liq. **332**, 115823 (2021). https://doi.org/10.1016/j.molliq.2021.115823

[11] H. Guterres, W. Im. J. Chem. Inf. Model. **60**, 2189 (2020). https://doi.org/10.1021/acs.jcim.0c00057.

[12] J. Mortier, C. Rakers, M. Bermudez, M. S. Murgueitio, S.Riniker, G. Wolber, Drug Discovery Today, **20**, 686 (2015). https://doi.org/10.1016/j.drudis.2015.01.003

[13] S. Gu, C. Shen, J. Yu, H. Zhao, H. Liu, L. Liu, et al., *Briefings in Bioinformatics*, **24**, bbad008 (2023). https://doi.org/10.1093/bib/bbad008

[14] Z. Chen, X. Wang, X. Chen, J. Huang, C. Wang, J. Wang, Z. Wang, Comput Struct Biotechnol J. **21**, 2909 (2023). https://doi.org/10.1016/j.csbj.2023.04.027

[15] O. Zhytniakivska, U. Tarabara, K. Vus, V. Trusova, G. Gorbenko, East Eur. J. Phys. **4**, 318 (2023), https://doi.org/10.26565/2312-4334-2023-4-42

[16] O. Zhytniakivska, U. Tarabara, K. Vus, V. Trusova, G. Gorbenko, East Eur. J. Phys. **3**, 585 (2023), https://doi.org/10.26565/2312-4334-2023-3-69

[17] J. Lee, S.-H. Kim, Acta Cryst. D65, 399-402 (2009), https://doi.org/10.1107/S090744490900451X

[18] S. Jo, T. Kim, V. G. Iyer, W. Im. J. Comp. Chem. 29, 1859 (2008), https://doi.org/10.1002/jcc.20945

[19] E. Vanquelef, S. Simon, G. Marquant, E. Garcia, G. Klimerak, J.C. Delepine, P. Cieplak, and F.Y. Dupradeau, Nucleic Acids Res. **39**, W511 (2011), https://doi.org/10.1093/nar/gkr288

[20] C. Paissoni, D. Spiliotopoulos, G. Musco, and A. Spitaleri, Computer Physics Communications. **186**, 105 (2015), https://doi.org/10.1016/j.cpc.2014.09.010

[21] I. Massova, and P.A. Kollman, J. Am. Chem. Soc. **121**, 8133 (1999), https://doi.org/10.1021/ja990935j

[22] H.X. Cai, P. Yao, Nanoscale, **5**, 2892 (2013). https://doi.org/10.1039/C3NR00178D

[23] M. Haas, A.C.A. Kluppel, E.S. Wartna, F. Moolenaar, D.K.F. Meijer, P.E. deJong, D. deZeeuw, Kidney Int. **52**, 1693 (1997). https://doi.org/10.1038/ki.1997.504

[24] C. Mecitoglu, A. Yemenicioglu, A. Arslanoglu, Z.S. Elmaci, F. Korel, A.E. Cetin, Food Res. Int. **39**, 12 (2006).

[25] S. Lee-Huang, V. Maiorov, P.L. Huang, A. Ng, H.C. Lee, Y.-T. Chang, N. Kallenbach, P.L. Huang, H.-C. Chen, Biochemistry, **44**, 4648 (2005). https://doi.org/10.1021/bi0477081

МОЛЕКУЛЯРНО-ДИНАМІЧНЕ ДОСЛІДЖЕННЯ НАНОСИСТЕМ ДОСТАВКИ ЛІКАРСЬКИХ ЗАСОБІВ НА ОСНОВІ ЛІЗОЦИМУ, НАВАНТАЖЕНИХ АНТИВІРУСНИМИ ПРЕПАРАТАМИ ТА ЦІАНІНОВИМИ БАРВНИКАМИ

Ольга Житняківська, Уляна Тарабара, Катерина Вус, Валерія Трусова, Галина Горбенко
*Кафедра медичної фізики та біомедичних нанотехнологій, Харківський національний університет імені В.Н. Каразіна
м. Свободи 4, Харків, 61022, Україна*

Наноносії на основі білків набувають все більшого визнання як перспективні кандидати для ефективної доставки ліків, завдяки їх численним перевагам перед синтетичними матеріалами, таким як низька цитотоксичність, біосумісність та здатність до біодеградації, розповсюдженість у природі, здатність до самовідновлення, а також високий ступінь завантаження ліків завдяки різноманітним функціональним групам і взаємодіям. У даній роботі з використанням молекулярно-динамічного моделювання було визначено стабільність наносистем доставки ліків на основі лізоциму, функціоналізованих антивірусними препаратами (фавіпіравір, мольнупіравір, нірматрельвір та рітонавір) та ціаніновими барвниками (АК7-5, АК5-6, АК3-11). За допомогою програмного забезпечення GROMACS з використанням загального силового поля CHARMM при температурі 310 К, було проведено серію MD-симуляцій тривалістю 5 або 100 нс для систем з найвищою комплементарністю, отриманих за допомогою сервера PatchDock. Результати MD були проаналізовані в термінах таких параметрів, як середньоквадратичне відхилення остову ланцюга, радіус інерції, площа поверхні, доступна для розчинника та середньоквадратичні флуктуації. Аналіз розрахованих параметрів для вивчених систем дозволив поліпшити попередні результати, отримані з використанням методу молекулярного докінгу. В цілому, отримані результати вказують на те, що системи Lz-F-AK3-11, Lz-R-AK75, Lz-R-AK56, Lz-N-AK75, Lz-N-AK3-11 і Lz-M-AK75 мають найвищу стабільність серед досліджуваних систем барвник-лікарський препарат-білок та є потенційними кандидатами для спрямованої доставки досліджуваних антивірусних агентів.
Ключові слова: *комплекси білок-лікарський препарат-барвник; противірусні агенти; ціанінові барвники; молекулярна динаміка*

CHARACTERISTICS OF NONLINEAR DUST ACOUSTIC WAVES *(DAWS)* PROPAGATING IN AN INHOMOGENEOUS COLLISIONLESS MAGNETIZED DUSTY PLASMA

Hirak Jyoti Dehingia*, **Paramananda Deka**#

Department of Mathematics, Dibrugarh University, Assam, India
Corresponding Author e-mail: *hirakjyotidehingia11@gmail.com, #pndeka@dibru.ac.in

In this paper, we have presented our investigation on the characteristic of nonlinear dust acoustic waves *(DAWs)* propagating in an inhomogeneous collisionless magnetized dusty plasma *(MDP)*. In this problem, we have considered a collisionless plasma consisting of nonthermal ions, non-extensive electrons and negatively charged dust grains. Using the *reductive perturbation theory (RPT)* we have derived the modified *Zakharov-Kuznetsov (m-ZK)* equation. The solution of *m-ZK* equation indicates the nonlinear characteristics of the *DASWs* in plasma. Our investigation also predicts how the amplitudes of nonlinear *DASWs* are significantly modified due to the influence of magnetic field, non-extensive electrons and inhomogeneity parameters in plasma. The results obtained in this investigation may be useful for understanding the propagation characteristics and modification of structures of nonlinear waves in both laboratory and astrophysical plasmas.

Keywords: *Dusty plasma; RPT; $m-ZK$ equation; Inhomogeneous plasma; non-extensive electrons*
PACS: 52.27.Lw, 05.45.-a, 95.30.Qd

I. INTRODUCTION

Solitary waves or solitons are nonlinear wave packets which maintain their shapes during their propagation at a particular speed. Solitons occur due to the mutual cancellation of the nonlinear effects and dispersive effects in the medium. Washimi and Taniuti [1] derived the *Korteweg de-Vries (KdV)* equation to describe the ion-acoustic solitons *(IAS)*. Nishikawa and Kaw [2] discussed the propagation of ion-acoustic solitons in an inhomogeneous plasma. Theoretically, Kuehl [3] discussed the propagation and reflection of ion-acoustic solitons in an inhomogeneous plasma. He has observed the variations in the soliton amplitudes of incident and reflected solitons. Nejoh [4] investigated the effects of ion temperature on the characteristics of soliton propagation in a relativistic plasma. A few plasma physics researchers studied the properties and characteristics of solitary waves propagating in the presence of various physical situations such as negative ions [5,6] and dust grains [7] in the plasma and solitary wave excitation in nonequilibrium plasmas [30-33]. Kakad *et al.* [8] provided an experimental study on the validity of fluid theory and chain formation of nonlinear wave propagation in a collisional magnetized plasma. Later, using *Kundu-nonlinear Schrödinger equation (Kundu-NLS)* Shi *et al.* [9] discussed the dynamics of nonlinear nonlocal solitary wave solutions propagating in an inhomogeneous plasma. Rani and Yadav [10] studied the characteristics of electron acoustic-solitary waves *(EASWs)* propagating in a dense magnetized collisional plasma in the presence of degenerate quantum electrons. Recently, Dehingia and Deka [11] have discussed the variations of *IAS* structures propagating in an inhomogeneous plasma in the presence of hot isothermal electrons. They have observed that at a certain point the structure of *IAS* gets deformed due to the presence plasma inhomogeneity during their propagation through the system.

Dusty plasma *(DP)* is a very important research field in plasma physics. *DP* consists of ions, electrons, and charged dust particles. When the dust particles are included in the plasma, the system indicates some complex behaviours in the system. Thus, *DP* is also termed as the multicomponent plasma or complex plasma. These *DPs* are observed in planetary magnetospheres, cometary environments, planetary ring, and nebulas etc. [12]. The study of dusty plasma helps us to understand the astrophysical phenomena, the geophysical theories, and importance of space missions etc. Goertz [13] worked on the fundamental properties of dusty plasma in an astrophysical environment. Many researchers studied the basic properties of dust ion-acoustic waves (DIAWs) [14] and dust-acoustic waves (DAWs) [15] propagating in an inhomogeneous plasma. Shukla and Mamun [16] introduced basic structures, properties and propagation of *DAWs, DIAWs,* dust-cyclotron waves *(DCWs)* and dust lattice waves *(DLWs)* etc. in inhomogeneous plasmas. Using the kinetic theory Baluku and Hellberg [17] provided a brief description on the propagation of *DIAWs* in the presence of $k-$ distributed electrons and negatively charged dust grains in the plasma. Alinejad, and Khorrami [18] studied on the structures of *DAWs* propagation in the presence of trapped ions and polarized Debye sheath in a strongly coupled inhomogeneous plasma. Atteya, Sultana, and Schlickeiser [19] investigated the effect of superthermal electrons, positive ions as well as negative ions in the propagation of *DIAWs* in an inhomogeneous magnetized plasma. Akhtar *et al.* [20] discussed the dynamics of *DAWs* and *DCWs* during their propagation in the magnetized plasma. Rehman, Mahmood, and Hussain [21] studied the behaviour of nonlinear magneto-acoustic waves *(MAWs)* in the presence of warm, collisionless pair-ion (PI) fullerene plasma. In their analysis, they concluded that due to the presence of ion inertial length in the plasma, the effects of wave dispersion are observed in PI plasma. In the study of plasma physics, linear theory is used to study the

small amplitude waves without considering the nonlinearities in the plasma. But in the case of large amplitude waves, nonlinearities cannot be ignored. In the plasma studies, nonlinearities play an important role in the nature, properties and characteristics of the dusty wave phenomena. In experimental and theoretical studies, we observe various nonlinear dusty wave structures such as shock waves, rouge waves, solitons, supersolitons etc. Atteya *et al.* [22] studied the propagation of nonlinear *DAWs* in an inhomogeneous quantum plasma in the presence of magnetic field. They have observed that the low-frequency longitudinal waves have the potential to trap electrons which obtained from the high-intensity magnetic fields during the modulation of plasma species. Using the Pseudopotential method Pakzad and Nobahar [23] discussed the important properties of *DIASWs* propagating in an inhomogeneous unmagnetized plasma in the presence of superthermal electrons, inertial ions, and stationary dust grain particles. They have also analysed the modification of nonlinear wave structures of *DIAS* propagating in an inhomogeneous plasma in the presence of the critical parametric values of superthermal electrons and electron-ion density ratio. Dehingia and Deka [24-27] studied the various properties of *DAWs*, modification in *DASW* structures, effect of dust particles in soliton propagation and propagation of nonlinear waves in the presence of negatively charged dust grains with charge fluctuations in inhomogeneous plasma. There are still many scopes to study on the propagation characteristics of nonlinear wave structures in inhomogeneous plasma depending on the various astrophysical conditions. In this problem, we consider a collisionless magnetized plasma consisting of cold ions, non-extensive electrons and negatively charged dust grains. In this investigation, we have discussed the characteristics of nonlinear *DASWs* propagating in an inhomogeneous collisionless magnetized plasma in the presence of nonthermal ions with non-extensive electrons and negatively charged dust grains.

II. GOVERNING EQUATIONS

In this article, we have studied the characteristics of nonlinear *DASWs* propagation in the presence of negatively charged mobile dust grains, $q-$ distributed non-extensive electrons of temperatures T_{e1} and T_{e2}, and nonthermal ions with finite temperature T_i, where $T_i \ll T_{e1} \ll T_{e2}$ in an inhomogeneous magnetized plasma. These temperatures are expressed in the units of energy. The set of governing equations for nonthermal ions, non-extensive electrons and negatively charged dust grains in a dusty plasma system are given by [25-29]

$$\frac{\partial \vec{n}_d}{\partial t} + \vec{\nabla}.(n_d \vec{u}_d) = 0 \tag{1}$$

$$\frac{\partial \vec{u}_d}{\partial t} + (\vec{u}_d.\vec{\nabla})\vec{u}_d + \vec{\nabla}\phi + \alpha(\vec{u}_d \times \hat{z}) = 0 \tag{2}$$

$$\vec{\nabla}^2\phi = n_d + \mu_1[1 + (q_1 - 1)]^{\frac{(q_1+1)}{2(q_1-1)}} + \mu_2[1 + (q_2 - 1)]^{\frac{(q_2+1)}{2(q_2-1)}} - \mu_i[1 + (\beta\phi + \beta\phi^2 + \cdots)e^{-\phi}]^{\frac{(q_2+1)}{2(q_2-1)}} \tag{3}$$

$$n_i = n_{i0}\left[1 + \beta\left(\frac{e\phi}{T_i}\right) + \beta\left(\frac{e\phi}{T_i}\right)^2\right]e^{-\left(\frac{e\phi}{T_i}\right)} \tag{4}$$

$$n_{e1} = n_{e10}\left[1 + (q_1 - 1)\left(\frac{e\phi}{T_i}\right)\right]^{\frac{(q_1+1)}{2(q_1-1)}} \tag{5}$$

$$n_{e2} = n_{e20}\left[1 + (q_2 - 1)\left(\frac{e\phi}{T_i}\right)\right]^{\frac{(q_2+1)}{2(q_2-1)}} \tag{6}$$

Now, for equilibrium condition, the charge neutrality equation is given by $n_{i0} = n_{e10} + n_{e20} + Z_d n_{d0}$ where we consider n_{e10}, n_{e20} and n_{i0} are taken as number densities of low temperature and high temperature electrons and ion number density respectively in the plasma. In the above equations, Z_d is dust charge number, n_d is the density of dust grains, and q_1 and q_2 are the strengths of non-extensivity of two types electrons with temperatures T_{e1} and T_{e2} respectively in the plasma. In this mathematical model, $\vec{u}_d$ reparents the dust fluid velocity of the dust grain particles normalized by $C_d = \sqrt{\frac{Z_d T_i}{m_d}}$, m_d is the mass of dust grains, $\vec{\phi}$ is the electrostatic potential which is normalized by $\frac{T_i}{e}$, time t is also normalized by $\omega_{pd}^{-1} = \sqrt{\frac{m_d}{4\pi n_{d0} Z_d^2 e^2}}$ and the space variable x is normalized by $\lambda_{Dm} = \sqrt{\frac{T_i}{4\pi n_{d0} Z_d e^2}}$. We have also considered the nonthermal parameters are $\beta = \frac{4\gamma}{(1+3\gamma)}$, where γ is the parameter which determines the density population of nonthermal ions in the plasma. The values of the parameters β and γ are taken to be $0 \le \beta \le \frac{4}{3}$ and $\gamma \ge 0$. In the above equations, we have also considered some set of dimensionless quantities such as $\mu_i = \frac{n_{i0}}{Z_d n_{d0}}$, $\mu_1 = \frac{n_{e10}}{Z_d n_{d0}}$, $\mu_2 = \frac{n_{e20}}{Z_d n_{d0}}$, $\alpha = \frac{\omega_{cd}}{\omega_{pd}}$, $\sigma_1 = \frac{T_i}{T_{e1}}$, and $\sigma_2 = \frac{T_i}{T_{e2}}$ etc.

III. DERIVATION OF MODIFIED ZK-EQUATION

To study the propagation of nonlinear *DASWs* and their characteristics for small amplitude waves, we use the *RPT* to derive the *m-ZK* equation for the plasma system. The solutions of m-ZK equation show the propagation characteristics

of the nonlinear *DASWs* in the plasma. To use the *RPT*, we use a set of appropriate stretched coordinates [1, 24-27] for the weakly inhomogeneous plasma is as follows:

$$X = \varepsilon^{\frac{1}{2}}x, Y = \varepsilon^{\frac{1}{2}}y, Z = \varepsilon^{\frac{1}{2}}(z - Vt), \tau = \varepsilon^{\frac{3}{2}}t \tag{7}$$

where the phase velocity V is normalized by C_d, and the smallness parameter ε measures the strength of the dispersion. Here, all the axes X, Y, and Z are normalized by Debye length (λ_m), and τ is normalized by ion plasma period $\left(\frac{1}{\omega_{pd}}\right)$ respectively.

To apply the *RPT*, we use expanded dependent variables $u_{dx}, u_{dy}, u_{dz}, n_d$ and ϕ along with their perturbed values and in terms of ε is as follows [26]:

$$\begin{bmatrix} n_d \\ u_{dx} \\ u_{dy} \\ u_{dz} \\ \phi \end{bmatrix} = \begin{bmatrix} 1 \\ 0 \\ 0 \\ 0 \\ 0 \end{bmatrix} + \varepsilon \begin{bmatrix} n_{d1} \\ 0 \\ 0 \\ u_{dz1} \\ \phi_1 \end{bmatrix} + \varepsilon^{\frac{3}{2}} \begin{bmatrix} 0 \\ u_{dx1} \\ u_{dy1} \\ 0 \\ 0 \end{bmatrix} + \varepsilon^2 \begin{bmatrix} n_{d2} \\ u_{dx2} \\ u_{dy} \\ u_{dz2} \\ \phi_2 \end{bmatrix} + \cdots \tag{8}$$

Now, using Eqs. (7) and (8) into Eqs. (1) − (6), we obtain the 1st order quantities for z − component of momentum and Poisson's equations are as follows:

$$n_{d1} = -\frac{\phi_1}{V^2}, u_{dz1} = -\frac{\phi_1}{V}, \tag{9}$$

$$V = \frac{1}{\sqrt{\mu_i(1-\beta) + \frac{\mu_1\sigma_1}{2}(q_1+1) + \frac{\mu_2\sigma_2}{2}(q_2+1)}}, \tag{10}$$

The above Eq. (10) indicates the phase velocity of the *DASWs* under the influence of non-extensive electrons, nonthermal ions and negatively charged dust grains propagating in an inhomogeneous *MDP*.

Similarly, we obtain 1st order x and y components for the momentum equation are as follows:

$$u_{dx1} = -\frac{1}{\alpha}\frac{\partial \phi_1}{\partial Y}, \tag{11}$$

$$u_{dy1} = \frac{1}{\alpha}\frac{\partial \phi_1}{\partial X}. \tag{12}$$

The above Eqs. (11) and (12) represents the velocities of *DASWs* in x and y components in the plasma. These two equations also satisfy the 2nd order continuity equation for *DASWs* in the plasma. Again, using Eqs. (7) and (8) in Eqs. (1) − (6) and eliminating the 1st order terms of x and y components in momentum and Poisson's equation, we get the 2nd order terms are as follows:

$$u_{dx2} = -\frac{V}{\alpha^2}\frac{\partial^2 \phi_1}{\partial Z \partial X}, \tag{13}$$

$$u_{dy2} = -\frac{V}{\alpha^2}\frac{\partial^2 \phi_1}{\partial Z \partial Y}, \tag{14}$$

$$\frac{\partial^2 \phi_1}{\partial X^2} + \frac{\partial^2 \phi_1}{\partial Y^2} + \frac{\partial^2 \phi_1}{\partial Z^2} = \mu_1 M + \mu_2 N - \mu_i P + n_{d2}, \tag{15}$$

where,

$$M = (q_2 + 1)\left\{\frac{\sigma_2\phi_2}{2} + \frac{(3-q_2)\sigma_2^2\phi_1^2}{8}\right\}, \tag{16}$$

$$N = (q_2 + 1)\left\{\frac{\sigma_2\phi_2}{2} + \frac{(3-q_2)\sigma_2^2\phi_1^2}{2}\right\}, \tag{17}$$

$$P = (\beta - 1)\phi_2 + \frac{\phi_1^2}{2}. \tag{18}$$

The above Eqs. (13) − (15) represents the x and y components of the dust polarization drift. Now, proceeding the same way we will obtain the higher order terms of continuity equation and z − components from momentum equations. Now, eliminating the higher order terms n_{d2}, u_{dy2}, and ϕ_2 finally we obtain the equation is as follows:

$$\frac{\partial \phi_1}{\partial \tau} + EF\phi_1\frac{\partial \phi_1}{\partial Z} + \frac{1}{2}E\frac{\partial}{\partial Z}\left[\frac{\partial^2}{\partial Z^2} + G\left(\frac{\partial^2}{\partial X^2} + \frac{\partial^2}{\partial Y^2}\right)\right]\phi_1 = 0, \tag{19}$$

where,

$$E = V^3, \tag{20}$$

$$F = \frac{1}{2}\left[\mu_i - \frac{1}{4}\left\{\begin{array}{l}\mu_1\sigma_1^2(q_1+1)(3-q_1)\\ +\mu_2\sigma_2^2(q_2+1)(3-q_2)\end{array}\right\} - \frac{3}{V^4}\right], \tag{21}$$

$$G = 1 + \frac{1}{\alpha^2}. \tag{22}$$

The above equation (19) represents the $m - ZK$ equation which describes the oblique propagation of $DASWs$ in the presence of non-extensive electrons having two distinct temperatures in the MDP.

IV. SOLUTION OF m-ZK EQUATION

To study the characteristics of nonlinear $DASWs$ propagating in an inhomogeneous plasma, we have considered the plasma with an effect of magnetic field at an angle δ with Z-axis. Considering the Y-axis fixed, the coordinate axes are assumed to be rotated at an angle δ which is significantly modified under the influence of magnetic field, non-extensive electrons and inhomogeneity parameters in the plasmas. Thus, we use a set of transformation equations for the independent variables is as follows:

$$\left.\begin{array}{ll}\rho = X\cos\delta - Z\sin\delta, & \tau = t,\\ \xi = X\sin\delta + Z\cos\delta, & \eta = Y,\end{array}\right\}. \tag{23}$$

Using the above transformation equations [1], [26], [27], we rewrite the above $m - ZK$ Eq. (19) is as follows:

$$\frac{\partial\phi_1}{\partial\tau} + \delta_1\phi_1\frac{\partial\phi_1}{\partial\xi} + \delta_2\frac{\partial^3\phi_1}{\partial\xi^3} + \delta_3\phi_1\frac{\partial\phi_1}{\partial\rho} + \delta_4\frac{\partial^3\phi_1}{\partial\rho^3} + \delta_5\frac{\partial^3\phi_1}{\partial\xi^2\partial\rho} + \delta_6\frac{\partial^3\phi_1}{\partial\rho^2\partial\xi} + \delta_7\frac{\partial^3\phi_1}{\partial\xi\partial\eta^2} + \delta_8\frac{\partial^3\phi_1}{\partial\rho\partial\eta^2} = 0, \tag{24}$$

where

$$\left.\begin{array}{l}\delta_1 = EF\cos\delta\\ \delta_2 = \frac{1}{2}E(\cos^3\delta + G\sin^2\delta\cos\delta)\\ \delta_3 = -EF\sin\delta\\ \delta_4 = -\frac{1}{2}E(\sin^3\delta + G\sin\delta\cos^2\delta)\\ \delta_5 = E\left\{G\left(\sin\delta\cos^2\delta - \frac{1}{2}\sin^3\delta\right) - \frac{3}{2}\sin\delta\cos^2\delta\right\}\\ \delta_6 = -E\left\{G\left(\sin^2\delta\cos\delta - \frac{1}{2}\cos^3\delta\right) - \frac{3}{2}\sin^2\delta\cos\delta\right\}\\ \delta_7 = \frac{1}{2}EG\cos\delta\\ \delta_8 = -\frac{1}{2}EG\sin\delta\end{array}\right\}, \tag{25}$$

Now, using the transformation equation [27], the steady state solution for $m - ZK$ equation is given by

$$\phi_1 = \phi_0(H), \tag{26}$$

where $H = \xi - V_0t$ and V_0 represents the constant speed normalized by C_d. Using the above transformation equation, the above $m - ZK$ equation can be rewritten in steady state form is as follows:

$$-V_0\frac{d\phi_0}{dH} + \delta_1\phi_0\frac{d\phi_0}{dH} + \delta_2\frac{d^3\phi_0}{dH^3} = 0. \tag{27}$$

Now, using appropriate boundary conditions, i.e., $\phi_1 \to 0$, $\frac{d\phi_1}{dH} \to 0$, $\frac{d^2\phi_1}{dH^2} \to 0$ as $H \to \pm\infty$. Then solitary wave solution of Eq. (27) is given by

$$\phi_0(H) = \phi_m \text{sech}^2(WH), \tag{28}$$

where $\phi_m = \frac{3V_0}{\delta_1}$ and $W = \sqrt{\frac{V_0}{4\delta_1}}$ represents the amplitude and inverse width of the solitary wave solutions respectively. Since $V_0 > 0$, so it is clear from the Eqs. (19), (21) and (24) that based on the sign of F, the solitary waves or solitons will only be associated with negative potential ($\phi_m < 0$) of the wave propagation in the plasma.

In the above derivations, we have observed that the Eq. (27) is the one-dimensional steady state form of $m - KdV$ equation. The steady state solution of $m - ZK$ Eq. (27) and standard $m - KdV$ equation both gives the same results in one-dimensional steady state cases. To obtain the localized solitary wave solution, we use appropriate boundary conditions and transformation equations [27] to solve the Eq. (27). In this problem, we have considered the steady state solution of $m - ZK$ Eq. (19) in one-dimensional cases where all $\delta's \to 0$ provided δ_1 and δ_2. Thus, δ_1 and δ_2 will occur in our wave solutions obtained in our above derivations.

V. RESULTS AND DISCUSSIONS

Using the above results and derivations, we have plotted some figures to describe the propagation and characteristics of nonlinear *DASWs* propagating in an inhomogeneous *MDP* consisting of nonthermal ions, non-extensive electron with different temperatures and negatively charged massive dust grains. In Fig. 1 and Fig. 2, we have plotted the graphs to show the variations of amplitudes of *DASWs* w.r.t. σ_1 and σ_2 depending on the various parametric values of non-extensive parameters q_1 and q_2 respectively. Fig. 3 shows the variations of width (W) of *DASWs* w.r.t. number density of relative electrons (μ_1) depending on the various parametric values of nonthermal parameter (β). Depending on the various values of the magnetic parameter α, the variations of width (W) of *DASWs* w.r.t. oblique parameter δ are also shown in Fig. 4. Finally, Fig. 5 describes the variations of phase velocities of *DASWs* w.r.t. the nonthermal parameter (β) propagating in an inhomogeneous magnetized dusty plasma. In this problem, we have also investigated the effect of magnetic field on the propagation of *MDP* under the above considered plasma situations.
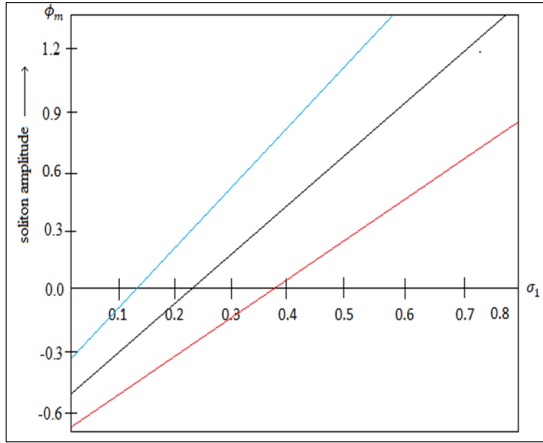
Figure 1. Variation of soliton amplitude (ϕ_m) of *DASWs* with σ_1 for various values of $q_1 = 0.3, -0.3, -0.8$ with $\delta = 35°$, $q_2 = 1.5, \sigma_2 = 0.05, \mu_1 = 0.3, \mu_2 = 0.2, U = 0.2$ and $\beta = 0.1$
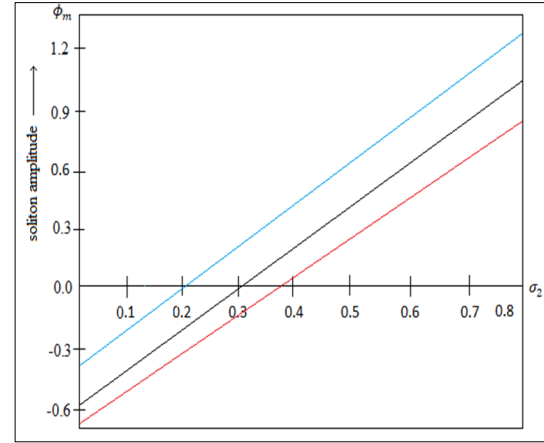
Figure 2. Variation of soliton amplitude (ϕ_m) of *DASWs* with σ_1 for various values of $q_2 = 0.4, 0.6, -0.8$ with $q_1 = -0.8, \sigma_1 = 0.3, \sigma_2 = 0.2, U = 0.2, \beta = 0.1$.

To study the effects of magnetic field and propagation characteristics of *DASWs* propagating in an inhomogeneous plasma in the nonthermal ions, non-extensive electron with different temperatures and negatively charged massive dust grains, we have used *RPT* to derive and solve the $m - ZK$ equation for small amplitude waves by using the various dependent variables of perturbed number densities of ions, electrons and dust grains with dust velocities and electrostatic potentials in the plasma. From the above investigations, Fig. 1 indicate that the magnitudes of amplitudes of *DASWs* increases gradually with the increase in the temperature ratios (σ_1) and non-extensive parameter (q_1).
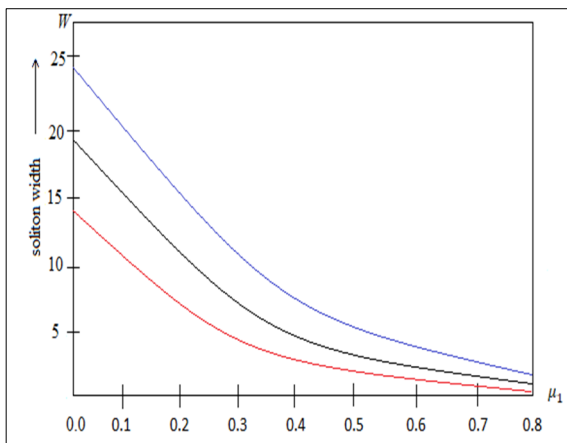
Figure 3. Variation of soliton width (W) of *DASWs* with μ_1 for various values of $\beta = 0.2, 0.4, 0.6$ with $\delta = 35°$, $q_1 = -0.8, \mu_2 = 1.5, \sigma_1 = 0.3, U = 0.2$ and magnetic field parameter $\alpha = 0.1$.
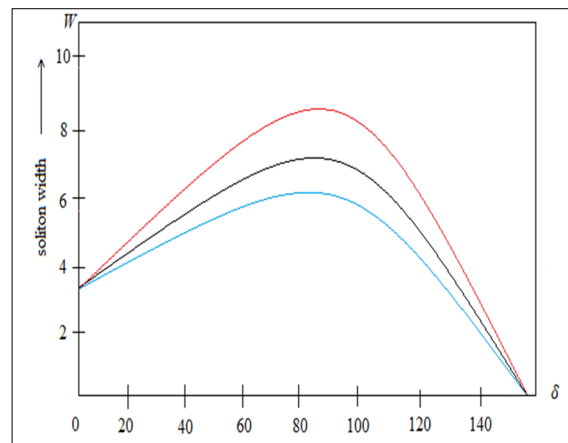
Figure 4. Variation of soliton width (W) of *DASWs* with δ for various values of $\alpha = 0.2, 0.3, 0.4$ with $q_1 = -0.8, \sigma_2 = 0.01, \delta = 35°, U = 0.2, \sigma_1 = 0.3, q_2 = 1.5, \mu_1 = 0.3, \mu_2 = 0.2, U = 0.2, \beta = 0.1$.

On the other hand, Fig.2 shows that the magnitudes of widths of *DASWs* decreases gradually with the increase in the temperature ratios (σ_2) and non-extensive parameter (q_2). However, in Fig. 3, we have observed that the width of *DASWs* vary adversely with the increasing or decreasing values of number density of relative electrons (μ_1) depending on the various parametric values of nonthermal parameter (β). The above figures also indicate that with the increase in

the number density of relative electrons (μ_1) and the values of nonthermal parameter (β) for ions, increases the width of *DASWs* during their propagation through the plasma. This shows the importance of nonthermal ions which play an important role on stabilizing, forming and the propagation of *DASWs* in an inhomogeneous plasma with various physical situations e.g., nonthermal ions and non-extensive electrons present in the laboratory and astrophysical plasmas such as protostellar disk, circumstellar and interstellar clouds, cometary tails, Saturn's rings, earth's magnetospheres, solar winds and in asteroid zones etc. In Fig. 4, we have seen that the variations in the oblique parameter δ effects the width (W) of *DASWs* which increases due to the presence of δ with lower angles in between $0°$ and $45°$. On the other hand, the width (W) of *DASWs* which decreases with higher angles of δ in between $45°$ and $90°$. Also, when $\delta \to 90°$, the amplitude and width of the soliton tends to ∞ and 0 respectively. This concludes that the waves will not be considered as electrostatic anymore. In this investigation, we have considered the magnetic field parameter as $\alpha = \frac{\omega_{cd}}{\omega_{pd}}$, where ω_{cd} and ω_{pd} are dust cyclotron frequency and dust plasma frequency respectively. Fig. 4 also shows that while dust cyclotron frequency i.e., α increases, the width (W) of the soliton decreases in the plasma.
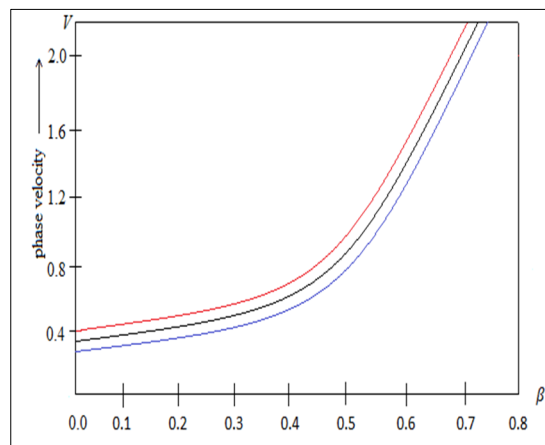
Figure 5. Variation of phase velocity (V) of *DASWs* with β for various values of $q_1 = q_2 = -0.9, 0.5, 1.5$ with $\delta = 35°$, $\mu_1 = 0.3, \mu_2 = 0.2, \sigma_1 = 0.3, \sigma_2 = 0.05$.

In the above derivations, we have also derived the dispersion relation and phase velocity in Eq. (10). However, in Fig. 4, it is also observed with the increase in the values of α, the amplitudes of the solitary wave structures become relatively spiky and so that the system become destabilized. On the other hand, the width (W) of *DASWs* decreases with the increase in the value of external magnetic field parameter α. In Fig. 5, we have shown the effects of nonthermal ions and non-extensive electrons and the phase velocity of the *DASWs* propagating in an inhomogeneous *MDP*. In Fig. 5, we have also shown the increase of phase velocity of the *DASWs* slowly and steadily but later it increases rapidly with the increasing values of nonthermal parameter (β) for ions in the plasma. When the parameters other than β are considered to be constant, the phase velocity of the *DASWs* increases rapidly with the increase in critical value of β. The critical value of nonthermality parameter (β) depends on the relatively non-extensive electrons present in the plasma. Also, when the electron non-extensivity increases, the nonthermality of ions increases in the modelled plasma which are shown in Fig. 5. From the above discussions, it is clear that the phase velocity of *DASWs* especially much depend on the nonthermality of ions. However, the phase velocity of *DASWs* less dependent on the non-extensivity of electrons present in the system.

VI. CONCLUSION

In this paper, we have studied the fundamental properties of *DASWs* propagating obliquely in an *MDP* consisting of nonthermal ions, non-extensive with distinct two temperature electrons and negatively charged dust grains. In this problem, we have also discussed the fundamental characteristics of the *DASWs* propagating in an inhomogeneous plasma under the above considered physical situations. We have observed that with the increase in dust cyclotron frequency, there is an increase in the spikes of amplitudes of *DASWs* structures in the plasma. The above results also indicate that with the increasing values of μ_1 and β, the width of *DA* solitons increases during their propagation through the inhomogeneous collisionless magnetized plasma. We have also observed that the oblique parameter δ effects the variations in the width (W) of *DASWs* which increases due to the presence of δ with lower angles in between $0°$ and $45°$. However, the width (W) of *DA* soliton decreases with the increasing angles of δ in between $45°$ and $90°$. In this investigation, the above results also imply that slowly and steadily the phase velocity of the *DA* soliton will increase but later, it will increase rapidly with the increasing values of β in the plasma. When the parameters are supposed to be constant except β, the phase velocity of the *DA* soliton rapidly increases with the rapid increase of critical value of β. The above results also indicate that with the increase in the magnitude of external magnetic field in *DASWs*, the width of the soliton decreases adversely. The results obtained in this problem may be useful for understanding the propagation of

localized electrostatic waves in both laboratory plasmas such as earthquake dynamics, dating of geological and archaeological minerals, dissipative optical lattices, double plasma machines, hot turbulent thermonuclear plasmas, radio frequency discharged plasmas etc. and astrophysical plasmas such as cosmology, galaxy clusters, self-gravitation polytopic systems, solar winds, Auroral regions, noctilucent clouds in Earth's atmosphere. Our results may also be useful for further study of the dynamics of the various nonlinear wave propagation in an inhomogeneous plasma under the various physical astrophysical situations.

ORCID

Hirak Jyoti Dehingia, https://orcid.org/0000-0002-3119-0842; **Paramananda Deka,** https://orcid.org/0000-0001-9485-9294

REFERENCES

[1] H. Washimi, and T. Taniuti, "Propagation of ion-acoustic solitary waves of small amplitude," Phys. Rev. Lett. **17**, 996–998 (1966). https://doi.org/10.1103/PhysRevLett.17.996

[2] N. Nishikawa, and K. Kaw, "Propagation of solitary ion-acoustic waves in inhomogeneous plasmas," Phys. Lett. A, **50**, 455–456 (1975). https://doi.org/10.1016/0375-9601(75)90124-3

[3] H.H. Kuehl, "Reflection of an ion-acoustic soliton by plasma inhomogeneities," Phys. Fluids, **26**(6), 1577–1583 (1983). https://doi.org/10.1063/1.864292

[4] Y. Nejoh, "The effect of the ion temperature on the ion-acoustic solitary waves in a collisionless relativistic plasma," J. Plasma Phys. **37**(3), 487–495 (1987). https://doi.org/10.1017/S0022377800012320

[5] D.K. Singh, and H.K. Malik, "Soliton reflection in a negative ion containing plasma: Effect of magnetic field and ion temperature," Phys. Plasmas, **13**(8), 082104(1–10) (2006). https://doi.org/10.1063/1.2335427

[6] D.K. Singh, and H.K. Malik, "Modified Korteweg–de Vries soliton evolution at critical density of negative ions in an inhomogeneous magnetized cold plasma," Phys. Plasmas, **14**(6), 062113 (2007). https://doi.org/10.1063/1.2743026

[7] D. Xiao, J.X. Ma, Y. Li, Y. Xia, and M.Y. Yu, "Evolution of nonlinear dust-ion-acoustic waves in an inhomogeneous plasma," Phys. Plasmas, **13**(5), 052308 (2006). https://doi.org/10.1063/1.2196247

[8] A. Kakad, Y. Omura, and B. Kakad, "Experimental evidence of ion acoustic soliton chain formation and validation of nonlinear fluid theory," Physics of Plasmas, **20**(6), 062103 (2013). https://doi.org/10.1063/1.4810794

[9] X. Shi, J. Li, and C. Wu, "Dynamics of soliton solutions of the nonlocal Kundu-nonlinear Schrödinger equation," Chaos, **29**, 023120 (2019). https://doi.org/10.1063/1.5080921

[10] N. Rani, and M. Yadav, "Propagation of nonlinear electron acoustic solitons in magnetized dense plasma with quantum effects of degenerate electrons," AIP Conference Proceedings, **2352**, 030008 (2020). https://doi.org/10.1063/5.0052436

[11] H.J. Dehingia, and P.N. Deka, "Structural Variations of Ion-Acoustic Solitons," in: *Nonlinear Dynamics and Applications: Proceedings of the ICNDA 2022* (pp. 97-104). (Springer International Publishing, Cham, 2022).

[12] L. Spitzer Jr., "Review of Publications: Physical Processes in the Interstellar Medium", Journal of the Royal Astronomical Society of Canada, **72**, 349 (1978). https://articles.adsabs.harvard.edu/pdf/1978JRASC..72..349S

[13] C.K. Goertz, "Dusty plasmas in the solar system", Reviews of Geophysics, **27**(2), 271-292 (1989). https://doi.org/10.1029/RG027i002p00271

[14] N.N. Rao, P.K. Shukla, and M.Y. Yu, "Dust-acoustic waves in dusty plasmas", Planetary and space science, **38**(4), 543 (1990). https://doi.org/10.1016/0032-0633(90)90147-I

[15] P.K. Shukla, and V.P. Silin, "Dust ion-acoustic wave", Physica Scripta, **45**(5), 508 (1992). https://doi.org/10.1088/0031-8949/45/5/015

[16] P.K. Shukla, and A.A. Mamun, *Introduction to dusty plasma physics*, (Institute of Physics Publishing Ltd, Bristol, 2015).

[17] T.K. Baluku, and M.A. Hellberg, "Kinetic theory of dust ion acoustic waves in a kappa-distributed plasma", Physics of Plasmas, **22**(8), 083701 (2015). https://doi.org/10.1063/1.4927581

[18] H. Alinejad, and V. Khorrami, "Effects of Polarized Debye Sheath and Trapped Ions on Solitary Structures in a Strongly Coupled Inhomogeneous Dusty Plasma", IEEE Transactions on Plasma Science, **46**(4), 755 (2017). https://doi.org/10.1109/TPS.2017.2749382

[19] A. Atteya, S. Sultana, and R. Schlickeiser, "Dust-ion-acoustic solitary waves in magnetized plasmas with positive and negative ions: The role of electrons superthermality", Chinese journal of physics, **56**(5), 1931 (2018). https://doi.org/10.1016/j.cjph.2018.09.002

[20] N. Akhtar, S.A. El-Tantawy, S. Mahmood, and A.M. Wazwaz, "On the dynamics of dust-acoustic and dust-cyclotron freak waves in a magnetized dusty plasma", Romanian Reports in Physics, **71**, 403 (2019). https://rrp.nipne.ro/2019/AN71403.pdf

[21] H. Ur-Rehman, S. Mahmood, and S. Hussain, "Magneto-acoustic solitons in pair-ion fullerene plasma", Waves in Random and Complex Media, **30**(4), 632-642 (2020). https://doi.org/10.1080/17455030.2018.1549762

[22] A. Atteya, M.A. El-Borie, G.D. Roston, and A.S. El-Helbawy, "Nonlinear dust acoustic waves in an inhomogeneous magnetized quantum dusty plasma", Waves in Random and Complex Media, **33**, 329-344 (2021). https://doi.org/10.1080/17455030.2021.1880030

[23] H.R. Pakzad, and D. Nobahar, "Dust-ion acoustic solitons in superthermal dusty plasmas", New Astronomy, **93**, 101752 (2022). https://doi.org/10.1016/j.newast.2021.101752

[24] H. Dehingia, "Various Aspects of Dust-Acoustic Solitary Waves (DAWs) in Inhomogeneous Plasmas," in: *Plasma Science - Recent Advances, New Perspectives and Applications*, edited by S. Singh, (IntechOpen, 2022). https://doi.org/10.5772/intechopen.109160

[25] H. Dehingia, and P.N. Deka, "Effects of dust particles on dust acoustic solitary waves (DASWs) propagating in inhomogeneous magnetized dusty plasmas (MDPs) with dust charge fluctuations," in: *Int. Conf. Adv. Trans. Phenomena*, **1**(4), 56-58 (2022).

[26] H.J. Dehingia, and P.N. Deka, "Structural Variations of Dust Acoustic Solitary Waves (DASWs) Propagating in an Inhomogeneous Plasma," East European Journal of Physics, (1), 19-27 (2023). https://doi.org/10.26565/2312-4334-2023-1-02

[27] H.J. Dehingia, and P.N. Deka, "Propagation of nonlinear dust-acoustic solitary waves under the effect of non-extensive electrons in inhomogeneous collisional magnetized dusty plasma," J. Korean Phys. Soc. **83**, 337–343 (2023). https://doi.org/10.1007/s40042-023-00854-2

[28] F. Verheest, and M.A. Hellberg, "Nonthermal effects on existence domains for dust-acoustic solitary structures in plasmas with two-temperature ions," Physics of Plasmas, **17**(2), 023701 (2010). https://doi.org/10.1063/1.3299356

[29] N.N. Rao, and P.K. Shukla, "Coupled Langmuir and ion-acoustic waves in two-electron temperature plasmas," Physics of Plasmas, **4**(3), 636-645 (1997). https://doi.org/10.1063/1.872160

[30] V. Maslov, and H. Schamel, "Growing electron holes in drifting plasmas," Physics Letters A, **178**(1-2), 171 (1993). https://doi.org/10.1016/0375-9601(93)90746-M

[31] H. Schamel, and V.I. Maslov, "Adiabatic growth of electron holes in current-carrying plasmas," Physica Scripta, T50, 42 (1994). https://doi.org/10.1088/0031-8949/1994/T50/006

[32] H. Schamel, and V.I. Maslov, "Langmuir Wave Contraction Caused by Electron Holes," Physica Scripta T, **82**, 122 (1999). https://doi.org/10.1238/Physica.Topical.082a00122

[33] V.I. Maslov, "Electron beam excitation of a potential well in a magnetized plasma waveguide," Physics Letters A, **165**(1), 63-68 (1992). https://doi.org/10.1016/0375-9601(92)91055-V

ХАРАКТЕРИСТИКИ НЕЛІНІЙНИХ ПИЛОВИХ АКУСТИЧНИХ ХВИЛЬ (DAWS), ЩО ПОШИРЮЮТЬСЯ В НЕОДНОРІДНІЙ НАМАГНІЧЕНІЙ ПИЛОВІЙ ПЛАЗМІ БЕЗ ЗІТКНЕНЬ

Хірак Джйоті Дехінгія, Парамананда Дека

Факультет математики, Університет Дібругарх, Ассам, Індія

У цій статті ми представили наше дослідження характеристик нелінійних пилових акустичних хвиль (DAWS), що поширюються в неоднорідній намагніченій пиловій плазмі (MDP) без зіткнень. У цій задачі ми розглядали плазму без зіткнень, що складається з нетеплових іонів, непротяжних електронів і негативно заряджених частинок пилу. Використовуючи відновну теорію збурень (RPT), ми вивели модифіковане рівняння Захарова-Кузнєцова (m-ZK). Рішення рівняння m-ZK вказує на нелінійні характеристики *DASW* у плазмі. Наше дослідження також передбачає, як амплітуди нелінійних *DASW* значно модифікуються через вплив магнітного поля, непротяжних електронів і параметрів неоднорідності в плазмі. Результати, отримані в цьому дослідженні, можуть бути корисними для розуміння характеристик розповсюдження та модифікації структур нелінійних хвиль як у лабораторній, так і в астрофізичній плазмі.

Ключові слова: *запилена плазма; RPT; рівняння m-ZK; неоднорідна плазма; неекстенсивні електрони*